

The effect of Knockout and Mutation of the Transmembrane  
BAX Inhibitor Motif containing protein 5 (TMBIM5) on  
cellular and mitochondrial function in cells and mice

---

Dissertation

Zur Erlangung des Grades

Doktor der Naturwissenschaften

– Doktor rerum naturalium (Dr. rer. Nat.) –

Am Fachbereich Biologie

Der Johannes Gutenberg-Universität

in Mainz

Felicia Maja Dietsche (geb. Maull)

Geboren am 03.09.1991 in München

Mainz, 2021

When Prometheus stole fire from the gods and presented it to man, it was a gift of immense value (1). It provided heat against the cold, light against the dark, and a means of communication. Yet, with this gift came also the destructive power of uncontrolled fire with its ability to imperil man's very existence.

This myth of the gift of fire to man can serve as the life motif for the evolutionary gift of  $\text{Ca}^{2+}$  to the cell. This ion has become the means of regulating heat production and of facilitating intracellular communication. Yet, with this gift has also come a destructive potential: excess calcium ions are cellular toxins (2). Because of the potential for toxicity, an elaborate system has been developed to ensure the maintenance of cellular  $\text{Ca}^{2+}$  homeostasis over a wide range of circumstances (3).

From: Rasmussen, H.; Barrett, P.; Smallwood, J.; Bollag, W.; Isales, C. (1990): Calcium ion as intracellular messenger and cellular toxin. Environmental health perspectives. 84. S. 17–25.

---

Erstbetreuer:

Zweitbetreuer/Erstgutachter:

Zweitgutachter:

Date of oral examination:

This work was supported by funding from the *Deutsche Forschungsgemeinschaft* and by fellowships from the Mainz Research School of Translational Biomedicine and the *Joachim Herz-Stiftung*. It was performed in the laboratory of [REDACTED] [REDACTED] University Medical Center of Johannes Gutenberg-University Mainz, Germany. Some experiments were conducted in the laboratory of [REDACTED] [REDACTED].

Parts of the results presented in this work were already published in: Seitaj, Bruno #; Maull, Felicia #; Zhang, Li; Wüllner, Verena; Wolf, Christina; Schippers, Philipp; La Rovere, Rita; Distler, Ute; Tenzer, Stefan; Parys, Jan B.; Bultynck, Geert; Methner, Axel (2020): Transmembrane BAX Inhibitor-1 Motif Containing Protein 5 (TMBIM5) Sustains Mitochondrial Structure, Shape, and Function by Impacting the Mitochondrial Protein Synthesis Machinery. *Cells*, 9. 2147. DOI: 10.3390/cells9102147

# These authors equally contributed and share first-authorship



### Declaration of Authorship

I, Felicia Dietsche, hereby declare that the submitted thesis is my own unaided work. All direct or indirect sources used are acknowledged as references. Moreover, I declare that this thesis has not been submitted for a higher degree to any other University or Institution.

Mainz, 18.11.2021

Felicia Dietsche

## Table of content

---

List of tables .....	V
List of figures .....	V
1. Abstract .....	1
2. Zusammenfassung.....	2
3. Introduction .....	3
3.1. Mitochondrial functions and functionality .....	3
3.1.1. Mitochondrial morphology and dynamics .....	4
3.1.1.1. Molecular regulation of fusion and fission .....	4
3.1.1.2. Cristae structure organisation.....	7
3.1.1.2.1. Composition of the Mitochondrial Contact Site and Cristae Organizing System	8
3.1.1.2.2. The CHCHD-family.....	9
3.1.2. Mitochondrial functions.....	10
3.1.2.1. ATP generation .....	10
3.1.2.2. Generation of reactive oxygen species .....	11
3.1.2.3. Generation of iron-sulfur-clusters.....	12
3.1.2.4. Lipid metabolism .....	12
3.1.2.5. Induction of apoptosis.....	14
3.1.2.6. Calcium buffering .....	16
3.2. The players involved in mitochondrial calcium handling.....	18
3.2.1. Calcium influx .....	19
3.2.1.1. The Mitochondrial Calcium Uniporter complex.....	19
3.2.1.2. mtCU-independent calcium uptake .....	23
3.2.2. Calcium export .....	26
3.2.2.1. mNCX.....	26
3.2.2.2. mCHX.....	27
3.2.2.3. mPTP.....	28
3.3. TMBIM5.....	30
4. Material and Methods.....	34
4.1. Material .....	34
4.1.1. Reagents.....	34
4.1.2. Commercial kits.....	36
4.1.3. Antibodies .....	36

4.1.4.	Buffers .....	37
4.2.	Methods .....	38
4.2.1.	Mouse line and genotyping.....	38
4.2.2.	Cell culture .....	40
4.2.2.1.	HAP1.....	40
4.2.2.2.	HEK293 (T).....	42
4.2.2.3.	Isolation and culture of primary mouse embryonic fibroblasts.....	43
4.2.2.4.	Transfection of cells .....	44
4.2.3.	Protein biochemistry .....	44
4.2.3.1.	Protein samples.....	44
4.2.3.1.1.	From cell lines .....	44
4.2.3.1.2.	From mouse tissue.....	44
4.2.3.1.3.	From splenocytes.....	45
4.2.3.2.	Mitochondrial Isolation.....	45
4.2.3.2.1.	From cell lines .....	45
4.2.3.2.2.	From mouse tissue.....	46
4.2.3.3.	BCA Assay .....	48
4.2.3.4.	Lowry Protein Assay .....	48
4.2.3.5.	Self-made gels .....	49
4.2.3.6.	Western Blotting .....	49
4.2.3.7.	Stripping of stained Western Blots .....	50
4.2.3.8.	Blue native polyacrylamide gel electrophoresis .....	51
4.2.4.	Glutathione assay.....	52
4.2.4.1.	Sample preparation from HEK 293 cells.....	52
4.2.4.2.	Sample preparation from mouse tissue.....	52
4.2.4.3.	Measurement of glutathione concentration .....	53
4.2.5.	Cloning of pPB-CAG-HA-mitoCepia-IRES-mitoBFP2 .....	54
4.2.6.	Flow cytometry.....	55
4.2.7.	Confocal microscopy .....	56
4.2.7.1.	Live cell imaging .....	56
4.2.7.1.1.	Transiently transfected HAP1 cells .....	56
4.2.7.1.2.	Stained primary mouse embryonic fibroblasts.....	57
4.2.7.2.	Fixed cells .....	58
4.2.7.2.1.	Immunocytochemistry.....	58
4.2.7.2.2.	Proximity ligation assay .....	59

4.2.8.	Transmission electron microscopy.....	60
4.2.9.	High-resolution respirometry.....	61
4.2.9.1.	Primary mouse embryonic fibroblasts .....	61
4.2.9.2.	Permeabilised cardiac fibres .....	62
4.2.10.	Mitochondrial Calcium uptake assay .....	64
4.2.11.	Mitochondrial swelling assay .....	65
4.2.12.	Pre-swelling test.....	66
4.2.13.	Mouse experiments .....	67
4.2.13.1.	Behavioural tests.....	67
4.2.13.1.1.	Open field.....	67
4.2.13.1.2.	Elevated plus-maze .....	67
4.2.13.1.3.	Rotarod .....	68
4.2.13.1.4.	Prepulse inhibition .....	68
4.2.13.1.5.	Inverted grid.....	69
4.2.14.	Metabolic chambers.....	69
4.2.15.	Respirometry during exhaustive exercise .....	69
4.2.16.	Blood analyses.....	72
4.2.16.1.	Lactate .....	72
4.2.16.2.	Interleukin-6 .....	72
4.2.16.3.	Oxidative burst .....	73
4.2.17.	Echocardiography.....	74
4.2.18.	Statistics .....	74
5.	Results .....	76
5.1.	TMBIM5 is not involved in the Mitochondrial contact site and cristae organizing system but affects OPA1 expression and splicing .....	76
5.2.	Ionomycin-induced mitochondrial Ca <sup>2+</sup> uptake is reduced in HAP1 TMBIM5 KO cells....	79
5.3.	The loss of TMBIM5 affects the Mitochondrial Calcium Uniporter complex.....	81
5.4.	TMBIM5 might interact with the EF-hand-containing protein LETM1.....	84
5.5.	TMBIM5 containing a point mutation in a conserved critical residue (D326R) is downregulated in primary mouse embryonic fibroblasts with mild effects on mitochondrial characteristics .....	87
5.6.	Homozygous D326R mice show increased perinatal lethality and reduced TMBIM5 expression in all tissues.....	92
5.7.	Behaviour and coordination of the D326R mice do not differ from the WT mice. ....	95
5.8.	The mutation does not affect the basal systemic metabolism in mice .....	97

5.9.	Even during exhaustive exercise, the systemic metabolism is not compromised by the point mutation in D326R mice .....	99
5.10.	Immune cells of D326R mice exhibit an impaired innate immune response .....	103
5.11.	Despite considerable expression, TM6IM5 does not seem to play a major role in neuronal cells .....	106
5.12.	Calcium homeostasis is imbalanced in liver mitochondria .....	109
5.13.	The point mutation affects basic cardiac function and the morphology of cardiac mitochondria .....	113
5.14.	Respiration of D326R cardiac mitochondria is slightly reduced due to a reduced coupling efficiency .....	115
5.15.	The calcium handling of D326R cardiac mitochondria is not altered .....	118
5.16.	D326R mice present with a severe myopathy with reduced grip strength .....	121
5.17.	The point mutation in TM6IM5 impairs mitochondrial calcium handling in skeletal muscle mitochondria.....	123
6.	Discussion.....	126
7.	References.....	<b>Fehler! Textmarke nicht definiert.</b>
8.	Appendix .....	163
8.1.	Abbreviations .....	163
8.2.	Acknowledgements.....	165
8.3.	Curriculum Vitae.....	168

## List of tables

---

Table 1: List of reagents .....	34
Table 2: List of commercial kits.....	36
Table 3: List of antibodies .....	36
Table 4: List of buffers.....	37
Table 5: PCR conditions for D326R mouse genotyping.....	40
Table 6: PCR conditions for HAP1 WT and TMBIM5 KO genotyping.....	41
Table 7: Conditions for the calcium uptake assay.....	64
Table 8: Protocol for treadmill habituation .....	70
Table 9: Protocol for the treadmill exercise.....	71

## List of figures

---

Figure 1: Simplified depiction of the ion channels and transporters in the mitochondrial membranes. ....	30
Figure 2: 3D-Structure of Transmembrane BAX Inhibitor Motif containing protein 5 (TMBIM5)...	31
Figure 3: Sequence alignment of the 32 bp deletion in TMBIM5 knockout HAP1 cells. ....	41
Figure 4: Graphical depiction of the open reading frame (ORF) in the plasmid pPB-CAG-HA-mitoCepia-IRES-mitoBFP2. ....	54
Figure 5: Exemplary gating for the flow cytometry analysis of transfected cells. ....	56
Figure 6: Detection of a protein-protein interaction via proximity ligation. ....	59
Figure 7: TMBIM5 is not involved in the Mitochondrial Contact Site and Cristae Organizing System (MICOS) but affects OPA1 processing. ....	77
Figure 8: Ionomycin-induced mitochondrial Ca <sup>2+</sup> uptake is reduced in HAP1 TMBIM5 KO cells.....	80
Figure 9: The loss of TMBIM5 affects the Mitochondrial Calcium Uniporter complex (mtCU) proteins. ....	83
Figure 10: TMBIM5 might interact with the Leucine Zipper-EF-hand-containing transmembrane protein 1 (LETM1).....	86
Figure 11: Reduced expression of TMBIM5 and mild alterations in mitochondrial characteristics in primary cells from a mouse model with a mutation named D326R in the TMBIM5 loop domain..	90
Figure 12: Homozygous D326R mice show increased perinatal lethality and reduced TMBIM5 expression in all tissues.....	93
Figure 13: The behaviour and coordination of the D326R mice do not differ from the WT mice...	96

Figure 14: The D326R mutation does not affect the basal systemic metabolism in mice..... 98

Figure 15: The D326R mutation does not alter systemic metabolism during exhaustive exercise.  
..... 101

Figure 16: Immune cells of D326R mice exhibit an impaired innate immune response. .... 105

Figure 17: TMBIM5 does not seem to play a major role in neuronal cells. .... 108

Figure 18: Calcium homeostasis is imbalanced in liver mitochondria. .... 111

Figure 19: D326R mice exhibit minor changes in basic cardiac function and mitochondrial  
morphology. .... 114

Figure 20: Respiration of cardiac mitochondria is slightly reduced due to an attenuated coupling  
efficiency in D326R mice. .... 117

Figure 21: The point mutation in TMBIM5 does not affect the calcium handling in cardiac  
mitochondria. .... 120

Figure 22: D326R mice present with reduced grip strength and severe myopathy. .... 122

Figure 23: D326R skeletal muscle mitochondria have a reduced Ca<sup>2+</sup> uptake rate and capacity.. 124

## 1. Abstract

---

Mitochondria are dynamic organelles with a central role in many vital processes. Besides ATP generation and other functions, they are crucial for cellular  $\text{Ca}^{2+}$  buffering. In close cooperation with the endoplasmic reticulum, mitochondria can shape cytosolic  $\text{Ca}^{2+}$  signals by taking in  $\text{Ca}^{2+}$ . Free  $\text{Ca}^{2+}$  in the mitochondrial matrix enhances ATP production which links mitochondrial metabolism to the cellular energy demand. Only a decade ago, the mitochondrial  $\text{Ca}^{2+}$  uptake pore was identified as the Mitochondrial Calcium Uniporter (MCU). However, MCU knockout (KO) mice are viable and lack a drastic phenotype. This created doubts about the singularity of MCU. We propose the Transmembrane BAX Inhibitor Motif containing protein (TMBIM) 5 as a novel mitochondrial  $\text{Ca}^{2+}$  channel.

TMBIM5 is ubiquitously expressed, localises to the inner mitochondrial membrane and shares conserved sequence homologies with TMBIM6 and the bacterial homologue BsYetJ. Both are pH-dependent  $\text{Ca}^{2+}$  channels. Loss of TMBIM5 leads to a disruption in the cristae structure. Using TMBIM5 KO cell lines (HAP1/HEK293), I demonstrated that it does not interact with the mitochondrial contact site and cristae organizing system. The KO impairs mitochondrial  $\text{Ca}^{2+}$  uptake and affects the expression of MCU and its regulator Mitochondrial Calcium Uptake 1. In addition, I detected changes in the abundance and processing of Optical Atrophy 1 (OPA1), a protein involved in cristae stabilisation. Its dysregulation may cause the observed abnormal cristae structure. To study the effect of TMBIM5 *in vivo*, we obtained a mouse line containing an amino acid exchange (D326R) in the putative pore domain. The analogue mutation induces a loss-of-function in TMBIM6. Similar to MCU KO, the mice did not show any gross phenotype. Yet, they were born at a reduced Mendelian rate and the mutated protein was downregulated in the adult animals. Screening for functional abnormalities revealed a striking cell-type dependence. The skeletal muscle is most severely affected by myopathy and dysregulation in mitochondrial  $\text{Ca}^{2+}$  uptake and buffering.

My results indicate that TMBIM5 is involved in mitochondrial  $\text{Ca}^{2+}$  handling and presumably only indirectly affects mitochondrial cristae structure. The tissue-specificity in the mouse suggests that additional regulatory elements may exist that affect TMBIM5 function.

## 2. Zusammenfassung

---

Mitochondrien spielen in vielen lebenswichtigen Prozessen eine zentrale Rolle, unter anderem als zellulärer Kalziumpuffer. Zusammen mit dem endoplasmatischen Retikulum können Mitochondrien durch Kalziumaufnahme zytosoläre Kalziumsignale beeinflussen. Freies Kalzium in der Matrix steigert die ATP-Produktion und verknüpft so die mitochondriale Aktivität mit dem zellulären Energiebedarf. Das Protein *Mitochondrial Calcium Uniporter* (MCU) wurde als die mitochondriale Kalziumpore identifiziert. Allerdings führte das Fehlen eines ausgeprägten Phänotyps in MCU *knockout*- (KO-) Mäusen zu Zweifeln über dessen Einzigartigkeit. Wir schlagen das Protein *Transmembrane BAX Inhibitor Motif containing protein* (TMBIM) 5 als neuen mitochondrialen Kalziumkanal vor.

TMBIM5 wird ubiquitär exprimiert, ist in der inneren Mitochondrienmembran lokalisiert und eng mit TMBIM6 und dem bakteriellen Homolog BsYetJ verwandt, beides pH-abhängige Kalziumkanäle. Verlust von TMBIM5 führt zu einer Störung der Cristae-Struktur. Mithilfe von TMBIM5 KO-Zelllinien (HAP1/HEK293) habe ich gezeigt, dass TMBIM5 nicht mit dem Proteinkomplex interagiert, der die Cristae formt und stabilisiert. Das Fehlen von TMBIM5 mindert die mitochondriale Kalziumaufnahme und beeinflusst die Expression von MCU und dem regulatorischen Protein *Mitochondrial Calcium Uptake 1*. Zudem habe ich eine Veränderung in der Menge und dem Verhältnis der Spleißvarianten von *Optical Atrophy 1* (OPA1) festgestellt. Da OPA1 in die Cristae-Stabilisation involviert ist, könnte dies die beobachteten Strukturstörungen verursachen. Den Effekt von TMBIM5 *in vivo* habe ich in einer Mauslinie mit einer Punktmutation (D326R) in der vermuteten Porendomäne untersucht. Die entsprechende Mutation führt zu einem Funktionsverlust in TMBIM6. Ähnlich wie die MCU KO-Mäuse, zeigten auch diese Tiere keinen auffälligen Phänotyp. Allerdings war die Mendel'sche Rate der Nachkommen verändert und in erwachsenen Mäusen war das mutierte Protein vermindert. Die Suche nach funktionellen Störungen ergab eine ausgeprägte Zelltyp-Abhängigkeit. Der Skelettmuskel ist mit einer Myopathie sowie Störungen der Kalziumaufnahme und -pufferung am stärksten betroffen.

Meine Ergebnisse legen nahe, dass TMBIM5 an der Regulation des mitochondrialen Kalziumgleichgewichts beteiligt ist und sich wohl nur indirekt auf die Cristae-Struktur auswirkt. Die Gewebeabhängigkeit in der Maus lässt vermuten, dass zusätzliche regulatorische Elemente die Funktion von TMBIM5 beeinflussen.

## 3. Introduction

---

### 3.1. Mitochondrial functions and functionality

*„The land flourished because it was fed from so many sources - because it was nourished by so many cultures and traditions and peoples.”(Learning for Justice, 2015)*

Possibly the earliest example of successful migration and integration is the presence of mitochondria in nearly every eukaryotic cell. Although strictly speaking, the currently accepted theory on mitochondrial origin says that it was not migration but phagocytosis that started this endosymbiosis. Nevertheless, it turned out to be an extremely profitable one as this event is estimated to date back 1.45 to 1.8 billion years (Martin, W. & Mentel, M., 2010). Since then, both organisms have changed, adapted and intermingled. The ancestral mitochondria evolved a mechanism to import targeted proteins which enabled gene transfer from their genome to the host-DNA (Roger et al., 2017). As a relict of their past, today's mitochondria still contain their own circular DNA (mtDNA) but it only encodes less than a hundred proteins (depending on the organism 2-60 (Martin, W. & Mentel, M., 2010; Roger et al., 2017)). The vast majority of proteins present in mitochondria and required for their function are encoded on the nuclear genome and transported to the mitochondria only after their translation (Roger et al., 2017). Another reminder of the endosymbiotic origin of the mitochondria is their double-layered membrane. Different to other intracellular organelles, mitochondria are enclosed by two functionally distinct membranes, the outer mitochondrial membrane (OMM) and the inner mitochondrial membrane (IMM) that controls the composition of the mitochondrial matrix. Due to the high abundance of so-called porins e.g. the voltage-dependent anion channel (VDAC) the OMM is rather permeable to ions and even small molecules (Kühlbrandt, 2015). In contrast, diffusion through the IMM is highly selective and controlled by many specific channels and transporters (Kühlbrandt, 2015). The space in between the membranes is called intermembrane space (IMS) and plays a major role in mitochondrial functions (Nunnari and Suomalainen, 2012).

For a long time, the only function ascribed to mitochondria by scientists was the production of ATP as the cellular energy currency. Although this is obviously an essential function it

underestimates the capability of mitochondria by far. Only in the past 30 years, interest in mitochondria rose again and is evidenced by groundbreaking progress in the understanding of their tasks, organisation and regulation which I will briefly summarize in the following sections.

### 3.1.1. Mitochondrial morphology and dynamics

Mitochondria are highly dynamic organelles that undergo constant fusion (merging of two mitochondria) and fission (a division of one mitochondrion) to meet cellular demands. Fusion processes generate elongated, tubular mitochondria and facilitate the exchange of matrix components and mtDNA (Nunnari and Suomalainen, 2012). Moreover, fused mitochondria have a higher respiratory activity and produce more ATP (Meyer et al., 2017). Fission, on the other hand, results in smaller, fragmented mitochondria. This enables transportation to specific cellular compartments which is particularly critical in neurons where mitochondria have to be shuttled to dendritic or axonal synapses over long distances (Lin and Sheng, 2015). Besides that, fission is important for mitochondrial quality control. Several parameters indicating poor mitochondrial health such as a low membrane potential induce fission and thereby facilitate mitochondrial removal via mitophagy, a form of lysosomal degradation (Meyer et al., 2017). In addition, fissioned mitochondria are more likely to induce apoptosis by the release of cytochrome *c* (cyt *c*) from the matrix (Meyer et al., 2017).

#### 3.1.1.1. Molecular regulation of fusion and fission

Both processes, fusion and fission, are rather complex as two membranes, OMM and IMM, have to be merged or split respectively, which requires tight regulation and involves different sets of proteins. Mutations leading to an imbalance of fusion and fission are associated with a number of severe pathologies such as neurodegenerative (Itoh et al., 2013) or cardiovascular (Vásquez-Trincado et al., 2016) diseases and cancer progression (Srinivasan et al., 2017).

Fusion of two mitochondria takes place in three steps: 1. tethering and 2. docking of the outer membranes and finally 3. fusion of the outer membrane followed by the inner membrane (Tilokani et al., 2018). At the OMM, the contact between mitochondria and the

fusion of the two membranes is mediated by Mitofusin1 and 2 (MFN1/2). These are GTPases that are thought to undergo conformational changes upon hydrolysis of GTP and thereby alter membrane curvature and enable membrane fusion (Tilokani et al., 2018). Once the OMM is fused and allows contact of the inner membranes, this contact is established by the protein Optical Atrophy 1 (OPA1). OPA1 too contains a GTPase domain that might mediate the membrane fusion (Tilokani et al., 2018). Ban et al. (Ban et al., 2017) recently suggested a mechanism of heterotypic binding of OPA1 and the mitochondria-specific lipid cardiolipin. They showed that this interaction alone is sufficient to drive IMM fusion (Ban et al., 2017). OPA1 is a very interesting mitochondrial protein as it is involved in a plethora of diverse processes. Besides the mentioned influence on mitochondrial morphology (Ishihara et al., 2006; MacVicar and Langer, 2016), it was shown to affect mitochondrial DNA maintenance (Del Dotto et al., 2018) and apoptotic cristae remodelling facilitating the release of cyt c (Frezza et al., 2006). Beyond that, there is evidence that OPA1 is not only involved in cristae remodelling but also their formation (Harner et al., 2016). To meet all these demands, OPA1 mRNA is spliced into a total of eight different isoforms in mammals (Del Dotto et al., 2018). All isoforms contain a mitochondrial targeting sequence that is cleaved after import (Del Dotto et al., 2018). Moreover, depending on the splicing they harbour one or two additional proteolytic cleavage sites that allow further posttranslational modifications. The uncleaved protein isoforms, termed “long” OPA1 (l-OPA1), are integrated into the inner mitochondria membrane and are thought to be the main mediators of membrane fusion at the IMM (Ishihara et al., 2006). The cleaved variants (“short”, s-OPA1) are soluble and accumulate in the intermembrane space (Del Dotto et al., 2018). However, these short forms are not a mere side product but seem to have distinct, yet still largely unclear functions themselves (MacVicar and Langer, 2016). There is some evidence that s-OPA1 may counteract the long form and induce mitochondrial fission (Anand et al., 2014), however, this may depend on the site of processing.

OPA1 processing is performed by two membrane-bound metalloproteases, “overlapping with the m-AAA protease 1 homolog” (OMA1) and YME-1-like protein (YME1L). They have distinct proteolytic cleavage sites (S1 and S2) and are regulated by various factors related to cellular stress, e.g. oxidative stress, heat stress or changes in mitochondrial membrane potential (MacVicar and Langer, 2016). Rainbolt et al. provided evidence for a reciprocal

activation model (Rainbolt et al., 2016). YME1L exhibits a constitutive but weak level of activity under normal conditions that increases upon a reduction in MMP. Interestingly, besides OPA1, also OMA1 is a cleavage target of YME1L. This means that under certain conditions (low MMP with normal ATP levels) YME1L limits OPA1 processing through degradation of OMA1. In contrast, concomitant depletion of ATP stabilises OMA1 and activates its proteolytic activity whereas YME1L is being degraded (Rainbolt et al., 2016). YME1L activity seems to generate s-OPA1 isoforms that are able to induce fusion whereas OMA1 processing rather leads to mitochondrial fragmentation (Tilokani et al., 2018). Considering the importance of OPA1 and its multifaceted roles, its processing is a critical mechanism to adapt mitochondrial morphology and function to cellular needs.

The key protein of mitochondrial fission is the dynamin-1-like protein (DRP1 or DNM1L). DRP1 is a cytosolic protein that dynamically localises to the OMM and forms ring-like oligomeric structures around the mitochondria (Smirnova et al., 2001). Interestingly, the sites of DRP1 recruitment are marked by the endoplasmic reticulum (ER) which wraps around the mitochondria and introduces sites of constriction. This process is supported by the two proteins Inverted formin 2 (INF2) at the ER-membrane and Spire1C at the mitochondrial membrane (Manor et al., 2015; Chakrabarti et al., 2018; Tilokani et al., 2018). They promote actin polymerization which additionally strengthens the contact between ER and the mitochondrion and facilitates DRP1 recruitment. DRP1 cannot directly bind to the mitochondrial phospholipid membrane. Thus, it interacts with receptor proteins on the OMM, e.g. MFF, MiD49 and MiD51 (Tilokani et al., 2018) that stabilise the ring structure. Mears et al. reported that the yeast homologue of DRP1 (Dnm1) undergoes a conformational change upon GTPase activity and thereby further narrows the constriction sites (Mears et al., 2011). However, it has been debated whether this is enough to introduce fission. One possible candidate to mediate the final scission step is the protein dynamin-2 (DYN2). Similar to DRP1, DYN2 is recruited to the constriction sites and reinforces membrane curvature by its GTPase activity (Lee et al., 2016).

Necessarily, the described fission of the OMM is accompanied by the division of the IMM. However, very little is known about the molecular mechanisms driving it. Interestingly, an increase in matrix  $[Ca^{2+}]$  was found to induce mitochondrial fragmentation (Hom et al., 2007) indicating that  $Ca^{2+}$  is involved in the regulation. Chakrabarti and co-workers

(Chakrabarti et al., 2018) studied the relevance of  $\text{Ca}^{2+}$  for IMM fission in human osteosarcoma cells. They revealed that the F-actin-dependent tethering of the ER to the mitochondrial OMM enhances  $\text{Ca}^{2+}$  transfer from the ER to the mitochondrial matrix through the mitochondrial calcium uniporter (MCU) (Chakrabarti et al., 2018). This rise in matrix  $[\text{Ca}^{2+}]$  leads to a constriction of the IMM that is DRP1-independent but required electron transport system (ETS) activity (Chakrabarti et al., 2018). Based on their research on primary neurons Cho et al. (Cho et al., 2017) suggest an OPA1-dependent mechanism for IMM constriction:  $\text{Ca}^{2+}$  influx into the mitochondrial matrix lowers the MMP which in turn activates the proteolytic activity of Oma1. OPA1 is being processed, the short isoforms accumulate at the contact sites in the IMS and the lack of l-OPA1 detaches the inner from the outer membrane thereby facilitating membrane constriction and fission (Cho et al., 2017). Both groups observed that constriction of the IMM precedes OMM contraction (Cho et al., 2017; Chakrabarti et al., 2018). Yet, the molecular basis and the processes mediating the subsequent membrane constriction and division remain unresolved.

#### 3.1.1.2. Cristae structure organisation

The inner mitochondrial membrane forms invaginations towards the matrix that are termed cristae. Similar to the foldings of mammalian small intestines, this trick vastly increases the surface area and allows the integration of many proteins that are crucial to mitochondrial function. Of note, the core element of mitochondrial ATP production, the  $\text{F}_1\text{F}_0$ -ATP synthase forms dimers that introduce a membrane curvature and facilitate the formation of cristae (Strauss et al., 2008). At the sites where the IMM disconnects from the OMM and faces itself, it shapes narrow, tubular structures, the so-called cristae junctions (CJs). The strong membrane curvature at the CJ is shaped and stabilised by a conserved, hetero-oligomeric protein complex, the mitochondrial contact site and cristae organizing system (MICOS) (Rampelt and van der Laan, 2017). By connecting the two opposing inner membranes at the CJ, the MICOS generates a cristae lumen that is distinct from the intermembrane space. This is critical for mitochondrial function as it supports the accumulation of protons pumped out by the electron transport chain and prevents the diffusion of other soluble factors such as cyt c (Scorrano et al., 2002). Moreover, the MICOS prevents lateral diffusions of proteins within the IMM and thereby separates it into two

functionally and structurally distinct sections (Wollweber et al., 2017). The inner boundary membrane aligns with the outer membrane and mediates the exchange of molecules and ions across the membranes (Fox, 2012; Hu et al., 2020). The cristae membrane (CM) shapes the aforementioned infoldings and harbours the oxidative phosphorylation system (Bohnert et al., 2015).

#### 3.1.1.2.1. Composition of the Mitochondrial Contact Site and Cristae Organizing System

To date, seven subunits of the MICOS complex have been identified in mammals. These are MICOS complex subunits (MIC) MIC10, Mic12, Mic19 (also known as CHCHD3), Mic25 (also known as CHCHD6), Mic26, Mic27 and MIC60 (also known as mitofilin). The number represents the molecular weight of the protein. Yet, even more proteins may be involved through temporary or permanent interaction (Wollweber et al., 2017).

The two key players with distinct roles are MIC10 and MIC60. MIC10 forms oligomers and associates with the  $F_1F_0$ -ATP synthase and thereby facilitates the membrane curvature (Bohnert et al., 2015; Rampelt et al., 2017). MIC60 interacts with several protein complexes in the outer mitochondrial membrane and forms and stabilises contact sites between the two membranes (Wollweber et al., 2017; Tang et al., 2020). Moreover, MIC60 was found to form heterooligomers with I-OPA1 (Barrera et al., 2016; Glytsou et al., 2016). Barrera et al. (Barrera et al., 2016) provided evidence that OPA1 is not involved in cristae formation but plays a critical role during cristae remodelling in the context of apoptosis and/or disease. Glytsou and co-workers (Glytsou et al., 2016), however, published their results shortly after and suggested that OPA1 is constitutively involved in the determination of the number, width and stability of the CJ which was recently supported by Stephan et al. (Stephan et al., 2020). In addition, they hypothesise that OPA1 and MIC10 exert antagonistic effects on MICOS assembly. They show that the knockout (KO) of OPA1 leads to large clusters of MIC60-containing complexes while concomitant loss of MIC10 reversed the phenotype and resulted in small, scattered complexes (Stephan et al., 2020).

So far, no  $Ca^{2+}$ -sensing protein was found to be directly involved in the MICOS complex but there is some evidence that opening of the CJ may be involved in the cyt c release upon  $Ca^{2+}$  overload (Andreyev and Fiskum, 1999). Interestingly, the mtCU gatekeeper

mitochondrial calcium uptake 1 (MICU1) was identified as a possible interaction partner of MIC60 (Tomar et al., 2019). MICU1 contains two Ca<sup>2+</sup>-sensing EF-hands and its loss destabilises the CJ and facilitates cyt *c* release (Perocchi et al., 2010; Gottschalk et al., 2019). Whether this effect is Ca<sup>2+</sup>-dependent and MICU1 in fact confers Ca<sup>2+</sup>-sensitivity to the MICOS requires further clarification.

#### 3.1.1.2.2. The CHCHD-family

As mentioned above, several members of the CHCHD-family are included in or associated with the MICOS (Tilokani et al., 2018). In mammals, this protein family consists of 9 mitochondrial proteins that all share at least one coiled-coil-helix-coiled-coil domain which is reflected in the abbreviation (Liu et al., 2020c). The most prominent ones are CHCHD2 and CHCHD10 because they are associated with multiple human pathologies most of them affecting the nervous system. Mutations in CHCHD10 were linked to amyotrophic lateral sclerosis and frontotemporal lobar degeneration, both accompanied by mitochondrial myopathies (Bannwarth et al., 2014), Charcot-Marie-Tooth disease type 2 (Auranen et al., 2015) and late-onset spinal motor neuropathy (Penttilä et al., 2015). Of note, CHCHD10 evidently interacts with MIC60 and may be another subunit of the MICOS. Loss of CHCHD10 results in complex disassembly and a reduced number and deranged appearance of the cristae while its exact function remains elusive (Genin et al., 2016). CHCHD2 is a close homologue of CHCHD10 and was found to be involved in the pathogenesis of several forms of Parkinson`s disease (Funayama et al., 2015; Lee et al., 2018). Liu and colleagues (Liu et al., 2020b) studied the relevance of *Chchd2* in *Drosophila* which is a homologue for both, CHCHD2 and 10. They propose that *Chchd2* affects mitochondrial function and morphology by modifying OPA1 processing. *Chchd2* seems to compete against a chaperone-like protein named P32 for a binding site on the protease YME1L. The binding of P32 enhances the proteolytic activity of YME1L which processes l-OPA1 to s-OPA1. Hence, the abundance of CHCHD2 may indirectly influence the splicing of OPA1 which in turn modulates mitochondrial shape and dynamics.

Another interaction partner of CHCHD2 in mammals determined via mass spectrometric analysis and co-immunoprecipitation is cyt *c*. This interaction likely stabilises cyt *c* at the

IMM, facilitates the electron transfer from complex III to complex IV and thereby promotes oxidative phosphorylation (Meng et al., 2017).

Interestingly, during oxidative stress or under hypoxic conditions, CHCHD2 is not imported into the mitochondria but accumulates in the nucleus where it acts as a transcription factor. It stimulates transcription of a subunit of the cytochrome *c* oxidase and its own gene, *Chchd2* (Kee et al., 2021). Upregulation of these two proteins likely serves to stabilise mitochondrial oxidative phosphorylation and ensure cellular survival.

### 3.1.2. Mitochondrial functions

For far too long, mitochondria had been underestimated and reduced to their ATP-producing function. Only in the past two decades, research interest in mitochondria experienced a renaissance and yielded groundbreaking insights into mitochondrial physiology. This led to an appreciation of the manifold processes mediated or regulated by mitochondria but also revealed their involvement in the pathogenesis of countless severe diseases. In the next few sections, I will give a brief overview of the diverse functions – and malfunctions – of mitochondria.

#### 3.1.2.1. ATP generation

Despite the advanced understanding of other mitochondrial tasks, naturally, the production of the cellular energy equivalent ATP remains their key role. Two enzymatic systems constitute the core of mitochondrial ATP generation: the tricarboxylic acid (TCA) cycle and the electron transport system (ETS).

The TCA cycle is also known as Krebs cycle or citric acid cycle and describes a series of eight enzymatic reactions that integrate the catabolism of carbohydrates, fatty acids and amino acids to generate substrates for the ETS (Christen et al., 2016c). These substrates, NADH and FADH<sub>2</sub> then fuel the ETS by donating electrons (Christen et al., 2016a). The ETS consists of five different protein complexes. Complex I (NADH/ubiquinone reductase) and complex II (succinate dehydrogenase) reduce NADH and FADH<sub>2</sub> respectively and transfer the free electron to coenzyme Q. At complex III (cytochrome *c* reductase), the electrons are transferred to cyt *c* which passes them on to complex IV. Eventually, catalysed by complex IV (cytochrome *c* oxidase) one molecule of H<sub>2</sub>O is produced from oxygen, protons and

electrons (Campbell, 2000; Christen et al., 2016b). At every step of this electron transfer energy is released which is used by complex I, III and IV to pump protons from the mitochondrial matrix to the intermembrane space. This generates an electrical gradient (~180 mV), a pH gradient (pH 7.2-7.4 in the matrix, pH 7.9- 8 in the IMS) and a chemical gradient with a much higher concentration of protons in the IMS than in the matrix (Kühlbrandt, 2015). This electrochemical gradient is called mitochondrial membrane potential (MMP) and drives complex V, the  $F_1F_0$ -ATP synthase (for the sake of simplicity shortened to ATP synthase in the following). Protons crossing the membrane through the  $F_0$  subcomplex induce a rotating movement in the  $F_1$  unit that delivers the energy needed to phosphorylate adenosine diphosphate to adenosine triphosphate (ATP). This whole process is called oxidative phosphorylation (OXPHOS) (Campbell, 2000; Christen et al., 2016a).

#### 3.1.2.2. Generation of reactive oxygen species

As elegant as the described mechanism for ATP production is, it also implies its downsides. Electrons leaking from the different steps of the TCA cycle or the ETS react with free oxygen molecules and form reactive oxygen species (ROS) such as  $O_2^{\bullet -}$  and  $H_2O_2$ . They can cause oxidative stress and severely damage proteins, membranes and DNA (Yang and Lian, 2020). To avoid oxidative stress, cells have developed several protective strategies. One of the main antioxidative compounds - not only in the mitochondrial matrix but also in the cytosol - is glutathione ( $\gamma$ -glutamyl-L-cysteinylglycine, GSH). GSH is a molecule that consists of three amino acids. The central one is a cysteine that can be oxidised and form a disulfide bridge to a second GSH. The oxidised product is called glutathione disulfide (GSSG) and is rapidly recovered by the glutathione reductase (Giustarini et al., 2016). At a healthy balance, this circuit effectively limits the accumulation of ROS. Dysfunctions in the ATP generating machinery or the antioxidative system, however, can cause drastic damage and are associated with numerous diseases as diverse as Alzheimer`s disease (Esposito et al., 2006), cardiomyopathies (Li et al., 1995) and nonalcoholic fatty liver disease (Paradies et al., 2014). However, as always in life there is no clear separation of good and evil. It is now widely accepted that ROS are not only harmful byproducts of mitochondrial ATP production but that they also serve as intracellular messengers that modulate gene transcription and

protein activity (Shadel and Horvath, 2015). In addition, ROS have physiological roles in the extracellular space, e.g. in the regulation of vascular tone (Chen et al., 2008) and as a mechanism for immune defence. As part of the innate immune response, some phagocytic cells produce ROS and release them in large amounts as a so-called oxidative burst to eliminate infiltrating pathogens (Dahlgren C. and Karlsson A., 1991; Cathcart M., 2004; Ciz et al., 2012). In these cases, however, the released ROS do not stem from the mitochondria but are generated at specialised sites such as the NADPH-oxidase complex (Cathcart M., 2004; Chen et al., 2008).

#### 3.1.2.3. Generation of iron-sulfur-clusters

Iron-Sulfur-Clusters (Fe-S-Clusters) are inorganic cofactors that are involved in a wide range of cellular processes such as electron transport across the ETS (Wachnowsky et al., 2018), maintenance of telomeres (Stehling et al., 2012), DNA repair mechanisms (Rudolf et al., 2006) and heme biosynthesis (Liu et al., 2020a). Fe-S-clusters are vulnerable to oxidation but may also induce oxidative stress by the generation of free radicals which was linked to DNA damage and carcinogenesis (Okada, 1996). Hence, their formation and trafficking have to be tightly regulated. The major site for the generation of Fe-S-cluster is the mitochondrial matrix, not only for mitochondrial proteins but also for target proteins in the cytosol and nucleus (Lill et al., 2012). The synthesis comprises three steps: 1) assembly of the cluster on a scaffolding protein, 2) chaperone-assisted release of the cluster with subsequent export from the mitochondria, if necessary and 3) transfer of the cluster to the target protein (Lill et al., 2012; Wachnowsky et al., 2018). Mutations in the involved proteins have been linked to various human diseases most notably neurological diseases (Friedreich`s ataxia (Bridwell-Rabb et al., 2011), Parkinson`s disease (Wachnowsky et al., 2018), epilepsy (Zhou et al., 2018)) and several myopathies (Wachnowsky et al., 2018).

#### 3.1.2.4. Lipid metabolism

As mentioned before, not only carbohydrates are used to generate ATP, but also lipids and to some extent, proteins are catabolised and incorporated into the TCA cycle. Lipids present an important source of energy for mitochondrial metabolism as they can be stored as triglycerides in adipose tissue and retrieved during nutritional shortage (Knottnerus et

al., 2018). On-demand, stored fatty acids (FA) are hydrolysed and released into the bloodstream as free fatty acids which are then taken up into the cells through specific transporters. Short-chain FA simply diffuse into the mitochondria whereas intermediate- and long-chain FA need binding to carnitine to then cross the mitochondrial membrane via the carnitine shuttle (Mayr, 2015; Knottnerus et al., 2018). At their final destination, the mitochondrial matrix, FA are broken down to their bi-carbonic components generating Acetyl-CoA and NADH and FADH<sub>2</sub> in a multistep process termed  $\beta$ -oxidation. Acetyl-CoA fuels the TCA cycle while NADH and FADH<sub>2</sub> directly power the ETS.  $\beta$ -oxidation plays a major role in the metabolism of cardiac muscle cells and accounts for 60 – 90 % of their ATP production (Knottnerus et al., 2018). Hence, it is not surprising that dysfunctions in the FA oxidation are predominantly associated with cardiomyopathies and myopathies (Bonnet et al., 1999; Spiekerkoetter, 2010).

Nonetheless, mitochondria do not only catabolise lipids, they are also capable of *de novo* synthesis of fatty acids. Although the cytosol is the main cellular location for FA biosynthesis, mitochondria preserved their own pathway consisting of a series of proteins (Zhang et al., 2005; Witkowski et al., 2011; Clay et al., 2016). Not all components and functions are yet fully understood but it is known that fatty acids with up to 14 carbons can be generated from the precursors malonate, malonyl-CoA and Acyl-CoA (Witkowski et al., 2011). The most prominent product of mitochondrial FA synthesis is lipoic acid that serves as a cofactor for several mitochondrial dehydrogenases, e.g. the pyruvate dehydrogenase complex (Clay et al., 2016).

In addition, fatty acids are required for the generation of phospholipids that compose all biomembranes. Most of these phospholipids are produced in the ER but some are also assembled in the mitochondria namely phosphatidylglycerol, cardiolipin (diphosphatidylglycerol) and at least partially phosphatidic acid, phosphatidylethanolamine and CDP-diacylglycerol (Horvath and Daum, 2013). Of these, cardiolipin is a particularly interesting phospholipid as it is another remnant from the bacterial origin of the mitochondria and is unique to mitochondrial membranes (Mayr, 2015). Cardiolipin is no typical bilayer-forming phospholipid due to its peculiar structure. It consists of two glycerophosphates esterified with four fatty acid side chains (Falabella et al., 2021). This makes the head group substantially smaller than the tail which introduces curvature when cardiolipin is

incorporated into a lipid bilayer. Hence, it is not surprising that Cardiolipin is predominantly found in the IMM where it supports the membrane bending and in mammals accounts for nearly 20 % of the total phospholipid fraction (Horvath and Daum, 2013). It was shown to actively influence mitochondrial morphology by interacting with OPA1. Heterotypic binding between cardiolipin and l-OPA1, sometimes additionally s-OPA1, can induce mitochondrial fusion (Ban et al., 2017; Ikon and Ryan, 2017). Interestingly, the structure of cardiolipin is  $\text{Ca}^{2+}$ -sensitive.  $\text{Ca}^{2+}$  binding to the phosphate moiety induces a conformational change in the fatty acid side chains leading to a larger hydrophobic volume. This induces strong membrane curvature and a higher vulnerability to oxidation (Fox et al., 2019; Miranda et al., 2019). The effect of membrane lipids on cellular function is notoriously underestimated. IMM stability and its  $\text{Ca}^{2+}$  dependence is likely a relevant factor for the induction of apoptosis which will be described in the next section.

#### 3.1.2.5. Induction of apoptosis

Apoptosis is a form of programmed cell death. In contrast to necrosis, it is not necessarily a pathological process but is essential for many important physiological processes such as development, tissue renewal and a functional immune system. Nonetheless, apoptotic dysregulation can cause severe diseases. An overshoot is associated with (neuro-) degenerative diseases while a lack of apoptosis is related to autoimmune reactions and tumour growth and progression (Czabotar et al., 2014; Galluzzi et al., 2018).

Apoptosis describes the orchestrated degradation of the cellular components which are then wrapped into small vesicles, the so-called apoptotic bodies. After their release, they are removed from the extracellular space by rapid phagocytosis and lysosomal degradation in neighbouring cells (Jeong S.-Y. and Seol D.-W., 2008). The apoptotic degradation processes are energy-dependent and mediated by a group of proteases known as caspases. There are two distinct pathways for the initiation of this apoptotic cascade: an intrinsic and an extrinsic one. The extrinsic pathway is induced by extracellular signals that activate membrane-bound receptors which in turn start the apoptotic cascade. The intrinsic pathway is initiated at the mitochondria and can be triggered by several intracellular stressors, e.g. oxidative stress, DNA damage, ER stress and mitochondrial calcium overload (Jeong S.-Y. and Seol D.-W., 2008; Galluzzi et al., 2018). The key event at the mitochondria

is the formation of large pores in the outer mitochondrial membrane. This mitochondrial outer membrane permeabilization (MOMP) is mediated by the two pro-apoptotic members of the BCL-2-family, BAX (BCL-2-associated X protein) and BAK (BCL-2 antagonist/killer) (Czabotar et al., 2014). They oligomerise at the OMM and allow the release of proapoptotic stimulators – most importantly cyt *c* – from the intermembrane space (Czabotar et al., 2014). Free cyt *c* in the cytosol induces the formation and activation of the so-called apoptosome (including Apaf-1 and procaspase-9) which leads to the activation of several downstream effector caspases. However, MOMP alone is not sufficient to trigger the complete release of cyt *c*. The largest pool of cyt *c* (85 %) is enclosed in the mitochondrial cristae and is additionally tethered to the IMM by cardiolipin (Ott et al., 2002; Scorrano et al., 2002). Hence, cristae remodelling and solubilisation of cyt *c* are required for the initiation of apoptosis. The electrostatic interaction between cyt *c* and cardiolipin is reduced by other pro-apoptotic conditions such as low ATP levels, low MMP or oxidative stress which facilitates the release (Ott et al., 2002). The underlying processes of cristae remodelling are less understood. As mentioned above, subunits of the MICOS or interacting proteins like OPA1 may modulate CJ tightness in response to apoptotic signals (Andreyev and Fiskum, 1999; Frezza et al., 2006). Moreover, there is some evidence for a dual role of tBid (truncated BH3-interacting domain death agonist) in the initiation of apoptosis. tBid is another BCL-2 family member that is activated by cleavage by caspase-8 and is known to enhance the oligomerisation of BAX and BAK (Eskes et al., 2000; Wei et al., 2000). Beyond that, tBid was shown to affect membrane curvature and induce opening of the CJ and thereby facilitate cyt *c* diffusion (Epand et al., 2002; Grinberg et al., 2002; Scorrano et al., 2002). The mode of action is not fully understood but interestingly, its recruitment to the OMM and its destabilising effect seem to depend on cardiolipin and are greatly enhanced by calcium. Epand and co-workers (Epand et al., 2002) reported that in the presence of calcium, tBid promotes so-called lipid mixing in liposomes composed of various phospholipids. They describe lipid mixing as “a process that may be similar to that which allows lipids from the inner mitochondrial membrane to transfer to the outer membrane.” (Epand et al., 2002). This indicates that increasing mitochondrial calcium levels may induce the transfer of cardiolipin from the IMM to the OMM where it recruits other pro-apoptotic proteins and destabilises the membrane. Altogether, the initiation of

apoptosis is a strictly regulated process that is based on a highly complex interplay of pro- and anti-apoptotic signals of which only a few are described above.

#### 3.1.2.6. Calcium buffering

Calcium is a universal intracellular messenger involved in a myriad of processes such as cell cycle progression, cellular differentiation and transcription. In excitable cells like neuronal or muscle cells,  $\text{Ca}^{2+}$  is the key signal inducing synaptic transmission or muscle contraction, respectively.  $\text{Ca}^{2+}$  signals can occur very locally or propagate through the whole cell and even to neighbouring cells as a single wave or in an oscillating pattern (Giorgi et al., 2018). The length of a  $\text{Ca}^{2+}$  peak can range from milliseconds up to hours (Balaban, 2009; Prakriya and Lewis, 2015; Paillard et al., 2017). To be able to fulfil these diverse criteria and functions, cellular  $\text{Ca}^{2+}$  fluxes must be tightly regulated. For decades, the task of intracellular  $\text{Ca}^{2+}$  buffering and storage was exclusively assigned to the ER.  $\text{Ca}^{2+}$  is pumped from the cytosol into the ER lumen by the sarcoplasmic/endoplasmic reticulum  $\text{Ca}^{2+}$  ATPase (SERCA) at the expense of ATP. Under resting conditions  $[\text{Ca}^{2+}]_{\text{cyto}}$  is very low (100-200 nM), whereas it lies at  $\sim 300 \mu\text{M}$  in the ER and  $\sim 1\text{mM}$  in the extracellular milieu (Giorgi et al., 2018). Leak channels in the ER membrane prevent  $\text{Ca}^{2+}$  overload. Upon activation, further channels open (e.g. the Inositol-1,4,5-triphosphate-receptor (IP3R)/ryanodine receptor (RyR)) and release  $\text{Ca}^{2+}$ . This store depletion can induce the opening of plasma membrane  $\text{Ca}^{2+}$  channels which allow the influx of  $\text{Ca}^{2+}$  from the extracellular space. This phenomenon is called store-operated calcium entry (SOCE) and is responsible for prolonged  $\text{Ca}^{2+}$  signals and refilling of the ER  $\text{Ca}^{2+}$  store. It is terminated by the closing of the channels followed by rapid removal of the  $\text{Ca}^{2+}$  through SERCA at the ER membrane and a  $\text{Na}^+/\text{Ca}^{2+}$ -exchanger (NCX) and a  $\text{Ca}^{2+}$ -ATPase in the plasma membrane (Prakriya and Lewis, 2015).

However, in the last 20 years, several other organelles turned out to be involved in the shaping of cytosolic  $\text{Ca}^{2+}$  signals, e.g. the mitochondria and the Golgi apparatus (Dolman and Tepikin, 2006). Even lysosomes were found to affect local  $\text{Ca}^{2+}$  domains (Medina et al., 2015). In this work, I am focusing on mitochondrial calcium handling and its effect on cellular and mitochondrial physiology.

Mitochondria modulate cytosolic  $\text{Ca}^{2+}$  signals by sequestering considerable amounts of the  $\text{Ca}^{2+}$  released from the ER and – albeit to a lesser extent – of the  $\text{Ca}^{2+}$  entering through the

cell membrane. This is enabled by a strategic, nearby localisation of mitochondria. The reason why the mitochondrial  $\text{Ca}^{2+}$  uptake capacity was underestimated for so long was the low  $\text{Ca}^{2+}$  affinity of the putative uniporter. Long before the molecular representation for mitochondrial  $\text{Ca}^{2+}$  influx was even identified, it was characterised by the following hallmarks: 1) electrogenic transport (Crompton and Heid, 1978), 2) sensitivity to Ruthenium Red (RuR) (Crompton and Heid, 1978) and 3) a low affinity for  $\text{Ca}^{2+}$  ( $k_m = 5\text{-}10 \mu\text{M}$ ) (Carafoli, 2003; Nicholls, 2005). Thus, it was generally believed that the cytosolic  $\text{Ca}^{2+}$  concentration ( $[\text{Ca}^{2+}]_{\text{cyto}}$ ) never reaches concentrations that are high enough to enable substantial mitochondrial uptake. In parts, this is still true. Yet, in the 90s, Rizzuto and colleagues (Rizzuto et al., 1993) revealed the existence of so-called microdomains. They discovered that  $\text{Ca}^{2+}$  distribution in the cytosol is not uniform. Near the release sites,  $[\text{Ca}^{2+}]$  can reach values 20-fold higher than the bulk  $[\text{Ca}^{2+}]_{\text{cyto}}$  (up to  $100 \mu\text{M}$ ) (Csordás et al., 1999). Since then, a lot of progress has been made in the understanding of the close interplay of mitochondria and the ER. They interact at so-called mitochondria-ER contact sites (MERCs) at a distance of 10-50 nm (Giacomello and Pellegrini, 2016). A specific set of proteins tethers the two membranes and facilitates the exchange of proteins, lipids and – of course –  $\text{Ca}^{2+}$  (Hayashi et al., 2009).

Yet, mitochondrial  $\text{Ca}^{2+}$  uptake at the MERCs does not only serve to modulate cytosolic  $\text{Ca}^{2+}$  signals. The mitochondrial  $\text{Ca}^{2+}$  concentration ( $[\text{Ca}^{2+}]_{\text{mito}}$ ) also has a regulatory effect on matrix enzymes. An increase in free  $[\text{Ca}^{2+}]_{\text{mito}}$  activates several dehydrogenases (isocitrate dehydrogenase,  $\alpha$ -ketoglutarate dehydrogenase, pyruvate dehydrogenase) resulting in increased availability of ETS substrates (Balaban, 2009). Moreover, it directly induces ATP synthase activity (Mildaziene et al., 1996; Balaban, 2009). Mitochondrial  $\text{Ca}^{2+}$  uptake thus serves as a feedback loop to adjust ATP production to the cellular need.

It is important to note that the concentration of free  $\text{Ca}^{2+}$  in the matrix is not necessarily identical to the total concentration. The ability of mitochondria to sequester large amounts of  $\text{Ca}^{2+}$  is based on their  $\text{Ca}^{2+}$  buffering system that can dynamically adapt to the rate of  $\text{Ca}^{2+}$  uptake (Blomeyer et al., 2013). The mechanisms of this buffering are poorly understood but one of the main factors involved is phosphate (Wei et al., 2012). It rapidly forms complexes with  $\text{Ca}^{2+}$  in the mitochondrial matrix and thereby limits the accumulation of free  $\text{Ca}^{2+}$  and lowers the risk of  $\text{Ca}^{2+}$  overload (Chinopoulos and Adam-Vizi, 2010).

Since mitochondria have been acknowledged for their role in  $\text{Ca}^{2+}$  regulation, a growing number of pathologies has been linked to mitochondrial dysfunction. It is no surprise that excitable tissues are most severely affected. Multiple neurodegenerative disorders such as amyotrophic lateral sclerosis (Debattisti et al., 2019; Dafinca et al., 2020), Alzheimer's (Jadiya et al., 2019), Parkinson's (Verma et al., 2017) and Huntington's (Wang et al., 2013) disease are associated with disruptions in the  $\text{Ca}^{2+}$  balance (König et al., 2016; Jung et al., 2020). A mismatch between  $\text{Ca}^{2+}$  influx and efflux is thought to be a causal event for several cardiomyopathies (Luongo et al., 2017; Sommakia et al., 2017). Moreover, excessive  $\text{Ca}^{2+}$  uptake seems to worsen the tissue damage following ischemia-reperfusion by altering downstream effects (Guan et al., 2019). In skeletal muscle, a  $\text{Ca}^{2+}$  dysregulation can cause serious muscular pathologies, e.g. Ullrich congenital muscular dystrophy and Bethlem myopathy (Angelin et al., 2008; Tiepolo et al., 2009). Nonetheless, also non-excitable organs may be affected. In the liver,  $\text{Ca}^{2+}$  signals play an important role in the regulation of "glucose production, bile fluid movement and excretion" (Arruda and Hotamisligil, 2015) and other metabolic processes. Accordingly, disturbances are involved in the pathogenesis of obesity and fatty liver diseases (Mantena et al., 2008). In the innate immune system, mitochondria facilitate the assembly of the so-called inflammasome and mitochondrial  $\text{Ca}^{2+}$  handling influences the initiation of inflammatory processes (Rimessi et al., 2015). Excessive  $\text{Ca}^{2+}$  uptake has been implicated in the disease progression during viral and bacterial infections (Rimessi et al., 2015; Giorgi et al., 2018).

In summary, what all these pathologies have in common is an imbalance of mitochondrial  $\text{Ca}^{2+}$  influx and extrusion. Depending on the mutation and the cell type, this causes diverse secondary effects like oxidative stress, lack of ATP, excessive apoptosis, faulty metabolic signals etc. which then lead to the patients' symptoms.

### 3.2. The players involved in mitochondrial calcium handling

The number of pathologies related to mitochondrial  $\text{Ca}^{2+}$  handling and their severity emphasize its critical role in cellular homeostasis. However, the diversity of symptoms demonstrates the versatile effects of  $\text{Ca}^{2+}$  in the different tissues. It is fascinating how various cell types have developed distinct strategies for  $\text{Ca}^{2+}$  regulation adapted to their

specific requirements but based on the same set of proteins. The proteins involved in  $\text{Ca}^{2+}$  uptake and extrusion and their regulation will be introduced in the following sections.

The high abundance of VDAC makes the outer mitochondrial membrane fairly permeable for  $\text{Ca}^{2+}$  (Kühlbrandt, 2015). I will therefore focus on the permeability of the IMM.

### 3.2.1. Calcium influx

Under resting conditions, the mitochondrial  $\text{Ca}^{2+}$  concentration is usually similar to the cytosolic. Yet, following activation, mitochondrial  $[\text{Ca}^{2+}]$  can be manyfold higher (10-500-fold) (Xu et al., 2016). But even though it is then directed against a concentration gradient,  $\text{Ca}^{2+}$  uptake into the mitochondria is a passive process that does not require ATP hydrolysis or antiporters. The reason for this is the activity of the ETS. By pumping protons out of the matrix it generates an electrochemical gradient that constitutes an inwards driving force for  $\text{Ca}^{2+}$  that is strong enough to overcome the concentration difference. However, the identity of the channel mediating this influx was long unknown and it is still under debate whether only one or several  $\text{Ca}^{2+}$  inward pathways exist in the IMM.

#### 3.2.1.1. The Mitochondrial Calcium Uniporter complex

As mentioned above, several characteristics of the mitochondrial  $\text{Ca}^{2+}$  uptake channel were known long before its molecular identity. This was uncovered only in 2011, but then simultaneously by two different groups, Stefani et al. (Stefani et al., 2015) and Boughman et al. (Baughman et al., 2011). The pore-forming unit is now known as Mitochondrial Calcium Uniporter, MCU. It is a ~35 kDa protein that contains two transmembrane domains, can be blocked by RuR and Ru360 (two related compounds) and forms oligomers, likely tetramers (Baughman et al., 2011; Stefani et al., 2011; Stefani et al., 2015). They exist as homo-oligomers and hetero-oligomers in a complex together with MCUB. MCUB is closely related to MCU and shares ~ 50 % similarity with MCU but interestingly exerts a dominant-negative effect on MCU channel function (Raffaello et al., 2013). Even a low level of MCUB expression efficiently reduces the MCU opening probability and  $\text{Ca}^{2+}$  flux. Control of the ratio MCU:MCUB seems to be one mean of the cell to regulate mitochondrial  $\text{Ca}^{2+}$  influx. In fact, in skeletal muscle mitochondria, a high ratio was observed (Fieni et al., 2012) in line with a high uptake activity. Cardiac mitochondria, in contrast, express more MCUB

relative to MCU (Raffaello et al., 2013) resulting in low  $\text{Ca}^{2+}$  currents (Fieni et al., 2012). This matches the physiological needs of the two tissues. Mitochondria in cardiomyocytes continuously face high-frequency  $\text{Ca}^{2+}$  oscillations and must limit their uptake to prevent  $\text{Ca}^{2+}$  overload. In contrast, in skeletal muscle mitochondria,  $\text{Ca}^{2+}$  serves as an important regulatory signal that enhances the TCA cycle and ATP synthase productivity. Hence,  $\text{Ca}^{2+}$  uptake is essential to ensure the activity-dependent increase in ATP production upon muscle exercise (Kavanagh et al., 2000; Zhou et al., 2016).

Stefani and co-workers demonstrated that the reconstitution of MCU in planar lipid bilayers alone was sufficient to allow  $\text{Ca}^{2+}$  flux (Stefani et al., 2011). However, the opening probability was lower than measured by patch-clamping of mitoplasts (mitochondria devoid of their outer membrane) (Kirichok et al., 2004) indicating that other proteins are necessary for full activity. In search for other components of the Mitochondrial Calcium Uniporter complex (mtCU), Sancak and co-workers (Sancak et al., 2013) identified the essential MCU regulator (EMRE). Loss of EMRE drastically diminishes mitochondrial  $\text{Ca}^{2+}$  uptake and affects the complex size detected via blue native polyacrylamide gel electrophoresis (BN PAGE) (Sancak et al., 2013) making it a core component of the mtCU. Yet, its precise role is not entirely clear. Two functions have been suggested and await clarification. Firstly, it may serve as a scaffolding protein that facilitates oligomerisation. Secondly, it may mediate the binding between MCU and the MICU (Mitochondrial Calcium Uptake) proteins. MICU1 was the first protein involved in the mitochondrial  $\text{Ca}^{2+}$  pathway that was described by Perocchi et al. (Perocchi et al., 2010). It contains two canonical  $\text{Ca}^{2+}$ -sensing EF-hands (Perocchi et al., 2010; Plovanich et al., 2013). Perocchi et al. hypothesised that it regulates  $\text{Ca}^{2+}$  flux through MCU which is now widely accepted. MICU1 does not insert into the IMM but resides in the intermembrane space (Lam et al., 2015; Stefani et al., 2015). It forms homodimers or heterodimers with MICU2 (Patron et al., 2014; Park et al., 2020). Together they modulate  $\text{Ca}^{2+}$  in a biphasic manner. At low  $[\text{Ca}^{2+}]_{\text{cyto}}$  they act as gatekeepers (Mallilankaraman et al., 2012b) and prevent  $\text{Ca}^{2+}$  influx whereas at high  $[\text{Ca}^{2+}]_{\text{cyto}}$  they have an enhancing effect (Patron et al., 2014). This dual mechanism generates the sigmoidal dose-response curve that was observed for MCU channel activity relative to increasing  $\text{Ca}^{2+}$  concentrations. Patron and colleagues suggested that MICU1 and MICU2 have opposing functions, MICU2 being the inhibitory and MICU1 being the

stimulatory element (Patron et al., 2014). However, it is difficult to study their function separately because they are closely entwined and the knockout of one affects the expression, binding and function of the other (Plovanich et al., 2013). Hence, there is conflicting data on their specific roles suggesting that MICU1 alone may be sufficient to act as gatekeeper and cooperating activator (Csordás et al., 2013) and further research is required for clarification. In vertebrates, there exists a third isoform, MICU3, but very little is known about it to date (Plovanich et al., 2013). Available data indicates that it is particularly important in neurons where it enhances  $\text{Ca}^{2+}$  uptake as a heterodimer with MICU1 and affects synaptic  $\text{Ca}^{2+}$  signals (Patron et al., 2019).

Beyond the direct inhibitory or stimulatory effect of MICU1/2, their expression levels and association with the mtCU may be additional regulatory modes for mitochondrial  $\text{Ca}^{2+}$  uptake. Similar to what was described above for the MCU:MCUb ratio, Paillard et al. observed that the MICU1:MCU ratio alters mtCU activity (Paillard et al., 2017). A low abundance of MICU1 relative to MCU reduces the threshold for  $\text{Ca}^{2+}$  uptake but also lowers the maximal influx and vice versa. Interestingly, this regulation is again tissue-specific. Liver mitochondria exhibit a high MICU1:MCU ratio which allows efficient  $\text{Ca}^{2+}$  uptake when the  $[\text{Ca}^{2+}]_{\text{cyto}}$  is high. This ensures demand-oriented ATP production as a reaction to  $\text{Ca}^{2+}$  signalling. The relatively rare, mild and slow changes in  $[\text{Ca}^{2+}]_{\text{cyto}}$  in hepatocytes, however, are in stark contrast to the  $\text{Ca}^{2+}$  signalling in excitable cells like (cardio-)myocytes. Interestingly, Paillard et al. found a low MICU1:MCU ratio in heart and skeletal muscle which results in a lack of gatekeeping at low  $[\text{Ca}^{2+}]_{\text{cyto}}$  but also a reduced maximal uptake rate during high  $[\text{Ca}^{2+}]_{\text{cyto}}$ . Likely, this represents another mechanism of the two cell types to avoid excessive  $\text{Ca}^{2+}$  accumulation in the matrix (Paillard et al., 2017).

Another layer of complexity was added to the topic of mtCU regulation by the discovery of a MICU1 splice variant in skeletal muscle mitochondria by Vecellio et al. (Vecellio Reane et al., 2016). The splice isoform named MICU1.1. contains an additional micro-exon and seems to lower the threshold for mtCU  $\text{Ca}^{2+}$  uptake. It appears likely that this is just the tip of the iceberg and more posttranscriptional or -translational modifications are yet to be identified.

Moreover, there is accumulating evidence that MICU1 is not only involved in the regulation of  $\text{Ca}^{2+}$  uptake but has additional, mtCU-independent functions. Gottschalk et al.

(Gottschalk et al., 2019) recently demonstrated that MICU1 is not permanently associated with the mtCU. In fact, at low  $[Ca^{2+}]_{cyto}$  only MICU1 localises to the inner boundary membrane whereas MCU and EMRE are evenly distributed across the whole inner membrane. Only upon elevation of the cytosolic  $[Ca^{2+}]$  do all mtCU components accumulate at the inner boundary membrane and allow  $Ca^{2+}$  influx (Gottschalk et al., 2019). They showed that the presence of MICU1 at the inner boundary membrane is crucial for CJ stability and the retention of cyt *c*. This notion was supported by the work of Tomar and colleagues (Tomar et al., 2019) who showed that MICU1 interacts with MIC60, a component of the MICOS and CHCHD2 which also has been associated with cristae organisation and cyt *c* stabilisation (Meng et al., 2017; Liu et al., 2020c). Loss of MICU1 alters mitochondrial morphology indicating that it is indispensable for cristae organisation (Liu et al., 2016; Tomar et al., 2019). Tomar et al. suggest that MICU1 confers  $Ca^{2+}$  sensitivity to the MICOS and mediates  $Ca^{2+}$ -dependent cristae remodelling (Tomar et al., 2019). This dual role of MICU1 may explain a finding of Mallilankaraman et al. (Mallilankaraman et al., 2012a) which was hard to explain at the time. They identified another putative regulatory unit of the mtCU that was named MCU regulator 1 (MCUR1) and affects mitochondrial  $Ca^{2+}$  uptake. It immunoprecipitates with MCU but not with MICU1. They hypothesised that there exist two different forms of the mtCU with distinct regulatory proteins, either MICU1/2 or MCUR1 (Mallilankaraman et al., 2012a). Considering the data from the studies mentioned above it seems possible that they assemble with MCU under different conditions potentially even replace each other. However, in a study by another group, MCUR1 was shown to facilitate complex IV assembly thereby affecting ETS function (Paupe et al., 2015). The authors claim that the reduced  $Ca^{2+}$  uptake is only a secondary effect due to diminished mitochondrial membrane potential. Further research is required to solve this question.

Hoffmann et al. (Hoffmann et al., 2014) identified another protein interacting with MCU and MICU1. SLC25A23 belongs to the solute carrier family and contains several  $Ca^{2+}$ -sensing EF-hands. Its loss diminished mitochondrial  $Ca^{2+}$  uptake indicating some stimulatory role on MCU.

To sum up, it is no surprise that the regulation of mitochondrial  $Ca^{2+}$  uptake through the mtCU is an extremely complex, fine-tuned machinery that involves adaptations on all

thinkable levels, transcription, translation, complex assembly, etc...Despite enormous progress in the last two decades, there remain a lot of unresolved questions. One of them is the question of whether the mtCU is the only  $\text{Ca}^{2+}$  uptake channel.

#### 3.2.1.2. mtCU-independent calcium uptake

Following the landmark identification of MCU as the pore-forming unit of the mtCU, two lines of *MCU* KO mice were generated and – to the surprise of the whole research field – one of them did not show a marked phenotype (Pan et al., 2013; Murphy et al., 2014). Homozygous knockout mice on an inbred C57Bl6 background die at an intermediate embryonal stage while *MCU* KO mice with an outbred CD1 background are viable and do not exhibit gross impairments. This challenged two established postulates: Does the mtCU represent the sole  $\text{Ca}^{2+}$  influx pathway and how important is it for the coupling of metabolism and  $\text{Ca}^{2+}$  signals?

Long before the excitement around MCU, several different uptake modes had been observed but did not receive a lot of attention. Sparagna and co-workers (Sparagna et al., 1995) were the first to describe the “rapid mode of uptake” (RaM) which is a high conductivity  $\text{Ca}^{2+}$  uptake mode that only occurs very shortly (<1 s) at the beginning of a  $\text{Ca}^{2+}$  pulse. It can be reset by a transient lowering of the extramitochondrial  $[\text{Ca}^{2+}]$  which enables more efficient  $\text{Ca}^{2+}$  uptake from a sequence of pulses compared to a continuous elevation of  $[\text{Ca}^{2+}]$ . Like  $\text{Ca}^{2+}$  flux through MCU, the RaM is also sensitive to RuR but only at higher concentrations. A low concentration of RuR (<0.1 nM/mg of mitochondrial protein) even seems to increase its opening probability (Sparagna et al., 1995). Similar fluxes and pharmacological characteristics were reported by other groups (Buntinas et al., 2001; Wei et al., 2012). Interestingly, Wei et al. (Wei et al., 2012) revealed that the two uptake modes (which they named  $\text{MCU}_{\text{mode1/2}}$ ) also differ in their effect on the matrix free  $[\text{Ca}^{2+}]$ . Although the rapid and less RuR/Ru360-sensitive mode ( $\text{MCU}_{\text{mode1}}$ ) is activated by lower extramitochondrial  $[\text{Ca}^{2+}]$  (0.1-2  $\mu\text{M}$ ) it results in a drastic increase in free  $[\text{Ca}^{2+}]_{\text{mito}}$ . In contrast, the change in  $[\text{Ca}^{2+}]_{\text{mito}}$  is less pronounced in response to the slower RuR/Ru360-sensitive uptake mode ( $\text{MCU}_{\text{mode2}}$ ) (Wei et al., 2012). The authors provide evidence that the slow  $\text{Ca}^{2+}$  influx allows simultaneous uptake of phosphate which then forms calcium-phosphate and prevents the increase of free  $\text{Ca}^{2+}$  in the matrix. Based on this observation,

they hypothesise that  $\text{MCU}_{\text{mode2}}$  which likely represents mtCU activity rather mediates a  $\text{Ca}^{2+}$  sink function of the mitochondria by removing  $\text{Ca}^{2+}$  from the cytosol.  $\text{MCU}_{\text{mode1}}$ , on the other hand, may be responsible for the coupling of cellular energy demand and mitochondrial ATP production by effectively raising matrix free  $[\text{Ca}^{2+}]$  (Wei et al., 2012). All mentioned studies were performed using isolated mitochondria and either labelled  $\text{Ca}^{2+}$  ( $^{45}\text{Ca}^{2+}$ ) or  $\text{Ca}^{2+}$ -sensitive dyes. Bondarenko and colleagues (Bondarenko et al., 2013) measured  $\text{Ca}^{2+}$  fluxes of mitoplasts using a patch-clamp setup. They were able to distinguish three different uptake modes which they termed intermediate, bursting and xl-mitochondrial calcium channel (i-MCC, b-MCC, xl-MCC). They differ in their conductivity (xl-MCC > b-MCC > i-MCC), their sensitivity to RuR/Ru360 (xl-MCC > b-MCC/i-MCC) and their occurrence (i-MCC > b-MCC > xl-MCC). However, what all these publications have in common is the fact that they merely describe mitochondrial  $\text{Ca}^{2+}$  currents. It is unclear whether the different modes are mediated by distinct channel proteins or if they only depict different conductivity states of the same molecular entity.

In a follow-up study with MCU knockdown cells, Bondarenko et al. showed that i-MCC most likely represents mtCU activity (Bondarenko et al., 2014). Notably, lack of MCU induces “a 2.3-fold increase in the occurrence probability of xl-MCC” (Bondarenko et al., 2014). This indicates that there are at least two distinct  $\text{Ca}^{2+}$  channels. Yet, the identity of a putative second (or third) channel protein besides MCU remains elusive. Discussed candidates are the mitochondrial ryanodine receptor 1 (mRyR1) (Beutner et al., 2001; Beutner et al., 2005; Ryu et al., 2011), the Leucine Zipper-EF-hand-containing transmembrane protein 1 (LETM1) (Jiang et al., 2009; Waldeck-Weiermair et al., 2011), the  $\text{Na}^+$ - $\text{Ca}^{2+}$ - $\text{Li}^+$ -exchanger (NCLX) (Trenker et al., 2007; Waldeck-Weiermair et al., 2011), the transient receptor potential channel 3 (TRPC3) (Feng et al., 2013) and the uncoupling proteins 2 and 3 (UCP2/3) (Trenker et al., 2007; Waldeck-Weiermair et al., 2011).

RyR1 is better known to be a  $\text{Ca}^{2+}$  release channel in the sarcoplasmic reticulum in skeletal muscle. However, it was found in mitochondria in cardiac cells and there affect the  $\text{Ca}^{2+}$  uptake rate (Beutner et al., 2001; Beutner et al., 2005). LETM1 is a much-disputed exchanger of cations. To date, it is debated whether it transports  $\text{K}^+$  or  $\text{Ca}^{2+}$  through the IMM while there is a consensus that it does so in exchange for  $\text{H}^+$  (Austin and Nowikovsky, 2019; Lin and Stathopoulos, 2019). Hence, under physiological conditions, it is thought to

use the proton gradient at the IMM to export cations from the matrix (Tsai et al., 2014). Yet, a decline in  $[Ca^{2+}]_{cyto}$  and/or cytoplasmic acidification may induce a reverse mode during which LETM1 imports  $Ca^{2+}$  and contributes to MMP by exporting protons (Jiang et al., 2009). The same applies to NCLX which mainly serves as a  $Ca^{2+}$  exporter in exchange for  $Na^+$  but may work in reverse under certain conditions (Griffiths, 1999). TRPC3 belongs to a family of ion channels that are mainly found at the plasma membrane. Feng et al. (Feng et al., 2013) suggested that it is partially localised at the mitochondria and impacts mitochondrial  $Ca^{2+}$  uptake. UCP 2 and 3 have been implicated in several mitochondrial processes such as the induction of apoptosis, ROS production and metabolism and also  $Ca^{2+}$  uptake (Trenker et al., 2007; Waldeck-Weiermair et al., 2011). Yet, their exact function is unclear. However, most of these proposed alternative  $Ca^{2+}$  uptake pathways have been excluded one way or another. The contribution of RyR1 was ruled out by the presence of ryanodine which suppresses its activity (Beutner et al., 2001; Wei et al., 2012). Similarly, the reverse activity of NCLX was excluded by the addition of the known NCLX-blocker CGP-37157 (CGP) or by measuring in the absence of  $Na^+$  which likewise abolishes NCLX activity (Bondarenko et al., 2013). LETM1 too can be disregarded as the observed currents are indicative for a channel not for an ion exchanger (Bondarenko et al., 2014). UCP 2/3 have recently been implicated in the regulation of MICU1 (Madreiter-Sokolowski et al., 2016). Thus, they most likely affect mitochondrial  $Ca^{2+}$  uptake by modulating mtCU. There is very little evidence for mitochondrial localisation of TRPC3 and its role in mitochondrial  $Ca^{2+}$  handling. Further research is required to substantiate the findings of Feng and co-workers. In summary, there is convincing evidence for the existence of at least one mtCU-independent  $Ca^{2+}$  influx pathway across the IMM. However, despite considerable research and a long list of candidates, the molecular identity remains elusive. Moreover, it is yet unclear what the physiological role of this putative alternative  $Ca^{2+}$  uptake mechanism is. It may exclusively mediate the coupling of mitochondrial metabolism and cellular activity which would mean that it is not only structurally but also functionally distinct from the mtCU. Or it may serve as a backup and only becomes activated in response to cellular stress and/or loss of mtCU function.

The unexpected survival and wellbeing of the MCU KO mice led to a renaissance of interest in these questions and considerable efforts will hopefully yield exciting answers in the upcoming years.

### 3.2.2. Calcium export

What goes in must go out. This is not only logical, even more so, it is of vital importance on the cellular level. Excessive matrix  $\text{Ca}^{2+}$  accumulation is one of the main triggers for the opening of the mitochondrial permeability transition pore (mPTP) which will be introduced in more detail later. In brief, the prolonged opening of this pore allows rapid efflux of ions and small molecules from the mitochondrial matrix (Carraro et al., 2019). This results in the collapse of the MMP which in turn is a major apoptotic signal that can lead to the recruitment of pro-apoptotic factors (e.g. BCL-2-proteins), the release of cyt *c* from the intermembrane space and ultimately apoptosis (Marzo et al., 1998). This emphasises the importance of a well-balanced mitochondrial  $\text{Ca}^{2+}$  import-export system.

In contrast to the  $\text{Ca}^{2+}$  influx which is a passive process driven by the MMP,  $\text{Ca}^{2+}$  extrusion requires active transport. Historically, two different systems for  $\text{Ca}^{2+}$  export have been described based on electrophysiological properties (Giorgi et al., 2018). Both export  $\text{Ca}^{2+}$  in exchange for other cations. The mitochondrial  $\text{Ca}^{2+}$ - $\text{H}^{+}$ - exchanger (mCHX) mediates  $\text{Ca}^{2+}$  transport at the expense of the proton gradient whereas the mitochondrial  $\text{Na}^{+}$ - $\text{Ca}^{2+}$ -exchanger (mNCX) uses sodium ions. What is known about the responsible proteins will be summarised briefly in the following sections.

#### 3.2.2.1. mNCX

It is today well accepted that the molecular representation of the mNCX is the protein  $\text{Na}^{+}$ - $\text{Ca}^{2+}$ - $\text{Li}^{+}$ -exchanger NCLX. As indicated by the name, in addition to  $\text{Na}^{+}$ , NCLX is capable of transporting lithium ions across the IMM to support  $\text{Ca}^{2+}$  efflux. Under physiological conditions, NCLX functions in an electrogenic mode by exporting one  $\text{Ca}^{2+}$  in exchange for three  $\text{Na}^{+}$  (Jung et al., 1995; Palty et al., 2006). As mentioned before, it can be completely blocked by CGP. It is strongly expressed in skeletal muscle, smooth muscle cells, pancreas and the liver (Palty et al., 2004; Palty et al., 2010; Rysted et al., 2021). Nonetheless, there is evidence that the transcript level does not necessarily correspond to the actual efflux activity in the tissue. Rysted and colleagues (Rysted et al., 2021) detected high expression

levels in the liver but no NCLX-mediated  $\text{Ca}^{2+}$  efflux. Whereas in brain and heart mitochondria  $\text{Ca}^{2+}$  was rapidly exported by NCLX even though it was less abundant (Rysted et al., 2021). This indicates that NCLX is the major  $\text{Ca}^{2+}$  export pathway in excitable tissues and less crucial in non-excitable cells. The discrepancy between transcript levels and sodium-dependent mitochondrial  $\text{Ca}^{2+}$  extrusion may be explained by previously reported extra-mitochondrial localisations of NCLX e.g. at the plasma membrane or in the ER (Palty et al., 2004; Palty et al., 2006; Han et al., 2015). Moreover, NCLX activity can be modulated by posttranslational modifications, the MMP and  $\text{Na}^+$  and  $\text{Ca}^{2+}$  concentration (Kostic and Sekler, 2019). To maintain a stable  $\text{Na}^+$  gradient across the IMM, the  $\text{Na}^+$  uptake into the mitochondrial matrix by NCLX is counterbalanced by a  $\text{Na}^+$ - $\text{H}^+$ -exchanger (mNHE) (Finkel et al., 2015).

#### 3.2.2.2. mCHX

In contrast to mNCX, mCHX is electro-neutral, meaning that one  $\text{Ca}^{2+}$  is exchanged for two  $\text{H}^+$  and seems to be more important in non-excitable tissue such as liver and kidney (Tsai et al., 2014; Rysted et al., 2021). The identity of the protein mediating this antiport is rather controversial and has been discussed for over a decade. To date, the strongest candidate is LETM1 which was previously mentioned as a possible alternative  $\text{Ca}^{2+}$  influx pathway. It contains only one – or based on newer calculations two – proposed transmembrane domains and two canonical  $\text{Ca}^{2+}$ -sensitive EF-hands both facing the mitochondrial matrix (Shao et al., 2016; Austin and Nowikovsky, 2019). Based on 3D reconstructions from electron microscopy data, Shao et al. (Shao et al., 2016) recently provided evidence that LETM1 homo-oligomerises and forms hexameric structures with a central cavity allowing ion flux. Moreover, they propose that the complex exhibits pH-dependent conformational changes that allow ion flux at alkaline pH (pH 8.0) but not at acidic pH (pH 6.5) (Shao et al., 2016).

LETM1 was first described as a  $\text{Ca}^{2+}$ - $\text{H}^+$ -exchanger by Jiang and co-workers in a genome-wide RNAi screen for proteins involved in mitochondrial  $\text{Ca}^{2+}$  transport (Jiang et al., 2009). They performed silencing and overexpression experiments and reconstituted purified LETM1 in liposomes. The results suggest that LETM1 is a  $\text{Ca}^{2+}$ - $\text{H}^+$ -antiporter that works bidirectional depending on the surrounding conditions. At low  $[\text{Ca}^{2+}]_{\text{mito}}$  and alkaline pH in

the cytosol,  $\text{Ca}^{2+}$  is imported and protons are exported. This uptake mode was observed at cytosolic  $\text{Ca}^{2+}$  concentrations  $<1\mu\text{M}$ . Uptake at higher  $[\text{Ca}^{2+}]_{\text{cyto}}$  was attributed to the mtCU. Acidification of the cytosol and increase in  $[\text{Ca}^{2+}]_{\text{mito}}$  activates the  $\text{Ca}^{2+}$  export mode with concomitant  $\text{H}^+$  import reducing the MMP (Jiang et al., 2009). This is not completely in line with the aforementioned conformational change that suggests low permeability at acidic pH. Yet, it is unclear whether it is the pH in the mitochondrial matrix or in the cytosol or both that determine the 3D structure. Further studies may be required to elucidate the proposed pH dependency and its effect on LETM1 function. Another unresolved debate concerns the sensitivity to inhibitory compounds. Jiang et al. (Jiang et al., 2009) observed that  $\text{Ca}^{2+}$  uptake into liposomes reconstituted with LETM1 was blocked by RuR and reduced by  $\sim 25\%$  in presence of CGP. With the same experimental setup but with higher protein purity and density, Tsai and co-workers did not detect any inhibitory effects of both reagents (Tsai et al., 2014).

Nonetheless, the involvement of LETM1 in mitochondrial  $\text{Ca}^{2+}$  handling was supported by several other studies (Waldeck-Weiermair et al., 2011; Tsai et al., 2014; Shao et al., 2016). Yet, its role as mCHX is challenged by advocates of its original identification as  $\text{K}^+-\text{H}^+$ -antiporter. Based on silencing and overexpression studies in different organisms they hypothesise that LETM1 exports  $\text{K}^+$  and only indirectly affects  $\text{Ca}^{2+}$  transport via the cross-linking of  $\text{K}^+$ -,  $\text{Na}^+$ - and  $\text{Ca}^{2+}$ -fluxes (Nowikovsky et al., 2004; Hashimi et al., 2013; Marchi et al., 2014). They suggest that by exporting  $\text{K}^+$ , LETM1 is crucial for mitochondrial volume control because  $\text{K}^+$  is one of the major regulators of cellular osmotic balance.

With advances in technology and methodology, it seems likely that this dispute will be solved in the upcoming years and mark another milestone in the understanding of mitochondrial ion handling.

### 3.2.2.3. mPTP

Mitochondrial permeability transition described a sudden increase in the permeability of the IMM that is mediated by the so-called mitochondrial permeability transition pore (mPTP) or mitochondrial megachannel (MMC) (Bernardi, 1999; Bernardi and Stockum, 2012). The mPTP is a large channel that allows the efflux of various mitochondrial solutes i.e. ions and molecules smaller than 1.5 kDa in size. As shortly described above, prolonged

opening leads to a loss in MMP, mitochondrial swelling and subsequently to the release of cyt c from the IMS and the induction of apoptosis (Marzo et al., 1998; Carraro et al., 2019). However, a transient short opening may also have a physiological function and serve as a rescue valve to prevent further  $\text{Ca}^{2+}$  accumulation which is the main inducer of permeability transition (Petronilli et al., 1999; Bernardi and Stockum, 2012; Agarwal et al., 2017). The opening propensity of the pore is influenced by multiple factors. Besides  $\text{Ca}^{2+}$ , phosphate and free fatty acids exert a stimulatory effect (Haworth and Hunter, 1979; Hunter and Haworth, 1979). On the contrary, high concentrations of adenine nucleotides,  $\text{Mg}^{2+}$  and an acidic pH prevent mitochondrial permeability transition (Haworth and Hunter, 1979; Hunter and Haworth, 1979). The antibiotic peptide cyclosporin A (CsA) is the best-known inhibitor of mPTP and is commonly used in mitochondrial research. Notably, it does not completely block its activity but only de-sensitises it (Broekemeier et al., 1989).

Similarly to mCHX, the molecular identity of the mPTP has not yet been conclusively defined. Several candidates have been proposed as subunits of the mPTP over the years, among them the adenine nucleotide transporter (ANT), the peripheral-type benzodiazepine receptor (PBR), cyclophilin D (CypD) and VDAC (Zamzami and Kroemer, 2001; Azarashvili et al., 2007; Karch et al., 2019; Winkvist and Gribkoff, 2020). Yet, the underlying evidence had its inconsistencies and was never quite sufficient to be widely accepted (Carraro et al., 2019). In 2013, Paolo Bernardi and his group came up with a novel suggestion (Giorgio et al., 2013) which they have extensively studied ever since to prove their point. In fact, the accumulated data now provides very strong evidence for their theory: Via various genetic manipulations and reconstitution of purified ATP synthase in liposomes and lipid bilayers they show that it gives rise to currents that exactly mirror the characteristics of the mPTP (Carraro et al., 2014; Urbani et al., 2019; Carrer et al., 2021). This includes the conductivity and the sensitivity to inhibitors and activators (Urbani et al., 2019). Moreover, it was observed that the ATP synthase forms dimers and tetramers and that only these multimers are capable of producing the PT-like currents (Urbani et al., 2019). CsA sensitivity is conferred via the interaction of CsA with CypD which binds to the lateral stalk (the  $\text{F}_1$  unit) of the ATP synthase (Giorgio et al., 2009).

This hypothesis has been challenged by several studies that still detected PT-like currents in cells lacking an assembled ATP synthase (He et al., 2017; Carroll et al., 2019). The current

was sensitive to bongkreikic acid, a known inhibitor of the ANT but also slower than the one observed in wildtype (WT) cells (Carroll et al., 2019). Bernardi and co-workers reason that this does not contradict their hypothesis of the ATP synthase forming the mPTP but only indicates that ANT may act as a compensatory  $\text{Ca}^{2+}$  efflux pathway under certain conditions.

Based on the described convincing evidence it seems reasonable to accept the ATP synthase as the molecular identity of the long-sought mPTP. Eventually, this likely solves one of the many riddles around mitochondrial  $\text{Ca}^{2+}$  handling.

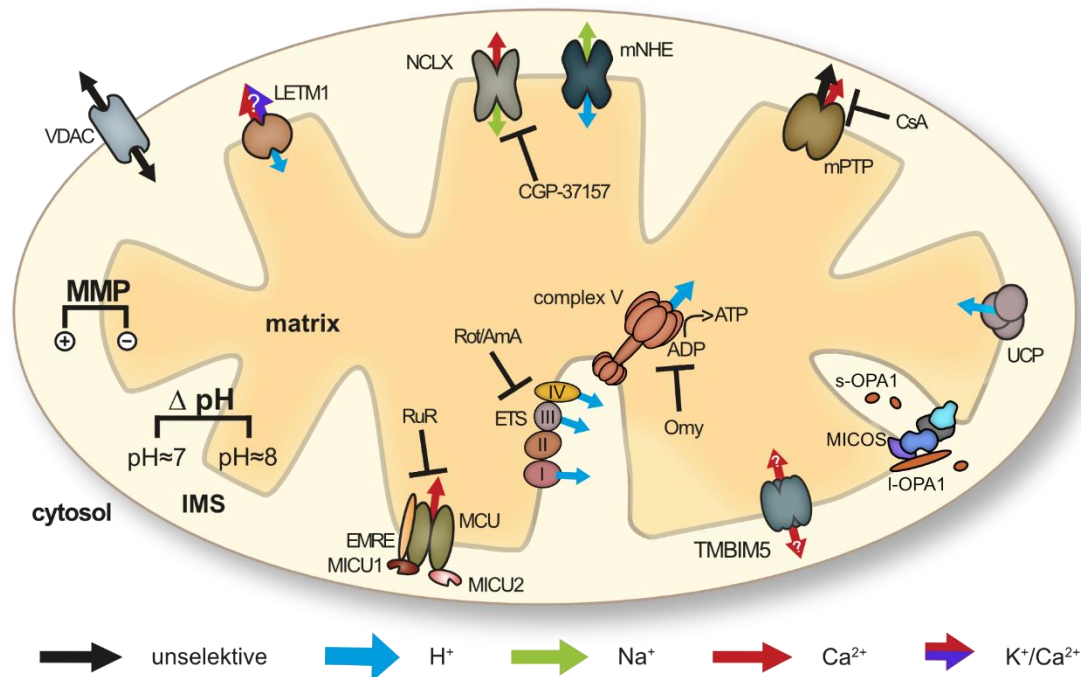


**Figure 1: Simplified depiction of the ion channels and transporters in the mitochondrial membranes.** VDAC=voltage-dependent anion channel, LETM1= Leucine Zipper-EF-hand-containing transmembrane protein 1, NCLX= $\text{Na}^+$ - $\text{Ca}^{2+}$ - $\text{Li}^+$ -exchanger, mNHE= $\text{Na}^+$ - $\text{H}^+$ -exchanger, mPTP=mitochondrial permeability transmission pore, UCP=uncoupling proteins, s-/l-OPA1=short/long isoform of Optical Atrophy 1, MICOS=mitochondrial contact site and cristae organizing system, TMBIM5=Transmembrane BAX Inhibitor Motif Containing protein 5, ETS=Electron Transport System with the complexes I-V, MCU=Mitochondrial Calcium Uniporter, MICU1/2=Mitochondrial Calcium Uptake 1/2, EMRE=Essential MCU Regulator, IMS=intermembrane space, MMP=mitochondrial membrane potential, CsA=Cyclosporin A, Omy=oligomycin, Rot=rotenone, AmA=antimycin A, RuR=Ruthenium Red;

### 3.3. TMBIM5

Any progress made in the understanding of mitochondrial  $\text{Ca}^{2+}$  handling only emphasises its extreme complexity and delicate fine-tuning. Without a doubt, there are even more players involved that await identification. I dedicated this work to the characterisation of

one promising candidate for a novel mitochondrial ion channel named Transmembrane BAX Inhibitor Motif containing protein 5 (TMBIM5/T5). TMBIM5 belongs to a family of six highly conserved membrane proteins (TMBIM1-6) with homologues found in many species (from *Drosophila melanogaster* to humans) (Reimers et al., 2007). It is rather ubiquitously expressed with particular high transcript levels in the brain, heart and skeletal muscle (Li et al., 2001; Yoshida et al., 2006; Lisak et al., 2015). It shares a common motif with the other family members (UPF0005) that is functionally not yet fully defined but confers a membrane-spanning structure with six to eight predicted transmembrane domains (Reimers et al., 2007). Several properties make TMBIM5 unique from its relatives. Whilst they are found in nearly all intracellular membranes (lysosomal/endosomal/ER/Golgi apparatus/plasma membrane), TMBIM5 is the only one that resides at the inner mitochondrial membrane. Its N-terminal mitochondrial targeting sequence (MTS) is presumably cleaved after membrane integration (Lisak et al., 2015). Moreover, a more recent bioinformatic analysis suggests that TMBIM5 contains eight instead of seven transmembrane domains which likely affects its orientation in the inner mitochondrial membrane with its C-terminus probably facing the intermembrane space (Oka et al., 2008). The predicted three-dimensional structure of TMBIM5 is depicted in Fig. 1.

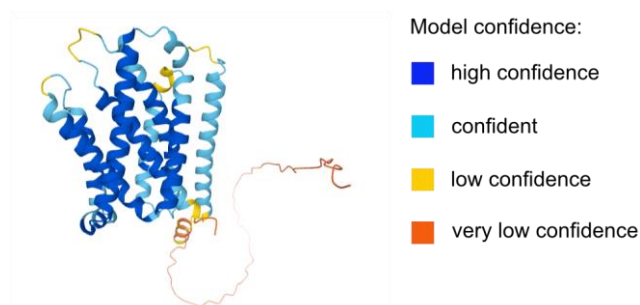


**Figure 2: 3D-Structure of Transmembrane BAX Inhibitor Motif containing protein 5 (TMBIM5).**

Tertiary protein structure prediction by AlphaFold (Jumper et al., 2021). The colours depict the model confidence as indicated.

Based on genetic screens, TMBIM5 has been implicated in diverse functions (e.g. immunology (Nagel et al., 2004) and ageing in *Drosophila* (Zou et al., 2000)) over the last 20 years and accordingly received multiple names. Aside from TMBIM5, it is known as GHITM, MICS1, DERP2 and the open reading frame (ORF) is termed My021 or UNQ244/PRO281. The first more detailed description was authored by Li and co-workers (Li et al., 2001) who identified TMBIM5 in a screen for genes that are differentially

regulated in a mouse line expressing a growth hormone (GH) antagonist which led to the name growth Hormone Inducible Transmembrane protein, GHITM. Oka et al. (Oka et al., 2008) called it Mitochondrial Morphology and Cristae Structure 1 (MICS1) because they observed that its knockdown strongly impairs mitochondrial shape and in particular the cristae organisation. This was later supported by Meng and co-workers (Meng et al., 2017) who detected a direct interaction between MICS1/TMBIM5 and CHCHD2. CHCHD2 is a close homologue of the putative MICOS-component CHCHD10 and may be involved in the maintenance of cristae organisation (Zhang et al., 2014). Yet, this may not be the main or at least not the only function of TMBIM5. Both groups report that it stabilises *cyt c* at the IMM and thereby prevents premature *cyt c* release. The loss of MICS1/TMBIM5 facilitates the release of *cyt c* and other proapoptotic proteins into the cytosol which is reversed by MICS1/TMBIM5 overexpression (Oka et al., 2008). Immunoprecipitations revealed physical contact between MICS1/TMBIM5 and *cyt c* (Oka et al., 2008; Meng et al., 2017). This hints towards the involvement of TMBIM5 in apoptotic processes. Indeed, several other TMBIM proteins are thought to act as anti-apoptotic factors (Lisak et al., 2015; Rojas-Rivera and Hetz, 2015). TMBIM6, the founding and most studied member of the family, was originally identified in a screen for genes that protect BAX-overexpressing yeast from apoptosis (Xu and Reed, 1998). The authors termed it BAX Inhibitor 1 (BI-1) which is a rather misleading name as they point out in the very same publication that the two proteins do not show any physical contact. Hence, the proapoptotic effect must be an indirect one. Interestingly, studies by our group and our cooperation partner Dr Geert Bultynck suggest that this indirect effect is achieved via the regulation of intracellular  $\text{Ca}^{2+}$  (Bultynck et al., 2012; Kiviluoto et al., 2013). BI-1 acts as a  $\text{Ca}^{2+}$  leak channel in the ER membrane and thereby lowers ER  $\text{Ca}^{2+}$  content (Westphalen et al., 2005). This, in turn, reduces ER stress and  $\text{Ca}^{2+}$  transfer to the mitochondria. Both events have a cytoprotective effect by preventing apoptotic signals (Chae et al., 2004; Westphalen et al., 2005). Notably, the  $\text{Ca}^{2+}$  channel activity of BI-1 is pH-dependent. The domain conferring pH-sensitivity is a di-aspartyl motif at the C-terminal loop-domain that is extremely conserved across species and also in all other TMBIM proteins (Bultynck et al., 2012; Lisak et al., 2015). Mutation of only one of the aspartic acids abolishes  $\text{Ca}^{2+}$  flux activity of BI-1 (Bultynck et al., 2012). In human TMBIM5 this domain is constituted by D294 and D325. Studies on the bacterial homologue BsYetJ

and BI-1 both showed a bell-shaped relation of the pH-dependency with low permeability at high ( $\geq$  pH 7.9) and low (pH  $\leq$  6) pH and the highest opening probability at a near-neutral pH (Kiviluoto et al., 2013; Chang et al., 2014). This can be explained by changes in the conformation and the charges within the putative pore. At acidic pH, the two aspartates become protonated and likely form dihydrogen bonds that block the cavity. An alkaline environment promotes the deprotonation of the acidic residues but also favours bond-formation with nearby positively charged amino acids (i.e. Arg60 in BsYetJ) (Chang et al., 2014). This again hinders  $\text{Ca}^{2+}$  flux. Hence, a near-neutral pH provides the best condition for the open state of the pore (Kiviluoto et al., 2013; Chang et al., 2014).

Based on the close phylogenetic relation of TMBIM5 to BI-1 and the sequence homologies to BsYetJ (Lisak et al., 2015), it seems very likely that TMBIM5 too possesses the ability to channel  $\text{Ca}^{2+}$  in a pH-dependent manner. However, TMBIM5 differs from BI-1 in a very important aspect: its localisation. BI-1 serves as a  $\text{Ca}^{2+}$  leak channel at the ER because there is an outwards driving force due to the concentration gradient of  $\text{Ca}^{2+}$ . This is maintained by the SERCA that actively transports  $\text{Ca}^{2+}$  into the ER lumen. The mitochondrial inner membrane, on the contrary, is electrically charged as a result of the proton export by the ETS. This negative potential (circa -180 mV) is such a strong inwards driving force for  $\text{Ca}^{2+}$  that it allows influx even against a concentration gradient. This means that TMBIM5 could serve as another mitochondrial  $\text{Ca}^{2+}$  uptake pathway.

To sum up, due to its mitochondrial localisation TMBIM5 is a unique member of the TMBIM family. Yet, little is known to date about its physiological role, its functionality and regulation. Is it involved in mitochondrial cristae organisation? Does it act as an anti-apoptotic factor by stabilising *cyt c*? Does it mediate  $\text{Ca}^{2+}$  flux across the IMM? Does it have multiple functions? Does it only influence some of the above-mentioned processes indirectly?

To clarify some of these open questions, I studied TMBIM5 in several knockout cell lines and in a mouse line containing a point mutation in the conserved di-aspartyl motif in the pore domain. We decided on this minimalistic modification to be able to specifically investigate the putative channel function of TMBIM5. As described above, TMBIM5 may be implicated in a number of activities and a complete KO would have made these indistinguishable.

## 4. Material and Methods

### 4.1. Material

#### 4.1.1. Reagents

**Table 1: List of reagents**

Context	Compound	Manufacturer
Genotyping	Direct PCR lysis reagent (ear/tail)	Viagen Biotech
	Proteinase K	Peqlab
	Nuclease-free water	Ambion
	dNTPs	Thermo Fisher/ Fermentas
	DMSO	Roth
	GoTaq Polymerase	Promega
	GoTaq Reaction buffer	Promega
	Fspl	New England Biolabs
	Cutsmart buffer	New England Biolabs
	Cell culture	Iscove's Modified Dulbecco's Medium
Dulbecco's modified eagle's medium (DMEM) with GlutaMax		Gibco
DMEM high glucose		Gibco
Fetal bovine serum		HyClone
10 000 Units/ml Penicillin and 10 mg/ml Streptomycin		Sigma Aldrich
L-Glutamine		Life Technologies
Dimethyl sulfoxide		Sigma Aldrich
Trypsin/EDTA (0.05 %/0.02 %)		Sigma Aldrich
Opti-MEM		Life Technologies
Turbofectin 8.0		Origene
DNAase I		Sigma Aldrich
BD Pharm Lyse™ Lysing Buffer (10x)		BD Biosciences
Mitochondrial isolation		Proteinase
	Subtilisin	Sigma Aldrich
	Bovine serum albumin	Sigma Aldrich
Immunoblotting	β-Mercaptoethanol	Bio-Rad
	Dithiothreitol	Roth
	Dodecyl-beta-D-maltoside (DDM)	Roth
	Laemmli buffer	Bio-Rad
	BN PAGE loading dye	Invitrogen/Thermo Fisher
	Digitonin	Sigma Aldrich
	G-250	Invitrogen/Thermo Fisher

	BN PAGE running/anode/cathode buffer	Invitrogen/Thermo Fisher
	Chameleon Duo Pre-stained Protein Ladder	LiCor
	Native Marker Kit	GE Healthcare/Thermo Fisher
GSH Assay	5-Sulfosalicylic acid (SSA)	Sigma Aldrich
	Tri-ethanolamine (TEA)	Sigma Aldrich
	5,5-Dithiobis(2-nitrobenzoic acid) (DTNB)	Sigma Aldrich
	NADPH	Sigma Aldrich
	Glutathione reductase	Sigma Aldrich
FACS	Fixable viability dye (FVD) eFluor™ 780	Invitrogen™
	Anti-Rat and Anti-Hamster Ig κ /Negative Control Compensation Particles Set	BD™ Biosciences
	Rat-anti-mouse CD4- FITC (GK 1.5)	Invitrogen™/ebioscience
	Rat-anti-mouse CD4 – brilliant violet (GK1.5)	Biolegend
	Rat-anti-mouse CD4 – APC-eFluor780 (GK 1.5)	Invitrogen™/ebioscience
Microscopy	Ionomycin	Sigma Aldrich
	Tetramethylrhodamine methyl ester (TMRM)	Sigma Aldrich
	CellMask™ deep red plasma membrane stain	Thermo Fisher
	Hoechst	Thermo Fisher
	Carbonyl cyanide-p-trifluoromethoxyphenylhydrazone (FCCP)	Sigma Aldrich
	Paraformaldehyde (PFA)/Roti® Histofix 4 %	Roth
	Roti®-block	Roth
	Triton-X-100	Thermo Fisher
	4',6-diamidino-2-phenylindole (DAPI)	Life Technologies
High-resolution respirometry	Rotenone	Sigma Aldrich
	Saponin	Sigma Aldrich
	Catalase	Sigma Aldrich
	Hydrogenperoxide (30 %)	Merck
	Adenosine diphosphate (ADP)	Merck Millipore
	Cytochrome C	Sigma Aldrich
	Oligomycin	Sigma Aldrich
	Antimycin A	Sigma Aldrich
Assays with isolated mitochondria	Cyclosporin A	Santa Cruz Biotechnology
	CGP-37157	Sigma Aldrich
	Calcium Green-5N	Life Technologies
	Thapsigargin	Life Technologies
	Polyethyleneglycol-3350 (PEG)	Merck Millipore

Oxidative burst	Citrate solution (4 %)	Sigma Aldrich
	Phorbol-12,13-Dibutyrate (PDBU)	Sigma Aldrich
	Zymosan A	Sigma Aldrich
	L-012	Wako

#### 4.1.2. Commercial kits

**Table 2: List of commercial kits**

Kit	Manufacturer
Quick-gDNA MiniPrep kit	Zymo Research
Bicinchoninic acid assay (BCA) kit	Interchim
Lowry protein assay reagent A/B	Bio-Rad
Clarity™ Western ECL kit	Bio-Rad
SuperSignal™ West Femto Maximum sensitivity kit	Thermo Fisher Scientific
Gateway LR clonase enzyme mix	Life Technologies
Duolink® in Situ red kit (mouse/rabbit)	Sigma Aldrich
ProcartaPlex™ Simplex kit IL-6	Thermo Fisher Scientific

#### 4.1.3. Antibodies

36

**Table 3: List of antibodies**

Specificity	Manufacturer (catalogue number)	Labelling	Host species	Dilution (IB/ICC)
$\alpha/\beta$ -Tubulin	Cell Signalling (2148)	unlabelled	rabbit	1:1.000/---
Actin	Merck chemicals (MAB1501)	unlabelled	mouse	1:1.000/---
ATP5	Abcam (ab14748)	unlabelled	mouse	1:1.000/---
coxIV	Cell Signalling (4844)	unlabelled	rabbit	1:1.000/---
coxIV	Abcam (ab33985)	unlabelled	mouse	1:1.000/---
G6PD	Cell Signalling (12263S)	unlabelled	rabbit	1:1.000/---
GAPDH	New England Biolabs (2118S)	unlabelled	rabbit	1:1.000/---
LETM1	Abcam (ab224361)	unlabelled	rabbit	1:1.000/ 3 $\mu$ g/ml
MCU	Millipore Sigma (HPA016480)	unlabelled	rabbit	1:500/---
MIC10	generated by Dr Alexander von der Malsburg	unlabelled	rabbit	1:500/---

MIC60	generated by Dr Alexander von der Malsburg	unlabelled	rabbit	1:500/---
MICU1	Millipore Sigma (HPA037480)	unlabelled	rabbit	1:500/---
MICU2	Abcam (ab101465)	unlabelled	rabbit	1:1.000/---
mouse IgG (H+L)	Cell Signalling (5470)	Dylight 680/ 800	goat	1:10.000/---
mouse IgG (H+L)	Life Technologies (A-11004/A-11001)	Alexa Fluor 568/488	goat	---/1:1.000
mouse IgG (H+L)	Cell Signalling (7076P2)	HRP-linked	goat	2.5:10.000
NDUFB8	Abcam (ab110242)	unlabelled	mouse	1:1.000/---
OPA1	BD Bioscience (612607)	unlabelled	mouse	1:2.000/---
Oxphos system "total oxphos human WB antibody cocktail"	Abcam (ab110411)	unlabelled	mouse	1:500/---
PDH (E2 & E3)	Abcam (ab110333)	unlabelled	mouse	1:1.000/---
rabbit IgG (H+L)	Cell Signalling (5151)	Dylight 680/ 800	goat	1:10.000/---
rabbit IgG (H+L)	Life Technologies (A-11011/A-11008)	Alexa Fluor 568/488	goat	---/1:1.000
rabbit IgG (H+L)	Cell Signalling (7074P2)	HRP-linked	goat	2.5:10.000
SDHA	Abcam (ab14715)	unlabelled	mouse	1:1.000/---
TMBIM5/ GHITM	Proteintech (16296-1-AP)	unlabelled	rabbit	1:350-1:500/1:50
TOM20	Millipore Sigma (HPA011562)	unlabelled	rabbit	1:1.000/1:400
TOM20	Abcam (ab205486)	Alexa Fluor 488	rabbit	---/1:1.500
UQCRC2	Abcam (14745)	unlabelled	mouse	1:1.000/---

#### 4.1.4. Buffers

**Table 4: List of buffers**

Buffer/Solution	Use	Content
Freezing medium	preparation of cell culture cryostocks	90 % FBS, 10 % DMSO
DDM-lysis buffer	protein sample preparation	50 mM HEPES, 150 mM NaCl, 0.2 % DDM, 0.5 mM EGTA, 0.3 mM CaCl <sub>2</sub>
Isolation buffer (cells)	mitochondrial isolation (cells, liver)	200 mM Sucrose, 10 mM Tris-MOPS, 1 mM EGTA-Tris, pH 7.4
Isolation solution	mitochondrial isolation (brain, heart)	225 mM Mannitol, 75 mM sucrose, 2 mM HEPES, 1 mM EGTA, pH 7.4
Basic medium	mitochondrial isolation (skeletal muscle)	140 mM KCl, 20 mM HEPES, 5 mM MgCl <sub>2</sub> , 5 μM EGTA, pH 7.0
Homogenisation medium	mitochondrial isolation (skeletal muscle)	140 mM KCl, 20 mM HEPES, 5 mM MgCl <sub>2</sub> , 1 mM EGTA, 1 mM ATP, 1 % BSA, 0.1 mg/ml Subtilisin A

Heart Mitochondria Isolation Medium	mitochondrial isolation (heart)	200 mM Sucrose, 20 mM Tris, 2mM EGTA, pH 7.35 at 4°C, freshly supplemented with 0.3 % BSA (w/v)
Laemmli- $\beta$ -Mercaptoethanol-buffer	Immunoblotting	1x Laemmli buffer with 710 mM $\beta$ -mercaptoethanol
Stripping buffer	Western Blot stripping	6 M Guanidin-HCl, 20 mM Tris-HCl, 0.2 % NP-40 with 0.1 M $\beta$ -mercaptoethanol added freshly
Transfer buffer	wet blotting	1.25 mM Bicine, 1.25 mM Bis-Tris, 50 $\mu$ M EDTA
GSH assay buffer	GSH assay	100 $\mu$ M Na <sub>2</sub> HPO <sub>4</sub> , 1.3 mM EDTA in water, pH 7.5, freshly supplemented with 0.24 mg/ml DTNB, 0.67 mg/ml NADPH and 0.475 mg/ml glutathione reductase
FACS buffer	flow cytometry	0.5 % BSA in PBS with 2 mM EDTA
Tyrode's buffer	live cell imaging	145mM NaCl, 5 mM KCl, 1.5. mM CaCl <sub>2</sub> , 1 mM MgCl <sub>2</sub> , 10 mM glucose, 10 mM HEPES, pH 7.4
BIOPS	high-resolution respirometry	10 mM Ca-EGTA buffer, 0.1 $\mu$ M free Ca <sup>2+</sup> , 20 mM imidazole, 20 mM taurine, 50 mM K-MES, 0.5 mM DTT, 6.56 mM MgCl <sub>2</sub> , 5.77 mM ATP, 15 mM phosphocreatine, pH 7.1
Mir05	high-resolution respirometry	0.5 mM EGTA, 3 mM MgCl <sub>2</sub> , 60 mM lactobionic acid, 20 mM taurine, 10 mM KH <sub>2</sub> PO <sub>4</sub> , 20 mM HEPES, 110 mM D-sucrose, 1g/l BSA
Mir06	high-resolution respirometry	Mir05 freshly supplemented with 280 U/ml catalase
PTP-buffer	Mitochondrial Ca <sup>2+</sup> uptake assay	120 mM KCl, 70 mM mannitol, 25 mM saccharose, 20 mM HEPES, 5 mM KH <sub>2</sub> PO <sub>4</sub> , pH 7.5
PTP-EGTA-buffer	Mitochondrial Ca <sup>2+</sup> uptake assay	PTP-buffer with 20 $\mu$ M EGTA, pH 7.5
Ca <sup>2+</sup> swelling buffer	Ca <sup>2+</sup> -induced swelling	125 mM KCl, 10 mM HEPES, 2 mM MgCl <sub>2</sub> , 2 mM K <sub>2</sub> HPO <sub>4</sub> , pH 7.2 (KOH), freshly supplemented with 100 mM succinate and 0.2 $\mu$ M thapsigargin
Na <sup>+</sup> swelling buffer	Na <sup>+</sup> -induced swelling	55 mM NaOAc, 5 mM TES, 0.1 mM EGTA, 0.1 mM EDTA
IL-6 assay buffer	Luminex assay to measure IL-6	PBS supplemented with 1 % BSA and 2 mM EDTA

## 4.2. Methods

### 4.2.1. Mouse line and genotyping

All mice used for this work were bred on a C57Bl6/J background. WT mice were purchased from Charles River. To study the physiological function of TMBIM5 *in vivo*, we obtained a transgenic founder mouse (a heterozygous male mouse) carrying a mutation in the gene of interest (*Ghitm*) from the University of Zurich, Switzerland. The original base pair sequence 5'-GAT-3' was converted into 5'-CGC-3' using the Crispr/Cas9 system. This resulted in the substitution of the amino acid aspartic acid (D) by arginine (R) at position 326 in the primary protein structure. The novel mouse line was therefore named D326R. The mutated aspartic

acid (D326R) is one of the residues constituting the pH-sensing di-aspartyl motif in the murine TMBIM5.

The point mutation was confirmed via commercial Sanger sequencing (GATC/Eurofins Genomics) using the following primer: 5' -GGT GTG TTT CTT TGA ACT TTT TTG G- 3'.

In order to maintain a clean background, so-called backcrossing was conducted after the first few generations of the breed. This means that heterozygous animals were bred with C57Bl6/J mice for one generation to reduce the risk of introducing other mutations than the desired one into the strain. For permanent breeding, heterozygous animals were crossed to obtain homozygous WT and homozygous D326R animals in order to use litter mates for the experiments.

Mice were housed with *ad libitum* access to food and water and a 12 h- 12 h light-dark cycle (light phase onset at 7.00 am) and all experiments were performed with permission of the local authorities in accordance with the German Animal Protection Law (*Tierversuchsnummer: AZ 177-07/G 18-1-026* ).

As it was a novel mouse line, it was closely monitored for any abnormality in health and development. Therefore, I selected several litters and performed optical health checks, weighed the mice and documented the process in fixed intervals.

As the gene sequence differs in only three base pairs between WT and D326R mice the genotyping had to be conducted in two steps: amplification of the DNA segment followed by restriction enzyme digestion. The enzyme used for digestion was FspI which cuts at the sequence 5'- TGC//GCA -3'. Due to the mutation, this sequence is present in D326R but not in the WT DNA. This enabled us to discriminate the three possible genotypes:

homozygous WT = 1 band, full-length PCR-product

homozygous D326R = 2 bands, digested PCR-product

heterozygous animals = 3 bands, full-length and digested PCR-product

Ear, tail or toe biopsies from mice were used for genotyping. To make the DNA accessible, the biopsies were lysed overnight in a commercially available lysis reagent (Viagen Biotech) supplemented with 0.3 mg/ml proteinase K at 55°C on a shaker. After lysis and inactivation (85 °C, 1 h) the solution was diluted by the addition of 1.5- 2 volumes of nuclease-free water and was then ready to be used. For the PCR amplification, 1 µl of the DNA-solution was added to a mix of 1x GoTaq reaction buffer, dNTPs (10 mM each), forward and reverse

Primer (10 pmol/ $\mu$ l each), 1.2 % dimethylsulfoxide (DMSO), 0.625 u GoTaq polymerase and water in a total volume of 25  $\mu$ l. The following primer pairs were used: 1) forward: 5'-GGT GTG TTT CTT TGA ACT TTT TTG G-3'/reverse: 5'-CTG CAG GTG CCT TTT ATC TCT C-3' or 2) forward: 5'- TTC CAT TGT CTG ACA CCC AGG -3'/reverse: 5'-AAA CTG ACT GCA GGT GCC TT -3'. The following thermocycler settings were applied for the amplification:

**Table 5: PCR conditions for D326R mouse genotyping**

temperature	time	
95 °C	2 min	
95° C	30 s	34x cycles
54° C	30 s	
72° C	50 s	
72° C	5 min	
4 °C	$\infty$	

The amplified DNA was digested by addition of 5 u FspI (New England Biolabs) and 1x of the supplied 10x CutSmart® buffer and incubation at 37 °C for  $\geq$ 30 min. Before gel electrophoresis, 6x loading dye (final 1x) and 0.1 % SDS were added. DNA fragments were then separated on a 2 % agarose gel stained with Midori Green (120-160 V, 40-80 min). The fluorescent signal of the DNA bands was detected using a Bio-Rad imaging system.

#### 4.2.2. Cell culture

##### 4.2.2.1. HAP1

HAP1 cells are human adherent fibroblast-like cells derived from the male chronic myelogenous leukaemia (CML) cell line KBM-7. HAP1 cells are near-haploid which makes them an ideal target for gene modifications (Essletzbichler et al., 2014). Both WT and TMBIM5 knockout cells were obtained from Horizon Genomics. TMBIM5 was knocked out by the induction of a 32 bp deletion in exon 3 of the gene (genomic location chr10:84142671) using the Crispr/Cas9-system which resulted in a frameshift mutation but did not generate a new stop codon. Hence, except for the deletion, the transcript encodes for the full-length protein. The knockout was validated by Sanger sequencing (sequencing primer: 5'-GGAAGTTGTTTCATGGACCTCTTAAA-3'). See Fig. 3 for the alignment.

Cells were cultured in Iscove's Modified Dulbecco's Medium (IMDM) supplemented with 10% fetal bovine serum (FBS) and 1 % Penicillin/Streptomycin. They were

```

GluTyrAlaThrLysThrArgT-----hrGlnArgGlySerIleGlyThrIleAspG1
GAATATGCCACCAAAAACAAGAA-----CTCAAAGAGGCAGCATTGGAACCATCGATGG
|||||                               |||||
GAATATGCCACCAAAAACAAGAAATGGGATCCGGCGTGGGAGAACTGGCCAAGAACTCAAAGAGGCAGCATTGGAACCATCGATGG
GluTyrAlaThrLysThrArgIleGlyIleArgArgGlyArgThrGlyGlnGluLeuLysGluAlaAlaLeuGluProSerMetG

yLysAsnIle***
AAAAAATATTTAAAA
|||||
AAAAAATATTTAAAA
luLysIlePheLysI

```

**Figure 3: Sequence alignment of the 32 bp deletion in TMBIM5 knockout HAP1 cells.**

kept at 37°C in a humidified atmosphere with 5 % CO<sub>2</sub> and passaged every 3 to 4 days.

For the preparation of cryostocks, cells were washed with phosphate-buffered saline (PBS) and detached from the plate by a trypsin/EDTA (0.05 %/0.02 %) solution. After resuspension in growth medium, cells were centrifuged at 1.300 x g for 3 min. After a second washing step with PBS, the cell pellet was resuspended in freezing medium (90 % FBS, 10 % DMSO) and quickly transferred to a freezing container and cooled to -80 °C overnight. For long-term storage, cryovials were kept in a liquid nitrogen tank.

In our lab, the identity of the cells in culture was verified regularly via PCR followed by gel electrophoresis. Genomic DNA (gDNA) was isolated from the cells using the "Quick-gDNA MiniPrep kit" (Zymo Research) following the manufacturer's protocol. The gDNA was then used as a template for the PCR conducted with the following composition for each sample: 1x GoTaq Buffer, dNTPs (each 2.5 mM), 1.2 % DMSO, forward and reverse primer (10 pmol/μl each, sequences: forward 5'-AGCACAGGGAAGGTCTACATTTATT-3'/reverse 5'-GGAAGTTGTTTCATGGACCTCTTAAA-3'), 1.5 u GoTaq DNA Polymerase, 3 μl gDNA template and nuclease-free water in a total volume of 25 μl. Settings for the PCR thermocycler were the following:

**Table 6: PCR conditions for HAP1 WT and TMBIM5 KO genotyping**

temperature	time	
95°C	2 min	
95°C	30 s	40x cycles
57°C	15 s	
72°C	23 s	
72°C	2 min	
4°C	∞	

For gel electrophoresis, a 2.2 % agarose gel stained with Midori Green was used and a voltage of 110-120V was applied for >1 h. Fluorescent bands were detected using a Bio-Rad imaging system. Due to the deletion of 32 bp in the TMBIM5 KO cells, the PCR resulted in a shorter product (344 bp) than for the WT (376 bp).

In the case of contamination or after 30- 40 passages cells were discarded and replaced by a freshly thawed culture.

#### 4.2.2.2. HEK293 (T)

HEK293 is a very commonly used adherent cell line derived from human embryonic kidney cells and immortalized with sheared adenovirus 5 DNA in 1973 (Lin et al., 2014). Since then, several sub-lines have been derived from the original, e.g. HEK293T which express a viral T antigen (Lin et al., 2014).

Several HEK cell lines were used in this work, which were obtained from different sources. HEK293T  $\Delta$ MIC10 and  $\Delta$ MIC60 cells with the corresponding HEK293T WT control cells were a kind gift of Dr Alexander von der Malsburg, University Saarland, Germany.  $\Delta$ MIC10 have a complete knockout of the protein MIC10, whereas MIC60 expression in  $\Delta$ MIC60 cells is reduced by approximately 95 %.

The HEK293T cells with a knockout for MCU, MICU1 or MICU2 respectively, and the corresponding WT control were a kind gift of Dr J. Kevin Foskett, University of Pennsylvania, USA.

HEK293 TMBIM5 KO cells and their corresponding WT control were a kind gift of Dr Geert Bultynck, Katholieke Universiteit Leuven, Belgium. Both WT and TMBIM5 KO cells were originally obtained from Synthego and the knockout was induced using the Crispr/Cas9 system. The insertion of an additional base (adenine) into the gene causes a frameshift mutation leading to a complete knockout of the protein.

All HEK293(T) cell lines were cultured in Dulbecco`s modified eagle`s medium (DMEM) with Glutamax (Gibco) supplemented with 10 % FBS and 1 % Penicillin/Streptomycin. They were kept at 37°C in a humidified atmosphere with 5 % CO<sub>2</sub> and passaged every 3 to 4 days. Cryostocks were prepared as described in section 4.2.2.1.

The identity of the cells was validated on a regular basis via immunoblotting as described below, section 4.2.3.6. In the case of contamination or after 30-40 passages cells were discarded and replaced by a freshly thawed culture.

#### 4.2.2.3. Isolation and culture of primary mouse embryonic fibroblasts

The fresh isolation of primary mouse embryonic fibroblasts (pMEF) from D326R mice was conducted following a modified protocol of Jozefczuk et al. (Jozefczuk et al., 2012). Pregnant mice from heterozygous breeding were sacrificed on day 13 p.c. by cervical dislocation. The uterine horns were dissected, briefly rinsed in 70 % ethanol, and placed in a petry dish with a small amount of PBS without  $Mg^{2+}$  and  $Ca^{2+}$ . Embryos were separated from the placenta and surrounding membranes and the head, the extremities, as well as all by eye visible organs were removed. The tail was used for subsequent genotyping. Blood was washed out with PBS ( $Mg^{2+}$  and  $Ca^{2+}$ ). The remaining tissue was finely minced using a razor blade followed by digestion in 1 ml Trypsin/EDTA (0.05 %/0.02 %) with 31 U/ml of DNase per embryo for 15 min at 37 °C. The solution was resuspended every 5 min using a pipet to shear the remaining tissue pieces.

After digestion 2 volumes of fresh MEF-medium (DMEM high glucose supplemented with 10 % FBS, 1 % L-glutamine and 1 % Penicillin/Streptomycin) were added to inactivate the trypsin. After a few minutes allowing any remaining tissue pieces to settle, the supernatant was transferred to a fresh tube and centrifuged at 500 x g for 5 min. The resulting pellet was resuspended in pre-warmed MEF-medium and plated one embryo per dish. After 24 h only fibroblasts were attached to the plate and any leftovers from the isolation process were washed off.

pMEFs were kept at 37°C in a humidified atmosphere with 5 % CO<sub>2</sub> and passaged every 3 to 4 days. After washing and trypsinization cells were centrifuged (3 min, 1.300 x g) and resuspended in fresh medium to remove trypsin.

The cells were discarded after a maximum of 8 passages because after passage 5-6 the onset of senescence was observed as alterations in morphology, e.g. the occurrence of enlarged „fried egg“-like cells.

#### 4.2.2.4. Transfection of cells

Cells were plated one day prior to transfection in an adequate cell number to reach confluency 2-3 days after seeding (e.g. 70.000 HAP1 cells/well or 100.000 HEK293 cells/well in a 6-well plate, 10.000 HAP1 cells/well in an 8-chamber  $\mu$ -slide). On the day of transfection 1  $\mu$ g of the desired plasmid DNA was diluted in 250  $\mu$ l serum-free Opti-MEM ( $\mu$ -slide: 0.3  $\mu$ g DNA in 9  $\mu$ l) and the transfection reagent Turbofectin 8.0 (Origene) was added at a DNA: Turbofectin ratio of 1:3. To allow complexation, this mix was incubated for 20-30 min at RT and then added dropwise directly onto the cells and the normal cell culture medium. Culture plates were placed back in the incubator. To reduce the stress for the cells, the Turbofectin-containing medium was removed after 4 h and replaced by fresh culture medium.

#### 4.2.3. Protein biochemistry

##### 4.2.3.1. Protein samples

##### 4.2.3.1.1. From cell lines

Cultured, adherent cells were washed with PBS, trypsinized and resuspended in the respective growth medium. After centrifugation (3 min, 1300 x g), the cell pellet was dissolved in Dodecyl- $\beta$ -D-maltoside-lysis buffer (DDM-lysis buffer; 50 mM HEPES, 150 mM NaCl, 0.2 % DDM, 0.5 mM EGTA, 0.3 mM CaCl<sub>2</sub>). Proteins were solubilized for 30 min on a rotator at 4 °C and then separated from cell debris by centrifugation at maximum speed, 10 min, 4 °C. The protein concentration in the supernatant was quantified with a bicinchoninic acid assay (BCA) kit (Interchim) following the manufacturer's protocol (see section 4.2.3.3).

##### 4.2.3.1.2. From mouse tissue

Mice were killed by cervical dislocation and the desired organ (e.g. heart, skeletal muscle, spleen, etc.) was dissected and either a) snap-frozen in liquid nitrogen for later use or b) directly washed in ice-cold PBS to remove as much blood as possible. Tissue was separated from connective tissue, cords, etc. and a small piece was transferred to a precooled glass-Teflon potter containing DDM-lysis buffer. The tissue was then homogenized with a mechanical homogeniser at 4.000 x rpm for 30 s. This was repeated as often as necessary

to achieve a homogeneous suspension with 30 s breaks on ice in between to prevent heating of the solution. The homogenate was then centrifuged at 21.000 x g, 10 min, 4 °C and the protein concentration in the supernatant was quantified with the BCA kit.

#### 4.2.3.1.3. From splenocytes

Mice were killed by cervical dislocation, the spleen was dissected and immersed in splenocyte medium (DMEM high glucose supplemented with 1 % Penicillin/Streptomycin) on ice. The tissue was mechanically shredded using a cell strainer (Greiner bio-one, pore size: 100 µM) and suspended in 25 ml medium followed by a centrifugation step (550 x g, 4 °C, 5 min). The resulting red pellet contained both, splenocytes and erythrocytes. The pellet was resuspended in 1x lysis buffer (BD Biosciences) and incubated at RT for 15 min. The process was stopped by the addition of splenocyte medium, the suspension was cleared through the same cell strainer as before and the now lysed erythrocytes were removed by centrifugation (550 x g, 4 °C, 5 min). The remaining white pellet consisting of splenocytes was resuspended in DDM-lysis buffer. Proteins were solubilised, separated from cell debris and quantified as described in section 4.2.3.3.

#### 4.2.3.2. Mitochondrial Isolation

##### 4.2.3.2.1. From cell lines

Mitochondria were isolated from cultured cell lines following the protocol of Frezza et al. (Frezza et al., 2007) with a few modifications. Cells were expanded to several large culture plates a few days prior to the isolation to achieve a sufficient mitochondrial yield. Cells were then washed with PBS and detached in a small volume of PBS using a cell scraper. After low-speed centrifugation (600 x g, 10 min, 4 °C), the cell pellet was resuspended in ice-cold isolation buffer for cells (IBc; 200 mM Sucrose, 10 mM Tris-MOPS, 1 mM EGTA-Tris, pH 7.4) and homogenised in a precooled glass-Teflon potter at 1.500 rpm, 3x 30 s with 30 s breaks on ice in between to prevent heating. All following steps were conducted on ice or at 4°C. Homogenate was centrifuged to pelletise cell debris at 600 x g, 10 min, 4°C. The supernatant was transferred to a fresh tube and centrifuged at 7.000 x g, 10 min, 4°C. The pellet containing the mitochondria was washed with ice-cold IBc followed by another centrifugation step (7.000 x g, 10 min, 4°C). The supernatant was discarded, and the

mitochondria were carefully resuspended in the appropriate buffer for the subsequent use, i.e. DDM-lysis buffer for immunoblotting or a small volume of IBc for BN PAGE. The protein concentration of the mitochondrial suspension was determined with a BCA assay.

#### 4.2.3.2.2. From mouse tissue

##### 4.2.3.2.2.1. For immunoblotting

For the preparation of mitochondrial samples from mouse hearts for BN PAGE, mitochondria were isolated in a similar way as described above, following a modified protocol based on Frezza et al. (Frezza et al., 2007).

In brief, the mouse was sacrificed by cervical dislocation and the heart was dissected and immersed in a small beaker containing ice-cold IBc. Any connective tissue or cords were removed, and blood was washed away by 4-5 rinses with IBc. The tissue was then cut into small pieces and if necessary, the buffer was replaced by fresh buffer again. The minced tissue was transferred to a precooled glass-Teflon potter containing ice-cold IBc and homogenised at 1.500 rpm, 2x 30 s with 30 s breaks on ice. After a low-speed centrifugation step (600 x g, 10 min, 4°C), the supernatant was transferred to a fresh tube, centrifuged at high speed (7.000 x g, 10 min, 4°C), washed with IBc and centrifuged again (7.000 x g, 10 min, 4°C). The resulting mitochondrial pellet was then processed as described above.

##### 4.2.3.2.2.2. For Calcium uptake assay

To obtain functional mitochondria from mouse tissue for Ca<sup>2+</sup> uptake measurements three different protocols were applied according to the tissue type (heart, brain, skeletal muscle). In any case, the mouse was sacrificed by cervical dislocation, the desired organ was dissected and immersed in isolation solution (IS; 225 mM Mannitol, 75 mM sucrose, 2 mM HEPES, 1 mM EGTA, pH 7.4) (brain, heart) or basic medium (BM; 140 mM KCl, 20 mM HEPES, 5 mM MgCl<sub>2</sub>, 5 μM EGTA, pH 7.0) (skeletal muscle). Any connective tissue or cords were removed from the skeletal muscle. The two atria were removed from the heart. The cortex was separated from the cerebellum and the mid-brain and split into the two hemispheres. The cropped tissue was then transferred to precooled tubes containing 500 μl (heart) or 1.000 μl (brain) BSA-proteinase-solution (1:10 Proteinase (1.6 mg/ml) : BSA (4 mg/ml)) or 500 μl homogenisation medium (skeletal muscle) (HM; 140 mM KCl, 20 mM

HEPES, 5 mM MgCl<sub>2</sub>, 1 mM EGTA, 1 mM ATP, 1 % BSA, 0.1 mg/ml Subtilisin A). The tissue was minced with scissors and manually homogenised on ice in precooled glass-Teflon potters for 7 min (heart, skeletal muscle) or with 10x strokes (brain). 500 µl of BSA-proteinase-solution or 1 ml of HM were added to the heart and muscle homogenate respectively, followed by another homogenisation for 7 min. The brain was homogenised further with additional 10 x strokes using a larger glass potter stick. The finished homogenate was then transferred to tubes and centrifuged (heart: 500 x g, 5 min; muscle: 800 x g, 10 min; brain: 2.000 x g, 3 min; all centrifugation steps at 4 °C). After the first centrifugation, the supernatant was transferred to a new tube and centrifuged again (heart: 7.700 x g, 10 min; muscle: 12.000 x g, 10 min). After the high-speed centrifugation, the pellets of heart and muscle contained the mitochondria and were washed with 1.4 ml mitochondria suspension solution (MSS; 225 mM Mannitol, 75 mM sucrose, 2 mM HEPES, 20 µM EGTA, pH 7.4) (heart, 2x) or with BM (muscle, 1x). The final mitochondrial pellet was then resuspended in 100 µl MSS (heart) or 200 µl BM (muscle).

For the brain, the pellet of the first low-speed centrifugation was resuspended in 1 ml BSA-proteinase-solution and centrifuged again at 2.000 x g, 3 min. The supernatant was transferred to the same tube as before and centrifuged at 12.000 x g for 8 min. The resulting pellet, containing mitochondria, was resuspended in 100 µl MSS.

The protein concentration of the mitochondrial suspensions was determined by a Lowry protein assay as described below (section 4.2.3.4.).

#### 4.2.3.2.2.3. For mitochondrial swelling assay

To assess mitochondrial swelling and pre-swelling in liver mitochondria, they were isolated as described above.

Cardiac mitochondria were isolated using a similar, yet optimised protocol. Mice were sacrificed by cervical dislocation and the heart was rapidly explanted and rinsed in ice-cold Heart Mitochondria Isolation Medium (HMIM, 200 mM Sucrose, 20 mM Tris, 2mM EGTA, pH 7.35 at 4°C, freshly supplemented with 0.3 % BSA (w/v)). As usual for mitochondrial isolation, all steps were performed with pre-cooled equipment and on ice or at 4°C. Connective tissue and as much blood as possible were removed in several washing steps in HMIM. To do so, the heart was torn open using forceps until it was flat and the fibres only

loosely connected. The tissue was then transferred to a 2ml-tube containing 500  $\mu$ l HMIM and minced with scissors. After slow centrifugation (300 x g, 3 min) the supernatant was removed and replaced by 1 ml of fresh HMIM. The solution was transferred to a glass-Teflon potter and homogenised at 1300 rpm, 4x 30 s with 30 s breaks on ice in between. Before the last homogenisation step, 800  $\mu$ l of HMIM was added. The homogenate was transferred back to the 2 ml-tube and any debris was removed by 10 min centrifugation at 600 x g. The supernatant was transferred to a fresh 2 ml-tube and mitochondria were pelleted (9.000 x g, 10 min). The supernatant was discarded and the mitochondria were washed with fresh HMIM and centrifuged again (9.000 x g, 10 min). The resulting mitochondrial fraction was resuspended in a small amount of HMIM (90-120  $\mu$ l) to maintain a high concentration. The protein concentration was determined by a BCA assay.

#### 4.2.3.3. BCA Assay

In our lab, protein concentration was determined via the colourimetric bicinchoninic acid assay with a kit from Interchim, following the manufacturer's protocol. In brief, samples were diluted in an appropriate volume of ultrapure H<sub>2</sub>O (usually 1:40- 1:60 for cellular samples, 1:100-1:500 for tissue samples or highly concentrated isolated mitochondria). The diluted samples and standard solutions (0-200  $\mu$ g/ $\mu$ l) were injected in triplicates (15  $\mu$ l each) into a clear 96-well plate. Reagents A and B from the kit were mixed (50:1) and 200  $\mu$ l were added into each well. After 30 min incubation at 37°C, absorbance at 562 nm was detected using a plate reader (Tecan NanoQuant infinite M200 pro). The concentration was calculated from the standard curve with the dilution factor taken into account.

#### 4.2.3.4. Lowry Protein Assay

In the lab of Dr Christoph Maack (Universitätsklinikum Würzburg, Germany) where the calcium uptake experiments with mouse mitochondria were conducted, protein concentration was assessed using a kit from Bio-Rad which is based on the colourimetric Lowry assay. In brief, samples were diluted at 1:20 in ultrapure water in triplicates. 100  $\mu$ l of reagent A and 800  $\mu$ l of reagent B were added to each dilution and mixed well. The same was done with standard solutions from 0.2  $\mu$ g/ml – 1.5 mg/ml. After 30 min incubation at RT, 200  $\mu$ l from each solution was pipetted into a clear 96-well plate and absorbance was

measured at 750 nm. The concentration was calculated from the standard curve with the dilution factor considered.

#### 4.2.3.5. Self-made gels

For most western blots, commercially available gels were used for the gel electrophoresis. However, to neatly separate the different splice variants of OPA1, I prepared self-made gels (8 %). First, the resolving gel was prepared (30 % acrylamide, 1.5 M Tris (pH 8.8), 10 % SDS, 10 % APS, 0.1 % (v/v) TEMED) and directly poured into the pre-arranged gel holder after addition of APS and TEMED as they immediately start the polymerization process. The remaining space was filled with isopropanol. When polymerization was complete (after 15-45 min) the isopropanol was removed and replaced by the freshly prepared stacking gel (30 % acrylamide, 1 M Tris (pH 6.8), 10 % SDS, 10 % APS, 0.1 % (v/v) TEMED). As before, APS and TEMED were added last, and the mix was immediately poured thereafter. Finally, a comb with the required number of pockets was put in place. After 30-45 min the polymerization was complete and the gel was ready to use or could be stored at 4 °C for later use.

#### 4.2.3.6. Western Blotting

For quantitative analysis of protein expression, protein samples were denatured using denaturing reagents and heat, followed by gel electrophoresis to separate the proteins by size and then blotted onto a nitrocellulose membrane. The membrane was then incubated with primary antibodies specific to the desired proteins. Protein bands were visualised with fluorescence-labelled secondary antibodies.

In more detail, after determination of the protein concentration, the desired amount of protein (20-35 µg) was diluted in water and 1x Laemmli-β-mercaptoethanol-buffer was added. Depending on the protein of interest of the subsequent staining, samples were either heated to 95 °C (most common proteins) or left at room temperature (e.g. MICU1) for 5 min. Samples were then loaded onto the appropriate gel (most commonly used: Mini-PROTEAN TGX Stain-Free Precast Gels, 4-15 %, Bio-Rad) and a voltage of 120 V was applied for an hour. After gel electrophoretic separation of the proteins, they were transferred to a nitrocellulose membrane by using a semi-dry blotting system (Bio-rad). To improve

sensitivity and signal-to-noise-ratio the membranes were allowed to dry for at least 5 min (RT or at 55 °C). Due to their hydrophobicity membrane proteins like TMBIM5 are sometimes tricky to detect on western blots. To improve the binding of the anti-TMBIM5 primary antibody, especially for mouse tissue samples, I modified the standard protocol at this point, following the recommendation of Kaur and Bachhawat (Kaur and Bachhawat, 2009). Membranes that were subject to later TMBIM5 staining were immersed in SDS- $\beta$ -mercaptoethanol solution (100 mM  $\beta$ -mercaptoethanol, 2 % SDS, 62.5 mM Tris-HCL, pH 6.7) and incubated at 55 °C for 15 min on a shaker, followed by washing with tris-buffered saline with 0.05 % Tween20 (TBST) (2x 5 min, RT). Thereafter (and for all other membranes directly after blotting and drying) the blocking step followed, typically by incubating the membrane in 3 % non-fat dry milk powder in TBST for 1 h at RT. Afterwards, the membrane was incubated with the respective primary antibodies overnight at 4°C on a rotator (antibody dilutions as specified in the list of antibodies). The next day, membranes were washed 3x 5 min with TBST and incubated with fluorescence-labelled secondary antibody for 1 h at RT on a shaker. Unbound or unspecifically bound antibody was removed by another 3 washing steps with TBST. Fluorescence intensity was then detected using a Li-Cor Odyssey imaging system and analysed with the Image Studio Lite software. For the analysis, usually two steps of normalisation were applied: First, the protein of interest was normalised to the appropriate loading control (usually a housekeeping protein like actin,  $\alpha/\beta$ -Tubulin or cytochrome c oxidase subunit IV (coxIV) for mitochondria). Secondly, all values were normalised to the overall mean intensity of protein bands on the same blot. This ensured an optimum of comparability between samples and blots.

#### 4.2.3.7. Stripping of stained Western Blots

In some cases, it was necessary to remove primary and secondary antibodies from a western blot to be able to re-probe it with different antibodies. To do so, the blots were incubated in stripping buffer (6 M Guanidin-HCl, 20 mM Tris-HCl, 0.2 % NP-40 with 0.1 M  $\beta$ -mercaptoethanol added freshly) for 2x 10 min at RT on a shaker. After the first 10 min, the stripping buffer was removed and replaced by fresh one. After this procedure, all antibodies were detached and were washed off by 3x 10 min washing with TBST (on a

shaker, RT). Afterwards, I proceeded with the usual blocking step and primary and secondary antibody incubations as described above.

#### 4.2.3.8. Blue native polyacrylamide gel electrophoresis

Protein complexes in their native conformation were visualised using blue native polyacrylamide gel electrophoresis (BN PAGE). Similar to the western blotting protocol, proteins are separated by size via gel electrophoresis and blotted onto a membrane, followed by incubation with primary and secondary antibodies. Yet, the big difference is that everything happens under non-denaturing conditions to conserve the quaternary structure of the protein complexes.

Protein complexes are very sensitive to degeneration e.g. by heat. Therefore, it was critical for the electrophoresis and blotting that all steps were performed at 4°C or on ice and with precooled equipment. For the sample preparation, 5 µg of isolated mitochondria were added to 1x loading dye (Invitrogen), 5 % digitonin and water in a total volume of 10 µl. After mixing, samples were incubated on ice for 15 min to allow solubilisation followed by centrifugation at 20.000x g for 30 min at 4°C. The supernatant was transferred to a new tube and 0.25 % of G-250 was added. The protein complexes were then separated on a 4-16 % Bis-Tris gel (NativePAGE™, Thermo Fisher) by stepwise increasing voltages (40-180 V). The electrophoresis was stopped when the dye front had migrated to the end of the gel which was usually the case after ~3 h. The electrophoretic chamber was kept on ice for the whole duration. Three different running buffers (Invitrogen) were used: 1x native PAGE running buffer as anode buffer, 1x running buffer with 1x native PAGE cathode additive for the first 1.5 h and 1x running buffer with 0.1x native PAGE cathode additive for the remaining time. After gel separation, the proteins were transferred to a PVDF membrane using either the semi-dry system as described (4.2.3.6.) with ready-to-use PVDF-membranes (Bio-Rad) or via wet blotting. For the wet blotting, Roti®-PVDF membranes (Roth) were used which had to be activated in 100 % methanol for 30 s while fibre pads and filter paper were soaked in 1x transfer buffer (1.25 mM Bicine, 1.25 mM Bis-Tris, 50 µM EDTA). The gel was then placed on top of the membrane and stacked into the transfer cassette with filter paper and fibre pads on both sides. Together with a cooling block, the cassettes were placed in the transfer box in 1x transfer buffer, and a voltage of 100 V was

applied for 1h. After the transfer was complete, proteins were fixed on the membrane with 8 % acetic acid for 15 min at RT on a shaker followed by destaining (in 50 % methanol and 25 % acetic acid) as long as necessary to eliminate the blue coomassie-staining. To remove acids the blots were washed 2x 5 min with TBST before 1 h blocking with 3 % milk. The membranes were stained overnight with the primary antibodies diluted in 3 % milk at 4 °C on a rotator. The following day, membranes were washed 3x 5 min with TBST, incubated with HRP-coupled secondary antibodies and washed again. HRP signal was detected using either the Clarity™ Western ECL Kit (Bio-Rad) or the SuperSignal™ West Femto Maximum sensitivity Kit (Thermo Fisher Scientific). In both cases, membranes were incubated with a 1:1 mix of peroxide reagent and luminol/enhancer reagent for 1 min and detected using a Bio-Rad detection system.

#### 4.2.4. Glutathione assay

##### 4.2.4.1. Sample preparation from HEK 293 cells

Cells were plated in 6-well plates and harvested 24 h later. First, they were washed with ice-cold PBS and, scraped in 2 volumes of PBS with 2 mM EDTA and then added to 1 volume of 10 % 5-sulfosalicylic acid (SSA) which precipitates proteins. All following steps were now performed on ice or at 4 °C. For complete precipitation samples were incubated for 10 min on a shaker followed by a centrifugation step (10 min, 14.000 rpm). The supernatant was transferred to a tube containing 24 µl tri-ethanolamine/H<sub>2</sub>O (1:1), thoroughly vortexed and stored at -20 °C overnight. The cell pellet was dissolved in 0.2 N NaOH at 37 °C overnight. The protein concentration in this cellular fraction was determined by a BCA assay and used for the normalisation of the GSH measurement.

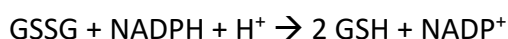
##### 4.2.4.2. Sample preparation from mouse tissue

Mice were sacrificed by cervical dislocation and the spleen was rapidly explanted and washed in ice-cold PBS. The tissue was then transferred to a pre-cooled glass-Teflon potter and homogenised in 1.5 ml PBS supplemented with 2 mM EDTA at 9.000 rpm, 2x 30 s with a 30 s break on ice to prevent heating. Cell/tissue debris was pelleted by a low-speed centrifugation step (700 x rpm, 5 min at 4°C) and the supernatant was added to 100 µl 10 % SSA and kept on ice for 10 min on a shaker to allow precipitation of proteins as described

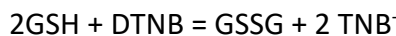
above. Proteins were then separated from the soluble compounds by centrifugation and the pellet, as well as the supernatant, were processed as described above. However, tissue samples proved to have a much higher GSH content than cell line samples which is why the supernatant containing GSH was prediluted 1:3 in water before being stored overnight at -20°C.

#### 4.2.4.3. Measurement of glutathione concentration

The concentrations of the antioxidant glutathione (GSH) and its oxidised form GSSG in a cell give information about its redox state and the burden of oxidative stress. The assay used in this work to determine the GSH/GSSG abundance makes use of two different chemical reactions. The first is the reduction of GSSG to GSH catalysed by the glutathione reductase:



GSH, in turn, is oxidized in the second reaction to GSSG with 2-Nitro-thiobenzoat ( $\text{TNB}^-$ ) as a byproduct:



The absorbance of  $\text{TNB}^-$  at 412 nm can easily be measured. To be able to draw quantitative conclusions, a GSH standard with increasing concentrations from 0 to 20  $\mu\text{M}$  GSH was prepared. Both, the standard solutions, and the samples were diluted (cell samples 1:5, tissue samples 1:10) with water in a 96-well plate. Only just before the measurement 0.24 mg/ml 5,5-Dithiobis(2-nitrobenzoic acid) (DTNB) and 0.67 mg/ml NADPH and 0.475 mg/ml glutathione reductase were added to the assay buffer (100  $\mu\text{M}$   $\text{Na}_2\text{HPO}_4$ , 1.3 mM EDTA in water, pH 7.5). 100  $\mu\text{l}$  of the mix were injected into each well and the measurement was started immediately. Absorbance at 412 nm was measured every minute over 30 min using a plate reader (Tecan Spark®).

The GSH concentration in the samples was calculated from the standard curve and normalised to the protein amount in the cellular fraction. Strictly speaking, in this assay GSH and GSSG cannot be differentiated. Only the total concentration of both can be determined. Yet, the amount of GSSG usually accounts for less than 1 % of the total GSH/GSSH pool (Giustarini et al., 2016) which is why I neglect the differentiation and call the readout GSH concentration for the sake of simplicity.

#### 4.2.5. Cloning of pPB-CAG-HA-mitoCepia-IRES-mitoBFP2

To quantify mitochondrial  $\text{Ca}^{2+}$  in living cells with an intrinsic control, I generated a plasmid coding for the  $\text{Ca}^{2+}$  sensitive fluorescent protein Cepia (Suzuki et al., 2014) and the constitutively blue fluorescent protein BFP2 as depicted below (Fig. 3). Both sequences were preceded by a mitochondrial targeting signal and were separated by an internal ribosome entry site (IRES) motif. The whole construct is contained in one open reading frame (ORF) meaning that it was transcribed as a single mRNA. The IRES motif allows binding of ribosomes not only at the 5' cap but also in the middle of the RNA strand which enables the translation of two proteins from one mRNA. This was important to us as it ensures the equal expression of both proteins and therefore allows normalisation of Cepia fluorescence to BFP fluorescence.

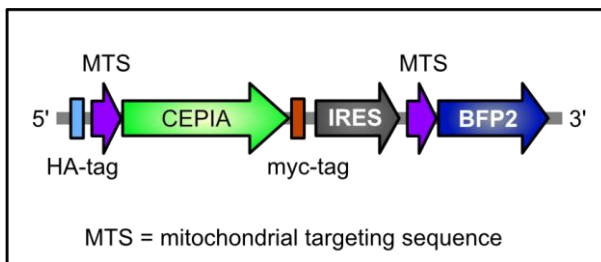


**Figure 4: Graphical depiction of the open reading frame (ORF) in the plasmid pPB-CAG-HA-mitoCepia-IRES-mitoBFP2.**

To achieve the desired construct several cloning steps were necessary. For the final plasmid generation, we used the Invitrogen Gateway® cloning. This technology is based on a bacteriophage recombination system that allows the integration of DNA at specific sites. It uses so-called entry- and destination-vectors that contain certain *att*-sites which facilitate insertion of the desired sequence into the desired backbone in a single cloning step.

First, Cepia and the mitochondrial targeting sequence were cloned into an entry vector (pEntr1A). The targeting signal was amplified via PCR from an existing plasmid (pEntr3C-mitoKeima). Cepia was removed from another stock plasmid (pCMV-Cepia3) via restriction enzyme digestion using Sall and XbaI. Both fragments were inserted into pEntr1A, correct clones were selected by kanamycin resistance and the sequence was verified via commercial Sanger Sequencing (GATC/Eurofins Genomics).

Second, the IRES and the BFP2 sequence were both amplified by PCR using existing plasmids as a template (pPB-CAG-HA-IRES-mcherry-NLS-dest, pPB-CAG-mitoBFP2). The BFP sequence already contained the mitochondrial signal. Both fragments were inserted into the vector pPB-CAG-HA-dest3. Correct clones were selected by ampicillin resistance and verified via commercial Sanger Sequencing (GATC/Eurofins Genomics).

Using an LR-clonase™ enzyme mix, the construct from the entry vector was then transferred to the destination vector resulting in the desired plasmid, pPB-CAG-HA-mitoCepia-IRES-mitoBFP2, which was selected by the ampicillin resistance and verified by Sanger sequencing.

#### 4.2.6. Flow cytometry

To investigate basal mitochondrial calcium content, HAP1 cells were transfected with the plasmid described above coding for the Ca<sup>2+</sup>-sensitive Cepia and the invariable fluorescent BFP2, both targeted to the mitochondria.

The fluorescent signal was detected via a flow cytometer (BD FACS Canto II). The cells were transfected 2 days prior to the measurement. On the day of the experiment, cells were washed, trypsinized and pelleted (1300 rpm, 3 min, RT). The cell pellet was resuspended in PBS containing a red fluorescent viability dye (1:1.000, Invitrogen) and stained for 15 min on ice. After centrifugation (1300 rpm, 3 min, RT), cells were taken up in 350 µl FACS-buffer (0.5 % BSA in PBS with 2 mM EDTA) and transferred to a flow cytometry tube. Compensation of the cytometer was conducted using rat compensation beads (BD biosciences, 6:100 in PBS) stained with anti-CD4-antibodies (all mouse-anti-rat, 1:400, incubation 5 min, 4°C) tagged with the required fluorophores (APC-eFluor780 for the viability dye, Ex/Em: 633/780 nm; FITC for Cepia, Ex/Em: 488/510 nm; brilliant violet for BFP2, Ex/Em: 399/454 nm).

Data were analysed using the software FlowJo. For the analysis, cells that were positive for the viability dye were excluded as dead cells. The living cells formed two populations that differed in size and granularity (see Fig. 4). Thus, they were analysed separately. Both populations were gated on the BFP signal to avoid a bias for Cepia intensity. Cepia intensity of BFP-positive cells was quantified and normalised to the blue fluorescent signal.

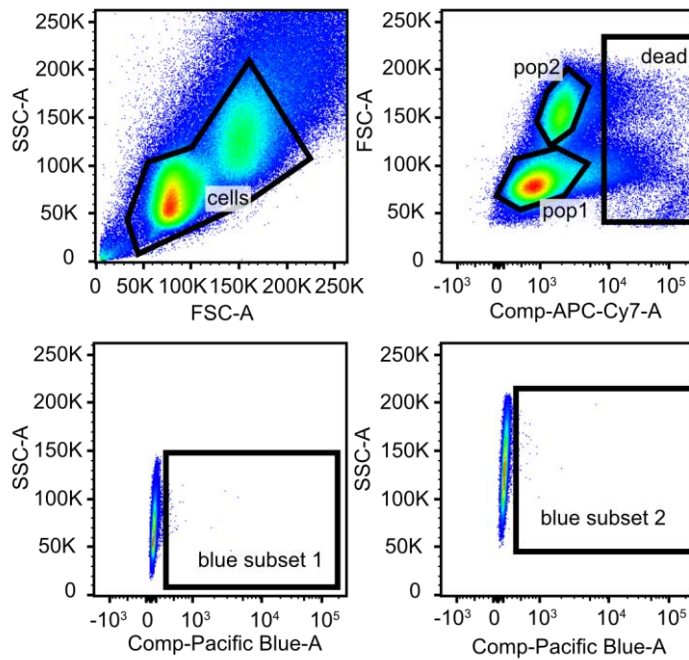


**Figure 5: Exemplary gating for the flow cytometry analysis of transfected cells.**

In three gating steps, the cells expressing the plasmid pPB-CAG-HA-mitoCepia-IRES-mitoBFP2 were selected. In the first step, two cellular populations were identified. In the second step, dead cells were excluded. In the third step, blue fluorescent cells from the two populations were selected for the quantification. SSC-A = sideward scatter area, FSC-A = forwards scatter area.

#### 4.2.7. Confocal microscopy

##### 4.2.7.1. Live cell imaging

The live cell imaging was conducted at the microscopy core facility of the Institute for molecular biology (IMB), Johannes Gutenberg-University (JGU) Mainz, Germany and with the support of Dr Sandra Ritz.

##### 4.2.7.1.1. Transiently transfected HAP1 cells

To investigate intracellular calcium handling upon Ionomycin induction, I imaged HAP1 cells using a spinning disk confocal microscope (Visitron). The cells were seeded in 8-chamber  $\mu$ -slides (Ibidi) and transfected with the same plasmid (mtCepia-IRES-mtBFP) and the same procedure as described above (4.2.2.4.). On the day of measurement, the cell culture medium was removed and replaced by HBSS<sup>+/+</sup>. The cells were imaged at 37°C and 5 % CO<sub>2</sub>. Sequential scanning was used to avoid overlapping of the laser frequencies. Fluorescent signal was detected using the above-stated excitation and emission wavelengths for Cepia

and BFP. Images were taken every 3 s over 6 min. After a 2 min baseline 1  $\mu$ M Ionomycin was added directly into the well.

The time-lapse images were analysed using Fiji/ImageJ. Clusters of cells were marked as regions of interest (ROI) based on two reasons: a) HAP1 cells grow very densely making it hard to separate or distinguish single cells and b) the manual Ionomycin injection sometimes subtly moved the focus frame which could have moved cells out of the selected ROI. The signal intensity of these clusters was quantified over time and Cepia intensity was normalised to the BFP signal and the baseline values.

#### 4.2.7.1.2. Stained primary mouse embryonic fibroblasts

For the analysis of mitochondrial morphology in primary MEFs from WT and D326R mice, live cell imaging was conducted using a confocal spinning disk high-content screening system (Opera Phenix™, Perkin Elmer). Tetramethylrhodamine methyl ester (TMRM) was used to visualise mitochondria and to assess mitochondrial membrane potential and shape. TMRM is a cell-permeant, cationic dye which accumulates in the mitochondrial matrix depending on the membrane potential. Nuclei were stained with Hoechst and the cellular area was marked by the dye CellMask™ deep red plasma membrane stain (Thermo Fisher). Only cells between passage number 2 and 5 were used for the analysis.

Two days prior to the imaging, the cells were plated in a black 96-well plate with a transparent bottom (3.000 cells/well). On the day of measurement, the medium was removed and replaced by serum-free medium without phenol-red supplemented with 2.5  $\mu$ g/ml CellMask™. After 15 min incubation at 37°C, the CellMask™ staining solution was replaced by Tyrode's buffer containing 25 nM TMRM and 1  $\mu$ g/ml Hoechst. Both dyes were present during image acquisition. Cells were imaged using the Opera Phenix™ system at 37°C and 5 % CO<sub>2</sub> with a 40x magnification for mitochondrial shape, 20x for membrane potential quantification. Z-stacks with 6 planes (each 0.6- 1 $\mu$ m) and 25 images per well were acquired. As a proof-of-concept, 2  $\mu$ M Carbonyl cyanide-p-trifluoromethoxyphenylhydrazone (FCCP) was added after the acquisition and the same cells were imaged again. FCCP is an ionophore that depolarizes the mitochondrial membrane which results in a strong decrease of TMRM fluorescent signal as it is rapidly released into the cytosol.

The analysis was conducted through the Columbus software by Perkin Elmer. The nuclear staining by Hoechst was used to define the number of cells. The TMRM staining was utilised to quantify mitochondrial shape as well as the mitochondrial membrane potential. To compare membrane potential between WT and TMBIM5 KO cells the TMRM signal was normalized to the cell area determined by the far red CellMask™ signal. The mitochondrial shape was quantified through a machine learning algorithm. Based on a "learning session" during which I selected mitochondrial clusters in the microscopic images and defined them as either tubular, fragmented or mixed, the software conducted a batch analysis and assigned these definitions to all images.

#### 4.2.7.2. Fixed cells

Fixed cells were imaged at the Imaging Core Facility of the *Forschungszentrum für Immuntherapie* (FZI), Mainz, Germany, with the help of Dr Gregory Harms.

##### 4.2.7.2.1. Immunocytochemistry

Cells were plated on sterile glass coverslips and allowed to attach overnight. On the next day, cells were carefully washed with PBS and then fixed with 4 % paraformaldehyde (PFA) for 20-30 min on a shaker. All following treatments and washing steps were conducted at RT on a shaker if not stated otherwise. Every treatment step was followed by 3x 5 min washing with PBS. This will be omitted in the following description to avoid iteration. After fixation, the cells were permeabilised using 0.25 % Triton-X-100 in PBS for 10 min followed by a blocking step with Roti®-block (Roth) for >1 h. The coverslips were then incubated in the dark, in a wet chamber at 4°C overnight with the desired primary antibodies diluted in Roti®-block with 0.1 % Triton-X-100 (no shaking). On the next day, the same Triton-blocking-solution was used to dilute the secondary antibodies. The coverslips were stained with Alexa Fluor-488 or -568 labelled secondary antibodies and incubated in the dark for 1 h (no shaking). Nuclei were stained with 4',6-diamidino-2-phenylindole (DAPI) for 3-5 min. Lastly, the coverslips were mounted on microscopic slides using an appropriate mounting medium and dried and stored at 4°C in the dark.

#### 4.2.7.2.2. Proximity ligation assay

To investigate a possible interaction between TMBIM5 and LETM1, a proximity ligation assay (PLA) was conducted using the Duolink<sup>®</sup> in Situ red kit (mouse/rabbit) (Sigma) similar as described by M. Alam (Alam, 2018). The underlying concept is depicted in Fig. 5. For this assay, two possibly interacting proteins are labelled in fixed cells with primary antibodies from different species, in this case, mouse and rabbit. A pair of secondary antibodies tagged with two different oligonucleotide probes (PLUS and MINUS) binds to the F<sub>c</sub> termini of the primary antibodies. If the two proteins are in sufficient proximity (<40 nm), in the next step a ligase connects the two oligonucleotide strands and forms a piece of circular DNA. This serves as a template for a DNA polymerase which amplifies the sequence through rolling circle amplification. Fluorescence-labelled oligonucleotides in the amplification buffer attach to the amplicon and can be detected as red dots via microscopy.

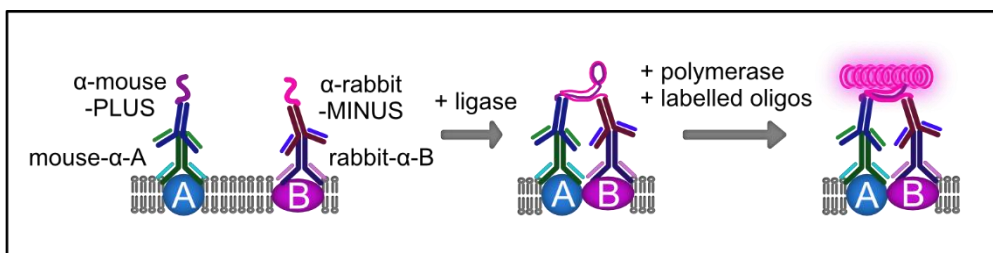


**Figure 6: Detection of a protein-protein interaction via proximity ligation.**

Cells were plated, fixed, permeabilised, blocked and stained with primary antibodies as described above but before fixation, the cells were treated with either 4 μM Antimycin A and 2 μM Oligomycin to abolish the mitochondrial membrane potential or the same volume of 100 % ethanol as vehicle control, both for 10 min at 37°C. Primary antibodies against TMBIM5 and LETM1 were used for the proteins of interest. The number of spots in TMBIM5 KO HEK293 cells was used as a negative control for TMBIM5 and the combination of primary antibodies against LETM1 and the mitochondrial import receptor subunit TOM20 were used as a negative control for LETM1 in HEK293 WT cells as these two proteins are not expected to interact. After primary antibody incubation overnight, the cells were washed with Duolink<sup>®</sup> wash buffer A. All following washing steps were conducted with the wash buffer A if not stated otherwise and will not be described as stated above. The coverslips were then incubated with the PLUS and MINUS probes (1:1:5 diluted in BSA) in a wet chamber, at 37 °C for 1 h. All incubation steps were performed at 37°C in the dark in

a wet chamber. The ligase was diluted in 1x ligase buffer (1:40) and incubated on the coverslips for 30 min. The DNA Polymerase was diluted in 1x amplification buffer (1:80) and the amplification took place during 1.5 h incubation. After the amplification, the coverslips are washed with Duolink<sup>®</sup> wash buffer B for 3x 10 min. For proof-of-concept images to show that the red dots were indeed localised in or at the mitochondria some of the coverslips were now additionally stained with a fluorescence-labelled (AF-488) primary antibody against TOM20 (diluted 1:1.500 in BSA) overnight. Just before mounting the coverslips on microscopic slides, they were briefly washed with 0.01 x wash buffer B. For the mounting, the Duolink<sup>®</sup> in Situ Mounting medium was used which contains DAPI to stain the nuclei.

Images were taken using a Leica TCS SP8 inverse confocal fluorescence microscope. For the proof-of-concept images, a 63x objective was used, for the quantification 40x. Z-stacks were acquired with 6-8 planes (~1 µm thickness/plane). The analysis was conducted using the Imaris software which is able to analyse and quantify 3D structures. The blue fluorescence from DAPI was used to shape so-called "surfaces" which then yielded the number of nuclei. The number of red punctae was quantified as single dots with fixed thresholds for size, intensity, and quality. From these two readouts, the number of puncta per nucleus was calculated.

#### 4.2.8. Transmission electron microscopy

Tissue preparation and image acquisition were conducted by Ilse von Graevenitz (Institute for anatomy and neurobiology, JGU Mainz, Germany). A similar protocol as described by Koch et al. (Koch et al., 2011) was applied. In brief, mice were killed by cervical dislocation and the desired tissues were rapidly explanted and immersed in a fixative solution (2 % paraformaldehyde, 1 % glutaraldehyde in PBS). After fixation, tissues were washed in PBS with 3 % saccharose followed by incubation in 0.1- 2 % OsO<sub>4</sub> (in PBS) for 90 min. Tissues were washed again in PBS and then dehydrated in an ascending ethanol series and incubated overnight in 70 % ethanol with 3 % uranyl acetate. The next day, the samples were washed 3x with 100 % ethanol and embedded in epon/glycid ether 100. Slices were cut using a Reichert Ultracut S ultramicrotome (Leica Microsystems, Wetzlar, Germany) and

contrasted with uranyl acetate and lead citrate. Images were acquired with a Zeiss - Leo 906e electron microscope at an acceleration voltage of 100 kV.

#### 4.2.9. High-resolution respirometry

High-resolution respirometry was conducted using an Oroboros O2K (Oroboros Instruments, Austria) in combination with the supplied software, Oroboros Datlab which was used for the recording and the analysis of the experiments. All experiments were conducted in technical duplicates by simultaneous measurement of two samples of the same cell suspension or tissue preparation in the two glass chambers of the instrument.

##### 4.2.9.1. Primary mouse embryonic fibroblasts

Basic respiratory states were assessed in intact (i.e., non-permeabilised) primary MEFS from WT and D326R mice in growth medium (see 4.2.2.3.).

For each measurement, 2-3  $\times 10^6$  pMEFs were needed per chamber and were seeded one or two days before ( $2.5 \times 10^6$  cells in two 15 cm dishes per line). Cells were then washed, detached with Trypsin, diluted in pre-heated (37°C) growth medium and centrifuged (1.500 rpm, 3min). The cells were resuspended in an estimated volume of growth medium to reach a concentration of  $1.5-2 \times 10^6$  cells/ml. This concentration was controlled using an automated cell counter (Luna) and adjusted if necessary.

Cleaning and calibration of the two glass chambers of the Oroboros O2k were performed and completed before. 2 ml of the cell suspension were filled into each chamber, and they were closed airtight with two stoppers. The recordings of oxygen concentration and consumption (flux) were allowed to stabilize for several minutes. Once both reached a plateau this value was defined as routine respiration meaning normal cellular respiration without any enhancers or inhibitors. Next, 2.5 mM oligomycin was injected using a Hamilton syringe which blocks the ATP synthase (complex V). This induces the so-called leak state, meaning that any oxygen consumed at this point is not utilised for ATP production but only to balance proton leak through the inner mitochondrial membrane bypassing the ATP synthase. Following, the maximum capacity of the electron transport system (ETS) is assessed by the stepwise addition of FCCP (0.5  $\mu$ M each injection). FCCP is an ionophore that enables the free diffusion of protons across the inner mitochondrial

membrane. This forces the electron transport complexes into their maximal activity trying to maintain the mitochondrial membrane potential. Once the respiration does not increase further, 0.5  $\mu\text{M}$  rotenone is injected to inhibit complex I (NADH-dehydrogenase). Lastly, complex III (cytochrome c oxidase) is blocked by 2.5  $\mu\text{M}$  antimycin A. Any remaining  $\text{O}_2$  flux is titled residual oxygen consumption (ROX) and stems from non-mitochondrial oxidative processes in the cytosol as all relevant components of mitochondrial respiration are inhibited. Therefore, all respiratory states were corrected for ROX during the analysis. Moreover, respiratory values were automatically normalised to the cell number and to the instrumental background by the software. The instrumental background had to be pre-recorded with medium alone at different  $\text{O}_2$  concentrations.

#### 4.2.9.2. Permeabilised cardiac fibres

In a more direct approach to measuring respiration in cells from WT and D326R mice, I established a protocol for the permeabilisation of cardiac fibres with the help of Dr Rob Wüst, Vrije Universiteit Amsterdam, Netherlands. This enabled me to investigate mitochondrial respiration *in situ*.

Preparation of fibres and respirometry was performed as described (Lemieux et al., 2017). Adult (18-26 w), male mice were sacrificed by cervical dislocation and the heart was rapidly explanted. As much blood as possible was squeezed out and washed away with cold PBS. A piece of the apex region was cut off and immersed in ice-cold BIOPS (10 mM Ca-EGTA buffer, 0.1  $\mu\text{M}$  free  $\text{Ca}^{2+}$ , 20 mM imidazole, 20 mM taurine, 50 mM K-MES, 0.5 mM DTT, 6.56 mM  $\text{MgCl}_2$ , 5.77 mM ATP, 15 mM phosphocreatine, pH 7.1) in a small petry dish. All following steps were performed on ice/at 4 °C and with precooled equipment. Sharp forceps were used to remove connective tissue and to tear the cardiac tissue into small pieces (1-2 mg). Tissue samples were then transferred to a well in a 12-well plate filled with 2 ml BIOPS with 50  $\mu\text{g}/\text{ml}$  Saponin. The plate was incubated on a shaker for 20 min, followed by 10 min washing in a well with pure BIOPS. After these two steps, the cell membranes of the fibres were permeabilised and the washing step removed all cytosolic content. The fibres were dried for 30 s on non-fibrillating blotting paper and dry weight was determined using a fine scale. Thereafter, the tissue piece was rapidly transferred back to a BIOPS-filled well. This procedure was repeated with a second tissue piece as every

measurement was conducted in duplicates with two samples from the same mouse. This weighing step was critical for correct normalisation and was performed as standardised as possible.

Cleaning and calibration of the chambers were performed previously, and the tissue pieces were directly immersed into the glass chambers filled with 2 ml Mir06 (Mir05 + 280 U/ml catalase) prewarmed to 37 °C. Chambers were closed and 200 mM H<sub>2</sub>O<sub>2</sub> was injected in 2-3 µl steps. The catalase in the medium immediately catalyses H<sub>2</sub>O<sub>2</sub> to water and oxygen. Like this, the O<sub>2</sub> concentration in the medium was increased to ≥500 µM and kept ≥300 µM throughout the experiment. It is crucial to maintain high oxygen concentrations for the respirometry of permeabilised fibres to ensure that mitochondria located deeper in the tissue do not suffer from oxygen deficiency. If reoxygenation was necessary H<sub>2</sub>O<sub>2</sub> was injected again as described before.

To investigate different respiratory states and the maximum respiratory capacity in the cardiac fibres, a substrate-uncoupler-inhibitor-titration (SUIT) protocol was conducted as recommended by the manufacturer (SUIT-008)(SUIT-008 O2 pfi D014 - Bioblast, 2021). The final concentrations of the injected reagents are indicated in brackets. The stable respiratory state measured even before the first injection was defined as residual oxygen consumption (ROX). Given that at this time point the mitochondrial OXPHOS system completely lacked substrates any oxygen use could only stem from other (non-mitochondrial) oxidative processes and was therefore subtracted from all other values for the final analysis. To fuel mitochondrial respiration, pyruvate (5 mM) and malate (2 mM) were then injected for a non-phosphorylating resting state (LEAK). Of note, any injection was administered only once the respiratory flux had reached a stable level. After stabilisation, a saturating amount of ADP (5 mM) was added for an active OXPHOS state. At this state cyt c (10 µM) was added to control for outer mitochondrial membrane integrity. If the outer membrane is damaged, the addition of cyt c increases respiration considerably. For additional activation of the glutamate dehydrogenase pathway glutamate (10 mM) was injected (CI). This state represents the maximum (coupled) activity of complex I alone as no substrates for complex II are present. Thus, the addition of succinate (10 mM) which fuels complex II led to a marked rise in respiration. Thereupon, respiration was uncoupled by FCCP (0.5 -1 µM) (ETS) which is then the maximum

respiratory capacity. After inhibition of complex I by rotenone (0.5  $\mu\text{M}$ ) activity of the uncoupled complex II alone was measured (CII\*).

All respiratory values were automatically normalised to the amount of tissue per ml and to the instrumental background by the software. The instrumental background was determined beforehand with MirO6 and high oxygen levels ranging from 300-500  $\mu\text{M}$ . All values were then corrected for ROX as mentioned above. I then calculated the response to the cyt c injection as a percentage of the preceding state.

$$\text{cyt c response} = (\text{value after cyt c} - \text{value before cyt c}) / \text{value before} * 100$$

All single chambers that increased by more than 15 % were excluded. From the remaining ones, the mean of the two chambers was calculated and considered as one biological replicate.

#### 4.2.10. Mitochondrial Calcium uptake assay

Mitochondrial calcium handling was measured in freshly isolated mitochondria from WT and D326R mice under different conditions. Isolation procedures as described above (4.2.3.2.2.2.). For the mitochondrial calcium uptake assay, PTP-EGTA-buffer (120 mM KCl, 70 mM mannitol, 25 mM saccharose, 20 mM HEPES, 5 mM  $\text{KH}_2\text{PO}_4$ , 20  $\mu\text{M}$  EGTA, pH 7.5) was used as experimental buffer. Mitochondrial substrates K-glutamate and Na-Malate were added freshly to a final concentration of 5  $\mu\text{M}$  and 2.5  $\mu\text{M}$ , respectively. This results in a basal sodium concentration of 2.5 mM. Five different conditions were measured as stated in the table below.

**Table 7: Conditions for the calcium uptake assay**

	Condition	Reagent added	Vehicle control
1	2.5 mM NaCl	--	DMSO+ diluted DMSO
2	2.5 mM NaCl + CsA	2.5 $\mu\text{M}$ CsA	DMSO
3	7.5 mM NaCl	7.5 mM NaCl	DMSO+ diluted DMSO
4	10 M NaCl	7.5 mM NaCl	DMSO+ diluted DMSO
5	10 mM NaCl + CGP	7.5 mM NaCl + 10 $\mu\text{M}$ CGP	diluted DMSO

The NaCl solution was prepared with buffer. CsA was dissolved in DMSO but prediluted 1:50 in buffer, thus the correct vehicle control was DMSO diluted with buffer. CGP is dissolved in DMSO and as a control pure DMSO was added to the other samples. Lastly, for

duplicates, 370 µg of isolated mitochondria from heart/brain or 185 µg of isolated mitochondria from skeletal muscle were diluted in the prepared solution of buffer and reagents (185/92.5 µg per well). Following a short incubation (5 min, RT), 1 µM Calcium-Green 5N was added and after extensive resuspending duplicates from the suspension were transferred to a black 96-well plate with clear bottom. Fluorescence was measured by a plate reader (Tecan M200 Pro) every 5 s, at Ex/Em 488/520 nm, at 37 °C for 312 cycles (>400 cycles for brain). 10 µM CaCl<sub>2</sub> diluted in PTP-buffer without EGTA was injected automatically every 2 min.

For the analysis, the first read-out was defined as  $F_0$  and used for normalisation. All traces are shown as  $F/F_0$ .

#### 4.2.11. Mitochondrial swelling assay

An increase in mitochondrial matrix volume is termed mitochondrial swelling and can be caused by different factors of which I investigated Ca<sup>2+</sup>- and Na<sup>+</sup>-induced swelling. The volume increase causes changes in light scattering and was detected as a decrease in absorbance. The swelling was assessed in isolated mitochondria (see section 4.2.3.2.2.3.) from liver and heart by measuring the absorbance of the suspension at 540 nm.

For calcium-induced swelling, a high concentration of Ca<sup>2+</sup> was added, which was taken up by the mitochondria and induced opening of the mPTP. This allowed rapid diffusion of ions and water leading to the observed effect of mitochondrial swelling (Elustondo et al., 2016). In more detail, 300 µg mitochondria per well were resuspended in assay buffer (125 mM KCl, 10 mM HEPES, 2 mM MgCl<sub>2</sub>, 2 mM K<sub>2</sub>HPO<sub>4</sub>, pH 7.2 (KOH), freshly supplemented with 100 mM succinate and 0.2 µM thapsigargin). Thapsigargin was added to the buffer to block the Ca<sup>2+</sup>-pump SERCA in the endoplasmic reticulum. This excludes the contribution of ER remainders in the suspension. The absorbance of 200 µl suspension per well in a clear 96-well plate was measured at 540 nm every 5 s using a plate reader (Spark<sup>®</sup> Tecan, preheated to 37 °C). After a 2 min baseline, CaCl<sub>2</sub> was injected (liver: 200 µM, heart: 1 mM) and the following decrease in absorbance was measured for 5-10 min. The swelling was measured in the absence and presence of 2 µM Cyclosporin A which is an inhibitor of the mPTP. It thereby served as a control that the observed swelling is Ca<sup>2+</sup>-induced.

For the Na<sup>+</sup>- induced swelling, I used a similar protocol as described by Austin et al. (Austin et al., 2017). In brief, mitochondria were de-energised by incubation with Antimycin A and then resuspended in a buffer containing sodium acetate (NaOAc). The acetic acid diffuses into the mitochondria and causes acidification of the matrix which in turn leads to Na<sup>+</sup> uptake in exchange for protons mediated by the Na<sup>+</sup>/H<sup>+</sup>-exchanger at the inner mitochondrial membrane. The accumulation of Na<sup>+</sup> is accompanied by water influx that is observed as swelling.

Isolated mitochondria were suspended in isolation buffer (IB<sub>c</sub>) at a concentration of 1.5 mg/ml and de-energised by incubation with 5 µM Antimycin A for 10 min at RT. The buffer was removed by centrifugation (8.000 x g, 2 min), rapidly replaced by sodium acetate swelling buffer (55 mM NaOAc, 5 mM TES, 0.1 mM EGTA, 0.1 mM EDTA) and the suspension was immediately transferred to a clear 96-well plate (200 µl/well). Resuspension in IB<sub>c</sub> served as a negative control. The addition of the buffer with NaOAc directly started the swelling process, therefore the measurement needed to be started as quickly as possible. Absorbance was measured as above, at 540 nm, every 5 s for 8 min. For the analysis, absorbance was normalised to the initial values.

#### 4.2.12. Pre-swelling test

Differences in mitochondrial swelling behaviour may be caused by differential pre-swelling which means the baseline matrix volume. To assess this, I induced the shrinking of mitochondria by altering the osmolarity in the buffer.

Similar to the swelling protocol, isolated liver mitochondria (as described above 4.2.3.2.2.3.) (300 µg per well) were resuspended in assay buffer and the absorbance of 100 µl suspension per well in a clear 96-well plate was measured at 540 nm every 5 s. After a 2 min baseline, 10 % polyethyleneglycol-3350 (PEG, final 5 %) was added and the following increase in absorbance was detected for 6 min. PEG is a highly viscous substance which makes it difficult to precisely inject small volumes. Thus, I added a volume of 100 µl 10 % PEG (diluted in assay buffer) to 100 µl mitochondrial suspension. Naturally, this drastic volume change led to a change in the absorbance by itself and I, therefore, included a control to which the same volume of assay buffer was added.

All values were normalised to the last values after PEG addition which uncovers variations in the baseline state.

#### 4.2.13. Mouse experiments

##### 4.2.13.1. Behavioural tests

All experiments were performed with the permission of the local authorities in accordance with the German Animal Protection Law. The experimenters were blinded for all experiments and initial quantitative analyses.

The battery of behavioural tests described below was performed with male WT and D326R mice (littermates) at 20-26 weeks of age in sound-attenuated rooms, during the light phase between 9 am and 5 pm. Except for the inverted grid test, all behavioural experiments were conducted by Dr Konstantin Radyushkin, head of the Mouse Behavior outcome Unit (MBU), JGU Mainz.

##### 4.2.13.1.1. Open field

Explorative behaviour in the open field was tested in the open field test as described (Radyushkin et al., 2009): Mice were placed on the ground in a grey Perspex arena (120 cm in diameter, 25 cm high; illumination 120 lux) and allowed to move freely for 7 min. The activity was recorded by a PC-linked overhead video camera. A video-tracking software, "Ethovision XT" (Noldus Information Technology, Wageningen, Netherlands), was used to calculate velocity, distance travelled, and time spent in the centre or the wall zones of the open field.

##### 4.2.13.1.2. Elevated plus-maze

Evasive behaviour and fear were investigated with the elevated plus-maze as described (Radyushkin et al., 2009). It consists of two open and two closed arms (made of grey Perspex with a central 5 x 5 cm central platform, two open arms, 30 x 5 cm, 2 enclosed arms, 30 x 5 x 15 cm, illumination 120 lux). Individual mice were placed on the central platform and their movement was recorded by an overhead video camera and a computer

equipped with “Ethovision XT” (Noldus Information Technology, Wageningen, The Netherlands) software to calculate the time each animal spent in open or closed arms.

#### 4.2.13.1.3. Rotarod

Rotarod (as described by (Bicker et al., 2017)) is a test for motor function, balance, and coordination. Mice were placed individually on a rotating drum. Once they were balanced, the drum was accelerated from 4 to 40 revolutions per min for 5 min. The latency to fall was recorded. This was repeated three times for every mouse and the longest time was used for analyses.

#### 4.2.13.1.4. Prepulse inhibition

The test was performed as described by Radyushkin et al. (Radyushkin et al., 2009). Briefly, mice were placed individually in small metal cages (90 × 40 × 40 mm) equipped with a movable platform floor attached to a sensor that records vertical movements of the floor. Cages were placed in four sound-attenuating isolation cabinets (Med Associates, St. Albans, USA). Acoustic stimuli were delivered by a loudspeaker suspended above the cage to evoke startle reflexes. The movement of the platform was recorded and analysed as an indicator for the startle reaction of the mouse. The experiment was started with 2 min habituation to 65 dB background white noise (continuous throughout the session) and a baseline recording for 1 min. The baseline recording was followed by 8 pulse-alone trials using startle stimuli of 120 dB intensity and 40 milliseconds duration to decrease the influence of within-session habituation. These data were not included in the analysis of the prepulse inhibition. The experimental session consisted of 40 trials with 4 different modes (10 trials each). The 120 dB/40 ms startle pulse was applied either alone or preceded by a prepulse stimulus of 70, 75- or 80-dB intensity and 20 ms duration. An interval of 100 ms with background white noise was employed between each prepulse and pulse stimulus. The different types of stimuli were applied in a pseudorandom order with varying inter-trial intervals (8 - 22 s). Amplitudes of the startle response were averaged for each mode of stimulus and for each animal. Prepulse inhibition was calculated as the percentage of the startle response with the following formula:

$$\text{PPI (\%)} = 100 - [(\text{startle amplitude after prepulse and pulse} / \text{startle amplitude after pulse only}) \times 100].$$

#### 4.2.13.1.5. Inverted grid

The inverted grid test (as described (Niewiadomski et al., 2016)) is a convenient way to assess leg muscle strength. Mice were placed in the middle of a large grid which was then inverted and placed on top of a transparent cylinder (height: 25 cm, diameter: 17 cm). The ground was covered with bedding. The time was measured for which the mice were able to cling on to the underside of the grid until they let go and fell to the ground.

#### 4.2.14. Metabolic chambers

Wholebody metabolism during unconstrained activity was measured using metabolic chambers as described (Philippaert et al., 2020). Male mice (25 to 26 weeks old) were single-housed and habituated to the special food and water delivery system for 2 days before the start of the recordings. Mice were then separately placed in the metabolic chambers (TSE Systems, Germany) and the following parameters were continuously recorded for 4 days every 30 min: water intake, food intake, ambulatory activity, heat production and gas exchange ( $O_2$  and  $CO_2$ ) (using the TSE LabMaster system, Germany). Food and water intake were determined by the integration of weighing sensors fixed at the top of the cage, from which the two containers have been suspended into the sealed cage environment. After 3 days (72 h) the food was removed from the cage for a 24 h starving period.

The first 48 h were considered as a habituation phase and were excluded from the analysis.  $V_{O_2}$ ,  $V_{CO_2}$ , and energy expenditure (EE) were automatically calculated by the PhenoMaster Software (TSE Systems). Resting energy expenditure (REE) was defined as the EE during the light cycle with the lowest counts for activity assuming that the mice were sleeping or resting. The respiratory exchange rate (RER) was estimated by calculating the ratio of  $V_{CO_2}/V_{O_2}$ . All values were analysed after normalisation to the body weight.

#### 4.2.15. Respirometry during exhaustive exercise

Whole-body respiratory activity during exercise was measured in two groups of mice using a similar protocol as described by Sliter et al. (Sliter et al., 2018).

The mice were placed on a treadmill in an airtight chamber which was connected to a gas analyser that controlled and continuously recorded O<sub>2</sub> and CO<sub>2</sub> concentration in the chamber. O<sub>2</sub> consumption and CO<sub>2</sub> production of the mouse were assessed under consideration of airflow and the bodyweight of the mouse. The respiratory exchange ratio was calculated as CO<sub>2</sub> production/O<sub>2</sub> consumption. Data were acquired and calculated by the software metabolism V.

The first group consisted of 22 adult males (10x WT/12x D326R, age 24 weeks). As the variance of behavioural and whole organism experiments is notoriously high, I wanted to increase statistic power with a second batch of mice (9x WT/10x D326R). Unfortunately, due to unexpected construction work at the MBU, I had to prepone the measurements with the second group which meant that they were 5- 8 weeks younger than their forerunners (age 16/19 w). I compared the bodyweight of the two groups and as there was a significant difference, I decided to refrain from pooling both measurements and analysed them separately.

Prior to the experiment, the mice were habituated to the setup for two weeks. The treadmill for habituation had several chambers to enable simultaneous training of up to 10 mice. It was adjusted to an inclination of 10° and speed was set as stated in the table below.

**Table 8: Protocol for treadmill habituation**

day of habituation	time [min]	speed [cm/s]	electric shocks
day 1	10	0	no
	5	5	no
day 2	5	0	no
	10	5	no
day 3	5	0	no
	5	5	no
	5	10	no
day 4	3	0	no
	5	5	no
	5	10	no
day 5	3	0	no
	5	5	no
	5	10	no
day 6	3	0	no
	5	5	no
	5	10	no

day 7	3	0	no
	3	5	no
	3	10	no
	5	15	no
day 8	3	0	no
	5	10	no
	5	15	no
day 8/2nd round	3	0	yes
	9	5	yes
	5	10	yes
	2	15	yes
day 9	3	0	yes
	3	5	yes
	5	10	yes
	5	15	yes
day 10	3	0	yes
	2	5	yes
	5	10	yes
	3	20	yes

On days 1-9, the mice were physically separated from the electrical grid by tape (indicated as "no electrical shocks"). On day 10 this barrier was removed, and the mice learned that they receive an electrical shock (0.1 mA) when they touch the grid. After the habituation period, the mice were allowed to rest for at least two days before the experiment.

On the day of the experiment, the treadmill and the gas analyser (Panlab LE 405) were switched on 2 h prior to the measurement to allow stabilisation of the sensors. These were then calibrated using high and low O<sub>2</sub>/CO<sub>2</sub> concentrations (high: O<sub>2</sub> = 50 %, CO<sub>2</sub> = 1.5 %, low: O<sub>2</sub> = 20 %, CO<sub>2</sub> = 0.0 %). The airflow to the chamber was set to 0.3 l/min and the treadmill had an inclination of 15°. Each mouse was weighed and then placed in the chamber. After 3-5 min, to allow stabilisation of the gas composition and accommodation of the mouse, the speed protocol was started. The settings are stated in the table below. At the beginning of each session, 1 min of room air monitoring was completed before switching to the input of the chamber. Thus, the first two minutes of each experiment were excluded from the analysis.

**Table 9: Protocol for the treadmill exercise**

time [min]	speed [cm/s]		electric shocks
	start	end	
10	0	0	yes
10	8	8	yes
5	8	20	yes
3	20	20	yes
3	25	25	yes
3	30	30	yes
3	35	35	yes
5	40	40	yes
5	45	45	yes
5	50	50	yes
5	55	55	yes
5	60	60	yes

The experiment was terminated when the number of shocks exceeded 50 or when the mouse failed to reengage with the belt with all four paws for >2s. All values used in the analysis (O<sub>2</sub> consumption, CO<sub>2</sub> production, respiratory exchange ratio (RER)) were

automatically calculated in the software according to the air calibration and the entered weight of the mice.

#### 4.2.16. Blood analyses

##### 4.2.16.1. Lactate

Lactate is a by-product of anaerobic respiration and is, therefore, a commonly used indirect marker for muscular fatigue (Lucertini et al., 2017). Following the treadmill exercise, blood samples were taken from the mice through a small incision at the tail. For the lactate measurement, a 20 µl-capillary were used to absorb the correct volume and immediately immersed and diluted in lactate-haemolysis-solution (provided by the manufacturer). The diluted samples (1:51) could be stored on ice for several hours until all treadmill runs were finished. Lactate concentration was then measured in triplicates after mixing well using the Biosen C-Line - Clinic/GP+ (EKF-diagnostic GmbH, Magdeburg, Germany) following the manufacturer's instructions.

##### 4.2.16.2. Interleukin-6

Interleukin-6 (IL-6) is a proinflammatory cytokine which - amongst others - is released from muscles during exercise (Hojman et al., 2019) and can be indicative of dysregulation in mitochondrial degradation after exhaustive exercise (Sliter et al., 2018). For the determination of the IL-6 concentration, blood samples were collected via a K<sub>2</sub>-EDTA-microvette and stored on ice until the end of the treadmill experiments. The plasma was then separated from the cellular fraction via centrifugation at 15.000xg at 4°C and stored at -20°C.

For the IL-6 detection the IL-6 mouse ProcartaPlex™ Simplex Kit was used (following the manufacturer's protocol), which works similar to the traditional ELISA but with the difference that antibody labelled magnetic beads are used for the detection. In brief, beads labelled with the desired antibody specificity are placed in the wells of a 96-well plate and incubated with the samples. A second (detection) antibody binds to the target and is made visible by the addition of fluorescently-labelled streptavidin (streptavidin-phycoerythrin (PE), Ex/Em: 496,546,565/578 nm).

In more detail, the beads were diluted at 1:50 in assay buffer (PBS supplemented with 1 % BSA and 2 mM EDTA) and 20 µl of this bead mixture was added per well and washed using the assay buffer. After every washing or incubation step, the magnetic beads were collected at the bottom of the plate by quick centrifugation and 2 min on a flat magnet. The lyophilized standard mix supplied with the kit was reconstituted in 250 µl assay buffer and diluted 1:4 in 7 steps constituting a 4-fold serial dilution. The plasma samples were prediluted 1:5. 20 µl of the samples and the standard dilutions were added to the beads. The plate was sealed, wrapped in tin foil to protect it from light and first incubated at RT for 30 min on a shaker. The incubation was then continued at 4°C overnight. The next morning, it was again incubated at RT for another 30 min. Beads were collected at the bottom of the plate as described above and washed 3x with assay buffer after removal of the sample/standard. The detection antibodies were diluted at 1:50 in assay buffer and 20 µl were added per well followed by incubation (dark, RT) for 30 min on a shaker. Later, the solution was removed, and the beads were washed 3x as before. To stain the detection antibodies, 20 µl of the streptavidin-PE solution was added and again incubated (dark, RT) for 30 min on a shaker followed by the known washing steps. Before detection, the beads were washed in PBS alone.

The fluorescent signal was detected using a Luminex MAGPIX and the results were calculated using the Luminex software according to the standard curve.

#### 4.2.16.3. Oxidative burst

As part of the innate immune response, phagocytes, primarily neutrophils produce a so-called respiratory or oxidative burst which is the sudden release of a high amount of reactive oxygen species such as superoxide, hydrogen peroxide and others (Dahlgren C. and Karlsson A., 1991). The capacity to produce this burst was measured via a chemiluminescent assay (similar as described (Daiber et al., 2003; Karbach et al., 2016)) using fresh whole blood samples from WT and D326R mice. In brief, after induction of the oxidative burst by Phorbol-12,13-Dibutyrate (PDBU) or zymosan A the released radicals were detected by the dye L-012 (8-Amino-5-Chloro-7-Phenylpyrido[3,4-d] pyridazine-1,4-(2H,3H) Dione) which reacts with a broad range of reactive oxygen species and produces chemiluminescence.

Blood samples were either taken from the Vena facialis (submandibular) from living animals or the left cardiac ventricle in deep anaesthesia. For the latter, analgesia was confirmed by the lack of reflexes to toe pinching. The blood was immediately mixed with citrate (1:9 with 4 % citrate solution) to prevent coagulation. It was then diluted 1:50 in warm PBS supplemented with 1 mM MgCl<sub>2</sub> and 1 mM CaCl<sub>2</sub> and the chemiluminescent dye L-012 (100 µM). 2 µl of zymosan A (final 50 µg/ml) or PDBU (10 µM) were prepared in a white 96-well plate. 200 µl per well of the diluted blood was added in triplicates and the measurement was immediately started. Luminescence was detected every 5 min for a total of 90 min at 37 °C using a Tecan Spark® plate reader.

To be able to compare the degree of oxidative burst to the cellular composition of the blood, the rest of the undiluted blood samples was used to determine the number and ratio of the different cell types using a VETSCAN® HM5 haematology analyser.

#### 4.2.17. Echocardiography

Echocardiography and the analysis were conducted by Dr Stefanie Finger (Centre for Thrombosis and Haemostasis (CTH), University Medicine Mainz, Germany) as described by Karbach et al. (Karbach et al., 2016). Anaesthesia of mice was induced in a chamber (2–4 % isoflurane mixed with 0.2 L/min 100 % O<sub>2</sub>) and continued throughout the measurement via a face mask (1–2 % isoflurane with 0.2 L/min 100 % O<sub>2</sub>). Animals were kept on a heated table mounted on a rail system (VisualSonics, Toronto, Ontario, Canada). Ultrasound was performed with the Vevo 3100 Imaging System (FUJIFILM Sonosite Europe, Amsterdam, Netherlands) and the MX400 transducer (range: 20-46 MHz, centre transmit: 30 MHz). The body temperature was monitored using a rectal probe and maintained at 37°C. The analysis was conducted using the software Vevo LAB 5.6.1 (FUJIFILM Sonosite).

#### 4.2.18. Statistics

Statistical analysis was performed with GraphPad Prism. Data are displayed as mean ± standard error of the mean (SEM) or as violin blot with median and quartiles. Before analysis, outliers were excluded with the ROUT method (Q = 1 %). Data were controlled for Gaussian distribution with the D`Agostino-Pearson omnibus normality test. In the case of normal distribution, two pairs of data sets were tested for statistically significant

differences by unpaired two-tailed t-test. If several data sets from different time points (same samples/subjects) were compared, the mixed-effects analysis with multiple comparisons was applied. More than two data sets from different samples/subjects were analysed using the ordinary one-way ANOVA with multiple comparisons. For the comparison of several parameters within two groups of samples/subjects, two-way ANOVA with Šídák's multiple comparisons test was calculated. Aberrancy from expected values was tested for statistical significance via the Chi-square test. Survival curves were compared with the Mantel-Cox test. P-values < 0.05 were considered significant.

## 5. Results

---

### 5.1. TMBIM5 is not involved in the Mitochondrial contact site and cristae organizing system but affects OPA1 expression and splicing

Mitochondria are enclosed by two membranes, the flat outer membrane and the folded inner membrane. The inner mitochondrial membrane is folded into cristae which are tethered at the cristae junctions (CJs). These are critical for maintaining the specific distribution of proteins, molecules and ions in the inner membrane and the intermembrane space which is important for mitochondrial function. The CJ are shaped by a conserved, hetero-oligomeric protein complex, the mitochondrial contact site and cristae organizing system (MICOS) (Rampelt and van der Laan, 2017). The two key players are the subunits MIC10 and MIC60.

TMBIM5 has been reported to be involved in the structural organisation of mitochondrial cristae by Oka et al. (Oka et al., 2008). Knockdown of TMBIM5/MICS1 reduced the number of invaginations of the inner mitochondrial membrane, the cristae were shorter and had abnormal curved or ring-like shapes (Oka et al., 2008). In our lab, electron microscopy analysis revealed widened and irregular cristae in HAP1 TMBIM5 KO cells, too. I, therefore, investigated whether TMBIM5 is directly involved in mitochondrial cristae structure organisation and the MICOS.

We obtained WT and TMBIM5 KO HAP1 cells from Horizon Genomics and received  $\Delta$ MIC10 and  $\Delta$ MIC60 with the corresponding HEK 293T WT cells as a kind gift from Dr von der Malsburg (University Saarland, Germany).  $\Delta$ MIC10 cells have a complete knockout of the protein MIC10 (Fig. 7A, left), whereas MIC60 expression in  $\Delta$ MIC60 cells is strongly reduced as shown in Fig. 7A) (middle). The 32 bp deletion in the TMBIM5 gene (*Ghitm*) in the HAP1 cells was verified via PCR (Fig. 7A, right).

Loss of TMBIM5 in the HAP1 KO cells did not alter the protein expression of MIC10 or MIC60 and vice versa TMBIM5 was not differentially expressed in  $\Delta$ MIC10 and  $\Delta$ MIC60 cells, tested via denaturing immunoblotting, shown in Fig. 7B)-D). Moreover, I examined the complex formation of the three proteins in the different knockout lines via blue native polyacrylamide gel electrophoresis (BN PAGE). As expected, MIC10 and MIC60 showed the same pattern of bands on the gel meaning that they localised in the same complex. In addition, it was very apparent how closely entwined the two proteins are from the near-

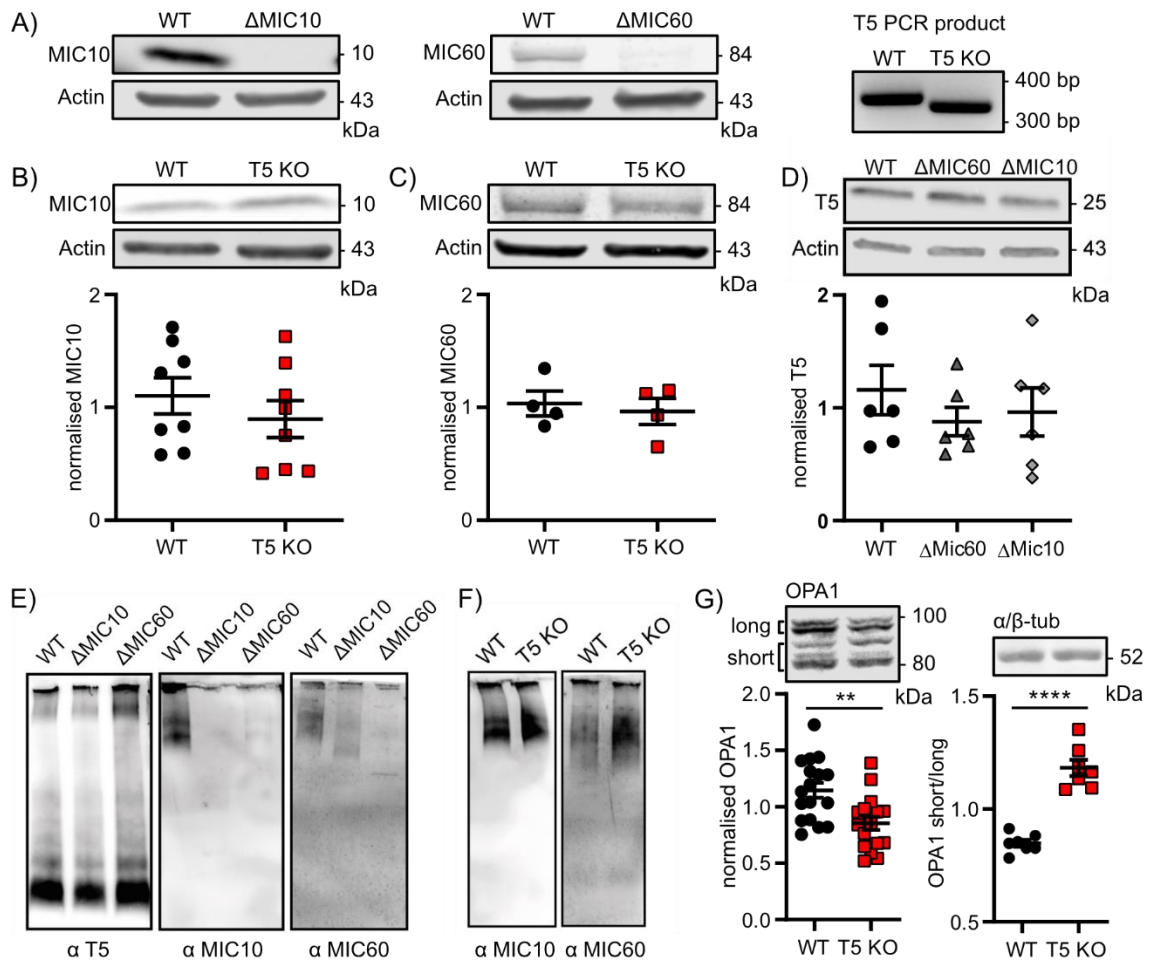


**Figure 7: TMBIM5 is not involved in the Mitochondrial Contact Site and Cristae Organizing System (MICOS) but affects OPA1 processing.**

**A)** Exemplary western blots showing the loss of the MICOS complex subunits (MIC) MIC10 (left) and MIC60 (middle) expression in  $\Delta$ MIC10/ $\Delta$ MIC60 HEK293T cells. On the right, PCR product verifying the deletion in the Ghitm gene in the TMBIM5 (T5) KO HAP1 cells. **B), C)** The protein expression of MIC10 and MIC60, core proteins of the MICOS, was not altered in TMBIM5 KO HAP1 cells compared to WT. **D)** TMBIM5 expression in  $\Delta$ MIC60 and  $\Delta$ MIC10 HEK293T cells was not affected either. **B)- D)** Expression was normalised to the loading control actin and the overall mean per blot. Unpaired t-test. **E)** No change in the complex formation of TMBIM5 in cells lacking MIC10 or MIC60. **F)** MIC10 and MIC60 complexes were not altered in the absence of TMBIM5. **E), F)** Images show protein complexes separated via blue native polyacrylamide gel electrophoresis (BN PAGE) and stained against the indicated proteins ( $\alpha$  = anti). **G)** Total expression of Optical Atrophy 1 (OPA1) was reduced in TMBIM5 KO cells with a strong shift from long to short isoforms of the protein which indicates increased splicing. Signal was normalised to loading control and overall mean per blot. Unpaired t-test.

Data are shown as mean  $\pm$  SEM. Differences are not significant if not indicated otherwise, n.s.  $p \geq 0.05$ ,  $p^{**} < 0.01$ ,  $p^{****} < 0.0001$ ;

complete loss of MIC10 in the  $\Delta$ MIC60 background and vice versa. The complexes stained by the anti-TMBIM5 antibody on the other hand clearly appeared on different heights and were not affected by the lack of MIC10 or MIC60 (Fig. 7E). The same was true for the

MIC10/MIC60-complex which was not altered in the absence of TMBIM5 in the HAP1 KO cells (Fig. 7F). All of this indicates that TMBIM5 does not directly interact with the MICOS. However, there might be an indirect influence of TMBIM5 on cristae structure. In mammals, MIC60 was found to interact with the dynamin-like GTPase Optic Atrophy 1 (OPA1) (Wollweber et al., 2017). And interestingly, Oka et al. observed “(...)that actinomycin D-dependent processing of OPA1 was enhanced by MICS1 [TMBIM5] knockdown” (Oka et al., 2008) indicating that TMBIM5 expression affects OPA1 splicing. OPA1 is not part of the MICOS and is implicated in many different functions. Among them are the regulation of mitochondrial morphology (Ishihara et al., 2006; MacVicar and Langer, 2016), mitochondrial DNA maintenance (Del Dotto et al., 2018) and apoptotic cristae remodelling facilitating the release of cyt c (Frezza et al., 2006). Beyond that, there is evidence that OPA1 is not only involved in cristae remodelling but also their formation (Harner et al., 2016). To cover all these different roles, OPA1 exists in different isoforms - in humans not less than eight (Del Dotto et al., 2018). Of these eight isoforms, the long variants are membrane-bound and are thought to be critical for mitochondrial fusion, whereas the short, soluble forms are more relevant for mitochondrial energetics and can even induce fission (MacVicar and Langer, 2016; Del Dotto et al., 2018).

I investigated OPA1 expression and splicing via immunoblotting and indeed found a reduction in total protein expression in TMBIM5 KO HAP1 cells with an altered ratio of the isoforms (Fig. 7G). In the absence of TMBIM5, OPA1 splicing was enhanced resulting in an increased abundance of the short isoforms compared to long. Thus, the disorganisation of the cristae observed in cells lacking TMBIM5 might be caused by faulted OPA1 processing. OPA1 is mainly processed by the two peptidases OMA1 and YME1L whose activity is modulated by several factors including mitochondrial membrane potential and ATP levels (Del Dotto et al., 2018). We hypothesised that TMBIM5 does not directly interact with OPA1 but causes these changes in an indirect manner by modulating calcium homeostasis which in turn affects ATP production and the membrane potential.

## 5.2. Ionomycin-induced mitochondrial $\text{Ca}^{2+}$ uptake is reduced in HAP1 TMBIM5 KO cells

TMBIM5 belongs to a family of six proteins and is closely related to TMBIM6 (or BI-1) (Lisak et al., 2015) which is a  $\text{Ca}^{2+}$ -leak channel in the ER (Bultynck et al., 2014). Overexpression experiments with TMBIM5 also showed an effect on the cellular  $\text{Ca}^{2+}$  homeostasis (Lisak et al., 2015). Thus, I investigated the effect of TMBIM5 KO in HAP1 cells on mitochondrial  $\text{Ca}^{2+}$  uptake.

To do so, I generated a plasmid that contained the sequence for a fluorescent  $\text{Ca}^{2+}$  sensor (Cepia) and a uniformly fluorescent protein as baseline (BFP2). Both were tagged with a mitochondrial targeting sequence. See Fig. 8A) for a graphical depiction of the plasmid. The plasmid was transiently transfected into HAP1 WT and TMBIM5 KO cells, and the cells were imaged over 5 min using a spinning disk confocal microscope. Exemplary images are shown in Fig. 8B). The fluorescent signal of BFP was used to normalise the signal of Cepia which excludes an effect of transfection efficiency. After a baseline of 2 min 1  $\mu\text{M}$  Ionomycin was added. Ionomycin is an ionophore that increases  $[\text{Ca}^{2+}]_{\text{cyto}}$  and subsequently  $[\text{Ca}^{2+}]_{\text{mito}}$ . This rise in  $[\text{Ca}^{2+}]_{\text{mito}}$  was detected as an increase in the Cepia/BFP ratio and was reduced in cells lacking TMBIM5 compared to the WT, as seen in Fig. 8C). Quantification and comparison of the area under the curve did not reach significance but showed a clear tendency (Fig. 8D). This reduction could have several reasons: a) an impaired uptake pathway, b) a reduced driving force for  $\text{Ca}^{2+}$  due to a reduced membrane potential or c) an increased  $\text{Ca}^{2+}$  preload due to an impaired export pathway. To rule out that this reduction was caused by an increased  $[\text{Ca}^{2+}]_{\text{mito}}$  at baseline in TMBIM5 KO cells I additionally measured untreated cells expressing the fluorescent proteins using flow cytometry. This method has the advantage over microscopy that I was able to measure and analyse a much larger number of cells. Data analysis using the software FlowJo revealed that the cells for both, WT and TMBIM5 KO occurred in two distinct populations differing in size and granularity. To avoid missing an effect in one of them, I quantified the mean fluorescent intensity (MFI) for each population separately. Besides a marginal difference between the two populations, there was no difference between WT and TMBIM5 KO for either of them (Fig. 8E). Hence, the reduced uptake does not seem to be caused by an increased preload.

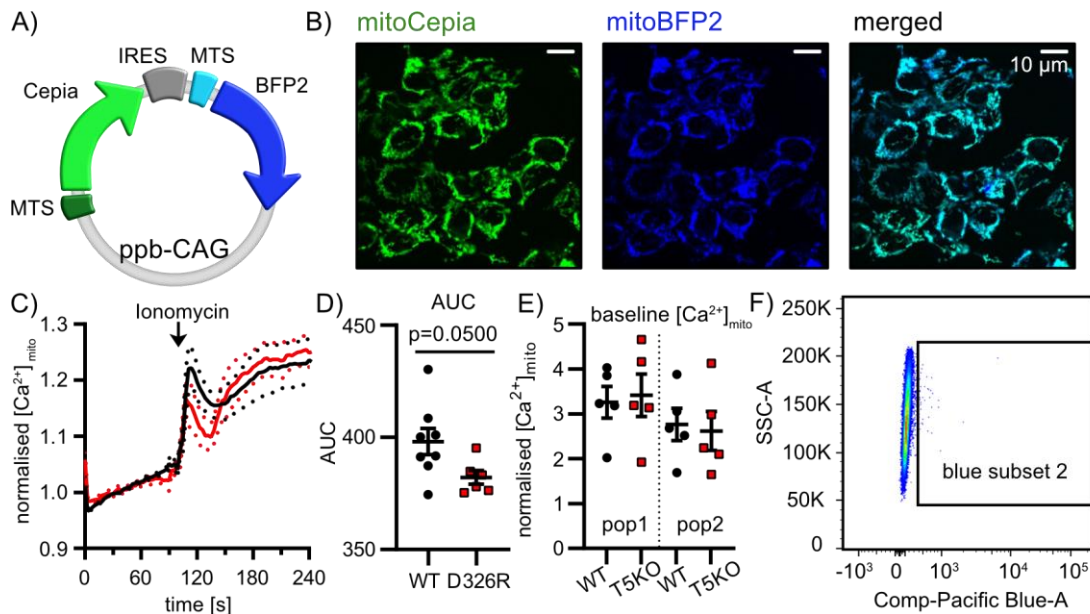


**Figure 8: Ionomycin-induced mitochondrial  $\text{Ca}^{2+}$  uptake is reduced in HAP1 TMBIM5 KO cells.**

**A)** Graphical depiction of the transfected plasmid pPB-CAG-HA-mtCepia-HA-IRES-mtBFP2. MTS = mitochondrial targeting sequence, IRES = internal ribosome entry site; **B)** Live HAP1 cells transiently expressing mitochondrially-targeted Cepia ( $\text{Ca}^{2+}$  sensor) and BFP (control) were imaged using a spinning disc confocal microscope. Exemplary images. **C)** Cells were imaged over 5 min at  $37^\circ\text{C}$  and 5%  $\text{CO}_2$ .  $1 \mu\text{M}$  Ionomycin was added at the indicated time point. Cepia (Ex/Em: 488/510 nm) signal was normalised to BFP signal (Ex/Em: 399/454 nm) and to the individual baseline value. **D)** Quantification of the area under the curve (AUC). Unpaired t-test. **E)** Basic  $[\text{Ca}^{2+}]_{\text{mito}}$  did not differ in WT and TMBIM5 KO cells. Untreated Cepia-BFP-expressing cells were analysed using flow cytometry. In each line, two distinct populations were detected which were analysed individually (1 and 2). Cepia fluorescence was normalised to the BFP signal. Unpaired t-tests. **F)** Exemplary gating on one of the blue fluorescent populations demonstrating the low transfection efficiency.

Data are shown as mean  $\pm$  SEM. Differences are not significant if not indicated otherwise, n.s.:  $p \geq 0.05$ ;

It should be considered though that the transfection efficiency was consistently very low as shown in the exemplary gating in Fig. 8F). As it was a ratiometric approach, theoretically, this should not affect the result. However, there may have happened a pre-selection for healthy cells that survived the transfection which could indeed influence the outcome. A different approach should be considered to verify this result before an increased mitochondrial  $\text{Ca}^{2+}$  preload is ultimately excluded as a possible cause for the decrease in  $\text{Ca}^{2+}$  uptake.

The second potential explanation mentioned above is a reduction in mitochondrial membrane potential. Under healthy conditions, the proton gradient at the inner membrane generates a negative charge at the matrix side of the membrane which drives  $\text{Ca}^{2+}$  influx even against the concentration gradient. Consequently, lower membrane

potential means lower inwards driving force for  $\text{Ca}^{2+}$ . This effect may explain the diminished mitochondrial  $\text{Ca}^{2+}$  influx in the HAP1 TMBIM5 KO HAP1 cells. Indeed, published results from our group show a reduction in membrane potential in the TMBIM5 deficient cells (Seitaj et al., 2020). However, there is evidence from unpublished data that the reduction in  $\text{Ca}^{2+}$  uptake is independent of membrane potential. A cooperation group of our lab conducted electrophysiological recordings with so-called mitoplasts (isolated mitochondria without outer membrane) in a patch-clamp setup where the membrane potential is controlled. Nevertheless, they still found a dramatic decrease in uptake indicating that it is not only the membrane potential that causes the changes. That leaves the third option: an impaired uptake. I, therefore, sought to explore the effect of TMBIM5 KO on the Mitochondrial Calcium Uniporter complex (mtCU) which is the only known  $\text{Ca}^{2+}$  influx pathway to date.

### 5.3. The loss of TMBIM5 affects the Mitochondrial Calcium Uniporter complex

The Mitochondrial Calcium Uniporter (MCU) is the pore-forming and core unit of the mtCU that mediates  $\text{Ca}^{2+}$  influx (Baughman et al., 2011; Stefani et al., 2011). It is tightly regulated by MICU1 and its homolog MICU2 which act as gatekeepers and enhancers (Mallilankaraman et al., 2012b; Patron et al., 2014).

Analysis of protein expression levels in HAP1 cells via immunoblotting revealed that a loss of TMBIM5 results in a downregulation of MCU whereas the expression of MICU1 and MICU2 was not affected (Fig. 9A). The fact that MICU1 and MICU2 expression was unaltered rules out that the reduction was due to a general reduction of mitochondrial protein. The partial loss of MCU might explain the diminished  $\text{Ca}^{2+}$  uptake for two reasons: Not only is the abundance of channels reduced but as a consequence, the ratio of MICU1:MCU and MICU2:MCU presumably also increases. Paillard et al. (Paillard et al., 2017) discovered that in mouse tissue the stoichiometry of the mtCU mediates tissue-specific differences in  $\text{Ca}^{2+}$  sensitivity and uptake. A low MICU1:MCU ratio means less gatekeeping and a low threshold to  $\text{Ca}^{2+}$  whereas a higher ratio leads to the opposite: a higher  $\text{Ca}^{2+}$  threshold. This effect could further decrease  $\text{Ca}^{2+}$  uptake as an indirect effect of TMBIM5 KO. Yet, it remains unclear why MCU is downregulated in the absence of TMBIM5. It could indicate that

TMBIM5 is an outwards pathway and MCU is degraded to compensate for the lack of efflux and to prevent mitochondrial  $\text{Ca}^{2+}$  overload. Another explanation could be that TMBIM5 directly interacts with MCU and stabilises the protein.

To test this and to study the interplay of TMBIM5 and the mtCU components not only in absence of TMBIM5 but also vice versa we obtained MCU KO, MICU1 KO and MICU2 KO HEK 293T cells as a kind gift from Dr J. Kevin Foskett (University of Pennsylvania, USA). The verification of the respective protein knockout is shown in Fig. 9B). The antibody staining against MICU1 and MCU appeared as a double band in the WT cells of which in both cases only the upper band seemed to be specific as it is lost in the respective KOs.

In both WT cells lines, HAP1 and HEK 293T, TMBIM5 did not seem to reside in the mtCU complex with MCU which appears at a height of approximately 480 kDa on a BN PAGE (Baughman et al., 2011) (Fig. 9C). In line with this, the absence of TMBIM5 or MCU did not affect the complex formation of the respective other protein. Accordingly, it is unlikely that TMBIM5 directly interacts with MCU. Nevertheless, there is an evident link between TMBIM5 and the mtCU because I again observed changes in expression. In the absence of MCU and MICU1, TMBIM5 was upregulated, while it was not altered in the MICU2 KO cells (Fig. 9D). This was a surprising finding as it would indicate that TMBIM5 can somehow rescue or balance the lack of MCU and MICU1 which is conflicting with the downregulation of MCU in the TMBIM5 KO cells. HAP1 cells are a fast-growing, near-haploid cell line which means that they are an ideal target for Crispr/Cas9 gene knockout as only one allele needs to be modified. On the downside, however, their genome is fairly unstable and they tend to become diploid over time (Beigl et al., 2020) making them less attractive and less accepted in the research field. To exclude that the observed changes in MCU expression are specific to this cell line, we obtained HEK 293 WT and TMBIM5 KO cells as a kind gift from Dr Geert Bultynck (Katholieke Universiteit Leuven, Belgium). The complete loss of TMBIM5 was verified by immunoblotting, as shown in Fig. 9E) and indeed, the reduction of MCU in the TMBIM5 background was reproduced, making it a very robust finding (Fig. 9F, left). Similarly, the expression levels of MICU1 and MICU2 were not altered (Fig. 9F).

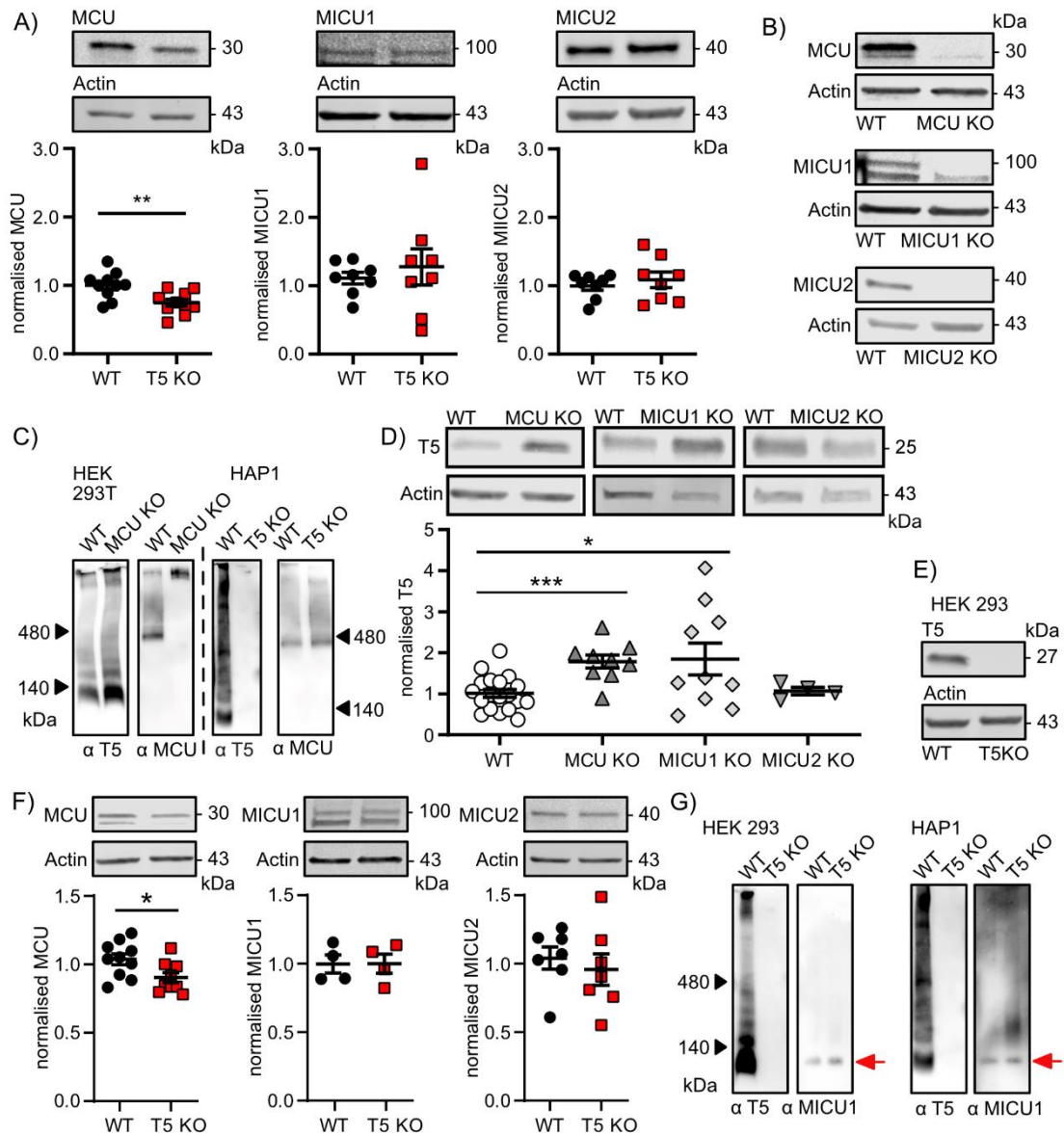


**Figure 9: The loss of TMBIM5 affects the Mitochondrial Calcium Uniporter complex (mtCU) proteins.**  
**A)** The expression of the Mitochondrial Calcium Uniporter (MCU) was reduced in HAP1 TMBIM5 KO cells compared to the WT whereas its regulators, the Mitochondrial Calcium Uptake 1 and 2 (MICU1/MICU2) were not affected. Signal was normalised to WT after normalisation to loading control (actin) and overall mean per blot. Unpaired t-test. **B)** Exemplary western blots for cell line verification of MCU/MICU1/MICU2 HEK293T KO cells. **C)** TMBIM5 does not seem to be a part of the mtCU with MCU as core protein. TMBIM5 did not run on the same height in BN PAGE in both cell lines, HEK293T and HAP1, and its complex was not altered when MCU was not present in HEK 293T MCU KO cells. The same was true for the MCU-containing complex in absence of TMBIM5 in HAP1 T5 KO cells. **D)** TMBIM5 expression was upregulated in MCU KO and MICU1 KO HEK293T cells and not changed in MICU2 KO compared to WT. Signal was normalised to WT after normalisation to loading control and overall mean per blot. Unpaired t-tests. **E)** Exemplary blot for the verification of the TMBIM5 knockout in HEK293 cells. **F)** In line with the expression data for HAP1 cells, also in HEK293 TMBIM5 KO cells MCU was downregulated whereas MICU1/2 were unchanged. The staining signal was normalised to WT after normalisation to loading control and overall mean per blot. Unpaired t-test. **G)** Interestingly, analysis of complex formation via BN PAGE showed a MICU1-band at the same height as TMBIM5, as indicated by

the red arrows, albeit this was unvaried in absence of TMBIM5. This too was observed in both, HAP1 and HEK293 cells.

Data are shown as mean  $\pm$  SEM. Differences are not significant if not indicated otherwise, n.s.:  $p \geq 0.05$ , \*  $p < 0.05$ , \*\*  $p < 0.005$ , \*\*\*  $p < 0.001$ ;

Interestingly, I observed in both cell lines, HAP1 and HEK 293, that MICU1 and the most pronounced band for TMBIM5 run at the same height on a BN PAGE, at approximately 100–120 kDa (Fig. 9G), pointing towards a possible direct contact between the two proteins. As TMBIM5 has a protein size of  $\sim 25$  kDa and MICU1 is commonly observed as a homodimer ( $\sim 100$  kDa) or in a heterodimer with MICU2 of  $\sim 95$  kDa (Patron et al., 2014), this would fit the observed complex size. Yet, it is hard to explain that there was no band at all stained against MICU1 at the expected height of  $\sim 480$  kDa where the mtCU is detected. Moreover, to date MICU1 and TMBIM5 are not listed as interaction partners in any of the available, large interactome databases (The Human Reference Protein Interactome mapping project (HuRI), String, BioGrid) and several attempts in our lab to co-immunoprecipitate the two proteins failed.

We, therefore, moved on to looking for other possible interaction partners of TMBIM5 featuring the ability to sense  $\text{Ca}^{2+}$ .

#### 5.4. TMBIM5 might interact with the EF-hand-containing protein LETM1

Another EF-hand containing protein at the inner mitochondrial membrane and, thus, a promising candidate for an interactor of TMBIM5 is the Leucine Zipper-EF-hand-containing transmembrane protein 1, LETM1. Indeed, unpublished data from yeast studies by our cooperation partner Dr Karin Nowikovsky (VU Vienna, Austria) suggested a possible interaction between TMBIM5 and LETM1. LETM1 is an ion transporter in the inner mitochondrial membrane that is crucial for the maintenance of osmotic balance (Austin and Nowikovsky, 2019) by importing  $\text{H}^+$  in exchange for cations. Yet, it is controversial, whether it exports  $\text{K}^+$  (Nowikovsky et al., 2004) or  $\text{Ca}^{2+}$  (Jiang et al., 2009; Tsai et al., 2014). I investigated a possible interaction of the two proteins by conducting a proximity ligation assay (PLA). Fixed HEK 293 cells were stained with primary antibodies from two different species. The secondary antibodies were tagged with oligonucleotide probes that were

ligated in the next step if the distance between the two proteins was short enough (<40 nm)(Alam, 2018). The ligated probes served as a template for a polymerase that amplified the sequence and fluorescence-labelled oligos in the amplification buffer attached to the amplicon. Thereby, every red punctum detected by confocal microscopy represented the proximity of LETM1 and TMBIM.

Initially, I verified the correct and specific binding of the two primary antibodies against LETM1 and TMBIM5 by common immunocytochemistry. The exemplary images in Fig. 10A) show the mitochondrial localisation of both proteins and their colocalisation, TMBIM5 in green and LETM1 in magenta. Colocalisation appears white in the merged image. The nuclei were stained with DAPI and are illustrated in blue. As a quality control for the PLA puncta, I used a fluorescently labelled primary antibody specific to TOM20, another mitochondrial protein, to verify mitochondrial localisation of the puncta. Exemplary images of the puncta (magenta) in untreated WT cells and their overlapping with the TOM20-staining (green) are shown in Fig. 10B). As in A), the nuclei are shown in blue and were stained with DAPI and in the merged image, the white spots represent an overlap of magenta and green, i.e. mitochondrial localisation of the puncta.

To ensure that the PLA amplification product specifically showed the interaction of the two proteins, I performed two negative controls. First, I used the same primary antibodies in TMBIM5 KO cells and second, I combined the LETM1 antibody with an anti-TOM20 antibody. TOM20 is part of a complex at the outer mitochondrial membrane and is involved in the protein import into mitochondria (Ahting et al., 1999). Consequently, it is not expected to interact with the inner membrane protein LETM1. Both negative controls should not contain a substantial number of puncta which was observed and quantified and is shown in Fig. 10C). In untreated WT cells, a significantly higher number of puncta was detected indicating that TMBIM5 and LETM1 interact (Fig. 10C). Inspired by Gottschalk et al. (Gottschalk et al., 2019), who de-energised mitochondria by incubation with antimycin A and oligomycin, I performed the same treatment prior to fixation and PLA to test whether the contact of TMBIM5 and LETM1 is dependent on the membrane potential. In fact, the two proteins seemed to interact only at basal conditions and dissociated once the mitochondrial membrane potential was dissipated (Fig. 10C). A graphical representation of the different conditions and their outcome is shown in Fig. 10D).

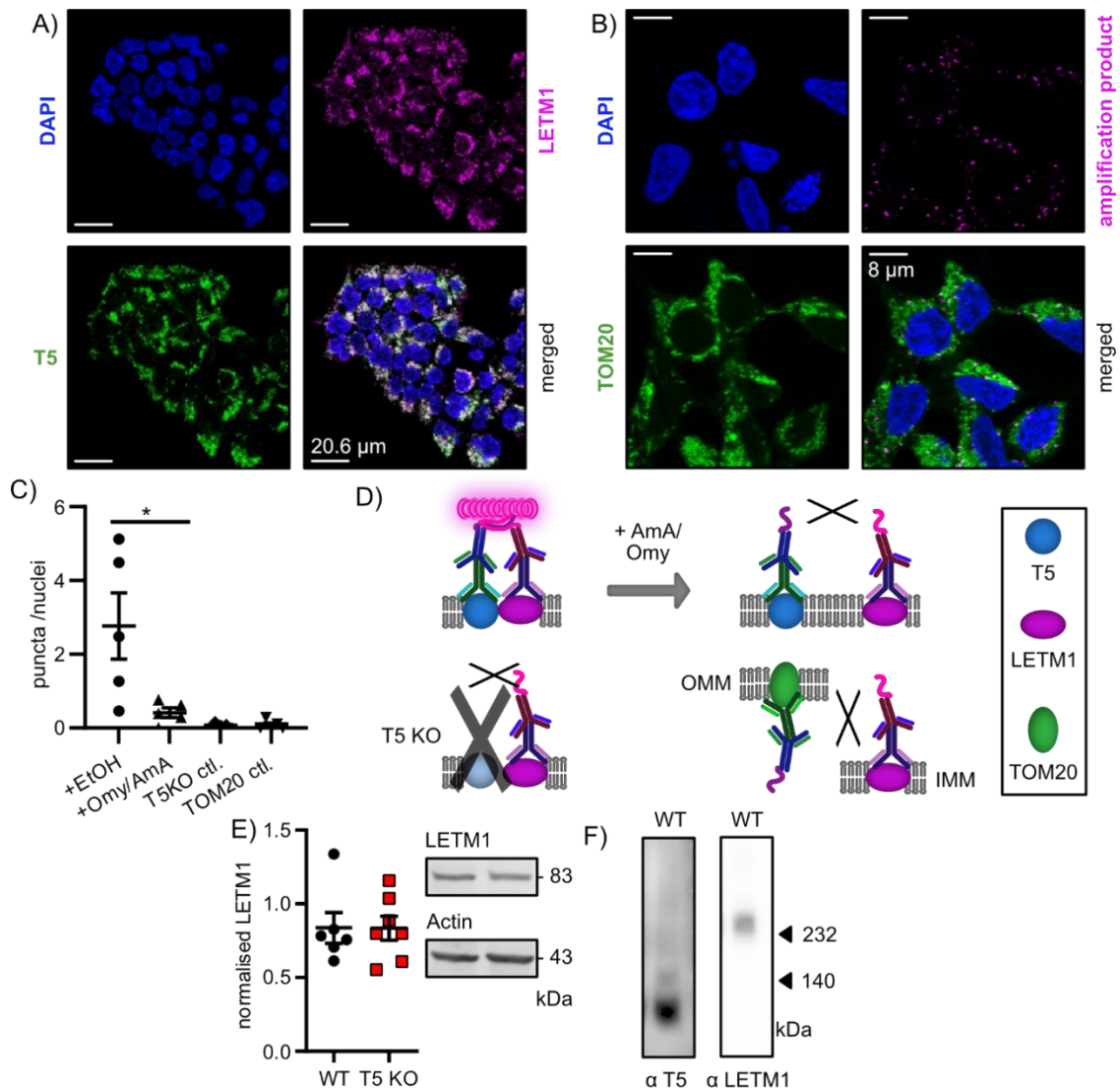


**Figure 10: TMBIM5 might interact with the Leucine Zipper-EF-hand-containing transmembrane protein 1 (LETM1).**

TMBIM5 and LETM1 reside in close proximity at basal conditions and dissociate when mitochondria are de-energised. A) Verification of the two primary antibodies against TMBIM5 (green) and LETM1 (magenta) showing the mitochondrial localisation and proximity of both proteins in HEK293 cells. DAPI-stained nuclei in blue. B) A proximity ligation assay (PLA) was performed using the two primary antibodies rabbit-anti-TMBIM5 and mouse-anti-LETM1. Proximity enables ligation and amplification of the oligonucleotides linked to the secondary antibodies. The amplification product appears as puncta (magenta). The mitochondria were stained with a fluorescence-labelled primary antibody against the mitochondrial import receptor subunit TOM20 (green) to prove mitochondrial localisation of the amplification product (magenta). DAPI-stained nuclei in blue. C) Cells were treated with either 4  $\mu\text{M}$  antimycin A (AmA) and 2  $\mu\text{M}$  Oligomycin (Omy) or with ethanol (EtOH) as vehicle control for 10 min followed by fixation and the PLA. TMBIM5 KO cells and the combination of LETM1 and TOM20 antibodies were used as negative controls (ctl.). Data are shown as mean per experiment  $\pm$  SEM, 3-7 images were analysed per experiment, unpaired t-test. D) Graphical depiction of the PLA and its results for TMBIM5, LETM1 and TOM20. E) Protein expression of LETM1 was not altered in TMBIM5 KO cells, data are shown as mean  $\pm$  SEM, unpaired t-test. F) T5 and LETM1 do not reside in the same protein complex as shown via BN PAGE.

Differences are not significant if not indicated otherwise, n.s.  $p \geq 0.05$ , \*  $p < 0.05$ ;

This finding raised the question of whether the expression of LETM1 is affected by the knockout of TMBIM5. I revised this by quantifying the protein abundance via western blotting and did not observe any alteration in the amount of LETM1 in the KO cells (Fig. 10E). Thus, the interaction with TMBIM5 does not seem to be indispensable for LETM1 function or stabilisation. Similarly, TMBIM5 and LETM1 did not appear at the same height on a BN PAGE indicating that they do not form a permanent protein complex together.

In summary, TMBIM5 and LETM1 seemed to interact or at least reside in close proximity under basal conditions. Dissipation of the membrane potential abrogated the contact while loss of TMBIM5 did not have an impact on LETM1 expression. The possible interaction of TMBIM5 and LETM1 is quite an intriguing finding considering that also for LETM1 and TMBIM5 no interaction is listed so far on the above-mentioned interactome databases and certainly calls for further investigation.

Nevertheless, research with immortalised cell lines implies several inevitable disadvantages. Not only do they grow in a non-natural monolayer which affects their morphology, polarity and cell-cell-contacts (Kapałczyńska et al., 2018), but they are also constantly exposed to much higher oxygen levels than in most physiological environments. This causes oxidative stress and changes in the intracellular redox system (Halliwell, 2014). Yet, even more important for our research is the so-called Crabtree effect which describes a metabolic shift from oxidative phosphorylation to predominant glycolytic energy production in cultured cells (Kok et al., 2021). Thus, we aimed to study TMBIM5 function in a more physiological setting.

### 5.5. TMBIM5 containing a point mutation in a conserved critical residue (D326R) is downregulated in primary mouse embryonic fibroblasts with mild effects on mitochondrial characteristics

To study the function of TMBIM5 *in vivo*, we generated a mouse model carrying a point mutation in the protein sequence. On the DNA level, this means an exchange of only three base pairs, from 5'-GAT-3' to 5'-CGC-3' which then leads to the integration of the alkaline arginine (R) instead of acidic aspartic acid (D) at the residue 326. This exchange was eponymous for the line named D326R. The original aspartic acid is part of the highly conserved di-aspartyl-motif which is thought to confer pH sensitivity to the channel.

Moreover, it is located in the putative channel-forming loop domain. This led us to assume that the mutation would exhibit a loss-of-function phenotype.

It was a well-reasoned, albeit quite a bold decision not to obtain a complete knockout line. As TMBIM5 seems to be somehow implicated in the formation or maintenance of the mitochondrial cristae structure and may also have multiple functions, the idea was to specifically target its channel function. By exclusively compromising a critical residue of the supposed pore domain all other functions of the protein should be conserved.

The mutated triplet in the DNA was verified via Sanger sequencing (GATC/Eurofins Genomics) in random samples and regularly determined via PCR followed by restriction enzyme digestion. As only three basepairs were exchanged, the two PCR products for WT and D326R did not differ in length. Hence, enzyme digestion was necessary to distinguish the genotypes. The mutation D326R generated a recognition sequence for the cutting of the restriction enzyme FspI which is not present in the WT DNA. Therefore, the digestion resulted in two short bands for D326R, one long band for the WT and three bands for heterozygous mice. The results for WT and D326R are shown in Fig. 11A). To examine mitochondrial hallmarks at a cellular level, I isolated primary mouse embryonic fibroblasts (pMEFs) and cultured them only for a few passages without immortalisation to avoid culture artefacts. Immunoblotting against TMBIM5 revealed that the mutated protein was downregulated in the D326R cells (Fig. 11B, left). This demonstrates that the point mutation has a drastic effect, and it suggests that the mutated protein has either completely lost its function or that it is even detrimental in its mutated form. On the other hand, it also means that the plan described above to specifically target the channel function was only partially successful. Considering the protein expression, it is rather a knockdown model which is something I had to keep in mind.

Surprisingly, the pMEFs did not show the same reduction in MCU expression as the immortalised cell lines (Fig. 11B, middle). The total amount of mitochondrial protein was also not altered which is shown by the ratio of coxIV to actin (Fig. 11B, right).

I then sought to examine the effect of the mutation and partial loss of TMBIM5 on basic mitochondrial characteristics. One of the main functions of mitochondria is to produce the energy equivalent ATP via oxidative phosphorylation. By the use of oxygen and different substrates, the electron transport system (ETS) generates a proton gradient across the

inner mitochondrial membrane which then drives the ATP synthase. I assessed the respiratory capacity and different states of activity in intact pMEFs with a high-resolution respirometer that measures cellular O<sub>2</sub> consumption. The starting level is called routine as it represents the basal respiration of the cells. I then injected oligomycin into the chambers which inhibits the ATP synthase and induced the so-called leak-state meaning that any oxygen consumed at this state cannot be used for ATP production but is necessary to compensate for proton leakage to maintain the mitochondrial membrane potential. Step-wise addition of FCCP pushes the ETS to its maximum capacity. FCCP is an ionophore that allows unhindered proton flux across the IMM while the ETS is trying to maintain the proton gradient with its maximum activity. This state is simply called ETS. In the end, rotenone and antimycin are added to block complex I and complex III, the oxygen users and main drivers of the ETS. Any remaining oxygen consumption stems from non-mitochondrial oxidative processes and is therefore called residual oxygen consumption (ROX) and subtracted from all other values. An exemplary graph for a typical measurement is shown in Fig. 11C). Analysis of the different states did not reveal any differences between WT and D326R cells (Fig. 11D), nor did the flux control ratio that depicts the proportion of routine or leak compared to the maximum capacity. The ratio of routine/leak seemed marginally, yet not significantly, higher in D326R cells (Fig. 11E). Mitochondria are highly dynamic organelles that undergo constant fission and fusion to meet cellular demands. Thus, I analysed the effect of the mutation on mitochondrial shape by staining the mitochondria in living cells with the cell-permeant cationic dye TMRM. I programmed a machine-learning software to identify tubular and fragmented mitochondrial networks as shown in Fig. 11F), TMRM in yellow, nuclei stained with DAPI in blue. The quantification did not reveal any significant difference, however, D326R cells showed a slight shift towards more fragmented mitochondria (Fig. 11G). Due to its positive charge, TMRM accumulates in the mitochondria according to their membrane potential. Therefore, the same staining was used to assess mitochondrial membrane potential as depicted in Fig. 11H). Additionally, the cells were stained with a membrane dye called CellMask™ (in red) as a marker for the total cellular area. As a proof of concept, the cells were treated with FCCP at the end of every experiment to abolish the MMP. Fig. 11I) shows the marked decrease of TMRM signal due to the loss

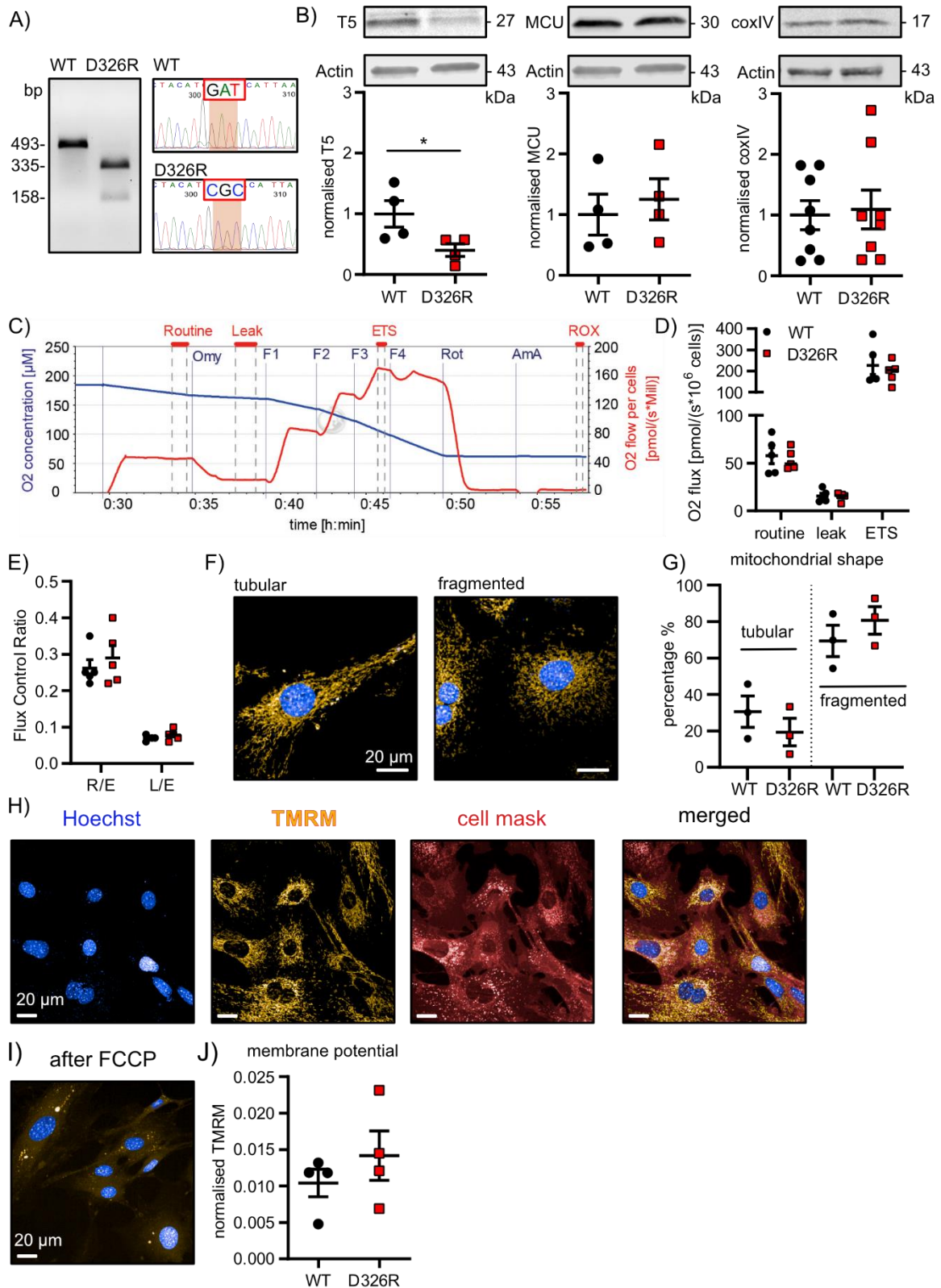


**Figure 11: Reduced expression of TMBIM5 and mild alterations in mitochondrial characteristics in primary cells from a mouse model with a mutation named D326R in the TMBIM5 loop domain.**

**A)** The D326R mutation was verified via PCR followed by restriction enzyme digestion (left) or Sanger sequencing (right). The recognition sequence for the restriction enzyme FspI (3' A-CGC-GT 5') was only present in the mutated gene. Hence, WT DNA was not cleaved and appeared as one band while the transgenic DNA was cut into two segments. **B)** Expression of the mutated TMBIM5 was reduced whereas

protein expression of MCU was not affected and also total mitochondria abundance (represented by the coxIV expression) was not altered. Normalised to WT after loading control and overall mean per blot. Unpaired t-test. **C)** Exemplary trace of a high-resolution respirometry measurement using an Oroboros O2k. Omy = oligomycin (2.5 mM), F = FCCP (titration, 0.5  $\mu$ M), Rot = rotenone (0.5  $\mu$ M), AmA = Antimycin A (2.5  $\mu$ M), added at the indicated time points. Marked in red are the four states that were used for quantification, routine, leak, ETS (= electron transport system, maximum activity) and ROX (= residual oxygen consumption). **D)** Neither of the analysed respiratory states was significantly different in WT and D326R isolated mouse embryonic fibroblasts (pMEFs). Values were normalised to cell number and ROX was subtracted. Mixed-effects analysis. **E)** Ratio of routine to ETS (R/E) or ETS to leak (E/L). Unpaired t-test. **F)** Exemplary images of the TMRM staining (yellow = tetramethylrhodamine methyl ester (TMRM), blue = Hoechst) which was used to quantify membrane potential and mitochondrial shape. A machine-learning software (Columbus) was used to distinguish tubular and fragmented mitochondrial networks as shown in the images. **G)** Quantification of mitochondrial shape. D326R fibroblasts had slightly more fragmented and less tubular mitochondria. 3-4 wells/experiment. Mean per experiment. One-way ANOVA. **H)** Exemplary images of the staining used for quantification of membrane potential and mitochondrial shape. From left to right: Blue = Hoechst, Yellow = TMRM, red = cell mask, merged, TMRM, cell mask and Hoechst. **I)** TMRM signal after addition of 2  $\mu$ M carbonyl cyanide-p-trifluoromethoxyphenylhydrazone (FCCP). FCCP is an ionophore that abolishes mitochondrial membrane potential. The loss of the TMRM signal verified its mitochondrial localisation and its sensitivity to the membrane potential. **J)** The membrane potential was slightly but not significantly increased in the D326R cells. TMRM signal was normalised to total cell area (cell mask staining), as shown in **H)**. Unpaired t-test.

All data are shown as mean  $\pm$  SEM. Differences are not significant if not indicated otherwise, n.s.  $p \geq 0.05$ , \*  $p < 0.05$ ;

of the proton gradient which makes it a reliable indicator for MMP. D326R cells exhibited a non-significant trend towards an increase in membrane potential (Fig. 11J).

Nevertheless, it is important to state that the pMEFs had some major drawbacks. I observed large differences within one culture not only in the quantified results that had a substantial variance but also on the single-cell level under the microscope. Cells differed in size and morphology and these disparities became even more severe over time which strongly limited the timeframe in which I could use the cells for analysis. In the results shown above, I only included cells between passage number two and five. Moreover, the preparation from embryos was fairly time-consuming and unpredictable in its outcome as one litter does not necessarily contain the needed homozygous genotypes (WT and D326R). All of this made working with and analysing these cells rather troublesome.

Moreover, some of the above-mentioned negative implications of cell culture remained such as increased oxidative stress and a possible adaption to the high glucose supply

(Crabtree effect). We, therefore, decided to focus on *in vivo* or *in situ* experiments to characterise the D326R mice.

## 5.6. Homozygous D326R mice show increased perinatal lethality and reduced TMBIM5 expression in all tissues

To characterise the D326R mouse line, I first assessed basic parameters such as birth rate, health, weight and lifespan to clarify whether the mutation affects the animal's well-being.

The D326R mice did not exhibit any obvious phenotypic changes, they were not sterile and were not more vulnerable to infections or diseases than the WT animals. Development and ageing were normal. This evaluation was based on close monitoring by experienced animal caretakers and regular personal inspections, including optical health checks and weight tracking. However, there was an aberrance in the Mendelian distribution. According to Mendel's first law on genetic inheritance, from a heterozygous breeding one would expect 50 % heterozygous offspring and 25 % of each homozygous genotype. In my regular genotyping of animals at the age of 3-5 weeks, I observed a shift towards more WT than homozygous mutant mice (Fig. 12A, left panel). This shift, however, was not present in the embryos (embryonic day 14, E14) that I had genotyped for the pMEF cultures described above (Fig. 12A, right panel). They did not significantly differ from the expected 25 /50 /25 % ratio. This indicated that homozygous D326R pups were more likely to die at a late embryonic stage or just after birth. This is in line with the observation of Yoshida et al. (Yoshida et al., 2006) that TMBIM5 (in this publication named Ghitm) was not detected in mouse embryonic tissue until E9.5 and thus, likely does not play a role in early embryonic development. Unfortunately, during the perinatal phase, it was not possible to define a more exact time point for the increased lethality as the mothers rapidly remove dead pups by eating them. Continuous monitoring and quantitative sacrificing of pregnant females between E14 and E21 would yield more information.

Several cohorts of animals were allowed to age to enable a lifespan analysis. Comparison of the survival curves did not reveal a significant difference (Fig. 12B). It seems plausible that the most severely affected mice die very early whereas the remaining ones develop some rescue mechanism and can cope and live with the loss of TMBIM5.

In the adult mice, I quantified the expression of TMBIM5 in various tissues via immunoblotting. According to the literature, TMBIM5 is expressed rather ubiquitously (Yoshida et al., 2006). Although the calculated protein size of TMBIM5 is 36 kDa (Li et al., 2001; Yoshida et al., 2006), the observed molecular weight of murine TMBIM5 is most frequently reported as 23-27 kDa (Yoshida et al., 2006; Oka et al., 2008). This is in line with the detected size of TMBIM5 in the cell lines. In contrast to the cellular samples, I detected several unspecific bands for TMBIM5 via immunoblotting of mouse tissue samples.

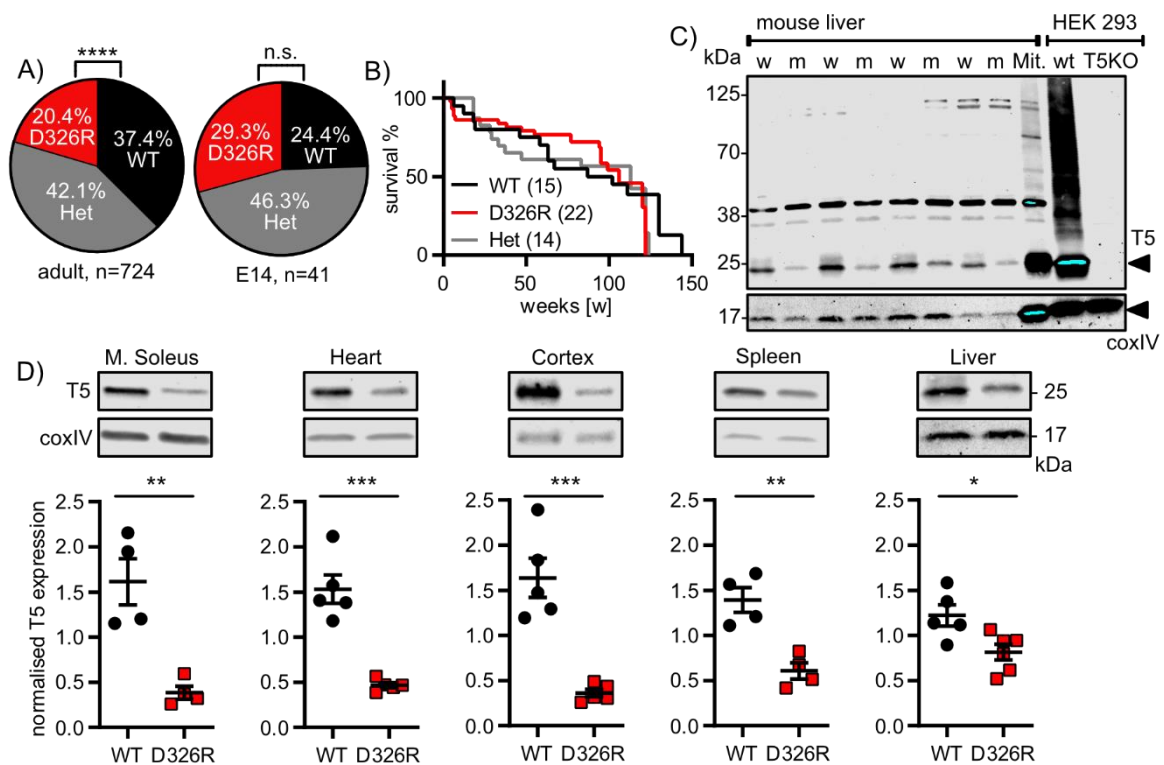


**Figure 12: Homozygous D326R mice show increased perinatal lethality and reduced TMBIM5 expression in all tissues.**

**A)** I observed an altered Mendelian distribution with a lower number of adult homozygous D326R mice than expected from heterozygous breeding. This was not the case for E14 embryos indicating increased lethality at a late embryonic state or just after birth. Chi-square test. **B)** Quantification of the lifespan of several cohorts of mice that were allowed to age. (WT/D326R/Heterozygous (Het): n = 15/22/14, as indicated in brackets) Mantel-Cox test. **C)** Antibody staining against TMBIM5 was verified for every tissue individually as some unspecific bands were detected and the pattern and quality of the staining depended on the tissue. Validation for liver tissue is shown here. The indicated band represents TMBIM5 as it is enriched in the mitochondrial fraction (Mit.), not present in the TMBIM5 KO cells and has the expected size. On the left are samples from several WT (w) and D326R (m) mice. **D)** In line with the pMEF data, the mutated TMBIM5 was strongly downregulated in all tested tissues. Normalised to loading control and overall mean per blot, Data are shown as mean  $\pm$  SEM. Unpaired t-test.

Differences are not significant if not indicated otherwise, n.s.  $p \geq 0.05$ , \*  $p < 0.05$ , \*\*  $p < 0.01$ , \*\*\*  $p < 0.001$ , \*\*\*  $p < 0.0001$ ;

Moreover, the staining pattern varied slightly with the tissue type. I, therefore, optimised the sample preparation and staining conditions for different tissues and included several controls to determine the correct band for TMBIM5. A band was accepted as TMBIM5 staining if the following criteria were fulfilled: 1. Enriched in the mitochondrial fraction of the corresponding tissue. 2. Present in the HEK WT cells. 3. Missing in the TMBIM5 KO cells. An exemplary blot (for liver) meeting all requirements is shown in Fig. 12C). For all tissues, the right band was detected at 25 kDa. Quantification of the signal revealed that in the surviving, adult D326R mice, TMBIM5 was strongly downregulated as it was found in the pMEFs (Fig. 12D). TMBIM5 signal was normalised to coxIV which rules out that differences are caused by a reduced abundance of mitochondria. The downregulation was observed in all tested tissues, albeit most pronounced in skeletal muscle, heart and cortex, which were also the tissues with the strongest expression in WT. It is arguable, though, if the immunoblot staining of samples from different tissues can be compared in a quantitative manner. Due to their hydrophobic nature, membrane proteins are notoriously tricky to stain by immunoblotting (Kaur and Bachhawat, 2009) and this is additionally hindered in tissue samples that naturally contain more contamination (e.g. fat, blood) than cell culture extracts. Hence, to achieve reliable and specific bands for TMBIM5, sample preparation and blotting had to be optimised for every tissue individually as mentioned above. This makes it probable that the signal intensity does not reflect the actual expression level and makes quantitative comparisons between tissues dubious. Yet, published qPCR data from our group (Lisak et al., 2015) show a similar trend with the lowest levels of TMBIM5 in mouse spleen and liver. Summarised, D326R mice did not appear to be grossly affected by the point mutation. Their general health, reproduction and lifespan were comparable to the WT. However, the Mendelian distribution indicated increased perinatal lethality and the protein levels of TMBIM5 were strongly reduced in all tested tissues. As mentioned above, the reduction of TMBIM5 expression in D326R mice was a central finding as it proves the significance of the conserved di-aspartyl domain. Nevertheless, it also turned the D326R mouse into a knockdown model with a point mutation in the remaining protein. Bearing this in mind, I assessed the behaviour of the mice in more detail.

## 5.7. Behaviour and coordination of the D326R mice do not differ from the WT mice.

In cooperation with the MBU of the JGU and its head Dr Konstantin Radyushkin, I studied the behaviour of the D326R mice using a set of validated tests. The experiments were conducted and recorded by Dr Radyushkin and I analysed the data.

The open field test and the elevated plus-maze are very simple and classical tests to assess free movement and explorative behaviour as an indicator for anxiety versus curiosity of the mice. In the open field setup (see Fig. 13A), mice were placed in an empty box with walls around for 7 min while the movement was recorded. As mice are prey animals, they usually feel safer close to the wall (“wall zone”) and spend more time in this zone, particularly at the beginning. On the other hand, they also have an innate curiosity and need to scout the surroundings that motivate them to move towards the more exposed middle (“centre zone”). The time spent in the centre versus the wall zone (Fig. 13B) and the latency for the first visit (not shown) are indicators of anxious/explorative behaviour. No differences were observed between WT and D326R behaviour or movement, the quantification is displayed in Fig. 13B).

A similar test on fearful behaviour is the elevated plus-maze which is a plus-shaped platform elevated off the ground on which the mice are placed (depiction in Fig. 13C). Two of the arms are enclosed by walls which makes them darker and a “safe space” for the mouse while the other arms only consist of the open platform. As for the open field, the time spent in the open or closed arms were analysed as indicators of fear or curiosity. Neither of the values differed between WT and D326R mice as shown in Fig. 13D).

A common test on coordination, motility and dexterity is the Rotarod where mice are placed on a rotating bar with acceleration speed. The readout is the time each mouse manages to hold on to the moving bar before it loses its footing and falls. This too did not reveal any difference between D326R and WT mice (Fig. 13E). To study higher brain functions a setup called “prepulse inhibition” was used. Prepulse inhibition describes the phenomenon that after a loud noise the startle reaction to a following second loud noise is reduced. This reduction is based on a process called sensorimotor gating that prevents overstimulation by filtering out unnecessary stimuli (Gómez-Nieto et al., 2020). In our setup, the startle reaction of the mice to different intensities of acoustic stimuli (70/75 and

80 dB) was derived from the moving of the platform on which they were sitting. schizophrenia and other psychiatric disorders, this adaptation was found to be impaired (Gómez-Nieto et al., 2020).

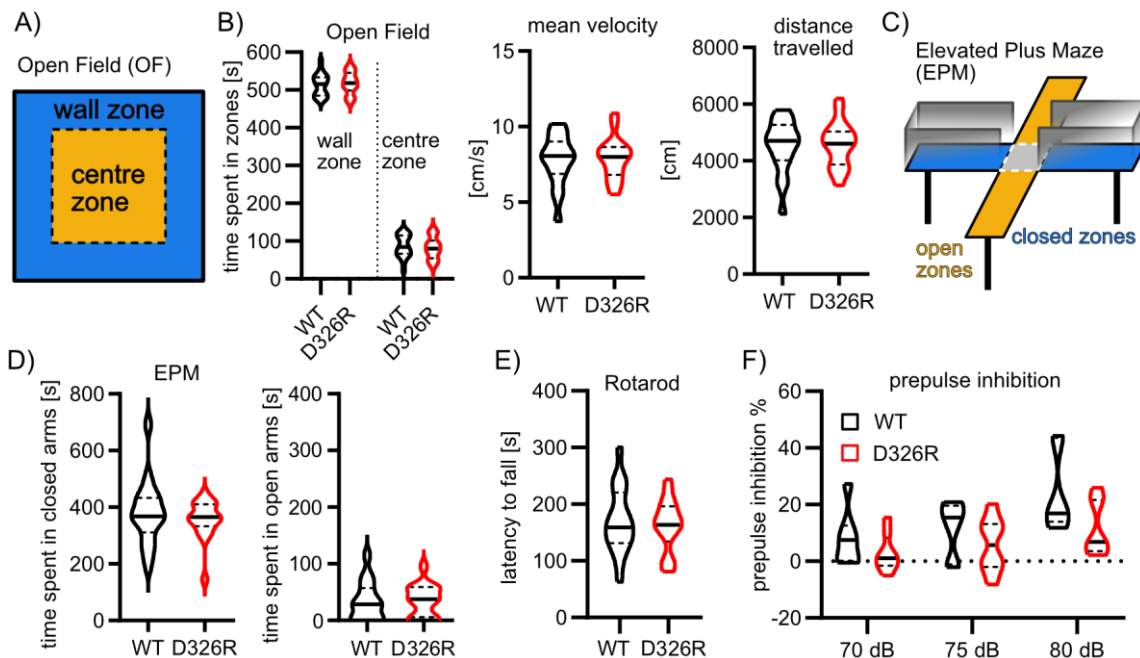


**Figure 13: The behaviour and coordination of the D326R mice do not differ from the WT mice.**

**A)** Depiction of the zones in the open field test. **B)** Mice did not show any behavioural discrepancy in the open field test, which is a test for anxiety, exploration and free movement. Mice were placed in an open arena and their movement (mean velocity and total distance travelled), as well as the time spent in different zones, were analysed. Two-way ANOVA for zones, unpaired t-test for velocity/ distance. **C)** Depiction of the elevated plus-maze. **D)** WT and D326R mice do not behave differently in the elevated plus maze (EPM). Mice were placed in a plus-maze which is elevated from the ground and has two open and two closed arms. The time spent in the different arms is used as an indicator for anxiety (left) versus explorative behaviour (right). **E)** Mice did not show impairment on the Rotarod, which is a test for coordination and motor deficits. Mice were placed on an elevated, rotating rod and the latency to fall was measured. **F)** The prepulse inhibition is indicative of sensorimotor gating and is slightly reduced in D326R mice. The mice were subjected to sudden loud noises and the startling reaction was recorded. The startling reaction to a stimulus preceded by a prepulse should be reduced. This reduction, following prepulses of different intensities, was quantified as percentual prepulse inhibition. (WT/D326R: n = 7/8) Mixed-effects analysis; **B), D), E)** Data are shown as median and quartiles (WT/ D326R: n = 17/18). **D), E)** Unpaired t-test.

Differences are not significant if not indicated otherwise, n.s.  $p \geq 0.05$ ;

In WT mice the inhibition got more pronounced with the increasing volume of the stimulus. This reaction was less evident in the D326R mice indicating an impaired adaption to external stimuli (Fig. 13F). However, the differences were not statistically significant.

Overall, the mutation did not seem to have a profound effect on the general well-being and behaviour of the mice. As TMBIM5 is a mitochondrial protein its loss should likely manifest in mitochondrial function. One of the main functions of mitochondria is the conversion of diverse substrates into the energy transducer ATP. Thus, I studied the effect of the loss of TMBIM5 on the systemic metabolism of the mice.

### 5.8. The mutation does not affect the basal systemic metabolism in mice

As mitochondrial metabolism can be modified by  $\text{Ca}^{2+}$  and TMBIM5 might be involved in mitochondrial  $\text{Ca}^{2+}$  homeostasis we assumed an indirect effect of the mutated TMBIM5 on cellular respiration in the D326R. Mitochondria are present in every single cell in an organism and provide energy for every type of tissue. Likewise, TMBIM5 is ubiquitously expressed and similarly downregulated in all tissues in the D326R mice as shown before. Hence, we hypothesised that if its loss affects mitochondrial respiration this should be a systemic effect. This led us to choose an experimental setup that measures whole-body respiration.

Simplified, cellular respiration is the use of oxygen to generate ATP while  $\text{CO}_2$  and water are produced as side products. The ratio of  $\text{O}_2$  and  $\text{CO}_2$  consumed and produced depend on the efficiency and type of respiration (aerobic versus anaerobic) and the type of substrates that are used to fuel the TCA cycle and the ETS. All these parameters, in turn, are influenced by many other factors such as substrate availability, nutritional status, activity. The fact that educt ( $\text{O}_2$ ) and product ( $\text{CO}_2$ ) of these complex processes are gases that are inhaled and exhaled makes them an ideal readout to assess metabolism in living organisms. Recording the two gases in a closed system as an indirect and non-invasive approach for studying organismic metabolism is commonly used not only in animal experiments but also for human research. In addition, this approach has the beauty that the detected respiration is truly *in vivo* without any artefacts due to narcosis or preparatory steps such as tissue extraction or mitochondrial isolation.

I measured whole-body metabolism in freely moving mice during different phases of activity and nutritional status using so-called metabolic chambers. The chambers looked similar to normal housing cages but with several special features. They were equipped with

several sensors that continuously record the following parameters: heat production, food and water intake, the movement of the mouse inside and of course the gas composition in the chambers compared to the surrounding room air. For the last 24 h, the food containers were removed to survey the metabolic reaction to food deprivation as a mitochondrial stressor.

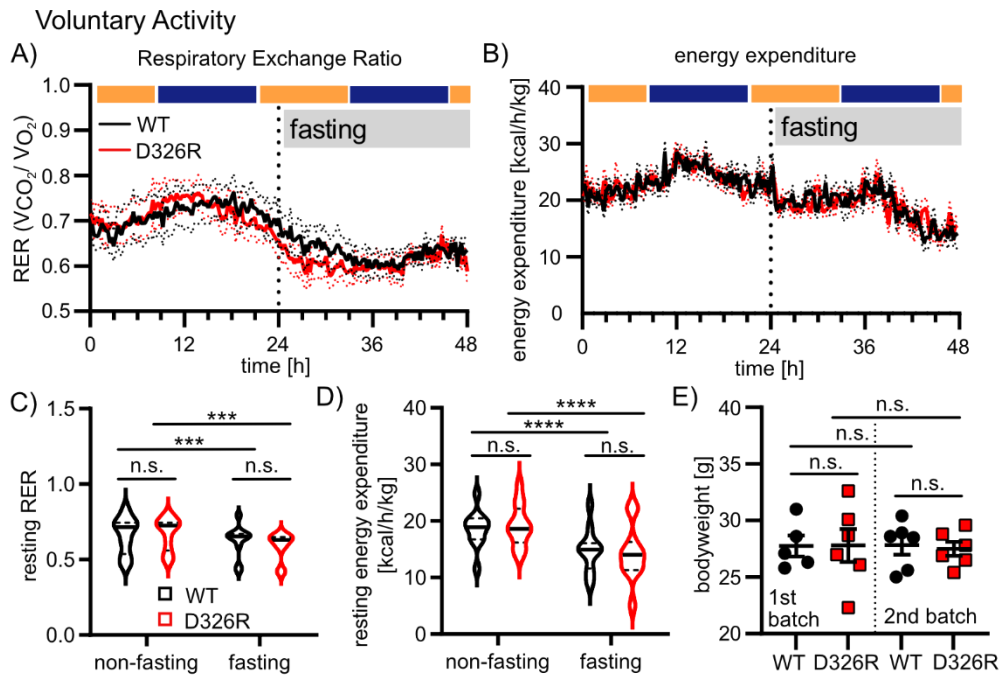


**Figure 14: The D326R mutation does not affect the basal systemic metabolism in mice.**

Mice were housed for four days in so-called metabolic chambers which allow monitoring of gas consumption/ production, food and water intake and the activity of the mice (WT/D326R: n = 11/12). Only the last 48 h were used for analysis. During the last 24 h, the mice were deprived of food (as indicated) to investigate metabolism during starvation. Yellow bars indicate light phases, blue bars dark phases. **A)** Respiratory exchange ratio (RER,  $V_{CO_2}$  produced per  $V_{O_2}$  consumed) over two days. **B)** Energy expenditure calculated by the PhenoMaster software (TSE systems) over 48 h. **A)** and **B)** Data are shown as mean  $\pm$  SEM. **C)** Lowest (= resting) RER during the non-fasting and fasting period. **D)** Energy expenditure at rest during the non-fasting and fasting period. **C)** and **D)** Data are shown as median with quartiles, mixed-effects analysis. **E)** The measurements with the metabolic chambers were conducted with two batches of mice. However, the animals were age-matched (30 w) and did not vary in body weight as shown here. Data are shown as mean  $\pm$  SEM, ordinary one-way ANOVA with multiple comparisons.

Differences are not significant if not indicated otherwise, n.s.  $p \geq 0.05$ , \*\*\*  $p < 0.001$ , \*\*\*\*  $p < 0.0001$ ;

The ratio of  $CO_2$  produced per  $O_2$  consumed is called the respiratory exchange ratio or short RER. The RER gives information about the relative contribution of the three major substrates for cellular respiration, i.e. glucose, lipids and fatty acids. An RER of 1.0 would theoretically represent the exclusive use of glucose for ATP production while the

predominant use of fatty acids would result in an RER of 0.7. An RER above 1.0 indicates anaerobic processes. Naturally, in living organisms, there is usually a mix of the different substrates.

The mean RER of 11 WT and 12 D326R mice over 48 h is shown in Fig. 14A). The yellow bars indicate light phases, the blue bars dark phases, fasting started as indicated.

The energy expenditure in [kcal/h/kg] was calculated from the heat production and the manually added weight of the mice and is depicted in Fig. 14B). Both, RER and energy expenditure (EE) clearly show the peaks of the nocturnal activity of the mice during dark cycles and the dampening effect of food deprivation. The same pattern was observed in the ambulatory activity (data not shown). However, neither substrate reliance nor energy expenditure was altered in D326R compared to WT. The same is shown by the quantifications in Fig. 14C) and D). RER and EE at rest (during light cycle and low ambulatory activity) were both significantly reduced during the fasting period but did not vary between WT and D326R.

The measurement was conducted with two age-matched batches of mice, each comprising 11-12 animals. They were first analysed separately, and the bodyweight of both cohorts was compared (Fig. 14E) which did not reveal any differences. Hence, we decided to pool the data and quantify it together as shown above.

Considering the strong downregulation of the mutated TMBIM5 and the effect on calcium handling in TMBIM5 KO cells we were fairly surprised not to see any effect on mouse metabolism. Potentially, TMBIM5 does not play a role at rest but is only active or required when there is a high energy demand and the mitochondria are stressed. Hence, I investigated metabolic parameters during and after exercise.

### 5.9. Even during exhaustive exercise, the systemic metabolism is not compromised by the point mutation in D326R mice

Mitochondria do not only sequester  $\text{Ca}^{2+}$  to buffer  $[\text{Ca}^{2+}]_{\text{cyto}}$  but beyond that  $\text{Ca}^{2+}$  is also an active regulator of mitochondrial activity.  $\text{Ca}^{2+}$  influx into the matrix activates several dehydrogenases and increases ATP synthase activity which boosts ATP production (Balaban, 2009). This way,  $\text{Ca}^{2+}$  is a crucial messenger linking cellular energy demand and ATP synthesis. This link is particularly important in tissues with a large variance in the

energy demand such as skeletal muscles and the heart. We, therefore, sought to investigate the mitochondrial performance of the D326R mice during intense exercise.

The mice were forced to run on a treadmill with 15° inclination and increasing speed until they showed signs of exhaustion. The treadmill was enclosed by an airtight chamber and connected to a gas analyser which recorded the inhaled and exhaled gases. Moreover, I drew blood samples before and after the exercise and analysed Interleukin-6 (IL-6) and lactate levels as markers for exhaustion. Lactate is a common indicator of muscular fatigue because its serum levels increase during and after exercise (Lucertini et al., 2017). Lactate also stimulates the release of IL-6 from muscle tissue during high-intensity training (Hojman et al., 2019). Circulating IL-6, in turn, induces the release of energy substrates from the liver and adipose tissue (Hojman et al., 2019). Besides this physiological function, pathologically increased serum levels of IL-6 have also been found in Parkinson's disease patients and mouse models after exhaustive exercise (Sliter et al., 2018). Sliter et al. linked this to a deficiency in mitochondrial quality control and their degradation (Sliter et al., 2018). Hence, it can also hint towards mitochondrial damage.

The experiment was conducted with two batches of mice each comprising ~ 20 animals. Unfortunately, due to external factors, it was not possible to measure the two groups at the same age. The first batch was measured at the age of 24 w whereas most of the animals in the second batch were 19 w old with four younger ones with 16 w. As depicted in Fig. 15A) there were significant weight differences between the cohorts, which is why I did not pool the data but analysed them separately. In the quantifications the first group is labelled as 24 w, the second group 16/19 w according to the respective age.

As described above, the RER was calculated as the ratio of CO<sub>2</sub> produced per O<sub>2</sub> consumed. During the first 10 min of the measurement, the mice were allowed to acclimatise to the surroundings while the treadmill was not moving. This was followed by 10 min of slow speed (8 cm/s) which was sufficient time for the mice to get accustomed to the movement and in addition, served as a baseline for slow but steady activity. The quantification of the mean RER at rest, when the treadmill was not moving (Fig. 15B) and at slow speed in (Fig. 15C) illustrates that there was indeed a variance between the two batches but no significant difference between WT and D326R. This is in line with the data from the metabolic chambers which is a good quality control for both experiments as the conditions

of the treadmill were very different to the chambers. On the one hand, the situation on the treadmill is a lot more constrained and thus, stressful for the mice which on the other hand, has the advantage that the activity of the mice can be controlled and thereby synchronised.

### Exhaustive Exercise

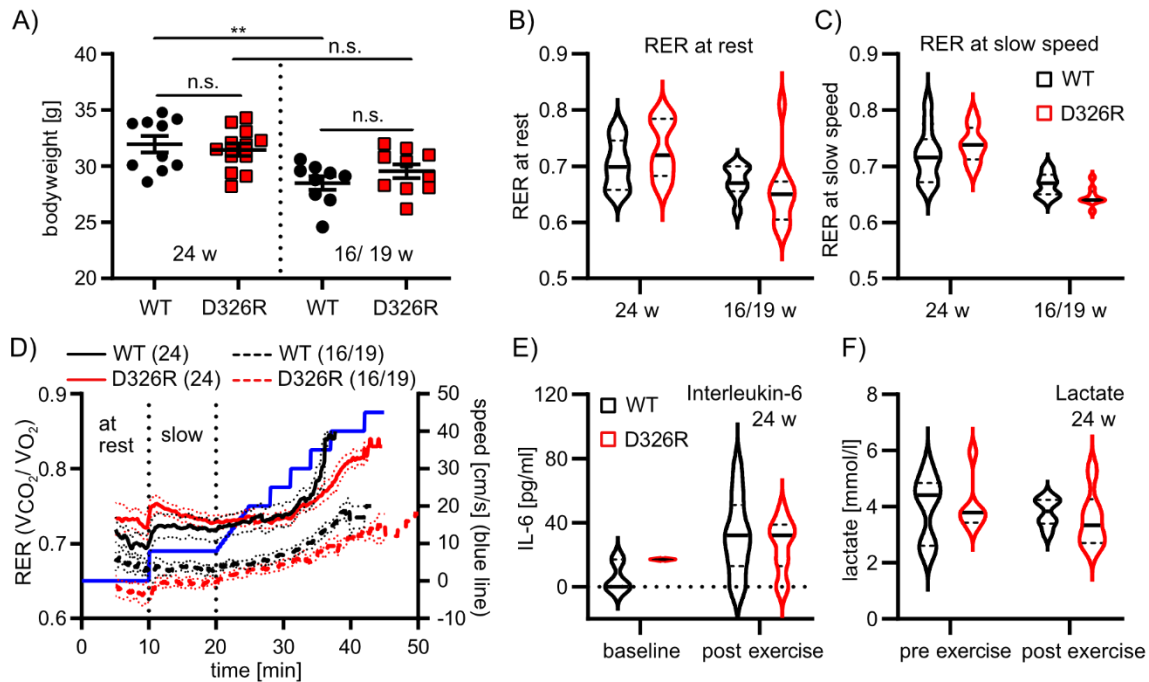


**Figure 15: The D326R mutation does not alter systemic metabolism during exhaustive exercise.**

The respiratory exchange ratio (RER) was measured while the mice were running in an airtight chamber on a treadmill that was connected to a gas analyser (panlab LE405). **A)** Two batches of mice were measured which differed in age and weight and were therefore analysed separately. Data are shown as mean  $\pm$  SEM, one-way ANOVA with multiple comparisons. **B)** and **C)** Quantification of the mean RER while the treadmill was not moving (at rest) or set to slow speed (8 cm/s). Data are shown as median with quartiles, ordinary one-way ANOVA with multiple comparisons. **D)** RER over the course of the ~40 min running protocol with the two different groups of mice (Continuous lines = 24 weeks, WT/D326R: n = 10/12; dashed lines = 16/19 weeks, WT/D326R: n = 9/10); age indicated in brackets). The speed of the treadmill belt is depicted by the blue line. Data are shown as mean  $\pm$  SEM. **E)** and **F)** In the first group (24 w) Interleukin-6 (IL-6) and lactate values in the blood were measured before and after the exercise, with no differences between WT and D326R. Data are shown as median with quartiles, unpaired t-test. **E)** IL-6 was detected in diluted serum using a Luminex<sup>®</sup>-Kit. **F)** Lactate was measured in diluted whole blood using a diagnostic instrument (Biosen C-line).

Differences are not significant if not indicated otherwise, n.s.  $p \geq 0.05$ , \*\*  $p < 0.01$ ;

After the initial accommodation phase, the speed of the treadmill was continuously increased in small steps as depicted in Fig. 15D) by the blue line (plotted to the right Y-axis). There appeared to be an age-dependent adaption of the RER as it was higher at any time

point in the older cohort. In both groups, most mice failed to continue running when the speed reached 35- 40 cm/s, albeit the younger mice were able to last a bit longer. The experiment was stopped when the number of shocks exceeded 50 or when the mouse failed to reengage with the belt with all four paws for >2s. Interestingly, in the first cohort (Fig. 15D), continuous lines) the D326R mice seemed to be more enduring than the WT mice and a similar trend was observed in the second cohort (dashed lines). However, in both cases, it was just a small fraction of the D326R group that continued running and quantification of the survival curves did not reveal any significant difference (not shown). During increasing exertion, the RER rose slightly earlier and higher in WT which corresponded with the somewhat lower endurance.

Nevertheless, this was not represented in the blood analyses. Blood samples were only collected from the mice in the first cohort making the differentiation into two groups obsolete. Moreover, it has to be mentioned that the baseline values for IL-6 were not determined in the same animals as the “post-exercise” values because the volume of blood needed to obtain a sufficient serum volume for the subsequent detection was too large for repeated withdrawals. Thus, baseline IL-6 values were determined in the blood of mice sacrificed for other experiments without any treatment. Lactate was measured in diluted whole blood with only a small volume needed which rendered it possible to compare pre- and post-exercise levels in the same mouse. The pre-exercise values were detected on the last day of the habituation protocol, two days prior to the experiment and post-exercise blood samples were drawn directly after the running.

The levels of IL-6 and lactate did not reveal any differences between WT and D326R (Fig. 15E) and F). The concentration of IL-6 in the serum increased in both groups after exercise as expected whereas the values for lactate pre- and post-exercise were similar or even reduced. This might not represent the actual status but rather be an implication of the sample collection and preparation. The pre-exercise blood samples were analysed within 1-2 h while the post-exercise samples were taken immediately after the running but then stored on ice until all treadmill measurements were finished which was up to 6 h later. In theory, the lactate should be stable in the diluted blood, yet this might not be the case and explain the reduction. Nevertheless, the time delay was similar for WT and D326R samples and should not corrupt the result.

In summary, besides a slight increase in endurance during exercise, no differences in systemic metabolism were observed, neither at low-intensity activity nor at high-intensity training. The substrate reliance of mitochondrial energy production in D326R mice was not altered by the mutation. Furthermore, physiological reactions to exhaustive exercise such as the release of IL-6 and lactate into the bloodstream were unchanged.

It deemed us possible that studying whole-body metabolism might be too large scale and that tissue-specific effects of the mutation may be masked. Hence, I changed perspective and looked more closely at tissue-specific mechanisms and functions. I focused on organs and organ systems that have a high energy demand and rely strongly on mitochondrial ATP production such as the immune system, cortex, liver, heart and skeletal muscle.

#### 5.10. Immune cells of D326R mice exhibit an impaired innate immune response

Immune cells have to be able to rapidly switch between two states: a quiescent, inactive state when no immune response is needed and a highly active state with diverse functions upon stimulation. This requires a large extent of metabolic flexibility that has to be covered by the mitochondria (Weinberg et al., 2015). Yet, mitochondria are not only the energy source for the immune response but are also involved in the maintenance and the establishment of the diverse cell types of immune cells and deliver macromolecules that are crucial for intracellular signalling (Weinberg et al., 2015). Thus, Mitochondria play a central role in an efficient immune system.

As TMBIM5 is expressed in the spleen and the mutated D326R is strongly downregulated I sought to elucidate the effect of this loss on basic immune function.

The first defence line of the mammalian immune system is the innate immune response which recognises pathogen- or damage-associated patterns (PAMP/DAMP) and reacts rapidly, but unspecifically with a range of defence or repair mechanisms (Weinberg et al., 2015). One of them is the so-called respiratory or oxidative burst which is performed by phagocytes and among them mainly neutrophils (Dahlgren C. and Karlsson A., 1991; Ciz et al., 2012). Upon encounter with a putative pathogen, neutrophils produce and release large amounts of reactive oxygen species (ROS) predominantly the superoxide anion radical which is highly toxic and efficiently eliminates invaders (Ciz et al., 2012).

In cooperation with the Centre for Thrombosis and Haemostasis (CTH) of the University Medicine Mainz and with support from Dr Stefanie Finger, I measured the oxidative burst in fresh whole blood samples from WT and D326R mice using a chemiluminescent assay. The blood samples were either collected from the Vena facialis from living animals or directly from the left ventricle from dead animals and the results were analysed separately. The respiratory burst was detected with the dye L-012 that produces luminescence upon reaction with ROS. It was induced using either zymosan A or PDBU, both reagents that mimic pathogenic structures and differ only in the time lag and in their potency. The zymosan A-induced burst is slower but has a larger amplitude.

We observed two striking features: first, the point of blood withdrawal had a major impact and second, in venous blood the burst was dramatically reduced in the D326R samples compared to WT, as shown in Fig. 16A) with the quantification of the peaks in Fig. 16B). In D326R blood samples, the burst was rather flat and only marginally higher in venous compared to ventricular blood whereas for the WT, the large peak in venous blood was nearly completely abolished in the cardiac samples. This was true for both stimulators, zymosan A and PDBU which is shown in Fig. 16C) and D).

Nevertheless, in the peripheral blood, D326R immune cells clearly had a deficiency in their capacity to produce the oxidative burst as an adequate innate immune response. This was not due to changes in the abundance of the cells producing the burst as shown in Fig. 16E). The composition of cell types was determined using a VETSCAN® HM5 haematology analyser in the same blood samples used for the burst assay.

The main source of ROS production in neutrophils is the NADPH-oxidase complex in the cell membrane (Dahlgren C. and Karlsson A., 1991) that uses NADPH as a substrate. NADPH is generated by multiple dehydrogenases, yet among them, the glucose-6-phosphate-dehydrogenase (G6PD) is the most important one as its loss cannot be compensated by the others and severely impairs all NADPH-dependent cellular processes (Stanton, 2012). One of these processes is the regeneration of glutathione. Glutathione is likely the most important antioxidant in most aerobic living species (Deponete, 2013). Its reduced form

(GSH) is a tripeptide containing glutamic acid, cysteine and glycine and can be oxidised to GSSG that consists of two GSH molecules linked by a disulfide bridge.

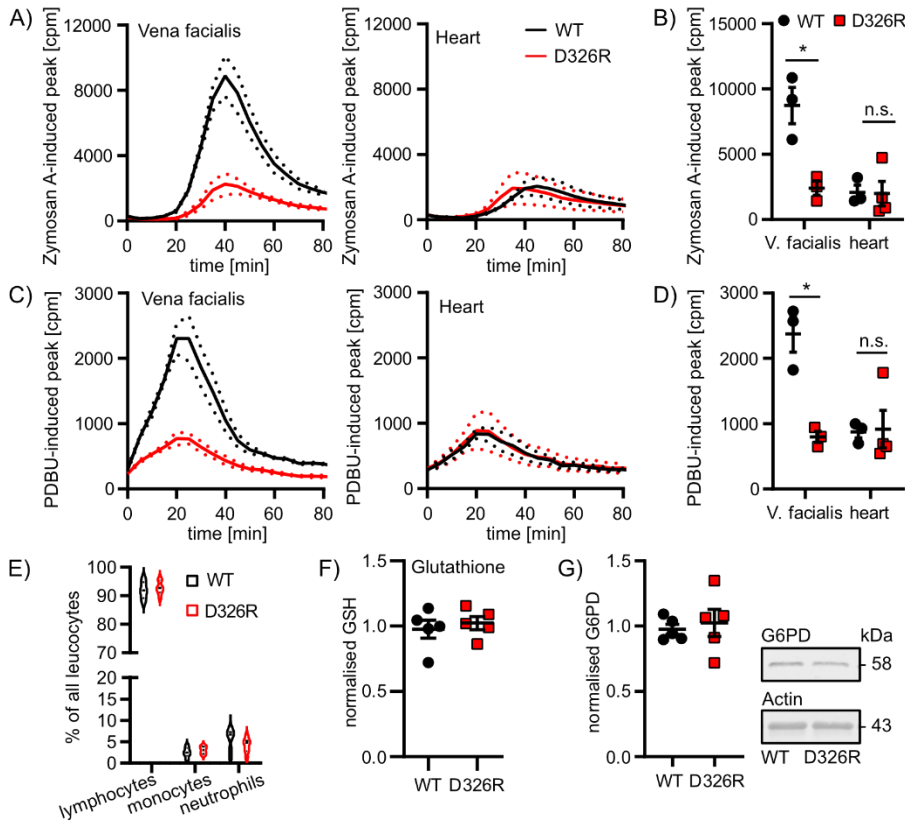


**Figure 16: Immune cells of D326R mice exhibit an impaired innate immune response.**

**A)-D)** The oxidative burst, a primary immune response by neutrophils and macrophages was measured via a luminescence assay using fresh whole blood samples drawn either from the Vena facialis (V. facialis, left) or from the heart after cervical dislocation (right). The burst was induced by the addition of 50  $\mu\text{g/ml}$  zymosan A (**A**) and (**B**) or 10  $\mu\text{M}$  phorbol-12,13-dibutyrate (PDBU) (**C**) and (**D**). The released reactive oxygen species react with the dye L-012 which then produces a chemiluminescent signal that was detected. **A)** The oxidative burst in response to zymosan A was strongly reduced in D326R animals compared to WT in deoxygenated blood from the V. facialis. Interestingly, in blood samples from the heart, it was very low for both, WT and D326R animals. **B)** Quantification of the maximum peak showed a significant reduction in the oxidative burst in the venous blood from D326R mice. Multiple unpaired t-tests with Holm-Sidak-method. **C)** and **D)** The same significant difference in blood samples from the V. facialis was observed for the PDBU-induced burst. Multiple unpaired t-tests with Holm-Sidak-method. **E)** The ratio of immune cells was not altered in either of the blood samples (V. facialis/ heart) of WT and D326R mice. The cell types were determined using a VETSCAN<sup>®</sup> HM5 haematology analyser (WT/D326R: n = 6/7). Two-way ANOVA with multiple comparisons. **F)** The amount of the cellular antioxidant glutathione (GSH) was comparable. This was measured using an enzymatic assay for which the absorbance of a side product TNB<sup>-</sup> was measured at 412 nm. Data were normalised to protein amount in cellular fraction. Unpaired t-test. **G)** The protein expression level of the Glucose-6-phosphate-dehydrogenase (G6PD) was unchanged. Normalised to WT after loading control and overall mean per blot. Unpaired t-test. **E)** shows a violin blot with median and quartiles, all other data are shown as mean  $\pm$  SEM.

Differences are not significant if not indicated otherwise, n.s.  $p \geq 0.05$ , \*  $p < 0.05$ ;

At the expense of NADPH, GSH is quickly regenerated by the glutathione reductase which maintains a stable GSH/GSSG balance in which the concentration of GSH is usually 300- to 800-fold higher (Giustarini et al., 2016) depending on the cell type and the cellular compartment. This circuit very efficiently protects cells from oxidative stress. To clarify whether the dramatic impairment in ROS production is based on alterations in the intracellular redox system and the available NADPH, I investigated the two key players, glutathione and G6PD.

It is notoriously difficult to reliably measure the concentration of GSH and GSSG separately as GSH is extremely sensitive to oxidation during the sample preparation process. Therefore, I determined the total antioxidative capacity as the GSH + GSSG abundance in spleen samples from WT and D326R mice. I did not observe a difference in the glutathione pool as depicted by the quantification in Fig. 16F). I analysed the protein expression of G6PD in isolated splenocytes from WT and D326R mice via immunoblotting which did not reveal any difference either (Fig. 16G). These findings indicated that the redox system was not affected by the point mutation in TMBIM5 and its downregulation and could not explain the drastic reduction of the oxidative burst.

In summary, the oxidative burst as part of the innate immune response in D326R mice was impaired which was not due to apparent alterations in the redox system. It may rather be an indirect consequence of dysfunctional mitochondria. As the cellular results pointed towards a malfunction of the calcium handling system, we continued studying organs with a delicate Ca<sup>2+</sup> signalling and a high energy demand such as the brain.

### 5.11. Despite considerable expression, TMBIM5 does not seem to play a major role in neuronal cells

Not only fulfils the brain the criteria of a high metabolic rate and vital calcium signalling but Yoshida et al. (Yoshida et al., 2006) reported that TMBIM5 (GHITM) is first expressed in neuronal tissue, precisely “in a nerve cord projecting from the prosencephalon to the rhombencephalon of E9.5 mice” (Yoshida et al., 2006). This led us to study protein expression and calcium handling in cortical mitochondria.

Since I detected differences in the abundance of several mitochondrial proteins in the TMBIM5 KO cell lines, I tested whether the same is reproducible in the cortical tissue from D326R mice, shown in Fig. 17A). Indeed, as in HAP1 and HEK 293 cells, there was a tendency towards a decrease in MCU expression. MICU1 and LETM1 were not significantly altered in the cell lines and neither are they in the mouse cortex, albeit LETM1 appeared to be diminished in the D326R samples. Unlike in the cells, the total OPA1 abundance was not considerably changed while the ratio of short and long isoforms again showed the same upward tendency that indicates enhanced splicing. Altogether, the protein expression pattern in the mouse cortex partially recalled the one from the cell lines. Nevertheless, these results illustrate that protein samples from mouse tissue are more heterogeneous than cellular samples and usually necessitate a larger number of biological replicates for statistical significance. Moreover, the D326R mice did not have a complete knockout of TMBIM5 as the cells had, but only a downregulation and the effect of the remaining protein is yet unclear. This too might blur differences between WT and mutation.

For the measurement of calcium handling in isolated mitochondria, I collaborated with Dr Christoph Maack, Universitätsklinikum Würzburg, Germany. Mitochondria were isolated from cortical tissue and subjected to a series of 10  $\mu\text{M}$   $\text{CaCl}_2$  injections. The  $\text{Ca}^{2+}$  concentration in the surrounding buffer was measured using the fluorescent  $\text{Ca}^{2+}$  dye Calcium Green-5N. An increase in the fluorescence, therefore, depicts a rise in buffer  $\text{Ca}^{2+}$  whereas a decrease represents mitochondrial  $\text{Ca}^{2+}$  uptake as illustrated by the arrow in Fig. 17B). Any contribution of ER  $\text{Ca}^{2+}$  uptake was excluded by the addition of thapsigargin which inhibits the ER-calcium pump SERCA. For better comparability of the results and to eliminate possible variations in the concentration of the dye, fluorescent values from each measurement were normalised to the initial value ( $F/F_0$ ). The sequential addition of small [ $\text{CaCl}_2$ ] pulses gives answers to two questions. Firstly, it allows the quantification of the  $\text{Ca}^{2+}$  uptake slope after the injection meaning how fast mitochondria can sequester  $\text{Ca}^{2+}$  and secondly, it demonstrates how much  $\text{Ca}^{2+}$  they can take up until the threshold for mPTP opening is reached. mPTP opening is observed as a deceleration of uptake followed by a sudden rise in fluorescence when  $\text{Ca}^{2+}$  is released from the mitochondria.

As seen in Fig. 17B) WT and D326R behaved very similarly in response to the  $\text{Ca}^{2+}$  pulses with uptake rates that were indistinguishable.

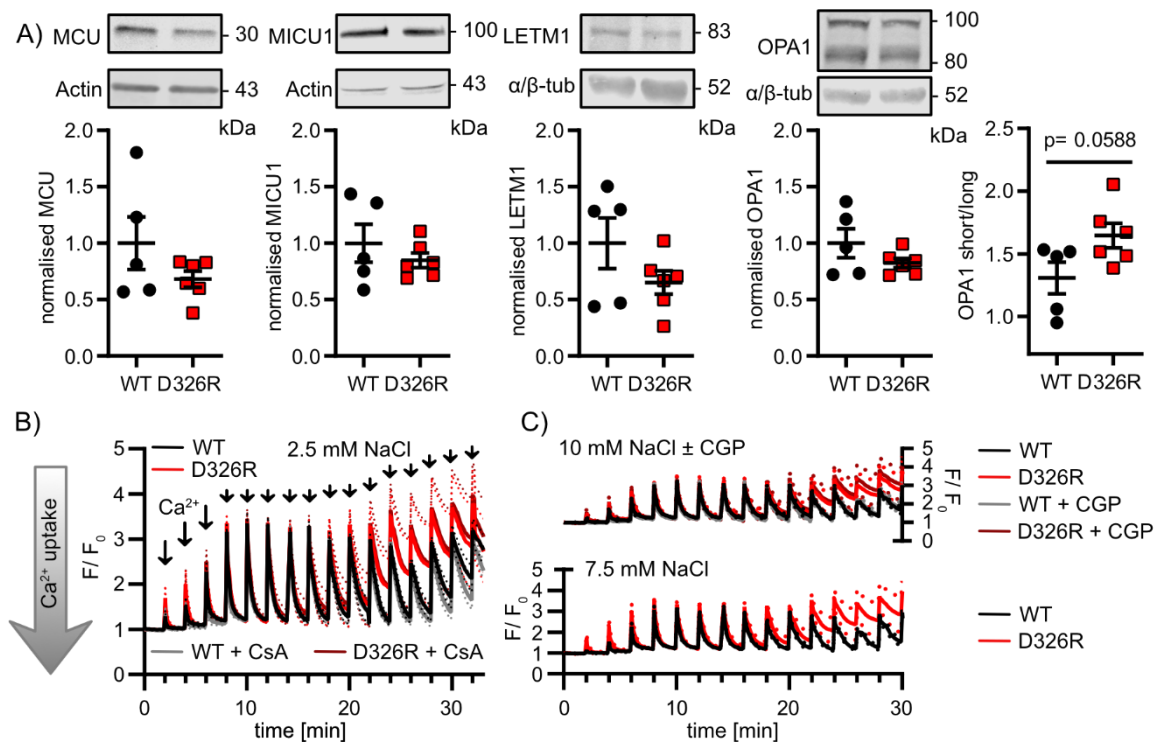


**Figure 17: TMBIM5 does not seem to play a major role in neuronal cells.**

**A)** In cortex tissue samples the protein expression of MCU, LETM1 and OPA1 seemed marginally reduced, yet the difference was not significant. MICU1 expression showed the same trend but it was even less pronounced. The ratio of short and long OPA1 isoforms was shifted towards the short isoforms, therefore, hinting at increased splicing. Values were normalised to WT after loading control and overall mean per blot. Unpaired t-test. **B)** Ca<sup>2+</sup> uptake in cortex mitochondria is normal in D326R mice. Mitochondria were isolated from the cortex and measured in assay buffer containing the fluorescent Ca<sup>2+</sup> sensor Calcium Green-5N (1  $\mu$ M, Ex/Em 488/520 nm). Ca<sup>2+</sup> uptake was detected indirectly by a decrease in fluorescence as indicated by the arrow on the left. When challenged with a series of CaCl<sub>2</sub> pulses (as indicated by the arrows, 10  $\mu$ M each), Ca<sup>2+</sup> uptake was not altered at first but seemed to slow down in D326R more than in WT mitochondria after several injections. However, this was not due to the opening of the mPTP as it was also observed in the presence of 2  $\mu$ M CsA, an inhibitor of the mPTP (WT/D326R: 7/8). **C)** The Ca<sup>2+</sup> uptake described in **B)** was measured with different Na<sup>+</sup> concentrations (7.5 mM or 10 mM as indicated) or in the presence of CGP-37157 (CGP), a blocker of the NCLX. Neither altered the Ca<sup>2+</sup> handling, indicating that it is not influenced by NCLX activity (n = 7). **B)** and **C)** Calcium Green-5N fluorescence was normalised to the initial value (F<sub>0</sub>).

Data are shown as mean  $\pm$  SEM. Differences are not significant if not indicated otherwise, n.s. p $\geq$ 0.05;

The peak height of the first few injections was gradually increasing for both genotypes as some Ca<sup>2+</sup> was immediately chelated by the EGTA present in the buffer. After 3 pulses it was saturated and the peaks always reached the same maximum height. Interestingly, after 11 cycles of Ca<sup>2+</sup> addition, the D326R traces did not reach the baseline anymore between two pulses which indicated that the uptake slowed down. Only 3-4 pulses later it was the case in the WT mitochondria. This was not due to mPTP opening though because no release

of  $\text{Ca}^{2+}$  was observed and the trace was identical in the presence of CsA, the mPTP inhibitor. Moreover, quantification of the area under the curve (not shown) did not reveal a statistically significant difference.

Overall, it was remarkable how much  $\text{Ca}^{2+}$  was sequestered in both genotypes. Usually, mPTP opening would be expected after 8-10 injections. To rule out whether the high uptake capacity was dependent on NCLX activity we tested different sodium concentrations in the buffer and added the NCLX inhibitor CGP-37157 (CGP). Higher  $\text{Na}^+$  concentrations are expected to increase NCLX activity thereby promoting the export of  $\text{Ca}^{2+}$  from the mitochondria. Surprisingly, the traces all showed an identical pattern (Fig. 17C) indicating that NCLX activity does not play a major role in the  $\text{Ca}^{2+}$  homeostasis in mouse cortical mitochondria.

Summing up, the protein expression in D326R cortical tissue showed a similar pattern as in TMBIM5 KO cells with a reduction in MCU and an increase in OPA splicing. However, the differences were not significant. Calcium uptake into mitochondria was not affected by the mutation but the mitochondria seemed to have a slightly lower buffering capacity. Yet, there was no mPTP opening detected in either genotype.

We were fairly surprised not to find a stronger phenotype considering the high expression of TMBIM5 in the WT and the central role of  $\text{Ca}^{2+}$  in the different neuronal cells. But maybe this is part of the reason: as they are relying so heavily on proper calcium homeostasis they likely evolved backup mechanisms to overcome disruptions. Moreover, the cortex is built of many different cell types, i.e. neurons, astrocytes, microglia, oligodendrocytes. They all have distinct functions and are highly specialised which I did not take into account for the analysis. Hence, I turned to investigate the liver as a more homogeneous organ.

### 5.12. Calcium homeostasis is imbalanced in liver mitochondria

Besides other functions, the liver is the central organ orchestrating whole-body metabolism. Depending on the nutritional status, it switches between anabolic and catabolic processes and balances blood glucose levels. Hepatocytes are able to store glucose in the form of glycogen or synthesise it *de novo* to supply other organs. In contrast to neuronal cells, hepatocytes are non-excitable cells meaning that they do not have to handle large and rapid  $\text{Ca}^{2+}$  influxes from the extracellular space that initiate intracellular

signalling cascades. Nevertheless, also in liver cells,  $\text{Ca}^{2+}$  signalling plays a central role, e.g. in modulating metabolism, gene expression and bile secretion (Gaspers et al., 2012), only the regulation is partially different than in excitatory cells. Cytosolic  $\text{Ca}^{2+}$  spikes can be induced by hormones such as epinephrine and norepinephrine that trigger  $\text{Ca}^{2+}$  release from the ER. These spikes often occur as oscillating waves that propagate through the cytosol and even to neighbouring cells transmitting information in a frequency-modulated manner (Gaspers et al., 2012). In mitochondria, these  $\text{Ca}^{2+}$  waves lead to increases in NADH production, ETS activity and membrane potential (Gaspers et al., 2012). All this results in accelerated ATP production to meet the current cellular demand. Considering the critical role of  $\text{Ca}^{2+}$  on liver metabolism, it is not surprising that mitochondrial dysfunction was found to be involved in metabolic pathologies such as obesity and fatty liver diseases (Arruda et al., 2014; Simões et al., 2018). Hence, I investigated the effect of the point mutation D326R on mouse liver mitochondria.

As for the cortex, I first quantified the protein expression in liver tissue and was very surprised to find that MCU abundance was higher in D326R than in WT (Fig. 18A, left). This was the opposite of both cell lines and mouse cortex. The total OPA1 expression was not changed whereas the ratio of short and long variants again pointed towards increased splicing as observed before (Fig. 18A, right).

Intrigued by the high MCU expression, I investigated mitochondrial swelling behaviour. Mitochondrial swelling describes a sudden matrix volume increase due to the influx of  $\text{H}_2\text{O}$ . This can be caused by a number of events *in vivo* and *in vitro* one of them being  $\text{Ca}^{2+}$ -overload (Kaasik et al., 2007). Following  $\text{Ca}^{2+}$ -induced mPTP opening, ions and small molecules can freely cross the IMM and the membrane potential is dissipated, leading to mitochondrial swelling (Kaasik et al., 2007). Due to changes in light scattering property, this process can be detected as a decrease in optical density/absorbance at 540 nm in a suspension of isolated mitochondria. A rise in absorbance marks mitochondrial shrinking as depicted in Fig. 18B). Swelling was induced by the injection of 200  $\mu\text{M}$   $\text{CaCl}_2$ . Cyclosporin A (CsA) is an inhibitor of the mPTP and served as control. The absorbance was normalised to the initial value to rule out inaccuracies in the determination of protein concentration (BCA assay). As shown in Fig. 18C), the rate of swelling was slightly yet not significantly reduced in D326R mitochondria.

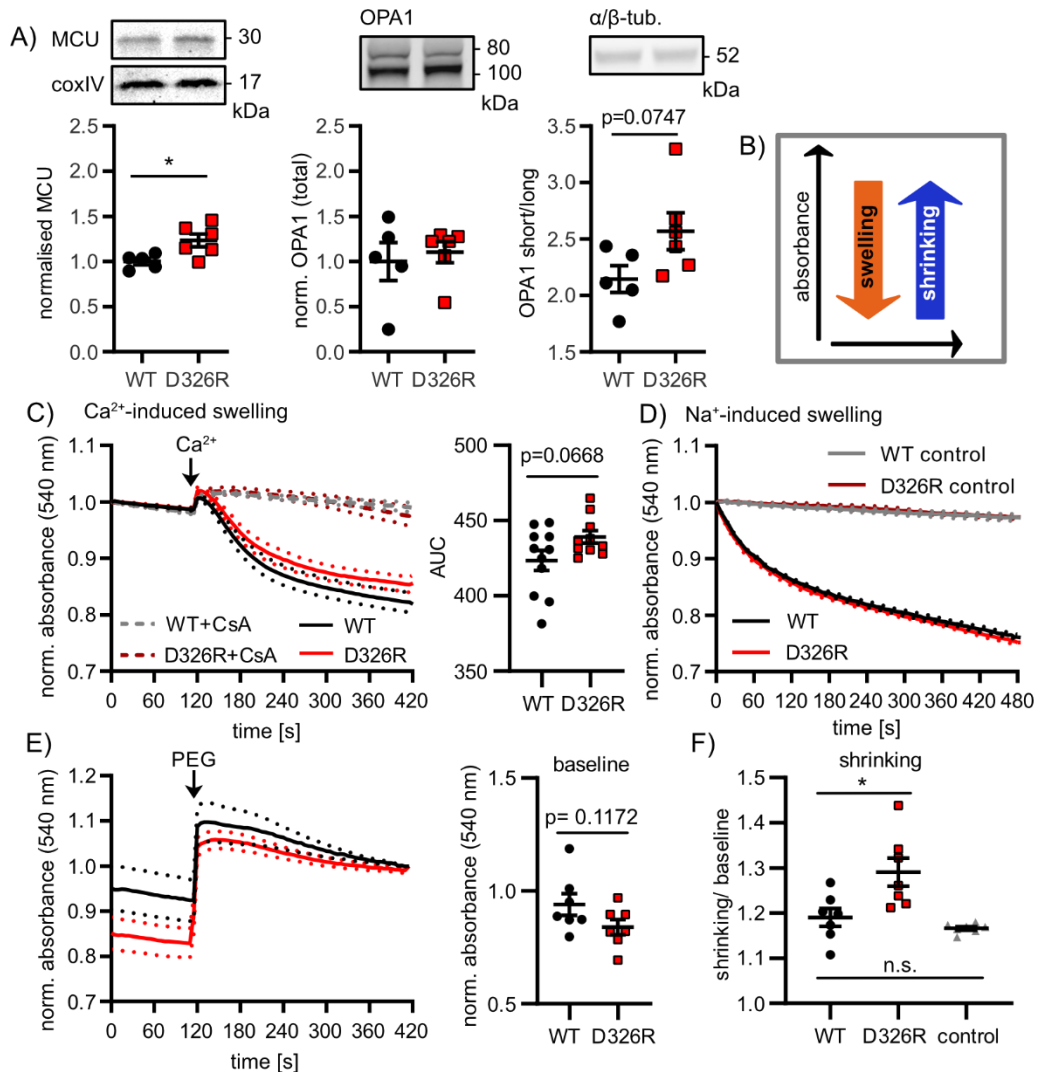


**Figure 18: Calcium homeostasis is imbalanced in liver mitochondria.**

**A)** Expression of MCU was increased in D326R liver mitochondria while abundance and processing of OPA1 were not altered. Values were normalised to WT after loading control and overall mean per blot. Unpaired t-test. **B)** Graphical depiction of mitochondrial swelling/shrinking measured as a change in absorbance. **C)** D326R mitochondria exhibit slightly reduced  $\text{Ca}^{2+}$ -induced swelling. Liver mitochondria were isolated and absorbance of the suspension was measured at 540 nm. A reduction in optical density marks increased mitochondrial swelling and vice versa. 200  $\mu\text{M}$   $\text{CaCl}_2$  was injected at the indicated time point to induce  $\text{Ca}^{2+}$  overload and mPTP opening. Inhibition of mitochondrial permeability transition (mPTP) with 2  $\mu\text{M}$  cyclosporin A (CsA) served as control. Values were normalised to the initial absorbance. Quantification of the area under the curve (AUC) on the right (WT/D326R:  $n = 11$ ). Unpaired t-test. **D)**  $\text{Na}^+$ -induced swelling did not differ between WT and D326R. The mitochondria were de-energised with 5  $\mu\text{M}$  antimycin A (AmA, inhibitor of complex III of the ETS) and resuspended in sodium acetate-based buffer and the swelling was immediately recorded. Acidification of the matrix led to  $\text{Na}^+$  influx and swelling. Resuspension in isolation buffer served as control. Absorbance was measured at 540 nm and normalised to the initial value (WT/D326R/controls:  $n = 6/5/4$ ). **E)** D326R liver mitochondria showed a larger delta in absorbance following osmotic shrinking with polyethylene glycol (PEG, added where indicated). Values were normalised to the last values after PEG-addition. The quantification shows the baseline absorbance. (WT/D326R:  $n = 7$ ). **F)** The ratio of absorbance after/before shrinking is increased in D326R mitochondria.

All data are shown as mean  $\pm$  SEM and analysed using unpaired t-test; n.s.  $p \geq 0.05$ , \*  $p < 0.05$ ;

One could argue though that the observed aberrance may not be  $\text{Ca}^{2+}$ -specific but may only be the manifestation of poor mitochondrial health in general.

To rule this out, I measured mitochondrial swelling induced by sodium acetate (NaOAc). The acetic acid diffuses into the mitochondria and causes acidification of the matrix which in turn leads to  $\text{Na}^+$  and  $\text{H}_2\text{O}$  uptake and swelling. This is called passive swelling because mitochondria are de-energised before by incubation with the complex III blocker Antimycin A. Mitochondria that were resuspended in isolation buffer do not exhibit any swelling and served as a control. As seen in Fig. 18D), there was no difference in the  $\text{Na}^+$  swelling between WT and D326R suggesting that the differences described above were indeed  $\text{Ca}^{2+}$ -dependent. We hypothesised that the mitochondria were already pre-swollen due to elevated basal  $\text{Ca}^{2+}$  content. We tested this assumption via a similar setup but instead of  $\text{CaCl}_2$ , polyethylene glycol (PEG) was added which osmotically shrinks the mitochondria to their minimum size (Luongo et al., 2017). To be able to compare the starting baseline, I normalised the measured absorbance to the value after PEG addition. In fact, this revealed that the D326R mitochondria seem to be pre-swollen as illustrated in Fig. 18E) by the lower baseline. The quantification in Fig. 18F) shows the significant difference in the delta between before and after PEG addition of D326R compared to WT.

PEG is a highly viscous substance which makes it difficult to precisely inject small volumes. Thus, I added a volume of 100  $\mu\text{l}$  10 % PEG (diluted in assay buffer) to 100  $\mu\text{l}$  mitochondrial suspension. Naturally, this drastic volume change led to a change in the absorbance by itself and therefore, I included a control to which the same volume of buffer was added. The rise in absorbance due to the larger volume is quantified in Fig. 18F) as control. It was not significantly different from the WT values. This provided further evidence that the WT mitochondria did not undergo any notable shrinking in response to PEG in contrast to the D326R mitochondria.

In summary, MCU was upregulated in D326R mouse liver which potentially led to  $\text{Ca}^{2+}$  accumulation in the mitochondria. This was indicated by a reduction in  $\text{Ca}^{2+}$ -induced swelling and a pre-swollen phenotype of isolated D326R mitochondria whereas  $\text{Na}^+$ -induced swelling was not affected.

However, the abundance of liver enzymes (e.g. alanine aminotransferase, alkaline phosphatase) in the peripheral blood was not altered or even reduced (aspartate

aminotransferase) in the D326R (data not shown) which did not indicate any major tissue damage in the liver. This was further supported by electron microscopy and histological images that did not show obvious aberrations (data not shown). The observed alterations were rather mild and presumably, liver mitochondria can compensate for them. Particularly, because they do not face drastic and frequent changes in  $[Ca^{2+}]_{cyto}$  as they occur in excitatory cells.  $Ca^{2+}$  oscillations in hepatocytes have a cycle time of 20 s or more and occur irregularly, sometimes with breaks of several minutes in between (Paillard et al., 2017) which likely gives the mitochondria sufficient time to recover. On the contrary,  $Ca^{2+}$  overload poses a much larger threat to cardiac mitochondria that constantly encounter hundreds of  $Ca^{2+}$  pulses every minute. Thus, we hypothesised that cardiac mitochondria must be especially vulnerable even to minor changes in the mitochondrial calcium homeostasis.

### 5.13. The point mutation affects basic cardiac function and the morphology of cardiac mitochondria

The heart is the organ with the highest continuous workload throughout life. A murine heart beats an impressive 400 to 600-times per minute and every contraction is induced by a cytosolic  $Ca^{2+}$  spike. On top of this remarkable basal performance, the heart still has to be able to adapt and increase its output during stress or fight or flight situations. All these challenges require tight control and strict maintenance of  $Ca^{2+}$  homeostasis. Is TMBIM5 involved in this and does the point mutation impair cardiac function?

In cooperation with the CTH, University Medicine Mainz, Germany, we measured basic cardiac parameters in narcotised mice using echocardiography. The measurements and the analysis were conducted by Dr Stefanie Finger. The ejection fraction describes the portion of blood ejected from the left ventricle during systole compared to the blood volume in the left ventricle at the end of the diastole (Ateet Kosaraju et al., 2021). The cardiac output is the volume of blood that is pumped through the body within 1 min. Statistical analysis of both parameters did not reveal any significant difference as shown in Fig. 19A). However, they showed a tendency to be decreased in D326R animals. Using transmission electron microscopy, we obtained high-resolution images from cardiac tissue from WT and D326R mice (Fig. 19B). This was done in cooperation with the IMAN, JGU Mainz, Germany, and

tissue preparation and image acquisition were performed by the technician, Ilse von Greavenitz. At first glance, no dramatic alterations in mitochondrial morphology or cristae structure were visible. Detailed analysis, however, revealed that the number of mitochondria per randomly chosen frame was increased in D326R tissue while the area per individual mitochondrion was reduced (Fig. 19C). This hinted towards an increased fission activity.

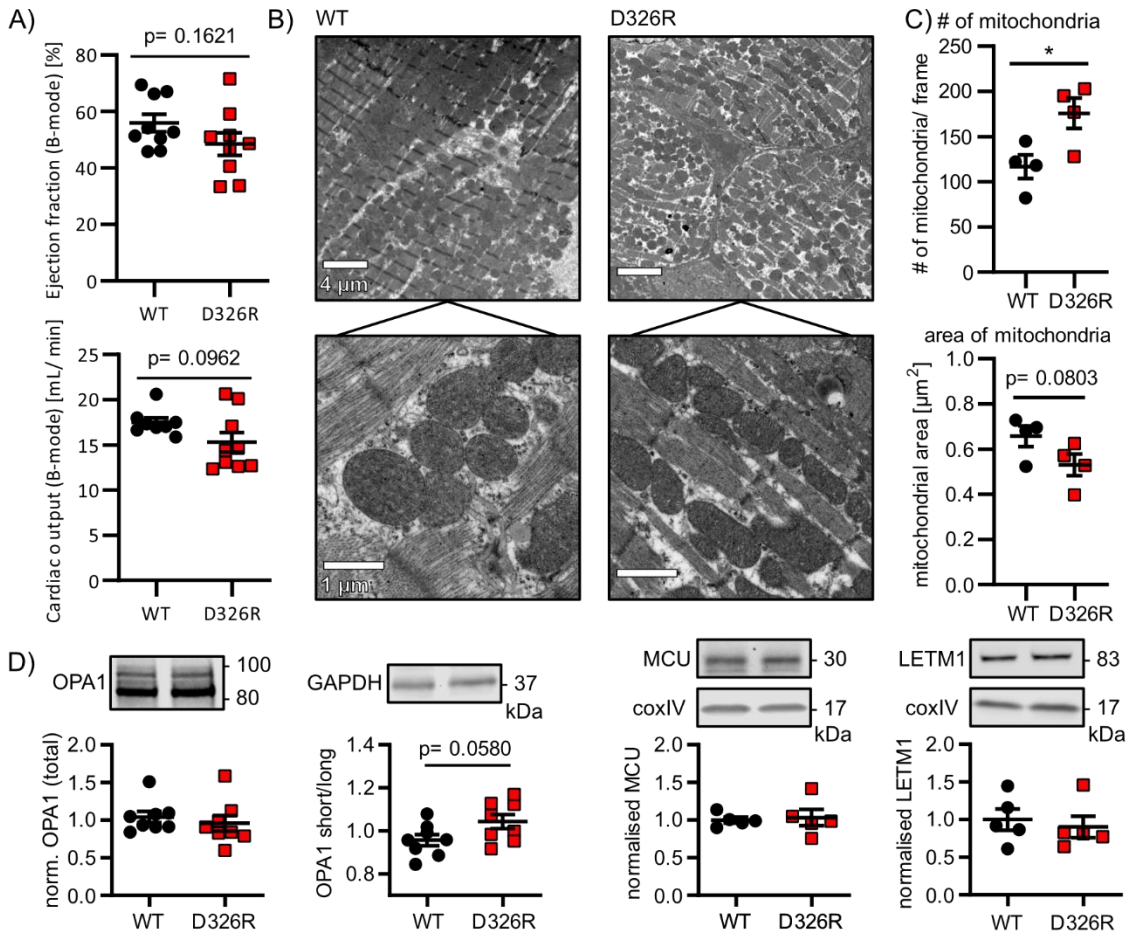


**Figure 19: D326R mice exhibit minor changes in basic cardiac function and mitochondrial morphology.**

**A)** The ejection fraction and the cardiac output were determined via cardiac ultrasound and were marginally reduced in homozygous D326R mice. Unpaired t-test. **B)** and **C)** D326R cardiac mitochondria looked healthy in transmission electron microscopy but were smaller and were present in a higher number. **C)** Quantification of mitochondrial number and size via manual analysis using the software Fiji/ImageJ. Unpaired t-test. **D)** The expression level of OPA1, MCU and LETM1 was unchanged in cardiac tissue, while the OPA1 splicing showed the same trend as in the cortex towards increased splicing. Values were normalised to WT after loading control and overall mean per blot. Unpaired t-test. Data are shown as mean ± SEM. Differences are not significant unless indicated otherwise, n.s. p≥0.05, \* p< 0.05;

Quantification of OPA1 protein expression revealed the same tendency as in the TMBIM5 KO cells and all other tested tissues: the total expression was unaltered, but the fraction of short isoforms was larger compared to the long isoforms indicating enhanced splicing (Fig. 19D, left). The expression of MCU and LETM1 was not changed (Fig. 19D, right). Summarised, D326R mice had a mild reduction in cardiac output and ejection fraction with optically healthy mitochondria. Yet, mitochondria displayed a fissioned phenotype which was likely due to increased processing of OPA1. The long OPA1 isoforms are necessary for fusion while the short variant may further increase fission (MacVicar and Langer, 2016). As discussed before, proteolytic processing of OPA1 is influenced by multiple factors including the mitochondrial membrane potential and ATP levels (Del Dotto et al., 2018). Reduction of both induces the generation of short OPA1 forms which might cause the observed mitochondrial phenotype.

Both, ATP and the mitochondrial membrane potential, are generated by the electron transport system which led us to study whether the point mutated TMBIM5 impairs cellular respiration.

#### 5.14. Respiration of D326R cardiac mitochondria is slightly reduced due to a reduced coupling efficiency

The use of oxygen and substrates to produce ATP as the cellular energy equivalent is the oldest known and most prominent mitochondrial function. The core elements, the electron transport system and the ATP synthase, are responsible for the main mitochondrial characteristics such as the membrane potential, ATP output, ROS production. In addition, the ATP synthase has been implicated in the formation of the cristae (Rampelt and van der Laan, 2017) and the mPTP (Elustondo et al., 2016) which demonstrates how central the respiratory system is for mitochondrial function and structure. Hence, we sought to elucidate the effect of the point mutation on the respiratory system in cardiac mitochondria.

Respiration was measured at different states using a high-resolution respirometer. To avoid mitochondrial isolation, I established a protocol that enabled me to measure respiration *in situ* in permeabilised cardiac muscle fibres. An exemplary trace of one measurement is shown in Fig. 20A). The oxygen consumption detected at the beginning was defined as

residual oxygen consumption (ROX). Given that at this time point the mitochondrial OXPHOS system completely lacked substrates, any oxygen use could only stem from other (non-mitochondrial) oxidative processes and was therefore subtracted from all other values for the final analysis. To fuel mitochondrial respiration, pyruvate and malate were then injected for a non-phosphorylating resting state (LEAK). After stabilisation, a saturating amount of ADP was added for an active OXPHOS state. At this point, cyt c was added as a test for outer mitochondrial membrane integrity. Rupture of the outer membrane releases cyt c from the intermembrane space and makes it a limiting factor of ETS activity. Thus, only when the OMM was damaged, the addition of cyt c increased respiration considerably. Measurements with a rise beyond 15 % (compared to the previous state) were excluded from the final analyses. Interestingly, this was more often the case for D326R than for WT samples (eight versus five out of 20) which might indicate that mitochondria were less robust potentially due to a more fragile cristae structure.

For additional activation of the glutamate dehydrogenase pathway, glutamate was injected. The resulting state (CI) represents the maximum (coupled) activity of complex I alone as no substrates for complex II are present. Thus, the addition of succinate which fuels complex II led to a marked rise in respiration. Thereupon, maximum respiratory capacity (ETS) was induced by the ionophore FCCP. After inhibition of complex I by rotenone, the activity of the uncoupled complex II alone was measured (CII\*).

Quantification of the different states is shown in Fig. 20B). The respiratory capacity in D326R cells was mildly but significantly reduced under all conditions. This reduction was likely due to an impaired coupling efficiency which was indicated by the ratio of LEAK to CI (receptor control ratio). The leak respiration represents the level of ETS activity that is required to balance any proton flux into the matrix that is not driving the ATP synthase. Theoretically, 100 % coupling efficiency would mean that every single proton that is transported out of the mitochondrial matrix by the ETS is utilised by the ATP synthase. This would correspond to a receptor control ratio of zero. In D326R samples, the relative level of proton leak was increased compared to WT meaning that the coupling was less efficient (Fig. 20C). To rule out that the lower respiration was due to a general reduction in ETS proteins I quantified the abundance of key proteins for every complex of the ETS.

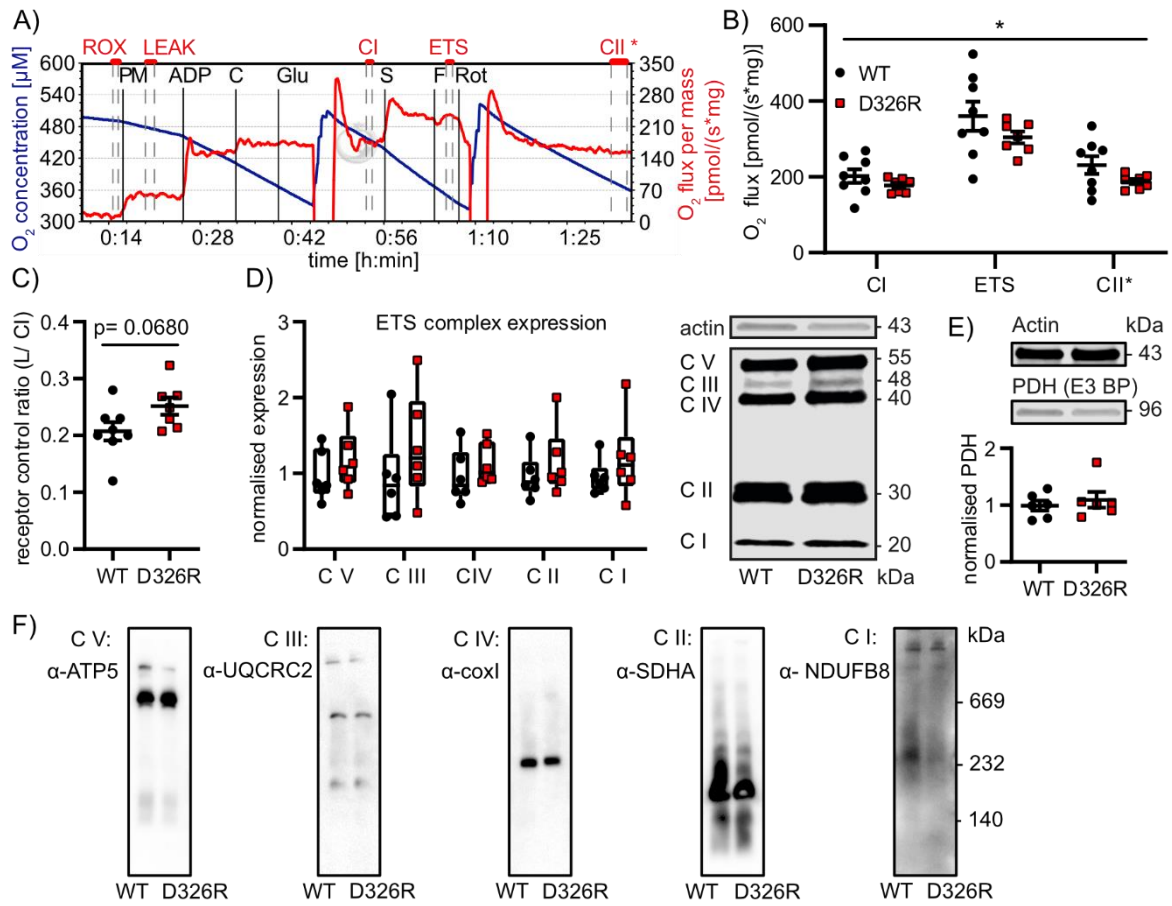


**Figure 20: Respiration of cardiac mitochondria is slightly reduced due to an attenuated coupling efficiency in D326R mice.**

**A)** Exemplary trace of a high-resolution respirometry measurement using an Oroboros O2k. PM = pyruvate (5mM) and malate (2 mM), ADP = adenosine diphosphate (5 mM) , C = cytochrome c (10  $\mu$ M), Glu = glutamate (10 mM), S = succinate (10 mM), F = FCCP (0.5 – 1  $\mu$ M), Rot = rotenone (0.5  $\mu$ M) were added at the indicated time points. Marked in red are the 5 states that were used for quantification, ROX (= residual oxygen consumption), leak, CI (complex I activity), ETS (= electron transport system, maximum activity) and CII \*(uncoupled complex II activity). **B)** and **C)** Respiration was measured in permeabilised tissue samples from the heart. All values were normalised to the wet weight of the tissue. Data are shown as mean  $\pm$  SEM. **B)** Mixed-effects analysis revealed a significant effect of the genotype on the three different respiratory states. **C)** The receptor control ratio is the ratio of leak to complex I activity and it was slightly increased in D326R samples. Unpaired t-test. **D)** The protein expression levels of the five different complexes (C I-V) of the electron transport system were not altered. An antibody cocktail was used to stain representative subunits of each complex. Antibodies against the following proteins were contained: NDUFB8 for C I, SDHB for C II, UQCRC2 for C III, MTCO2 for C IV and ATP synthase subunit  $\alpha$  for C V. Values were normalised to loading control and overall mean per blot. Data are shown as boxplots, min. to max.. Two-way ANOVA. **E)** Pyruvate dehydrogenase-E3-binding protein (PDH (E3 BP)) was stained and quantified as a marker for mitochondrial abundance. Its expression level was unchanged between WT and D326R. Normalised to WT after loading control and overall mean per blot. Unpaired t-test. **F)** Complex formation of the electron transport system complexes was not affected either. BN PAGE was stained with antibodies against core subunits of each complex (ATP5 for CV, UQCRC2 for CIII, coxI for C IV, SDHA for CII, NDUFB8 for CI).

Differences are not significant unless indicated otherwise, n.s.  $p \geq 0.05$ , \*  $p < 0.05$ ;

There was no statistical difference between WT and D326R (Fig. 20D). Surprisingly, there was even a tendency to higher expression levels in D326R, which was likely a compensatory upregulation and not the effect of a higher mitochondrial abundance in general. To verify this, I quantified the amount of a subunit of the pyruvate dehydrogenase (PDH E3 BP). The PDH is a protein complex in the mitochondrial matrix which generates substrates for the TCA cycle but is not directly linked to the ETS. I, therefore, used it as a marker for overall mitochondrial protein abundance relative to actin. The result is displayed in Fig. 20E) showing no variation between the genotypes. Not only does the quantity of the proteins determine the efficiency of the ETS but also the complex assembly is a critical step. Hence, I surveyed the complex formation of the ETS complexes using BN PAGE followed by antibody staining against core subunits of each complex. As shown in Fig. 20F) there were no striking discrepancies. In contrast to reducing and denaturing western blot stainings, the stained bands from BN PAGE should not be quantified and this has two reasons: firstly, there is no loading control and secondly, the bands are detected using a chemiluminescent reaction that relies on homogeneous substrate availability. Thus, minor differences in signal intensity may be caused by unequal loading of protein or substrate during detection and should not be confused with biological differences.

Altogether, no major dysfunction was observed for the respiratory system in cardiac mitochondria. They exhibited a slight reduction in respiration which was caused by a lower coupling efficiency and not by changes in the abundance or formation of the ETS complexes. We next investigated the effects of these alterations on mitochondrial calcium handling.

### 5.15. The calcium handling of D326R cardiac mitochondria is not altered

Ca<sup>2+</sup> signalling is abundant in all cell types but its exact mechanism varies greatly and is extremely tissue-specific. Consequently, the regulation and maintenance of the intracellular Ca<sup>2+</sup> are precisely adapted to the individual environment. Due to the constant oscillation of cytosolic Ca<sup>2+</sup> in cardiomyocytes, cardiac mitochondria are especially vulnerable to Ca<sup>2+</sup> overload. We sought to investigate a possible impact of the mutated TMBIM5 on this delicate balance.

Ca<sup>2+</sup> uptake and mPTP opening in isolated mitochondria was examined as described for cortical mitochondria in section 5.11. In brief, isolated cardiac mitochondria were challenged with a series of CaCl<sub>2</sub> pulses while extramitochondrial Ca<sup>2+</sup> was measured as the fluorescence of the Ca<sup>2+</sup> sensitive dye Calcium Green-5N. This was done in the absence and presence of the mPTP inhibitor CsA. In addition, buffers with different concentrations of Na<sup>+</sup> were used and the NCLX-blocker CGP was added to elucidate NCLX contribution.

The Ca<sup>2+</sup> uptake rate in 2.5 mM NaCl<sub>2</sub> buffer did not vary between WT and D326R as shown by the traces in Fig. 21A) with the quantified rate constant (K) in the two panels on the right. In both genotypes, the mPTP opened after 6-8 Ca<sup>2+</sup> injections, which was marked by the abolished uptake slope and a further increase in fluorescence after the injections. The presence of the mPTP inhibitor CsA delayed these effects providing further proof that they indeed represent mPTP opening. However, there was no difference between WT and D326R neither in Ca<sup>2+</sup> uptake rate nor its capacity. In the presence of higher Na<sup>+</sup> concentrations (7.5 and 10 mM), the NCLX is more active and exports Ca<sup>2+</sup> simultaneously to its influx. This effect can be seen in Fig. 21B) because the traces do not return to the initial baseline but gradually increase from injection to injection. This illustrates that the Ca<sup>2+</sup> is not only taken up and permanently stored in the mitochondria but it is slowly released too. Curiously, this effect seemed to be particularly strong in the WT in the 10 mM NaCl<sub>2</sub> buffer. The WT trace in Fig. 21B) on the right indicates an early rise in bath Ca<sup>2+</sup> that seemed to be NCLX-mediated because it was reversed by CGP. In D326R mitochondria, Na<sup>+</sup> concentration or CGP did not affect the Ca<sup>2+</sup> handling which might indicate that the NCLX is generally less active. Unfortunately, I could not test the protein abundance of NCLX in the tissue because no reliable antibody is available. Quantification of mRNA levels via qPCR, however, showed no difference at the mRNA level (unpublished data from our group, not shown).

As another measure of mPTP opening and to test the Ca<sup>2+</sup> preload in the matrix, I repeated the Ca<sup>2+</sup> -induced swelling assay with cardiac mitochondria, as described in section 5.12. for liver mitochondria. In brief, isolated mitochondria were subjected to a high concentration of CaCl<sub>2</sub> inducing mPTP opening and matrix swelling which was detected as a decrease in absorbance.

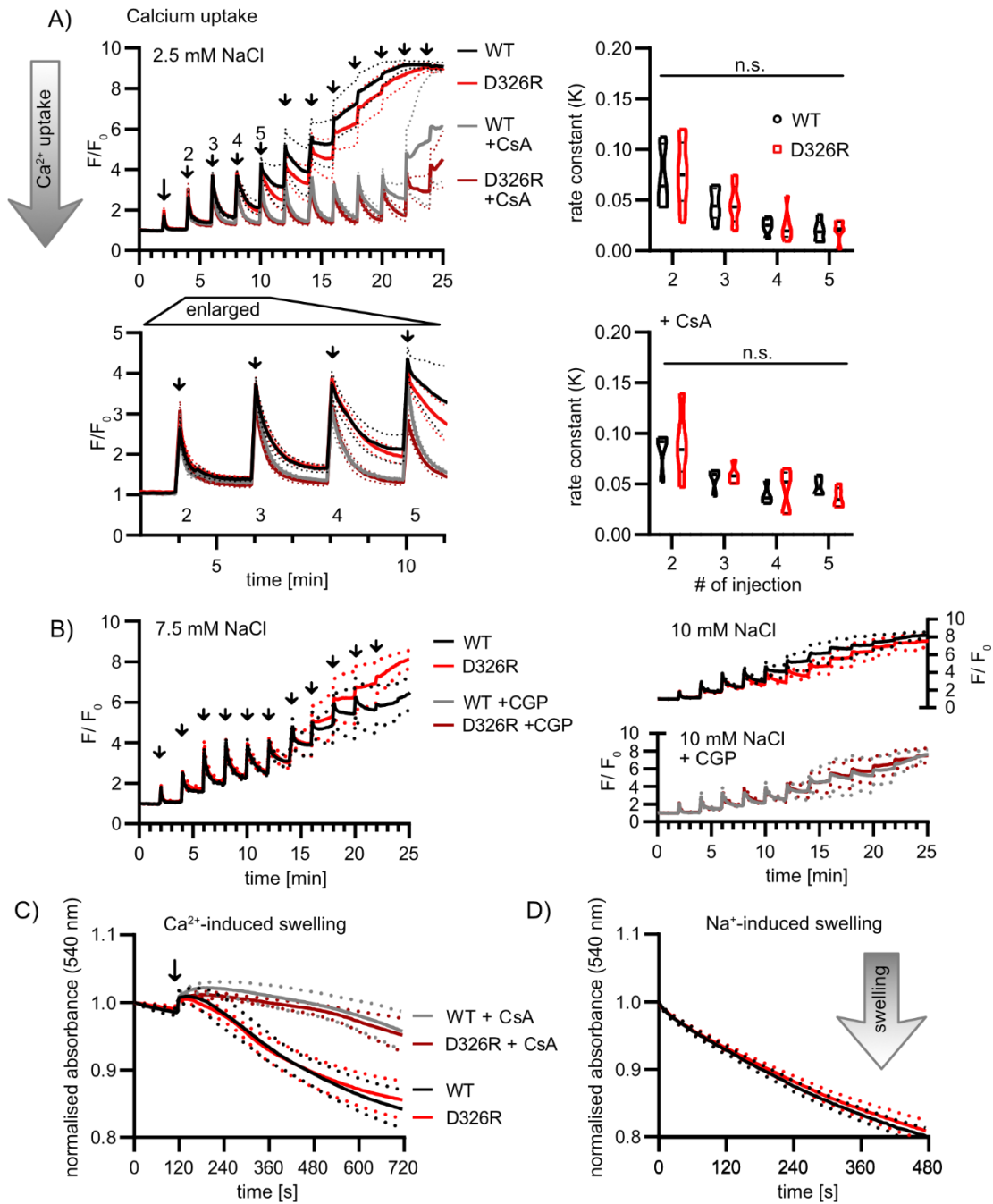


**Figure 21: The point mutation in TMBIM5 does not affect the calcium handling in cardiac mitochondria.**

**A)** The rate of Ca<sup>2+</sup> uptake and the uptake capacity were normal in D326R cardiac mitochondria. Mitochondria were isolated from the heart and subjected to a sequence of CaCl<sub>2</sub> pulses (as indicated by the arrows, 10 μM each). Ca<sup>2+</sup> uptake was observed as a decrease in the fluorescent signal of the Ca<sup>2+</sup> sensor Calcium Green-5N (1 μM, Ex/Em: 488/520 nm) in the assay buffer. As a control for mPTP opening, this was conducted in the absence and presence of 2 μM CsA. Quantification on the right shows the rate constant ± CsA, calculated from the slope after the indicated injections, numbered 2-5 (- CsA WT/ D326R: 6-8, + CsA WT/D326R: 4-5) Graphs on the left show mean ± SEM. Quantification is shown as violin plots with median and quartiles. Mixed-effects analysis. **B)** The same protocol as described for A) was conducted with higher Na<sup>+</sup> concentrations in the buffer (7.5 and 10 mM) and in the presence of the NCLX-inhibitor CGP (10 mM) (WT: n = 4-7, D326R: n = 5-8). Mean ± SEM. **A)** and **B)** Fluorescence was

normalised to the initial value ( $F/F_0$ ). **C**) D326R cardiac mitochondria did not show an aberrancy in  $Ca^{2+}$ -induced swelling. Absorbance of the isolated mitochondria was measured at 540 nm. A reduction in optical density marks increased mitochondrial swelling and vice versa. 1 mM  $CaCl_2$  was injected at the indicated time point to induce  $Ca^{2+}$  overload and mPTP opening. Inhibition of mPTP with 2  $\mu$ M CsA served as control. (WT/D326R n = 7/5) **D**)  $Na^+$ -induced swelling was not affected either in D326R mitochondria (n = 5). **C**) and **D**) Values were normalised to initial absorbance. Data are shown as mean  $\pm$  SEM.

Differences are not significant unless indicated otherwise, n.s.  $p \geq 0.05$ ;

In line with the previous results, there was no difference between WT and D326R mitochondria as displayed in Fig. 21C). Nevertheless, we compared it to  $Na^+$ -induced swelling which also did not reveal any variance (Fig. 21D).

To sum up, the  $Ca^{2+}$  uptake and the uptake capacity were not altered in cardiac mitochondria from D326R mice. The response to changes in the sodium concentrations was marginally different which may indicate a reduced NCLX activity. However, this certainly needs further investigation.

To complete the characterisation of tissues that heavily rely on mitochondrial ATP supply and  $Ca^{2+}$  signalling, I next sought to classify mitochondrial health in skeletal muscle.

### 5.16. D326R mice present with a severe myopathy with reduced grip strength

Different to the heart muscle, skeletal muscles do not have to endure constant, rather uniform contractions but they face a broad range of different challenges. They need the ability to switch between a resting state and intense exercise within milliseconds which can be vital in life-threatening situations. But besides fight-or-flight situations, they also have to be able to maintain a steady activity for hours. To meet these diverse demands, several muscle fibre types have evolved that differ in their contractility, morphology and metabolic properties and possess specialised regulatory mechanisms (Hennebry et al., 2009). Research in this field is still ongoing and we sought to answer the question of whether TM6SF1 is involved in this complex regulation. Does its loss affect skeletal muscle function in mice?

A very neat and straightforward approach to assess muscle strength in mice is the so-called inverted grid test. Mice are placed on a large grid and once they are holding on to it the

grid is inverted and positioned on a transparent cylinder, see Fig. 22A). The readout was the latency to fall. It is part of the natural behaviour of the mice to climb – also upside down - and cling to grid-like structures and they can do so in their housing cages. That makes it a physiological and stress-free test for mouse muscle strength. The comparison of WT and D326R mice showed that the mice carrying the point mutation had significantly reduced endurance and fell off the grid earlier (Fig. 22B).

To investigate if this macroscopic finding had a microscopic representation on the mitochondrial level, tissue samples from skeletal muscle (Musculus Gastrocnemius) were isolated, fixated and imaged using electron microscopy. The images revealed dramatic mitochondrial deformation in D326R muscle tissue (Fig. 22C). The large majority of mitochondria looked swollen and had deranged cristae (indicated by the white arrow). In addition, white gaps were found between muscle fibres signifying the loss of mitochondria that had been degraded (indicated by the orange arrows).

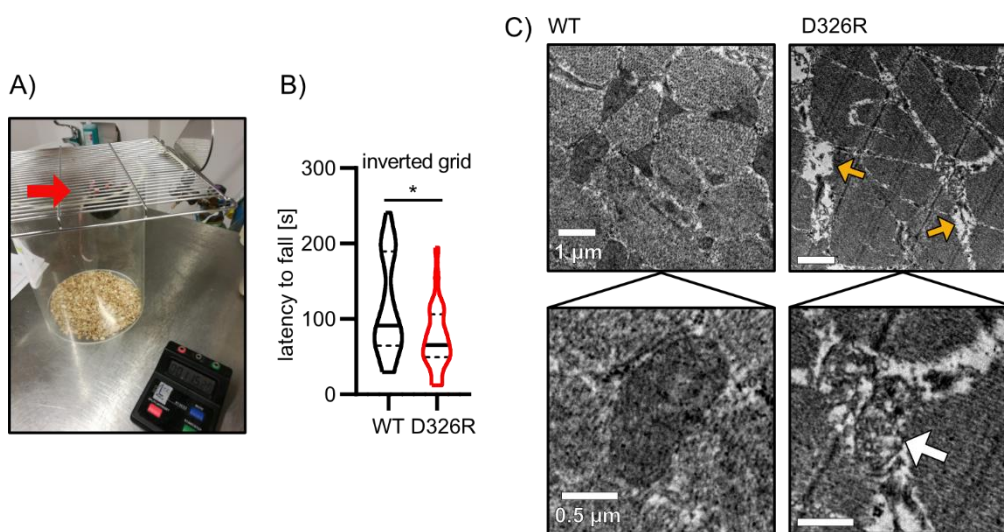


**Figure 22: D326R mice present with reduced grip strength and severe myopathy.**

**A)** Mice were placed on a horizontal grid and allowed to accommodate for 2 s, then the grid was turned 180° and it was measured how long they were able to cling to it (WT/D326R: n = 23/25). **B)** Latency to fall in the inverted grid test. Data are shown as violin blot with median and quartiles. Unpaired t-test. \* p<0.05. **C)** Exemplary transmission electron microscopy images showing severely damaged mitochondria in D326R skeletal muscle tissue. Mitochondria are swollen and have deranged cristae (white arrow). Tissue gaps indicating degraded mitochondria are marked with orange arrows.

Altogether, the reduced muscle strength and the striking mitochondrial defects on the electron microscopic level suggest a severe myopathy in the D326R mice. Mitochondrial myopathies are most commonly caused by deficiencies in the oxidative phosphorylation

system. Could this be a secondary effect of  $\text{Ca}^{2+}$  dysregulation caused by the mutated TMBIM5?

### 5.17. The point mutation in TMBIM5 impairs mitochondrial calcium handling in skeletal muscle mitochondria

As mentioned before,  $\text{Ca}^{2+}$  homeostasis has a double role in mitochondria. On the one hand, it serves as a signal enhancing TCA cycle activity and ATP production upon demand. On the other hand, mitochondrial  $\text{Ca}^{2+}$  uptake also has a buffering function and helps to modulate cytosolic free  $\text{Ca}^{2+}$ . Both functions are essential for skeletal muscle activity. The observed muscle dysfunction and mitochondrial degradation in D326R mice might be due to disturbed  $\text{Ca}^{2+}$  homeostasis. To test this hypothesis, I examined mitochondrial  $\text{Ca}^{2+}$  handling in D326R skeletal muscle tissue.

As a first approach, I quantified MCU expression in skeletal muscle protein samples. The abundance of MCU was unaltered in D326R tissue, as shown in Fig. 23A). To study mitochondrial  $\text{Ca}^{2+}$  uptake, the same  $\text{Ca}^{2+}$  uptake protocol as described for cortical and heart tissue was applied to skeletal muscle mitochondria. In brief, isolated mitochondria were challenged with a series of  $\text{CaCl}_2$  pulses to study the uptake rate and the threshold for mPTP opening. The  $\text{Ca}^{2+}$  concentration in the extramitochondrial buffer was determined using the fluorescent dye Calcium Green-5N. Thus, a decrease in the fluorescence depicts mitochondrial uptake and vice versa. The experiment was conducted with different conditions i.e. with low  $[\text{Na}^+]$  in the buffer (2.5 mM NaCl) and in the absence or presence of the mPTP inhibitor CsA which serves as a control for mPTP opening. To clarify the involvement of NCLX activity,  $\text{Ca}^{2+}$  uptake was measured with intermediate (7.5 mM) and high (10 mM) NaCl concentration in the buffer and in the presence of the NCLX blocker CGP. Differences between WT and D326R were most pronounced for the low  $[\text{Na}^+]$  condition without CsA. D326R mitochondria exhibited a reduced capacity to sequester  $\text{Ca}^{2+}$  which was marked by the increase in fluorescence after injection # 7 (Fig. 23B, left). In WT mitochondria mPTP opening was only observed after 11 pulses. The rise in fluorescence could clearly be attributed to the mPTP because in both genotypes it was delayed by the presence of CsA. Moreover, the uptake rate was reduced in the D326R mitochondria (Fig. 23B, right). Partially, this may have been due to the early opening of mPTP because  $\text{Ca}^{2+}$

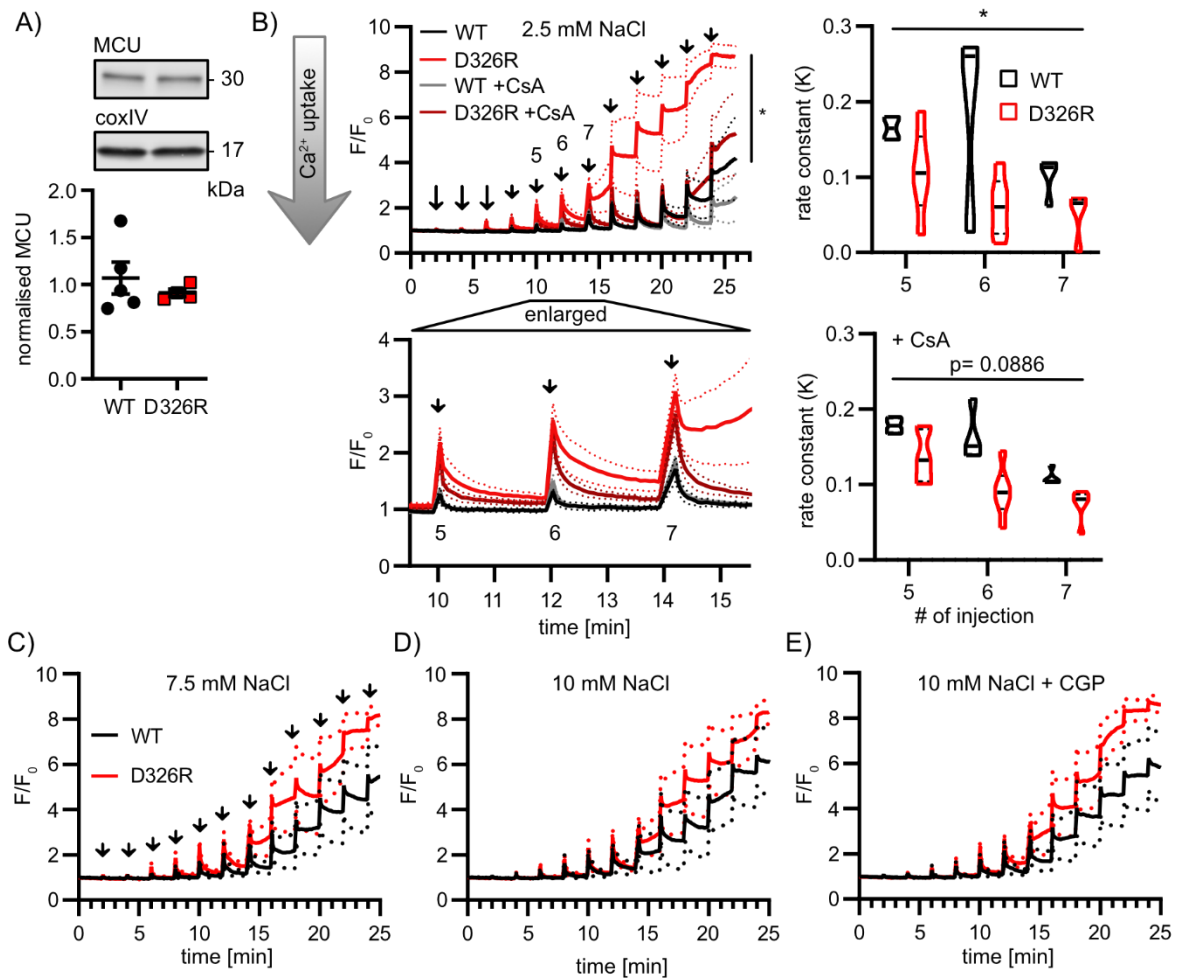


**Figure 23: D326R skeletal muscle mitochondria have a reduced  $\text{Ca}^{2+}$  uptake rate and capacity.**

**A)** Expression of MCU in skeletal muscle tissue was not affected by the point mutation. Mean  $\pm$  SEM. Unpaired t-test. **B)** Slower  $\text{Ca}^{2+}$  uptake and reduced capacity in isolated D326R skeletal muscle mitochondria. Mitochondria were isolated and measured in an assay buffer containing  $1 \mu\text{M}$  Calcium Green-5N. When challenged with a series of  $\text{CaCl}_2$  pulses ( $10 \mu\text{M}$  each), mPTP in D326R mitochondria opened earlier. Moreover, the  $\text{Ca}^{2+}$  uptake was slower in the absence and presence of  $2 \mu\text{M}$  CsA. On the right, rate constant (K) of the uptake slope after the indicated, numbered  $\text{Ca}^{2+}$  injections  $\pm$  CsA. Fluorescence was normalised to the initial value ( $F/F_0$ ) (WT  $\pm$  CsA:  $n = 4/5$ ; D326R  $\pm$  CsA:  $n = 6$ ). Data on the graphs are shown as mean  $\pm$  SEM, data on plots are shown as violin plots with median and quartiles. Analysed via mixed-effects analysis. **C)-E)** The same protocol as described for **B)** was conducted with higher  $\text{Na}^+$  concentrations in the buffer (7.5 and 10 mM) and in the presence of the NCLX-inhibitor CGP (10 mM). Surprisingly, the difference between WT and D326R was less pronounced under these conditions ( $n = 5-6$ ). Mean  $\pm$  SEM.

Differences are not statistically significant unless indicated otherwise, n.s.  $p \geq 0.05$ , \*  $p < 0.05$ ;

was released at the same time. However, the difference was still detectable in the presence of CsA which is shown in the enlarged graph and the quantification of the rate constant with CsA, both in Fig. 23B) in the two lower panels. This indicated that the  $\text{Ca}^{2+}$  uptake was slower in D326R mitochondria even if the release through mPTP was blocked. I noticed that

the fluorescent peaks from the first 4 injections were very low which may be explained by some remaining EGTA from the isolation buffer. This would result in rapid buffering of the injected  $\text{Ca}^{2+}$  and the observed low peaks. Yet, the fact that the WT peaks # 5,6,7 were considerably lower than for the D326R traces may be another effect of the uptake velocity. It is plausible that in the short lag time between injection and fluorescence detection by the plate reader mitochondria had already sequestered some of the added  $\text{Ca}^{2+}$ . Since uptake in the WT mitochondria was faster, the amount of  $\text{Ca}^{2+}$  missing in the peak detection was larger, resulting in smaller injection peaks.

With increasing NaCl concentration in the buffer the differences became attenuated (Fig. 23C-D) indicating involvement of the NCLX. As observed for cardiac mitochondria, the activity of the NCLX was depicted by the increasing baseline while the mitochondria were continuing to take up  $\text{Ca}^{2+}$ . The mPTP still seemed to open earlier in the D326R mitochondria but the difference was less clear because the traces approached each other. Nevertheless, it is difficult to explain why the measurement in the presence of CGP (Fig. 22E) does not mirror the one with low NaCl (Fig. 23B). One would expect that if the activity of NCLX affects the uptake slope and mPTP opening, its blocking should even intensify the phenotype observed under low  $[\text{Na}^+]$ . It cannot be excluded that the efficacy of the CGP was reduced or lost due to inappropriate storing conditions or faulty handling. Yet, it has to be mentioned that it did show an inhibitory effect on NCLX activity in cardiac mitochondria.

Summarised,  $\text{Ca}^{2+}$  uptake was impaired and the total  $\text{Ca}^{2+}$  retention capacity was reduced in D326R skeletal muscle mitochondria which was not caused by changes in MCU abundance. The differences were most pronounced under low  $[\text{Na}^+]$  conditions indicating that simultaneous  $\text{Ca}^{2+}$  extrusion through NCLX blurred the effect.

## 6. Discussion

---

It is quite impressive that with the term “powerhouse of the cell” mitochondria were underestimated for decades. Is it not sufficient to supply every eukaryotic organism with the energy needed for survival? This alone is an extremely complex interplay of countless proteins and molecules. Nonetheless, today mitochondria are acknowledged for their numerous other functions, e.g. the generation of iron-sulfur-clusters, ROS and lipids, the induction of apoptosis and their role in calcium buffering.

It is not exaggerated to say that “by using  $\text{Ca}^{2+}$  as an intracellular messenger, cells walk a tightrope between life and death” (Demaurex and Distelhorst, 2003).  $\text{Ca}^{2+}$  is a universal and versatile messenger involved in the regulation of multiple vital cellular functions (cell cycle progression, cellular differentiation, transcription, signal transmission etc.). However, it is also one of the main signals inducing apoptosis. Dysfunctions in the cellular  $\text{Ca}^{2+}$  handling machinery can tip this delicate balance and have devastating effects causing severe diseases such as cardiomyopathies (Jung et al., 2020), diabetes (Arruda and Hotamisligil, 2015), Alzheimer`s (Jadiya et al., 2019) and Parkinson`s disease (Jung et al., 2020). In fact, all of the listed pathologies have been linked to mitochondrial  $\text{Ca}^{2+}$  dysregulation. This emphasises the critical role of mitochondria in the maintenance of cellular  $\text{Ca}^{2+}$  homeostasis. Moreover, a thorough understanding of the underlying processes is very important for the development of therapeutic strategies for the mentioned pathologies.

This work focused on a novel candidate for mitochondrial  $\text{Ca}^{2+}$  channelling, the Transmembrane BAX Inhibitor Motif containing protein 5 (TMBIM5). TMBIM5 resides in the inner mitochondrial membrane and contains eight membrane-spanning domains. It is part of a family of evolutionarily highly conserved proteins (TMBIM1-6) and has strong sequence homologies with TMBIM6/BI-1 and the bacterial BsYetJ (Lisak et al., 2015). Notably, they share a putative pore-forming loop-domain with a pH-sensing di-aspartyl motif at the C-terminus. BsYetJ and BI-1 have been shown to be pH-dependent  $\text{Ca}^{2+}$  leak channels (Kiviluoto et al., 2013; Chang et al., 2014) which gave rise to the hypothesis that TMBIM5 may be a yet unidentified mitochondrial  $\text{Ca}^{2+}$  channel.

Nonetheless, TMBIM5 has been implicated in several other processes. It seems to affect mitochondrial cristae structure (Oka et al., 2008) and may act as an anti-apoptotic factor by stabilising cyt *c* at the IMM and preventing its release (Oka et al., 2008; Meng et al.,

2017). The mitochondrial cristae are predominantly organised and maintained by the so-called MICOS which is a conserved multi-heterooligomeric complex located at the cristae junctions (CJs). I excluded a significant involvement of TMBIM5 in this complex by investigating any mutual effects in TMBIM5/MIC10 or MIC60 KO cell lines. MIC10 or MIC60 are two core components of MICOS. Lack of MIC10 or MIC60 did not alter TMBIM5 protein abundance or complex size. Neither did the loss of TMBIM5 affect MIC10/MIC60 expression or complex assembly. Thus, it is safe to say that TMBIM5 is probably not part of the MICOS. Nonetheless, it may exert an indirect effect on cristae formation by influencing OPA1 processing. In HAP1 cells lacking TMBIM5, I detected a reduced abundance of total OPA1 and an accumulation of the processed short forms of OPA1. OPA1 is a multifunctional protein that regulates mitochondrial fusion and fission (MacVicar and Langer, 2016) but is also involved in cristae formation and their remodelling upon apoptotic stimuli (Frezza et al., 2006; Harner et al., 2016). In mammals, OPA1 exists in at least eight different isoforms with more or less distinct functions (Del Dotto et al., 2018). The abundance of the various splice variants is regulated by the activity of the two metalloproteases OMA1 and YME1L (Anand et al., 2014). Interestingly, both are activated by mitochondrial membrane depolarization. OMA1 is additionally stimulated by low ATP levels (Rainbolt et al., 2016). Hence, reduced MMP leads to enhanced processing of OPA1 to the short isoforms. In a recent publication, we showed that HAP1 TMBIM5 KO cells have a diminished MMP and ATP availability due to an attenuated ETS activity (Seitaj et al., 2020). This may induce OPA1 splicing and degradation and explain the observed changes in protein abundance. It remains unclear how the loss of TMBIM5 affects mitochondrial respiration. Is it impaired due to structural dysfunction or due to other functions of TMBIM5? The lack of interaction of TMBIM5 with the well-researched MICOS rather indicates that the observed detrimental effects on mitochondrial morphology and cristae organisation may lie downstream of the compromised MMP caused by the loss of TMBIM5.

The missing link between TMBIM5 and mitochondrial respiration may be the previously reported interaction of TMBIM5 and CHCHD2 (Meng et al., 2017). CHCHD2 shares some interesting features with TMBIM5. Firstly, the lack of either of them results in abnormal cristae structure, but for CHCHD2 there is a proposed mechanism. It modulates the activity of YME1L and thereby affects OPA1 processing (Liu et al., 2020c). The resulting imbalance

of OPA1 isoforms likely leads to the observed structural changes in mitochondria. The second common characteristic is that they can both bind to cyt *c* in a non-competitive manner (Meng et al., 2017). This interaction presumably stabilises cyt *c* at the IMM and supports the electron transfer from complex III to complex IV of the ETS as CHCHD2 additionally binds to the complex IV (cytochrome *c* oxidase). Loss of TMBIM5 in this trigonal binding may compromise its function and reduce ETS efficiency. This in turn would lead to the above-described effects: reduction in MMP, increased splicing of OPA1 by YME1L and ultimately disorganised cristae. Moreover, CHCHD2 is a multifunctional protein involved in several other processes that may be affected by the lost interaction with TMBIM5. As mentioned above, it is involved in the regulation of OPA1 splicing. CHCHD2 competes with P32 for the YME1L binding site. P32 induces YME1L proteolytic activity. The binding of CHCHD2 thereby reduces OPA1 splicing (Liu et al., 2020c). It is possible that in the absence of TMBIM5, more CHCHD2 is recruited to the ETS to compensate for the deficiency, leaving YME1L unregulated. This would exacerbate the cristae phenotype as it further enhances OPA1 processing. Yet, all of this is based on hypotheses and should be addressed in prospective studies.

Using quantitative proteomics, our group identified 21 proteins that were downregulated in HAP1 TMBIM5 KO cells (recently published data) (Seitaj et al., 2020)). Among these proteins were several subunits of the ETS complexes, such as UQCRC1 (subunit of complex III) and NDUFS1 (subunit of complex I). This reduction may additionally compromise the mitochondrial respiratory capacity. The link between the expression of TMBIM5 and subunits of the ETS is not clear yet. Interestingly, another cluster of proteins that was downregulated in the absence of TMBIM5 is associated with mitochondrial ribosome proteins (Seitaj et al., 2020). Hence, the loss of TMBIM5 may – indirectly or directly – impact the protein synthesis machinery.

Nonetheless, the putative Ca<sup>2+</sup> channel function of TMBIM5 may also affect oxidative phosphorylation. Mitochondrial Ca<sup>2+</sup> uptake does not only play a role in cytosolic Ca<sup>2+</sup> homeostasis but it also couples mitochondrial ATP production to the cellular demand. Rising Ca<sup>2+</sup> concentrations are a signal for an increased energy need. In the mitochondrial matrix, free Ca<sup>2+</sup> stimulates the ATP synthase and several dehydrogenases that supply substrates for the ETS. Hence, mitochondrial Ca<sup>2+</sup> uptake results in an augmentation of ETS

activity and ATP availability. Notably, only free  $\text{Ca}^{2+}$  exerts a stimulatory function. Phosphate-bound  $\text{Ca}^{2+}$  does not show an effect. The only mitochondrial  $\text{Ca}^{2+}$  uptake pathway currently known is the mtCU. Yet, there is convincing evidence that it may not be alone (Sparagna et al., 1995; Wei et al., 2012; Bondarenko et al., 2013). Wei and colleagues (Wei et al., 2012) made the intriguing observation that the mtCU-mediated uptake (that they named  $\text{MCU}_{\text{mode2}}$ ) activates an additional phosphate buffering system that prevents large changes in the concentration of free mitochondrial  $\text{Ca}^{2+}$ . On the contrary,  $\text{Ca}^{2+}$  uptake by  $\text{MCU}_{\text{mode1}}$  resulted in a considerable increase in free  $\text{Ca}^{2+}$  (Wei et al., 2012). Based on these findings they hypothesise that the – presumably mtCU-mediated –  $\text{MCU}_{\text{mode2}}$  constitutes the mitochondrial  $\text{Ca}^{2+}$  buffering function that prevents  $\text{Ca}^{2+}$  accumulation in the cytosol. This is in line with the fact that the MMP is not affected in MCU KO cells (Baughman et al., 2011; Stefani et al., 2011). The  $\text{MCU}_{\text{mode1}}$  is much more likely to mediate  $\text{Ca}^{2+}$  influx that serves to modulate oxidative phosphorylation. The molecular identity of this flux, however, remains elusive. Could it be TMBIM5?

I detected that TMBIM5 KO HAP1 cells displayed a reduced  $\text{Ca}^{2+}$  rate upon stimulation with Ionomycin. This may be due to the mentioned decrease in MMP which reduces the driving force for  $\text{Ca}^{2+}$  uptake. Yet, it seems unlikely that this is the sole reason as unpublished mitoplast patch-clamp data from a collaborating group also show a marked decrease of  $\text{Ca}^{2+}$  flux in TMBIM5 KO cells. Moreover, the protein expression analyses of the mtCU subunits revealed an effect of TMBIM5 KO and vice versa. This indicates that TMBIM5 is in some way involved in mitochondrial  $\text{Ca}^{2+}$  handling. Less MCU was found in both TMBIM5 KO cell lines whereas TMBIM5 abundance was increased in MCU and MICU1 KO cells. This was a surprising finding for us. The upregulation of TMBIM5 in MCU/MICU1 KO cells is in line with our hypothesis that TMBIM5 is an additional  $\text{Ca}^{2+}$  influx channel as it may compensate for the loss of MCU/MICU1. However, MCU does not seem to be able to make up for the loss of TMBIM5 or may even be detrimental. One possible explanation could be the different  $\text{Ca}^{2+}$  affinity. MCU has a very low affinity and therefore needs higher  $\text{Ca}^{2+}$  concentrations to be able to take it up (Stefani et al., 2011). The  $\text{MCU}_{\text{mode2}}$  on the other hand is able to sequester  $\text{Ca}^{2+}$  already at very low  $[\text{Ca}^{2+}]$  (Wei et al., 2012). If indeed TMBIM5 represents this  $\text{MCU}_{\text{mode2}}$  it may be able to replace MCU to some extent. It is less likely to work the other way around. Nonetheless, it is hard to explain why MCU is downregulated

in the absence of TMBIM5. This would rather point towards TMBIM5 as a  $\text{Ca}^{2+}$  efflux channel that balances MCU-mediated influx. In its absence, downregulation of MCU would prevent the accumulation of  $\text{Ca}^{2+}$ . The problem is that this model would not work under physiological conditions. Due to the MMP, the  $\text{Ca}^{2+}$  driving force is directed inwards and there is no such thing as a passive “mitochondrial  $\text{Ca}^{2+}$  efflux channel”. Ahn et al. (Ahn et al., 2009) suggested a  $\text{Ca}^{2+}/\text{H}^+$  antiporter activity for BI-1/TMBIM6 which they based on experiments with reconstituted liposomes. This is an unlikely mode of action for BI-1 as there is no proton gradient at the ER-membrane which would be necessary for the antiport (Bultynck et al., 2014). Yet, it may be an interesting approach to investigate if TMBIM5 is able to mediate  $\text{Ca}^{2+}/\text{H}^+$ -antiport.

In any case, the relationship between MCU and TMBIM5 can only be platonic i.e. via an intermediate mechanistic link because they do not show any sign of physical contact. Notably, MICU1 and TMBIM5 appeared to reside in the same protein complex. What made this pairing so interesting is that TMBIM5 does not contain any  $\text{Ca}^{2+}$ -sensing domain while MICU1 contains two canonical EF-hands. Furthermore, beyond its mtCU gatekeeping, MICU1 was recently reported to regulate mitochondrial cristae structure and the CJs (Gottschalk et al., 2019; Tomar et al., 2019). Hence, an interaction could explain the structural defects observed in TMBIM5 KO cells. We considered/hypothesised that MICU1 confers  $\text{Ca}^{2+}$  sensitivity to TMBIM5 and together they regulate cristae organisation. This idea was supported by a recent publication by Gottschalk et al. (Gottschalk et al., 2019) who demonstrated that MICU1 is not permanently associated with the mtCU. In fact, at low  $[\text{Ca}^{2+}]_{\text{cyto}}$  only MICU1 localises to the inner boundary membrane whereas MCU and EMRE, the essential MCU regulator and scaffolding protein, are evenly distributed across the whole inner membrane. Only upon elevation of the cytosolic  $[\text{Ca}^{2+}]$  do all mtCU components accumulate at the inner boundary membrane and allow  $\text{Ca}^{2+}$  influx (Gottschalk et al., 2019). Hence, TMBIM5 and MICU1 may interact only at low  $[\text{Ca}^{2+}]_{\text{cyto}}$ . However, despite considerable efforts, the interaction could not be verified with other methods. Potentially, the antibody staining of the BN PAGE membrane was not specific as I did not detect a MICU1-band at the expected size for the mtCU. Even under consideration of recent studies showing that MICU1 is not only and not permanently associated with MCU (Tomar et al., 2019) there should be assembled complexes detectable that contain both, MCU and

MICU1. However, it is of note that studies on the interaction between MCU and MICU1 are mainly based on co-immunoprecipitations and proteomic data (Baughman et al., 2011; Plovanich et al., 2013; Sancak et al., 2013). Plovanich et al. observed that the size of the MCU-containing complex is reduced in the absence of MICU1 (Plovanich et al., 2013). Yet, to my knowledge, there is no published data showing that they are detected in the same complex by using BN PAGE.

I did detect an interaction of TMBIM5 with another EF-hand containing protein, LETM1. LETM1 is a much-discussed antiporter at the IMM that exports either  $\text{Ca}^{2+}$  or  $\text{K}^+$  in exchange for protons (Shao et al., 2016; Austin et al., 2017). Interestingly, the two proteins dissociated upon depolarization of the mitochondria and loss of TMBIM5 did not affect LETM1 abundance or complex formation. Unfortunately, the interaction could not be verified via co-immunoprecipitation by a colleague. Yet, the proximity ligation assay which I conducted has some advantages over the co-IP. It is a lot more sensitive and does not require transfection/overexpression. In addition, the PLA can also detect very weak or transient contacts which may be the case for LETM1 and TMBIM5. They may only interact at certain conditions, e.g. depending on  $\text{Ca}^{2+}$  or pH. TMBIM5 and LETM1 have several interesting commonalities. Similar to the TMBIM5 KO, the deletion of the LETM1 homologous gene *YOL027* in yeast leads to a diminished MMP, reduced  $\text{Ca}^{2+}$  influx and a deranged, swollen mitochondrial morphology (Nowikovsky et al., 2004). Nowikovsky et al. attribute the structural changes to the loss of  $\text{K}^+$  export from the matrix. Besides  $\text{Na}^+$ ,  $\text{K}^+$  is the main osmoregulator of mitochondrial volume and the accumulation of  $\text{K}^+$  causes swelling and a disruption in the cristae structure. Another noteworthy parallel is the potential effect on the biogenesis of the ETS complexes. As mentioned above, the loss of TMBIM5 causes the downregulation of several subunits of the ETS and ribosomal proteins. Similarly, KO of two yeast homologs caused a reduction in complex III and IV abundance (Frazier et al., 2006). Interestingly, in this study, Frazier et al. also provided evidence for a possible direct interaction between LETM1 and mitochondrial ribosomes (Frazier et al., 2006) which was later supported and verified for mammalian LETM1 by Durigon et al. (Durigon et al., 2018). Hence, in addition to its ion exchanger function, LETM1 seems to play a role in the regulation of mitochondrial protein synthesis. Based on the many similarities and the putative transient interaction that I detected, TMBIM5 may be

somehow implicated in this process. Moreover, if TMBIM5 influences LETM1 function, this may also alter K<sup>+</sup> homeostasis in TMBIM5 KO cells and provide an additional explanation for the observed morphological aberrances. In summary, the identified interaction raises more questions than it answers and reveals a worthwhile new research topic.

Research with immortalised cell lines such as HEK293 or HAP1 cells is very attractive as it is easy to induce genetic modifications and the handling is simple and cost-effective. It is certainly useful to tackle some basic, mechanistic questions on a molecular level. Nonetheless, it comes with serious downsides. Cell cultures are rather artificial systems. Cells that originate from three-dimensional organs like the human liver are forced to grow in a monolayer attached to a plastic surface and are exposed to much higher oxygen levels than in their physiological environments. All of this leads to cellular stress and changes in physiological processes (Halliwell, 2014; Kapałczyńska et al., 2018). Of particular relevance is the so-called Crabtree-effect which describes a metabolic shift from oxidative phosphorylation to predominant glycolytic energy production in cultured cells (Kok et al., 2021). For obvious reasons, this makes mitochondrial research with cell lines somewhat dubious. This is why we decided to focus on the *in vivo* and *in situ* phenotype in our mouse model. We obtained a mouse line carrying a point mutation in TMBIM5. One of the two aspartic acids (D326) constituting the putative pH-sensing motif in the pore domain was exchanged for an alkaline residue (arginine, R). This exchange was eponymous for the line name D326R. The di-aspartyl motif is highly conserved and studies on BI-1 showed that replacing only one of the aspartic acids by arginine results in the loss of its Ca<sup>2+</sup> permeability (Bultynck et al., 2012). Based on the sequence homology, we presumed that D326R ought to act as a loss-of-function mutation in the mouse.

The brave idea behind this minimalistic mutation instead of a complete knockout was simple: From all that we know about TMBIM5 so far, it seems to be involved in multiple functions. A knockout would have affected them all and made them indistinguishable. We aimed to specifically target the putative channel function of TMBIM5 leaving possible other roles untouched.

This hope was only partially fulfilled. In primary embryonic fibroblasts and all tissue samples isolated from the D326R mice, I observed a strong decrease of TMBIM5 abundance compared to WT which means that all results have to be interpreted as a TMBIM5

knockdown. However, this also demonstrates that the point mutation must have a drastic effect on TMBIM5 function. Its degradation can either suggest that it is inoperable, as anticipated or the mutated form even has a detrimental effect on the cells. Nonetheless, the remaining protein may still exert some of its other functions – as hoped for – because mitochondrial characteristics were a lot less affected in D326R pMEFS than in the KO cell lines. They exhibited normal respiration, only minor changes in mitochondrial morphology and even a small increase in MMP. Nevertheless, another indicator for the impact of the mutation was an abnormality in the Mendelian distribution of the offspring. According to the Mendelian laws of inheritance, from a heterozygous breeding one would expect 50 % heterozygous and 25 % homozygous offspring for each allele. Quantification of the genotyping results, however, revealed a shift towards an increased fraction of homozygous WT animals which was not present in E14 embryos. This indicates increased perinatal lethality in homozygous D326R mice. Potentially, there is a class of severely affected individuals that cannot cope with the consequences of the mutation. In contrast, the animals surviving until the age of three weeks seem to have established some compensatory or rescue mechanism that allows them to develop and behave normally. I did not observe any differences in the longevity, general behaviour and basic metabolism of adult animals. It remains unclear what distinguishes these two groups, what are the mechanisms that kill one or rescue the other. Nonetheless, this outcome is not even very surprising considering that there are several viable *Mcu* knockout mouse models. The group of Toren Finkel made the interesting discovery that *Mcu* KO mice on an inbred C57Bl6 background die around E11.5- E13.5 whereas outbred mice (C57Bl6 and CD1) are viable and indeed unexpectedly healthy (Pan et al., 2013; Murphy et al., 2014). Although mitochondria from the outbred mice did not exhibit any considerable Ca<sup>2+</sup> uptake, their morphology and basic metabolism were not affected whatsoever (Pan et al., 2013). Interestingly, analogue to my observation, they observed a shift in the Mendelian distribution indicating increased perinatal lethality. Yet again, there seems to be a fraction of animals that are heavily affected while the rest can overcome the deficit. The same applies to the different outcomes of outbred versus inbred MCU KO. What is it that discerns them? What makes the difference between embryonic lethality and a very mild phenotype? There are two possible explanations. Either mitochondrial Ca<sup>2+</sup> uptake is a lot

less important than assumed. Or there are one or more backup mechanisms that can compensate for the lack of MCU. Notably, Pan et al. reported the complete loss of rapid  $\text{Ca}^{2+}$  uptake in isolated MCU KO mitochondria from the heart and skeletal muscle and in pMEFs. However, the basal  $[\text{Ca}^{2+}]$  in the mitochondrial matrix was lower but not zero indicating that there must be some - possibly slower and differentially activated -  $\text{Ca}^{2+}$  influx pathway. Very similar results concerning overall mouse phenotype and  $\text{Ca}^{2+}$  handling were obtained in other tissue-specific and/or inducible MCU KO lines (Luongo et al., 2015; Rasmussen et al., 2015; Wu et al., 2015). Wu et al. generated a mouse line expressing a dominant-negative form of MCU in cardiomyocytes and offer a possible third explanation. They stimulated isolated cardiac pacemaker cells and whole hearts with isoproterenol and showed that MCU or its loss do not affect basal cardiac function but is important during fight or flight responses (Wu et al., 2015). This again is in line with a reduced exercise capacity of MCU KO mice reported by the group of Dr T. Finkel (Pan et al., 2013). All of this suggests that mitochondrial  $\text{Ca}^{2+}$  uptake may not be essential under baseline or resting conditions but is only required in response to a sudden change of activity or during intense exercise. This adaptation is particularly important in cardiac and skeletal muscle cells.

To test whether our D326R mice exhibit a similar phenotype, I assessed their endurance by an exhaustive exercise protocol on an inclined treadmill. Simultaneously, the respiratory exchange ratio (RER,  $V_{\text{CO}_2}/V_{\text{O}_2}$ ) was monitored as a measure of whole-body metabolism. Surprisingly, neither of the readouts revealed a difference between WT and the transgene mice. The D326R even showed a slight, albeit not significant, tendency towards increased endurance. As biomarkers for exhaustion, I measured the concentration of IL-6 and lactate in the peripheral blood of the mice at baseline and after the exercise. Lactate is a by-product of anaerobic respiration and is, therefore, a commonly used indirect marker for muscular fatigue (Lucertini et al., 2017). IL-6 is a proinflammatory cytokine which - amongst others - is released from muscles during exercise (Hojman et al., 2019) but can also indicate a dysregulation in mitochondrial degradation after exhaustive exercise (Sliter et al., 2018). Yet, both markers were found at equal concentrations which further supports the conclusion that the two groups do not differ in their physical condition or metabolism during exercise.

If both, MCU and TMBIM5 act as  $\text{Ca}^{2+}$  uptake channels, they might be able to compensate for each other to some extent and thereby additionally mitigate the phenotype. However, it is hard to explain why the MCU KO mice exhibit stronger impairments than the D326R mice. This is in contrast to my prior hypothesis that TMBIM5 can balance the loss of MCU but not vice versa. Yet, this was based on protein expression data from cell lines and may not be transferrable to the mouse. Moreover, TMBIM5 may act as a compensatory  $\text{Ca}^{2+}$  channel in the viable MCU KO mice thereby attenuating the phenotype. But then it does not seem to have the same capacity in the inbred C57Bl6 MCU KO mouse line which is not viable. This would make C57Bl6 an unsuitable mouse strain to investigate TMBIM5 function. To clarify the role of TMBIM5 in the different MCU KO mouse lines, its expression levels should be compared.

Another lesson we can learn from the MCU KO mice lines is that even a remarkable phenotype may not be obvious at first glance. We speculated that alterations caused by the loss of TMBIM5 may not be detectable on the organismic level. Thus, I studied cell-type-specific functions on the molecular level. I focused on organs and organ systems that rely on proper  $\text{Ca}^{2+}$  signalling and have a high energy demand such as the immune system, the cortex, liver, heart and skeletal muscle.

In peripheral blood from D326R mice, I observed an impaired innate immune response. The phagocytes seemed to be less capable of producing the so-called oxidative burst. This is the sudden release of large amounts of ROS produced by the NADPH-oxidase complex (Dahlgren C. and Karlsson A., 1991). Interestingly, the difference was only observed in venous blood but not in samples withdrawn from the heart. It was not expected to find major differences between venous and cardiac blood and this was rather puzzling for us. One possible reason could be that – in contrast to the venous samples - the cardiac blood samples were taken *post mortem*. Possibly, the withdrawal took too long and the blood had already started to coagulate and deoxygenate which might have influenced the measurement. Another potential reason may be the status of oxygenation in the different blood samples. The blood in the heart is freshly oxygenised while venous blood has a much lower oxygen concentration. This may have affected the readout.

However, there are two possible explanations for the reduced respiratory burst in peripheral blood: 1. All cellular antioxidative systems are NADPH-dependent including the

recovery of GSH from GSSG but also the activity of catalases and superoxide dismutases (Stanton, 2012). It is possible that no changes for the redox system are detected *per se* but that the cells expressing the mutated TMBIM5 indeed suffer from increased oxidative stress and thereby use more NADPH for the antioxidative defence. This would leave a diminished NADPH pool and insufficient substrate for the NADPH-oxidase complex. 2. A second explanation could lie further downstream of the NADPH synthesis as another NADPH-producing enzyme is the nicotinamide nucleotide transhydrogenase (NNT). The NNT is localised at the inner mitochondrial membrane and uses the membrane potential to transform NADH to NADPH (Rao et al., 2020). Thus, it relies on proper mitochondrial functioning in two aspects, firstly a sufficient NADH supply by the TCA cycle and secondly, an intact membrane potential. Both are possibly affected by the loss of TMBIM5 function. Moreover, Rao et al. (Rao et al., 2020) recently published that knockdown of NNT leads to an increase of mitochondrial ROS production in combination with a decrease in the NADPH/NAD<sup>+</sup> ratio. This would increase oxidative stress and promote antioxidative reactions as described above. All these processes may drain the available NADPH pool which could then manifest in the observed loss of respiratory burst capacity. Nonetheless, all this is based on assumptions and requires further research. Unfortunately, this exceeded the scope of this work. Interesting parameters to examine would be the cellular NADPH abundance, mitochondrial ROS production and membrane potential in WT and D326R phagocytes.

In cortical tissue, I observed the same trends for protein expression as detected in the cell lines. MCU was marginally decreased and OPA1 splicing seemed to be enhanced. As mentioned before, both effects were less pronounced than in cells, possibly due to the incomplete knockout. The Ca<sup>2+</sup> handling detected in isolated mitochondria was not affected by the changes in protein expression. Of note, even after the addition of large amounts of Ca<sup>2+</sup> no mPTP opening was observed, neither in WT nor in D326R. This is in line with the findings from Andreyev et al. (Andreyev and Fiskum, 1999) who reported that brain mitochondria do not exhibit typical mPTP properties. The authors show that mitochondria isolated from the brain can accumulate much more Ca<sup>2+</sup> than liver mitochondria and that they have an mPTP independent mechanism for the release of cyt *c* (Andreyev and Fiskum, 1999). In my experiments, I repeatedly observed that the D326R mitochondria ceased

taking in  $\text{Ca}^{2+}$  earlier than the WT mitochondria. However, this effect was CsA-insensitive and could therefore not be attributed to the mPTP. Could this represent the mPTP-independent release mode described by Andreyev et al.? Yet, it is important to state that this was also just a tendency and not statistically significant. Moreover, mPTP activity in brain mitochondria was later shown in multiple publications (Friberg and Wieloch, 2002; Hamilton et al., 2018). It may be more sensitive to inhibitory compounds in the buffer, e.g. ATP or  $\text{Mg}^{2+}$  which could explain the high  $\text{Ca}^{2+}$  retention capacity observed by Andreyev et al. and me (Andreyev and Fiskum, 1999).  $\text{Ca}^{2+}$  uptake and the buffering capacity did not depend on NCLX activity which was shown by different concentrations of  $\text{Na}^+$  and in the presence of the NCLX-inhibitor CGP. It was quite unexpected, that  $\text{Ca}^{2+}$  uptake in brain mitochondrial was not affected by the loss of TMBIM5 at all. Hamilton and co-workers recently reported that  $\text{Ca}^{2+}$  uptake was completely abolished in MCU KO mitochondria isolated from the liver, heart and skeletal muscle but not in brain mitochondria (Hamilton et al., 2018). We hypothesised that the residual uptake may be mediated by TMBIM5 but this does not seem to be the case unless it is yet again compensated and masked by MCU activity.

The situation looked different in D326R liver mitochondria which did show a mild dysfunction in  $\text{Ca}^{2+}$  homeostasis. Liver mitochondria were pre-swollen and showed additional changes in swelling behaviour. This is specific to  $\text{Ca}^{2+}$  as no difference was detected in  $\text{Na}^+$ -induced swelling. This means that they had a higher basal matrix volume likely caused by an accumulation of  $\text{Ca}^{2+}$  and consequent mPTP activity. Both could be caused by several factors: the mPTP is sensitised by  $\text{Ca}^{2+}$ , phosphate and free fatty acids. We do not have a reason to believe that TMBIM5 affects one of the latter. Hence, it is likely that  $\text{Ca}^{2+}$ -induced transient mPTP opening led to the volume increase. Interestingly, the liver is the only tissue in which MCU is upregulated in the D326R background. This may be a compensatory response to the loss of TMBIM5. Yet, the lack of MCU gatekeeping could then cause excessive  $\text{Ca}^{2+}$  uptake. Normally, in liver mitochondria, the ratio of MICU1 to MCU expression is close to one (Paillard et al., 2017). This means that nearly every mtCU contains MICU1 as a gatekeeping unit. Increased MCU expression alone allows unregulated  $\text{Ca}^{2+}$  uptake. I did not quantify the ratio of MICU1:MCU in D326R liver because unfortunately, the anti-MICU1 antibody did not work reliably with liver samples. However,

it seems likely that the ratio is reduced in the D326R liver mitochondria due to the increased abundance of MCU which would be a plausible explanation for the swollen phenotype. The lack of gatekeeping of MCU may have caused excessive  $\text{Ca}^{2+}$  accumulation in the matrix leading to the detected swelling. Nonetheless, the impact of the mutation on the liver seems to be moderate as general hallmarks for liver health (e.g. liver enzymes in the peripheral blood, microscopic morphology) are not compromised.

In the heart, the point mutation of TMBIM5 caused mild impairments in cardiac function (i.e. ejection fraction and cardiac output) as well as changes in mitochondrial morphology. While the expression levels of MCU and LETM1 were not affected, OPA1 again showed the same tendency towards enhanced splicing. The accumulation of s-OPA1 likely explains the rather fragmented phenotype of the mitochondria. The respiratory capacity of cardiac cells was reduced at all states. This may be explained by the interaction of TMBIM5 with CHCHD2 and their joint stabilisation of cyt *c* at the IMM. Yet, this should only affect the electron transfer from complex III to IV. It is tempting to assume that the reduced respiratory capacity is due to changes in the matrix  $[\text{Ca}^{2+}]$ . However, the high concentration of EGTA in the preparation medium (BIOPS) chelates nearly all available  $\text{Ca}^{2+}$  and thereby equalises  $[\text{Ca}^{2+}]_{\text{mito}}$  in WT and D326R mitochondria. Thus, the lack of the stimulating effect of  $\text{Ca}^{2+}$  on ATP synthesis cannot be the cause. The increased receptor control ratio of D326R rather indicates an impaired coupling efficiency. Usually, this means that a larger amount of protons enters the mitochondrial matrix without passing the ATP synthase. This could have several reasons. There may be an increased proton flux through the uncoupling proteins (UCP1-3) (Demine et al., 2019) or a larger portion of protons is used by the activity of the cation- $\text{H}^+$ -antiporters, namely mNHE, KHE and CHX (Austin et al., 2017; Berry et al., 2018). I excluded that the reduction in respiration is caused or accompanied by a loss of the ETS complexes or their assembly or a general reduction in mitochondrial abundance. In contrast to the functional and morphological changes in D326R heart mitochondria, there were no differences detected in mitochondrial  $\text{Ca}^{2+}$  handling (i.e. uptake, retention capacity, matrix swelling). The fact that neither  $\text{Ca}^{2+}$ - nor  $\text{Na}^+$ -induced swelling showed any abnormality in D326R mitochondria speaks against an altered activity of mNHE or CHX as hypothesised above. All of this indicates that of the two supposed functions of TMBIM5 – cristae structure versus  $\text{Ca}^{2+}$  flux – the latter does not play a major role in cardiac

mitochondria. Could a structural change explain the described findings? In fact, destabilisation and widening of the CJs would allow proton diffusion from the cristae lumen to the IMS. This diminishes the availability of protons to drive the ATP synthase and lowers the coupling efficiency. The impact is rather weak and accordingly only causes minor deficiencies in cellular and cardiac function. The CJ weakening may be a result of the consistently observed dyshomeostasis of l- and s-OPA1 isoforms. The transmission electron microscopy images from cardiac tissue did not reveal striking changes in cristae organisation. Yet, a higher resolution would have been necessary to analyse the structure and width of the CJs. Therefore, this hypothesis certainly requires verification e.g. via high-resolution electron microscopy and quantification of the MMP in cardiac mitochondria as the potential inducer of OPA1 processing.

In skeletal muscle, the point mutation in TMBIM5 had a more dramatic effect. The mice displayed a reduced grip strength on the macroscopic level and a severe myopathy with changes in the mitochondrial  $\text{Ca}^{2+}$  uptake and the retention capacity on the molecular level. Unfortunately, in this case, we face again the “hen or egg”-problem. Do the structural defects cause dysfunctional  $\text{Ca}^{2+}$  handling? Or does the disturbance in  $\text{Ca}^{2+}$  uptake lead to downstream detrimental effects on mitochondrial morphology? Not the easiest but the most straightforward way to answer these questions would be a patch-clamp measurement with isolated mitochondria. This would at least rule out an involvement of the MMP and possible differences in the basal  $\text{Ca}^{2+}$  content. In addition, in this setup, it would be very interesting to subject the mitochondria to low  $[\text{Ca}^{2+}]$  ( $<2 \mu\text{M}$ ) in the absence or presence of submicromolar concentrations of RuR to elucidate whether TMBIM5 shows characteristics of the other reported  $\text{Ca}^{2+}$  modes (Sparagna et al., 1995; Wei et al., 2012). Ideally,  $\text{Ca}^{2+}$  currents should be measured in mitochondria isolated not only from skeletal muscle but also other tissues as conducted by Fieni et al. (Fieni et al., 2012).

Something that the D326R mouse definitely taught us is that the role of TMBIM5 is highly tissue-specific. While this makes it a lot more demanding to elucidate its function it is not very surprising. Although the analysed tissues have major common features such as the central role of  $\text{Ca}^{2+}$  signalling and high energy demand, these are mostly outweighed by the differences. This is emphasised by the drastic discrepancy in the outcome of skeletal muscle versus cardiac tissue even though these two share a lot of similarities. They are both

comprised of excitable cells that are regulated by the occurrence and frequency of  $\text{Ca}^{2+}$  spikes in the cytosol. In both tissues, mitochondria are the predominant source of ATP and  $\text{Ca}^{2+}$  is the main link matching energy demand and ATP production in a feed-forward/feedback loop (Balaban, 2009; Schiaffino and Reggiani, 2011). Nevertheless, striking differences in mitochondrial  $\text{Ca}^{2+}$  cycling have been revealed by others already. Fieni and co-workers (Fieni et al., 2012) measured  $\text{Ca}^{2+}$  uptake currents in isolated mitochondria from various tissues and detected a strong variance.  $\text{Ca}^{2+}$  influx to skeletal muscle mitochondria exceeds the one measured in cardiac mitochondria by far (Fieni et al., 2012). The authors argue that this may be explained by the physiological differences of the cell types: The continuous cytosolic  $\text{Ca}^{2+}$  oscillations in cardiac cells put the mitochondria at a high risk of  $\text{Ca}^{2+}$  overload. To prevent this, beat-to-beat  $\text{Ca}^{2+}$  influx has to be limited. For skeletal muscle mitochondria, on the other hand, cytosolic  $[\text{Ca}^{2+}]$  elevations are an important signal to enhance ATP generation. Hence, they must be able to sequester considerable amounts (Fieni et al., 2012). But how do the cells achieve this differential regulation of  $\text{Ca}^{2+}$  uptake? Although skeletal muscle exhibits the highest expression level of MCU (Stefani et al., 2011) this clearly cannot be the only regulatory mechanism. Paillard et al. (Paillard et al., 2017) provided evidence that the stoichiometry of MCU and MICU1 affects the threshold and uptake velocity for MCU. A high ratio of MICU1:MCU represents strict gatekeeping which results in a high  $\text{Ca}^{2+}$  threshold but also a higher maximal activity which is achieved by MICU1 cooperativity (Paillard et al., 2017). The abundance of MICU1 and the ratio MICU1:MCU is very low in cardiac tissue which correlates with a low threshold and a low maximal uptake rate (Paillard et al., 2017).  $\text{Ca}^{2+}$  uptake through mtCU is additionally controlled by the integration of MCUB in cardiac mitochondria (Raffaello et al., 2013). MCUB is a dominant-negative paralog of MCU and its abundance relative to MCU is manyfold higher in the murine heart compared to skeletal muscle tissue (Raffaello et al., 2013). Moreover, in skeletal muscle, a unique MICU1 splice variant (MICU1.1) was identified that increases the sensitivity of mtCU to  $\text{Ca}^{2+}$  and thereby induces uptake at lower  $[\text{Ca}^{2+}]$  (Vecellio Reane et al., 2016).

This is only to mention a few of the tissue-specific modifications of the mtCU. The evidence for further regulatory mechanisms e.g. posttranslational modifications of its components is rapidly growing (Tarasova et al., 2019; Feno et al., 2021). Coming back to TMBIM5: Why

did I mention the cell-type-dependence of MCU-mediated  $\text{Ca}^{2+}$  uptake at all? It was to demonstrate the diversity of this process. If it differs so much in similar cells like myocytes in the heart and in the skeletal muscle one can only imagine the complexity when it comes to neurons or hepatocytes. Can one protein complex meet this tremendous range of requirements? Even if so – it seems very unlikely that evolution would allow the cells to “walk the tightrope” (Demaurex and Distelhorst, 2003) without a rescue net.

TMBIM5 is ubiquitously expressed in mouse tissue and in the most common cell lines and there is no specific inhibitor known to date. This means that TMBIM5 was present in all the electrophysiological studies described above. Could it be that it partially contributed to the measured  $\text{Ca}^{2+}$  flux? Paillard et al. (Paillard et al., 2017) and Vecellio Reane et al. (Vecellio Reane et al., 2016) only verified the MCU-dependence of their measured current by the addition of 2-3  $\mu\text{M}$  RuR. This concentration would also block the putative alternative  $\text{Ca}^{2+}$  currents described by Sparagna et al. (Sparagna et al., 1995) and Wei et al. (Wei et al., 2012) and is therefore not an ideal control. Fieni et al. (Fieni et al., 2012), on the contrary, carefully verified the identity of the channel activity. By comparing the biophysical properties e.g. the response to submicromolar RuR, increasing  $[\text{Ca}^{2+}]$  and other cations, they validated that the diverse current densities they measured in the different mouse tissues (heart, skeletal muscle, liver etc.) are mediated by the same channel, MCU. Hence, it is unlikely that TMBIM5 activity contributed to the measured fluxes. Yet, it is not impossible and it would be of great interest to investigate a double knockout model of MCU and TMBIM5. In fact, this is currently being done in our lab in *Drosophila melanogaster* and the results are eagerly awaited.

To prevent  $\text{Ca}^{2+}$  accumulation in the mitochondrial matrix, its influx has to be balanced by the export via antiporters. Their activity level can additionally shape cytosolic and mitochondrial  $\text{Ca}^{2+}$  signals. In excitable tissues such as the heart and the brain,  $\text{Ca}^{2+}$  extrusion is predominantly mediated by NCLX while in the liver and other organs the yet unidentified mCHX seems to play a larger role (Crompton et al., 1978; Rysted et al., 2021). The strongest candidate for the molecular nature of the mCHX is LETM1. Yet, it is still under debate whether it exports  $\text{Ca}^{2+}$  or  $\text{K}^+$  in exchange for  $\text{H}^+$  (Austin and Nowikovsky, 2019). Interestingly, I detected an interaction between LETM1 and TMBIM5. Could it be that TMBIM5 influences  $\text{Ca}^{2+}$  extrusion? Most of my results obtained from cultured cell lines and

mouse tissue rather point towards involvement in  $\text{Ca}^{2+}$  uptake. Nonetheless, based on its homology to BI-1 and BsYetJ, TMBIM5 likely acts as a passive  $\text{Ca}^{2+}$  channel (Bultynck et al., 2012; Chang et al., 2014). This means that it can mediate influx or efflux – depending on the conditions. In healthy mitochondria, the negative MMP is the driving force for  $\text{Ca}^{2+}$  and it is directed inwards. Yet, by pumping protons from the matrix in the IMS, the ETS does not only generate an electrical gradient but also a  $\Delta\text{pH}$  between the two compartments. The pH in the matrix lies at around 7.3 whereas it reaches  $\text{pH} = 8$  in the IMS (Kühlbrandt, 2015). BsYetJ and BI-1 have the highest  $\text{Ca}^{2+}$  permeability at a near-neutral pH which is strongly decreased at alkaline pH (Kiviluoto et al., 2013; Chang et al., 2014). It is assumed that the di-aspartyl motif in the TMBIM5 pore domain exhibits the same pH sensitivity. This means that it may be closed under normal conditions in case it senses pH in the IMS as it was suggested by Oka and co-workers (Oka et al., 2008). To date, it is not entirely clear whether the pH-sensing motif in TMBIM5 faces the matrix or the IMS side. The transfer of a recent model for BsYetJ to TMBIM5 supports the notion of Oka et al. that it is directed towards the IMS (Guo et al., 2019). However, the additional eighth transmembrane domain which is present in TMBIM5 but not in BsYetJ/BI-1 may revert its membrane orientation. This is certainly a critical question that should be addressed in the near future. Assuming that TMBIM5 senses the pH in the IMS and is closed under healthy conditions it could act as a sort of rescue mechanism. A drop in MMP accompanied by a drop in pH in the IMS would increase TMBIM5 permeability and allow  $\text{Ca}^{2+}$  flux according to the concentration gradient. Yet, this is speculative and awaits elucidation.

In conclusion, with this work, I provide evidence that TMBIM5 is not associated with the MICOS and does not exert a direct effect on the mitochondrial cristae structure. The observed disorganisation in its absence is likely due to changes in OPA1 processing. It is not entirely clear how this is affected by the loss of TMBIM5. One explanation is the reduced MMP that we observed in TMBIM5 KO cells which induces the activity of the two proteases responsible for OPA1 splicing. The reduction in MMP, in turn, may be elicited by the loss of two putative functions of TMBIM5: 1) It is thought to support ETS efficiency by stabilising cyt *c* at the IMM. 2)  $\text{Ca}^{2+}$  influx through TMBIM5 can stimulate the activity of several dehydrogenases and the ATP synthase. My results obtained from TMBIM5 KO cells and the D326R mouse line suggest that TMBIM5 is involved in mitochondrial  $\text{Ca}^{2+}$  handling.

However, many open questions remain regarding its open or closed state, the direction and physiological function of the mediated  $\text{Ca}^{2+}$  flux. The mouse model revealed that the influence of TMBIM5 seems to be extremely tissue-specific. Similar observations have been made for other mitochondrial proteins involved in  $\text{Ca}^{2+}$  cycling. This is based on the fact that  $\text{Ca}^{2+}$  is not only a universal intracellular messenger but also one of the most versatile ones. Its signalling varies strongly from cell-type to cell-type and therefore requires a fine-tuned  $\text{Ca}^{2+}$  handling machinery that can adapt to the specific demands. Despite the impressive research progress in the last decades, many gaps and open questions persist particularly with regard to tissue-specific  $\text{Ca}^{2+}$  trafficking. What we know so far may not be the tip of the iceberg – but maybe half of it.

## 7. References

---

- Agarwal, A., Wu, P.-H., Hughes, E.G., Fukaya, M., Tischfield, M.A., Langseth, A.J., Wirtz, D., and Bergles, D.E. (2017). Transient Opening of the Mitochondrial Permeability Transition Pore Induces Microdomain Calcium Transients in Astrocyte Processes. *Neuron* 93, 587-605.e7. <https://doi.org/10.1016/j.neuron.2016.12.034>.
- Ahn, T., Yun, C.-H., Chae, H.Z., Kim, H.-R., and Chae, H.-J. (2009).  $\text{Ca}^{2+}/\text{H}^{+}$  antiporter-like activity of human recombinant Bax inhibitor-1 reconstituted into liposomes. *The FEBS journal* 276, 2285-2291. <https://doi.org/10.1111/j.1742-4658.2009.06956.x>.
- Ahting, U., Thun, C., Hegerl, R., Typke, D., Nargang, F.E., Neupert, W., and Nussberger, S. (1999). The TOM core complex: the general protein import pore of the outer membrane of mitochondria. *The Journal of cell biology* 147, 959-968. <https://doi.org/10.1083/jcb.147.5.959>.
- Alam, M.S. (2018). Proximity Ligation Assay (PLA). *Current protocols in immunology* 123, e58. <https://doi.org/10.1002/cpim.58>.
- Anand, R., Wai, T., Baker, M.J., Kladt, N., Schauss, A.C., Rugarli, E., and Langer, T. (2014). The i-AAA protease YME1L and OMA1 cleave OPA1 to balance mitochondrial fusion and fission. *The Journal of cell biology* 204, 919-929. <https://doi.org/10.1083/jcb.201308006>.
- Andreyev, A., and Fiskum, G. (1999). Calcium induced release of mitochondrial cytochrome c by different mechanisms selective for brain versus liver. *Cell Death and Differentiation* 6, 825-832. <https://doi.org/10.1038/sj.cdd.4400565>.
- Angelin, A., Bonaldo, P., and Bernardi, P. (2008). Altered threshold of the mitochondrial permeability transition pore in Ullrich congenital muscular dystrophy. *Biochimica et biophysica acta* 1777, 893-896. <https://doi.org/10.1016/j.bbabi.2008.03.026>.
- Arruda, A.P., and Hotamisligil, G.S. (2015). Calcium Homeostasis and Organelle Function in the Pathogenesis of Obesity and Diabetes. *Cell Metabolism* 22, 381-397. <https://doi.org/10.1016/j.cmet.2015.06.010>.

- Arruda, A.P., Pers, B.M., Parlakgöl, G., Güney, E., Inouye, K., and Hotamisligil, G.S. (2014). Chronic enrichment of hepatic endoplasmic reticulum-mitochondria contact leads to mitochondrial dysfunction in obesity. *Nature medicine* 20, 1427-1435. <https://doi.org/10.1038/nm.3735>.
- Ateet Kosaraju, Amandeep Goyal, Yulia Grigorova, and Amgad N. Makaryus (2021). Left Ventricular Ejection Fraction. In StatPearls [Internet], A. Kosaraju, A. Goyal, Y. Grigorova and A.N. Makaryus, eds. (StatPearls Publishing).
- Auranen, M., Ylikallio, E., Shcherbii, M., Paetau, A., Kiuru-Enari, S., Toppila, J.P., and Tynismaa, H. (2015). CHCHD10 variant p.(Gly66Val) causes axonal Charcot-Marie-Tooth disease. *Neurology Genetics* 1, e1. <https://doi.org/10.1212/NXG.0000000000000003>.
- Austin, S., and Nowikovsky, K. (2019). LETM1: Essential for Mitochondrial Biology and Cation Homeostasis? *Trends in Biochemical Sciences* 44, 648-658. <https://doi.org/10.1016/j.tibs.2019.04.002>.
- Austin, S., Tavakoli, M., Pfeiffer, C., Seifert, J., Mattarei, A., Stefani, D. de, Zoratti, M., and Nowikovsky, K. (2017). LETM1-Mediated K<sup>+</sup> and Na<sup>+</sup> Homeostasis Regulates Mitochondrial Ca<sup>2+</sup> Efflux. *Frontiers in Physiology* 8, 839. <https://doi.org/10.3389/fphys.2017.00839>.
- Azarashvili, T., Grachev, D., Krestinina, O., Evtodienko, Y., Yurkov, I., Papadopoulos, V., and Reiser, G. (2007). The peripheral-type benzodiazepine receptor is involved in control of Ca<sup>2+</sup>-induced permeability transition pore opening in rat brain mitochondria. *Cell calcium* 42, 27-39. <https://doi.org/10.1016/j.ceca.2006.11.004>.
- Balaban, R.S. (2009). The role of Ca(2+) signaling in the coordination of mitochondrial ATP production with cardiac work. *Biochimica et biophysica acta* 1787, 1334-1341. <https://doi.org/10.1016/j.bbabi.2009.05.011>.
- Ban, T., Ishihara, T., Kohno, H., Saita, S., Ichimura, A., Maenaka, K., Oka, T., Mihara, K., and Ishihara, N. (2017). Molecular basis of selective mitochondrial fusion by heterotypic action between OPA1 and cardiolipin. *Nat Cell Biol* 19, 856-863. <https://doi.org/10.1038/ncb3560>.
- Bannwarth, S., Ait-El-Mkadem, S., Chausseot, A., Genin, E.C., Lacas-Gervais, S., Fragaki, K., Berg-Alonso, L., Kageyama, Y., Serre, V., and Moore, D.G., et al. (2014). A mitochondrial origin for frontotemporal dementia and amyotrophic lateral sclerosis through CHCHD10 involvement. *Brain : a journal of neurology* 137, 2329-2345. <https://doi.org/10.1093/brain/awu138>.
- Barrera, M., Koob, S., Dikov, D., Vogel, F., and Reichert, A.S. (2016). OPA1 functionally interacts with MIC60 but is dispensable for crista junction formation. *FEBS letters* 590, 3309-3322. <https://doi.org/10.1002/1873-3468.12384>.
- Baughman, J.M., Perocchi, F., Girgis, H.S., Plovanich, M., Belcher-Timme, C.A., Sancak, Y., Bao, X.R., Strittmatter, L., Goldberger, O., and Bogorad, R.L., et al. (2011). Integrative genomics identifies MCU as an essential component of the mitochondrial calcium uniporter. *Nature* 476, 341-345. <https://doi.org/10.1038/nature10234>.
- Beigl, T.B., Kjosås, I., Seljeseth, E., Glomnes, N., and Aksnes, H. (2020). Efficient and crucial quality control of HAP1 cell ploidy status. *Biology open* 9. <https://doi.org/10.1242/bio.057174>.
- Bernardi, P. (1999). Mitochondrial transport of cations: channels, exchangers, and permeability transition. *Physiological reviews* 79, 1127-1155. <https://doi.org/10.1152/physrev.1999.79.4.1127>.
- Bernardi, P., and Stockum, S. von (2012). The permeability transition pore as a Ca(2+) release channel: new answers to an old question. *Cell calcium* 52, 22-27. <https://doi.org/10.1016/j.ceca.2012.03.004>.

Berry, B.J., Trewin, A.J., Amitrano, A.M., Kim, M., and Wojtovich, A.P. (2018). Use the Protonmotive Force: Mitochondrial Uncoupling and Reactive Oxygen Species. *Journal of Molecular Biology* 430, 3873-3891. <https://doi.org/10.1016/j.jmb.2018.03.025>.

Beutner, G., Sharma, V.K., Giovannucci, D.R., Yule, D.I., and Sheu, S.S. (2001). Identification of a ryanodine receptor in rat heart mitochondria. *Journal of Biological Chemistry* 276, 21482-21488. <https://doi.org/10.1074/jbc.M101486200>.

Beutner, G., Sharma, V.K., Lin, L., Ryu, S.-Y., Dirksen, R.T., and Sheu, S.-S. (2005). Type 1 ryanodine receptor in cardiac mitochondria: transducer of excitation-metabolism coupling. *Biochimica et biophysica acta* 1717, 1-10. <https://doi.org/10.1016/j.bbamem.2005.09.016>.

Bicker, F., Vasic, V., Horta, G., Ortega, F., Nolte, H., Kavyanifar, A., Keller, S., Stankovic, N.D., Harter, P.N., and Benedito, R., et al. (2017). Neurovascular EGFL7 regulates adult neurogenesis in the subventricular zone and thereby affects olfactory perception. *Nat Commun* 8, 15922. <https://doi.org/10.1038/ncomms15922>.

Blomeyer, C.A., Bazil, J.N., Stowe, D.F., Pradhan, R.K., Dash, R.K., and Camara, A.K.S. (2013). Dynamic buffering of mitochondrial Ca<sup>2+</sup> during Ca<sup>2+</sup> uptake and Na<sup>+</sup>-induced Ca<sup>2+</sup> release. *Journal of bioenergetics and biomembranes* 45, 189-202. <https://doi.org/10.1007/s10863-012-9483-7>.

Bohnert, M., Zerbes, R.M., Davies, K.M., Mühleip, A.W., Rampelt, H., Horvath, S.E., Boenke, T., Kram, A., Perschil, I., and Veenhuis, M., et al. (2015). Central Role of Mic10 in the Mitochondrial Contact Site and Cristae Organizing System. *Cell Metabolism* 21, 747-755. <https://doi.org/10.1016/j.cmet.2015.04.007>.

Bondarenko, A.I., Jean-Quartier, C., Malli, R., and Graier, W.F. (2013). Characterization of distinct single-channel properties of Ca<sup>2+</sup> inward currents in mitochondria. *Pflugers Archiv : European journal of physiology* 465, 997-1010. <https://doi.org/10.1007/s00424-013-1224-1>.

Bondarenko, A.I., Jean-Quartier, C., Parichatikanond, W., Alam, M.R., Waldeck-Weiermair, M., Malli, R., and Graier, W.F. (2014). Mitochondrial Ca(2+) uniporter (MCU)-dependent and MCU-independent Ca(2+) channels coexist in the inner mitochondrial membrane. *Pflugers Archiv : European journal of physiology* 466, 1411-1420. <https://doi.org/10.1007/s00424-013-1383-0>.

Bonnet, D., Martin, D., Pascale, D.L., Villain, E., Jouvet, P., Rabier, D., Brivet, M., and Saudubray, J.M. (1999). Arrhythmias and conduction defects as presenting symptoms of fatty acid oxidation disorders in children. *Circulation* 100, 2248-2253. <https://doi.org/10.1161/01.CIR.100.22.2248>.

Bridwell-Rabb, J., Winn, A.M., and Barondeau, D.P. (2011). Structure-function analysis of Friedreich's ataxia mutants reveals determinants of frataxin binding and activation of the Fe-S assembly complex. *Biochemistry* 50, 7265-7274. <https://doi.org/10.1021/bi200895k>.

Broekemeier, K.M., Dempsey, M.E., and Pfeiffer, D.R. (1989). Cyclosporin A is a potent inhibitor of the inner membrane permeability transition in liver mitochondria. *Journal of Biological Chemistry* 264, 7826-7830.

Bultynck, G., Kiviluoto, S., Henke, N., Ivanova, H., Schneider, L., Rybalchenko, V., Luyten, T., Nuyts, K., Borggraeve, W. de, and Bezprozvanny, I., et al. (2012). The C terminus of Bax inhibitor-1 forms a Ca<sup>2+</sup>-permeable channel pore. *J. Biol. Chem.* 287, 2544-2557. <https://doi.org/10.1074/jbc.M111.275354>.

Bultynck, G., Kiviluoto, S., and Methner, A. (2014). Bax Inhibitor-1 Is Likely a pH-Sensitive Calcium Leak Channel, Not a H<sup>+</sup>/Ca<sup>2+</sup> Exchanger. *Sci. Signal.* 7, pe22-pe22. <https://doi.org/10.1126/scisignal.2005764>.

- Buntinas, L., Gunter, K.K., Sparagna, G.C., and Gunter, T.E. (2001). The rapid mode of calcium uptake into heart mitochondria (RaM): comparison to RaM in liver mitochondria. *Biochimica et Biophysica Acta (BBA) - Bioenergetics* 1504, 248-261. [https://doi.org/10.1016/s0005-2728\(00\)00254-1](https://doi.org/10.1016/s0005-2728(00)00254-1).
- Campbell, N.A. (2000). *Biologie* (Heidelberg: Spektrum Akad. Verl. GmbH Heidelberg).
- Carafoli, E. (2003). Historical review: Mitochondria and calcium: ups and downs of an unusual relationship. *Trends in Biochemical Sciences* 28, 175-181. [https://doi.org/10.1016/S0968-0004\(03\)00053-7](https://doi.org/10.1016/S0968-0004(03)00053-7).
- Carraro, M., Checchetto, V., Szabó, I., and Bernardi, P. (2019). F-ATP synthase and the permeability transition pore: fewer doubts, more certainties. *FEBS letters* 593, 1542-1553. <https://doi.org/10.1002/1873-3468.13485>.
- Carraro, M., Giorgio, V., Šileikytė, J., Sartori, G., Forte, M., Lippe, G., Zoratti, M., Szabó, I., and Bernardi, P. (2014). Channel formation by yeast F-ATP synthase and the role of dimerization in the mitochondrial permeability transition. *J. Biol. Chem.* 289, 15980-15985. <https://doi.org/10.1074/jbc.C114.559633>.
- Carrer, A., Tommasin, L., Šileikytė, J., Ciscato, F., Filadi, R., Urbani, A., Forte, M., Rasola, A., Szabó, I., and Carraro, M., et al. (2021). Defining the molecular mechanisms of the mitochondrial permeability transition through genetic manipulation of F-ATP synthase. *Nat Commun* 12, 4835. <https://doi.org/10.1038/s41467-021-25161-x>.
- Carroll, J., He, J., Ding, S., Fearnley, I.M., and Walker, J.E. (2019). Persistence of the permeability transition pore in human mitochondria devoid of an assembled ATP synthase. *PNAS* 116, 12816-12821. <https://doi.org/10.1073/pnas.1904005116>.
- Cathcart M. (2004). Regulation of superoxide anion production by NADPH oxidase in monocytes/macrophages: contributions to atherosclerosis. *Arteriosclerosis, thrombosis, and vascular biology* 24, 23-28. <https://doi.org/10.1161/01.ATV.0000097769.47306.12>.
- Chae, H.-J., Kim, H.-R., Xu, C., Bailly-Maitre, B., Krajewska, M., Krajewski, S., Banares, S., Cui, J., Digicaylioglu, M., and Ke, N., et al. (2004). BI-1 regulates an apoptosis pathway linked to endoplasmic reticulum stress. *Molecular Cell* 15, 355-366. <https://doi.org/10.1016/j.molcel.2004.06.038>.
- Chakrabarti, R., Ji, W.-K., Stan, R.V., Juan Sanz, J. de, Ryan, T.A., and Higgs, H.N. (2018). INF2-mediated actin polymerization at the ER stimulates mitochondrial calcium uptake, inner membrane constriction, and division. *The Journal of cell biology* 217, 251-268. <https://doi.org/10.1083/jcb.201709111>.
- Chang, Y., Bruni, R., Kloss, B., Assur, Z., Kloppmann, E., Rost, B., Hendrickson, W.A., and Liu, Q. (2014). Structural basis for a pH-sensitive calcium leak across membranes. *Science* 344, 1131-1135. <https://doi.org/10.1126/science.1252043>.
- Chen, K., Pittman, R.N., and Popel, A.S. (2008). Nitric oxide in the vasculature: where does it come from and where does it go? A quantitative perspective. *Antioxidants & Redox Signaling* 10, 1185-1198. <https://doi.org/10.1089/ars.2007.1959>.
- Chinopoulos, C., and Adam-Vizi, V. (2010). Mitochondrial Ca<sup>2+</sup> sequestration and precipitation revisited. *The FEBS journal* 277, 3637-3651. <https://doi.org/10.1111/j.1742-4658.2010.07755.x>.
- Cho, B., Cho, H.M., Jo, Y., Kim, H.D., Song, M., Moon, C., Kim, H., Kim, K., Sesaki, H., and Im Rhyu, J., et al. (2017). Constriction of the mitochondrial inner compartment is a priming event for mitochondrial division. *Nat Commun* 8, 15754. <https://doi.org/10.1038/ncomms15754>.

- Christen, P., Jaussi, R., and Benoit, R. (2016a). ATP-Synthase in Mitochondrien. In *Biochemie und Molekularbiologie*, P. Christen, R. Jaussi and R. Benoit, eds. (Berlin, Heidelberg: Springer Berlin Heidelberg), pp. 177–192.
- Christen, P., Jaussi, R., and Benoit, R. (2016b). *Biochemie und Molekularbiologie* (Berlin, Heidelberg: Springer Berlin Heidelberg).
- Christen, P., Jaussi, R., and Benoit, R. (2016c). Glykolyse und Citratzyklus. In *Biochemie und Molekularbiologie: Eine Einführung in 40 Lerneinheiten*, P. Christen, R. Jaussi and R. Benoit, eds. (Berlin, Heidelberg: Springer Berlin Heidelberg), pp. 161–175.
- Ciz, M., Denev, P., Kratchanova, M., Vasicek, O., Ambrozova, G., and Lojek, A. (2012). Flavonoids inhibit the respiratory burst of neutrophils in mammals. *Oxidative medicine and cellular longevity* 2012, 181295. <https://doi.org/10.1155/2012/181295>.
- Clay, H.B., Parl, A.K., Mitchell, S.L., Singh, L., Bell, L.N., and Murdock, D.G. (2016). Altering the Mitochondrial Fatty Acid Synthesis (mtFASII) Pathway Modulates Cellular Metabolic States and Bioactive Lipid Profiles as Revealed by Metabolomic Profiling. *PLoS one* 11, e0151171. <https://doi.org/10.1371/journal.pone.0151171>.
- Crompton, M., and Heid, I. (1978). The cycling of calcium, sodium, and protons across the inner membrane of cardiac mitochondria. *European journal of biochemistry* 91, 599-608. <https://doi.org/10.1111/j.1432-1033.1978.tb12713.x>.
- Crompton, M., Moser, R., Lüdi, H., and Carafoli, E. (1978). The interrelations between the transport of sodium and calcium in mitochondria of various mammalian tissues. *European journal of biochemistry* 82, 25-31. <https://doi.org/10.1111/j.1432-1033.1978.tb11993.x>.
- Csordás, G., Golenár, T., Seifert, E.L., Kamer, K.J., Sancak, Y., Perocchi, F., Moffat, C., Weaver, D., La Perez, S.d.F., and Bogorad, R., et al. (2013). MICU1 controls both the threshold and cooperative activation of the mitochondrial Ca<sup>2+</sup> uniporter. *Cell Metabolism* 17, 976-987. <https://doi.org/10.1016/j.cmet.2013.04.020>.
- Csordás, G., Thomas, A.P., and Hajnóczky, G. (1999). Quasi-synaptic calcium signal transmission between endoplasmic reticulum and mitochondria. *The EMBO journal* 18, 96-108. <https://doi.org/10.1093/emboj/18.1.96>.
- Czabotar, P.E., Lessene, G., Strasser, A., and Adams, J.M. (2014). Control of apoptosis by the BCL-2 protein family: implications for physiology and therapy. *Nature reviews. Molecular cell biology* 15, 49-63. <https://doi.org/10.1038/nrm3722>.
- Dafinca, R., Barbagallo, P., Farrimond, L., Candalija, A., Scaber, J., Ababneh, N.A., Sathyaprakash, C., Vowles, J., Cowley, S.A., and Talbot, K. (2020). Impairment of Mitochondrial Calcium Buffering Links Mutations in C9ORF72 and TARDBP in iPS-Derived Motor Neurons from Patients with ALS/FTD. *Stem cell reports* 14, 892-908. <https://doi.org/10.1016/j.stemcr.2020.03.023>.
- Dahlgren C., and Karlsson A. (1991). Respiratory burst in human neutrophils. *journal of immunological methods*, 3-14.
- Daiber, August M., Baldus S., Wendt M., Oelze M., Sydow K., Kleschyov A. L., and Munzel T. (2003). MEASUREMENT OF NAD(P)H OXIDASE-DERIVED SUPEROXIDE WITH THE LUMINOL ANALOGUE L-012. *Free radical biology & medicine* 36, 101-111. <https://doi.org/10.1016/j.freeradbiomed.2003.09.023>.
- Debattisti, V., Horn, A., Singh, R., Seifert, E.L., Hogarth, M.W., Mazala, D.A., Huang, K.T., Horvath, R., Jaiswal, J.K., and Hajnóczky, G. (2019). Dysregulation of Mitochondrial Ca<sup>2+</sup> Uptake and Sarcolemma

Repair Underlie Muscle Weakness and Wasting in Patients and Mice Lacking MICU1. *Cell reports* 29, 1274-1286.e6. <https://doi.org/10.1016/j.celrep.2019.09.063>.

Del Dotto, V., Fogazza, M., Carelli, V., Rugolo, M., and Zanna, C. (2018). Eight human OPA1 isoforms, long and short: What are they for? *Biochimica et Biophysica Acta (BBA) - Bioenergetics* 1859, 263-269. <https://doi.org/10.1016/j.bbabi.2018.01.005>.

Demaurex, N., and Distelhorst, C. (2003). Cell biology. Apoptosis--the calcium connection. *Science (New York, N.Y.)* 300, 65-67. <https://doi.org/10.1126/science.1083628>.

Demine, S., Renard, P., and Arnould, T. (2019). Mitochondrial Uncoupling: A Key Controller of Biological Processes in Physiology and Diseases. *Cells* 8. <https://doi.org/10.3390/cells8080795>.

Deponte, M. (2013). Glutathione catalysis and the reaction mechanisms of glutathione-dependent enzymes. *Biochimica et biophysica acta* 1830, 3217-3266. <https://doi.org/10.1016/j.bbagen.2012.09.018>.

Dolman, N.J., and Tepikin, A.V. (2006). Calcium gradients and the Golgi. *Cell calcium* 40, 505-512. <https://doi.org/10.1016/j.ceca.2006.08.012>.

Durigon, R., Mitchell, A.L., Jones, A.W., Manole, A., Mennuni, M., Hirst, E.M., Houlden, H., Maragni, G., Lattante, S., and Doronzio, P.N., et al. (2018). LETM1 couples mitochondrial DNA metabolism and nutrient preference. *EMBO Molecular Medicine* 10, e8550. <https://doi.org/10.15252/emmm.201708550>.

Elustondo, P.A., Nichols, M., Negoda, A., Thirumaran, A., Zakharian, E., Robertson, G.S., and Pavlov, E.V. (2016). Mitochondrial permeability transition pore induction is linked to formation of the complex of ATPase C-subunit, polyhydroxybutyrate and inorganic polyphosphate. *Cell Death Discovery* 2, 16070. <https://doi.org/10.1038/cddiscovery.2016.70>.

Epand, R.F., Martinou, J.-C., Fornallaz-Mulhauser, M., Hughes, D.W., and Epand, R.M. (2002). The apoptotic protein tBid promotes leakage by altering membrane curvature. *Journal of Biological Chemistry* 277, 32632-32639. <https://doi.org/10.1074/jbc.M202396200>.

Eskes, R., Desagher, S., Antonsson, B., and Martinou, J.C. (2000). Bid induces the oligomerization and insertion of Bax into the outer mitochondrial membrane. *Molecular and Cellular Biology* 20, 929-935. <https://doi.org/10.1128/MCB.20.3.929-935.2000>.

Esposito, L., Raber, J., Kekoni, L., Yan, F., Yu, G.-Q., Bien-Ly, N., Puoliväli, J., Scarse-Levie, K., Masliah, E., and Mucke, L. (2006). Reduction in mitochondrial superoxide dismutase modulates Alzheimer's disease-like pathology and accelerates the onset of behavioral changes in human amyloid precursor protein transgenic mice. *The Journal of Neuroscience* 26, 5167-5179. <https://doi.org/10.1523/JNEUROSCI.0482-06.2006>.

Essletzbichler, P., Konopka, T., Santoro, F., Chen, D., Gapp, B.V., Kralovics, R., Brummelkamp, T.R., Nijman, S.M.B., and Bürckstümmer, T. (2014). Megabase-scale deletion using CRISPR/Cas9 to generate a fully haploid human cell line. *Genome research*, 2059-2065. <https://doi.org/10.1101/gr.177220.114>.

Falabella, M., Vernon, H.J., Hanna, M.G., Claypool, S.M., and Pitceathly, R.D.S. (2021). Cardiolipin, Mitochondria, and Neurological Disease. *Trends in Endocrinology & Metabolism* 32, 224-237. <https://doi.org/10.1016/j.tem.2021.01.006>.

Feng, S., Li, H., Tai, Y., Huang, J., Su, Y., Abramowitz, J., Zhu, M.X., Birnbaumer, L., and Wang, Y. (2013). Canonical transient receptor potential 3 channels regulate mitochondrial calcium uptake. *Proceedings of the National Academy of Sciences of the United States of America* 110, 11011-11016. <https://doi.org/10.1073/pnas.1309531110>.

- Feno, S., Rizzuto, R., Raffaello, A., and Vecellio Reane, D. (2021). The molecular complexity of the Mitochondrial Calcium Uniporter. *Cell calcium* 93. <https://doi.org/10.1016/j.ceca.2020.102322>.
- Fieni, F., Lee, S.B., Jan, Y.N., and Kirichok, Y. (2012). Activity of the mitochondrial calcium uniporter varies greatly between tissues. *Nat Commun* 3, 1317. <https://doi.org/10.1038/ncomms2325>.
- Finkel, T., Menazza, S., Holmström, K.M., Parks, R.J., Liu, J., Sun, J., Liu, J., Pan, X., and Murphy, E. (2015). The ins and outs of mitochondrial calcium. *Circulation research* 116, 1810-1819. <https://doi.org/10.1161/CIRCRESAHA.116.305484>.
- Fox, C.A., Ellison, P., Ikon, N., and Ryan, R.O. (2019). Calcium-induced transformation of cardiolipin nanodisks. *Biochimica et biophysica acta. Biomembranes* 1861, 1030-1036. <https://doi.org/10.1016/j.bbamem.2019.03.005>.
- Fox, T.D. (2012). Mitochondrial protein synthesis, import, and assembly. *Genetics* 192, 1203-1234. <https://doi.org/10.1534/genetics.112.141267>.
- Frazier, A.E., Taylor, R.D., Mick, D.U., Warscheid, B., Stoepel, N., Meyer, H.E., Ryan, M.T., Guiard, B., and Rehling, P. (2006). Mdm38 interacts with ribosomes and is a component of the mitochondrial protein export machinery. *J Cell Biol* 172, 553-564. <https://doi.org/10.1083/jcb.200505060>.
- Frezza, C., Cipolat, S., Martins de Brito, O., Micaroni, M., Beznoussenko, G.V., Rudka, T., Bartoli, D., Polishuck, R.S., Danial, N.N., and Strooper, B. de, et al. (2006). OPA1 controls apoptotic cristae remodeling independently from mitochondrial fusion. *Cell* 126, 177-189. <https://doi.org/10.1016/j.cell.2006.06.025>.
- Frezza, C., Cipolat, S., and Scorrano, L. (2007). Organelle isolation: functional mitochondria from mouse liver, muscle and cultured fibroblasts. *Nature protocols* 2, 287-295. <https://doi.org/10.1038/nprot.2006.478>.
- Friberg, H., and Wieloch, T. (2002). Mitochondrial permeability transition in acute neurodegeneration. *Biochimie* 84, 241-250. [https://doi.org/10.1016/S0300-9084\(02\)01381-0](https://doi.org/10.1016/S0300-9084(02)01381-0).
- Funayama, M., Ohe, K., Amo, T., Furuya, N., Yamaguchi, J., Saiki, S., Li, Y., Ogaki, K., Ando, M., and Yoshino, H., et al. (2015). CHCHD2 mutations in autosomal dominant late-onset Parkinson's disease: a genome-wide linkage and sequencing study. *The Lancet Neurology* 14, 274-282. [https://doi.org/10.1016/S1474-4422\(14\)70266-2](https://doi.org/10.1016/S1474-4422(14)70266-2).
- Galluzzi, L., Vitale, I., Aaronson, S.A., Abrams, J.M., Adam, D., Agostinis, P., Alnemri, E.S., Altucci, L., Amelio, I., and Andrews, D.W., et al. (2018). Molecular mechanisms of cell death: recommendations of the Nomenclature Committee on Cell Death 2018. *Cell Death and Differentiation* 25, 486-541. <https://doi.org/10.1038/s41418-017-0012-4>.
- Gaspers, L.D., Mémin, E., and Thomas, A.P. (2012). Calcium-dependent physiologic and pathologic stimulus-metabolic response coupling in hepatocytes. *Cell calcium* 52, 93-102. <https://doi.org/10.1016/j.ceca.2012.04.009>.
- Genin, E.C., Plutino, M., Bannwarth, S., Villa, E., Cisneros-Barroso, E., Roy, M., Ortega-Vila, B., Fragaki, K., Lespinasse, F., and Pinero-Martos, E., et al. (2016). CHCHD10 mutations promote loss of mitochondrial cristae junctions with impaired mitochondrial genome maintenance and inhibition of apoptosis. *EMBO Molecular Medicine* 8, 58-72. <https://doi.org/10.15252/emmm.201505496>.
- Giacomello, M., and Pellegrini, L. (2016). The coming of age of the mitochondria-ER contact: a matter of thickness. *Cell Death Differ* 23, 1417-1427. <https://doi.org/10.1038/cdd.2016.52>.

Giorgi, C., Marchi, S., and Pinton, P. (2018). The machineries, regulation and cellular functions of mitochondrial calcium. *Nature reviews. Molecular cell biology* *19*, 713-730. <https://doi.org/10.1038/s41580-018-0052-8>.

Giorgio, V., Bisetto, E., Soriano, M.E., Dabbeni-Sala, F., Basso, E., Petronilli, V., Forte, M.A., Bernardi, P., and Lippe, G. (2009). Cyclophilin D modulates mitochondrial FOF1-ATP synthase by interacting with the lateral stalk of the complex. *J. Biol. Chem.* *284*, 33982-33988. <https://doi.org/10.1074/jbc.M109.020115>.

Giorgio, V., Stockum, S. von, Antoniel, M., Fabbro, A., Fogolari, F., Forte, M., Glick, G.D., Petronilli, V., Zoratti, M., and Szabó, I., et al. (2013). Dimers of mitochondrial ATP synthase form the permeability transition pore. *PNAS* *110*, 5887-5892. <https://doi.org/10.1073/pnas.1217823110>.

Giustarini, D., Tsikas, D., Colombo, G., Milzani, A., Dalle-Donne, I., Fanti, P., and Rossi, R. (2016). Pitfalls in the analysis of the physiological antioxidant glutathione (GSH) and its disulfide (GSSG) in biological samples: An elephant in the room. *Journal of chromatography. B, Analytical technologies in the biomedical and life sciences* *1019*, 21-28. <https://doi.org/10.1016/j.jchromb.2016.02.015>.

Glytsou, C., Calvo, E., Cogliati, S., Mehrotra, A., Anastasia, I., Rigoni, G., Raimondi, A., Shintani, N., Loureiro, M., and Vazquez, J., et al. (2016). Optic Atrophy 1 Is Epistatic to the Core MICOS Component MIC60 in Mitochondrial Cristae Shape Control. *Cell Reports* *17*, 3024-3034. <https://doi.org/10.1016/j.celrep.2016.11.049>.

Gómez-Nieto, R., Hormigo, S., and López, D.E. (2020). Prepulse Inhibition of the Auditory Startle Reflex Assessment as a Hallmark of Brainstem Sensorimotor Gating Mechanisms. *Brain Sciences* *10*. <https://doi.org/10.3390/brainsci10090639>.

Gottschalk, B., Klec, C., Leitinger, G., Bernhart, E., Rost, R., Bischof, H., Madreiter-Sokolowski, C.T., Radulović, S., Eroglu, E., and Sattler, W., et al. (2019). MICU1 controls cristae junction and spatially anchors mitochondrial Ca<sup>2+</sup> uniporter complex. *Nat Commun* *10*, 3732. <https://doi.org/10.1038/s41467-019-11692-x>.

Griffiths, E.J. (1999). Reversal of mitochondrial Na/Ca exchange during metabolic inhibition in rat cardiomyocytes. *FEBS letters* *453*, 400-404. [https://doi.org/10.1016/s0014-5793\(99\)00726-7](https://doi.org/10.1016/s0014-5793(99)00726-7).

Grinberg, M., Sarig, R., Zaltsman, Y., Frumkin, D., Grammatikakis, N., Reuveny, E., and Gross, A. (2002). tBID Homooligomerizes in the mitochondrial membrane to induce apoptosis. *Journal of Biological Chemistry* *277*, 12237-12245. <https://doi.org/10.1074/jbc.M104893200>.

Guan, L., Che, Z., Meng, X., Yu, Y., Li, M., Yu, Z., Shi, H., Yang, D., and Yu, M. (2019). MCU Up-regulation contributes to myocardial ischemia-reperfusion Injury through calpain/OPA-1-mediated mitochondrial fusion/mitophagy Inhibition. *Journal of cellular and molecular medicine* *23*, 7830-7843. <https://doi.org/10.1111/jcmm.14662>.

Guo, G., Xu, M., Chang, Y., Luyten, T., Seitaj, B., Liu, W., Zhu, P., Bultynck, G., Shi, L., and Quick, M., et al. (2019). Ion and pH Sensitivity of a TMBIM Ca<sup>2+</sup> Channel. *Structure* *27*, 1013-1021.e3. <https://doi.org/10.1016/j.str.2019.03.003>.

Halliwell, B. (2014). Cell culture, oxidative stress, and antioxidants: avoiding pitfalls. *Biomedical journal* *37*, 99-105. <https://doi.org/10.4103/2319-4170.128725>.

Hamilton, J., Brustovetsky, T., Rysted, J.E., Lin, Z., Usachev, Y.M., and Brustovetsky, N. (2018). Deletion of mitochondrial calcium uniporter incompletely inhibits calcium uptake and induction of the permeability transition pore in brain mitochondria. *J. Biol. Chem.* *293*, 15652-15663. <https://doi.org/10.1074/jbc.RA118.002926>.

Han, Y.-E., Ryu, S.-Y., Park, S.-H., Lee, K.-H., Lee, S.-H., and Ho, W.-K. (2015). Ca<sup>2+</sup> clearance by plasmalemmal NCLX, Li(+)-permeable Na(+)/Ca<sup>2+</sup> exchanger, is required for the sustained exocytosis in rat insulinoma INS-1 cells. *Pflugers Arch - Eur J Physiol* *467*, 2461-2472. <https://doi.org/10.1007/s00424-015-1715-3>.

Harner, M.E., Unger, A.-K., Geerts, W.J., Mari, M., Izawa, T., Stenger, M., Geimer, S., Reggiori, F., Westermann, B., and Neupert, W. (2016). An evidence based hypothesis on the existence of two pathways of mitochondrial crista formation. *eLife* *5*. <https://doi.org/10.7554/eLife.18853>.

Hashimi, H., McDonald, L., Stríbrná, E., and Lukeš, J. (2013). Trypanosome Letm1 protein is essential for mitochondrial potassium homeostasis. *J. Biol. Chem.* *288*, 26914-26925. <https://doi.org/10.1074/jbc.M113.495119>.

Haworth, R.A., and Hunter, D.R. (1979). The Ca<sup>2+</sup>-induced membrane transition in mitochondria. *Archives of Biochemistry and Biophysics* *195*, 460-467. [https://doi.org/10.1016/0003-9861\(79\)90372-2](https://doi.org/10.1016/0003-9861(79)90372-2).

Hayashi, T., Rizzuto, R., Hajnoczky, G., and Su, T.-P. (2009). MAM: more than just a housekeeper. *Trends in cell biology* *19*, 81-88. <https://doi.org/10.1016/j.tcb.2008.12.002>.

He, J., Carroll, J., Ding, S., Fearnley, I.M., and Walker, J.E. (2017). Permeability transition in human mitochondria persists in the absence of peripheral stalk subunits of ATP synthase. *PNAS* *114*, 9086-9091. <https://doi.org/10.1073/pnas.1711201114>.

Hennebry, A., Berry, C., Siriatt, V., O'Callaghan, P., Chau, L., Watson, T., Sharma, M., and Kambadur, R. (2009). Myostatin regulates fiber-type composition of skeletal muscle by regulating MEF2 and MyoD gene expression. *American journal of physiology. Cell physiology* *296*, C525-34. <https://doi.org/10.1152/ajpcell.00259.2007>.

Hoffmann, Chandramoorthy H.C., Shanmughapriyaa, S., Zhang X.Q., Vallem S., Doonan P.J., Malliankaramana K., Guo S., Raja S., and Elrod J.W., et al. (2014). SLC25A23 augments mitochondrial Ca<sup>2+</sup> uptake, interacts with MCU, and induces oxidative stress-mediated cell death. *Molecular Biology of the Cell*, 936-947.

Hojman, P., Brolin, C., Nørgaard-Christensen, N., Dethlefsen, C., Lauenborg, B., Olsen, C.K., Åbom, M.M., Krag, T., Gehl, J., and Pedersen, B.K. (2019). IL-6 release from muscles during exercise is stimulated by lactate-dependent protease activity. *American journal of physiology. Endocrinology and metabolism* *316*, E940-E947. <https://doi.org/10.1152/ajpendo.00414.2018>.

Hom, J.R., Gewandter, J.S., Michael, L., Sheu, S.-S., and Yoon, Y. (2007). Thapsigargin induces biphasic fragmentation of mitochondria through calcium-mediated mitochondrial fission and apoptosis. *J. Cell. Physiol.* *212*, 498-508. <https://doi.org/10.1002/jcp.21051>.

Horvath, S.E., and Daum, G. (2013). Lipids of mitochondria. *Progress in Lipid Research* *52*, 590-614. <https://doi.org/10.1016/j.plipres.2013.07.002>.

Hu, C., Shu, L., Huang, X., Yu, J., Li, L., Gong, L., Yang, M., Wu, Z., Gao, Z., and Zhao, Y., et al. (2020). OPA1 and MICOS Regulate mitochondrial crista dynamics and formation. *Cell death & disease* *11*, 940. <https://doi.org/10.1038/s41419-020-03152-y>.

Hunter, D.R., and Haworth, R.A. (1979). The Ca<sup>2+</sup>-induced membrane transition in mitochondria. *Archives of Biochemistry and Biophysics* *195*, 468-477. [https://doi.org/10.1016/0003-9861\(79\)90373-4](https://doi.org/10.1016/0003-9861(79)90373-4).

- Ikon, N., and Ryan, R.O. (2017). Cardiolipin and mitochondrial cristae organization. *Biochimica et Biophysica Acta (BBA) - Biomembranes* 1859, 1156-1163. <https://doi.org/10.1016/j.bbamem.2017.03.013>.
- Ishihara, N., Fujita, Y., Oka, T., and Mihara, K. (2006). Regulation of mitochondrial morphology through proteolytic cleavage of OPA1. *The EMBO journal* 25, 2966-2977. <https://doi.org/10.1038/sj.emboj.7601184>.
- Itoh, K., Nakamura, K., Iijima, M., and Sesaki, H. (2013). Mitochondrial dynamics in neurodegeneration. *Trends in cell biology* 23, 64-71. <https://doi.org/10.1016/j.tcb.2012.10.006>.
- Jadiya, P., Kolmetzky, D.W., Tomar, D., Di Meco, A., Lombardi, A.A., Lambert, J.P., Luongo, T.S., Ludtmann, M.H., Praticò, D., and Elrod, J.W. (2019). Impaired mitochondrial calcium efflux contributes to disease progression in models of Alzheimer's disease. *Nature communications* 10, 3885. <https://doi.org/10.1038/s41467-019-11813-6>.
- Jeong S.-Y., and Seol D.-W. (2008). The role of mitochondria in apoptosis. *BMB Reports* 41, 11-22.
- Jiang, D., Zhao, L., and Clapham, D.E. (2009). Genome-Wide RNAi Screen Identifies Letm1 as a Mitochondrial Ca<sup>2+</sup> /H<sup>+</sup> Antiporter. *Howard Hughes Medical Institute* 2009, 144-147.
- Jozefczuk, J., Drews, K., and Adjaye, J. (2012). Preparation of mouse embryonic fibroblast cells suitable for culturing human embryonic and induced pluripotent stem cells. *Journal of visualized experiments : JoVE*. <https://doi.org/10.3791/3854>.
- Jumper, J., Evans, R., Pritzel, A., Green, T., Figurnov, M., Ronneberger, O., Tunyasuvunakool, K., Bates, R., Žídek, A., and Potapenko, A., et al. (2021). Highly accurate protein structure prediction with AlphaFold. *Nature* 596, 583-589. <https://doi.org/10.1038/s41586-021-03819-2>.
- Jung, D.W., Baysal, K., and Brierley, G.P. (1995). The sodium-calcium antiport of heart mitochondria is not electroneutral. *Journal of Biological Chemistry* 270, 672-678. <https://doi.org/10.1074/jbc.270.2.672>.
- Jung, H., Kim, S.Y., Canbakis Cecen, F.S., Cho, Y., and Kwon, S.-K. (2020). Dysfunction of Mitochondrial Ca<sup>2+</sup> Regulatory Machineries in Brain Aging and Neurodegenerative Diseases. *Frontiers in cell and developmental biology* 8, 599792. <https://doi.org/10.3389/fcell.2020.599792>.
- Kaasik, A., Safiulina, D., Zharkovsky, A., and Veksler, V. (2007). Regulation of mitochondrial matrix volume. *American journal of physiology. Cell physiology* 292, C157-63. <https://doi.org/10.1152/ajpcell.00272.2006>.
- Kapałczyńska, M., Kolenda, T., Przybyła, W., Zajączkowska, M., Teresiak, A., Filas, V., Ibbs, M., Bliźniak, R., Łuczewski, Ł., and Lamperska, K. (2018). 2D and 3D cell cultures - a comparison of different types of cancer cell cultures. *Archives of Medical Science : AMS* 14, 910-919. <https://doi.org/10.5114/aoms.2016.63743>.
- Karbach, S.H., Schönfelder, T., Brandão, I., Wilms, E., Hörmann, N., Jäckel, S., Schüler, R., Finger, S., Knorr, M., and Lagrange, J., et al. (2016). Gut Microbiota Promote Angiotensin II-Induced Arterial Hypertension and Vascular Dysfunction. *Journal of the American Heart Association: Cardiovascular and Cerebrovascular Disease* 5. <https://doi.org/10.1161/JAHA.116.003698>.
- Karch, J., Bround, M.J., Khalil, H., Sargent, M.A., Latchman, N., Terada, N., Peixoto, P.M., and Molkentin, J.D. (2019). Inhibition of mitochondrial permeability transition by deletion of the ANT family and CypD. *Science advances* 5, eaaw4597. <https://doi.org/10.1126/sciadv.aaw4597>.

Kaur, J., and Bachhawat, A.K. (2009). A modified Western blot protocol for enhanced sensitivity in the detection of a membrane protein. *Analytical Biochemistry* 384, 348-349. <https://doi.org/10.1016/j.ab.2008.10.005>.

Kavanagh, N., Ainscow, E.K., and Brand, M.D. (2000). Calcium regulation of oxidative phosphorylation in rat skeletal muscle mitochondria. *Biochimica et Biophysica Acta (BBA) - Bioenergetics* 1457, 57-70. [https://doi.org/10.1016/S0005-2728\(00\)00054-2](https://doi.org/10.1016/S0005-2728(00)00054-2).

Kee, T.R., Espinoza Gonzalez, P., Wehinger, J.L., Bukhari, M.Z., Ermekbaeva, A., Sista, A., Kotsiviras, P., Liu, T., Kang, D.E., and Woo, J.-A.A. (2021). Mitochondrial CHCHD2: Disease-Associated Mutations, Physiological Functions, and Current Animal Models. *Frontiers in aging neuroscience* 13, 660843. <https://doi.org/10.3389/fnagi.2021.660843>.

Kirichok, Y., Krapivinsky, G., and Clapham, D.E. (2004). The mitochondrial calcium uniporter is a highly selective ion channel. *Nature* 427, 360-364. <https://doi.org/10.1038/nature02246>.

Kiviluoto, S., Luyten, T., Schneider, L., Lisak, D., Rojas-Rivera, D., Welkenhuyzen, K., Missaen, L., Smedt, H. de, Parys, J.B., and Hetz, C., et al. (2013). Bax Inhibitor-1-mediated Ca<sup>2+</sup> leak is decreased by cytosolic acidosis. *Cell calcium* 54, 186-192. <https://doi.org/10.1016/j.ceca.2013.06.002>.

Knottnerus, S.J.G., Bleeker, J.C., Wüst, R.C.I., Ferdinandusse, S., IJlst, L., Wijburg, F.A., Wanders, R.J.A., Visser, G., and Houtkooper, R.H. (2018). Disorders of mitochondrial long-chain fatty acid oxidation and the carnitine shuttle. *Rev Endocr Metab Disord* 19, 93-106. <https://doi.org/10.1007/s11154-018-9448-1>.

Koch, D., Spiwoks-Becker, I., Sabanov, V., Sinning, A., Dugladze, T., Stellmacher, A., Ahuja, R., Grimm, J., Schüler, S., and Müller, A., et al. (2011). Proper synaptic vesicle formation and neuronal network activity critically rely on syndapin I. *The EMBO journal* 30, 4955-4969. <https://doi.org/10.1038/emboj.2011.339>.

Kok, M.J.C. de, Schaapherder, A.F., Wüst, R.C.I., Zuiderwijk, M., Bakker, J.A., Lindeman, J.H.N., and Le Dévédec, S.E. (2021). Circumventing the Crabtree effect in cell culture: A systematic review. *Mitochondrion* 59, 83-95. <https://doi.org/10.1016/j.mito.2021.03.014>.

König, T., Tröder, S.E., Bakka, K., Korwitz, A., Richter-Dennerlein, R., Lampe, P.A., Patron, M., Mühlmeister, M., Guerrero-Castillo, S., and Brandt, U., et al. (2016). The m-AAA Protease Associated with Neurodegeneration Limits MCU Activity in Mitochondria. *Molecular cell* 64, 148-162. <https://doi.org/10.1016/j.molcel.2016.08.020>.

Kostic, M., and Sekler, I. (2019). Functional properties and mode of regulation of the mitochondrial Na<sup>+</sup>/Ca<sup>2+</sup> exchanger, NCLX. *Seminars in cell & developmental biology* 94, 59-65. <https://doi.org/10.1016/j.semcd.2019.01.009>.

Kühlbrandt, W. (2015). Structure and function of mitochondrial membrane protein complexes. *BMC Biol* 13, 89. <https://doi.org/10.1186/s12915-015-0201-x>.

Lam, S.S., Martell, J.D., Kamer, K.J., Deerinck, T.J., Ellisman, M.H., Mootha, V.K., and Ting, A.Y. (2015). Directed evolution of APEX2 for electron microscopy and proximity labeling. *Nat Methods* 12, 51-54. <https://doi.org/10.1038/nmeth.3179>.

Learning for Justice (2015). Remarks on Signing the Immigration Act of 1965. <https://www.learningforjustice.org/classroom-resources/texts/remarks-on-signing-the-immigration-act-of-1965>. 25.10.2021.

- Lee, J.E., Westrate, L.M., Wu, H., Page, C., and Voeltz, G.K. (2016). Multiple dynamin family members collaborate to drive mitochondrial division. *Nature* *540*, 139-143. <https://doi.org/10.1038/nature20555>.
- Lee, R.G., Sedghi, M., Salari, M., Shearwood, A.-M.J., Stentenbach, M., Kariminejad, A., Goullee, H., Rackham, O., Laing, N.G., and Tajsharghi, H., et al. (2018). Early-onset Parkinson disease caused by a mutation in CHCHD2 and mitochondrial dysfunction. *Neurology. Genetics* *4*, e276. <https://doi.org/10.1212/NXG.0000000000000276>.
- Lemieux, H., Blier, P.U., and Gnaiger, E. (2017). Remodeling pathway control of mitochondrial respiratory capacity by temperature in mouse heart: electron flow through the Q-junction in permeabilized fibers. *Scientific Reports* *7*, 2840. <https://doi.org/10.1038/s41598-017-02789-8>.
- Li, Y., Huang, T.T., Carlson, E.J., Melov, S., Ursell, P.C., Olson, J.L., Noble, L.J., Yoshimura, M.P., Berger, C., and Chan, P.H., et al. (1995). Dilated cardiomyopathy and neonatal lethality in mutant mice lacking manganese superoxide dismutase. *Nature genetics* *11*, 376-381. <https://doi.org/10.1038/ng1295-376>.
- Li, Y., Kelder, B., and Kopchick, J.J. (2001). Identification, isolation, and cloning of growth hormone (GH)-inducible interscapular brown adipose complementary deoxyribonucleic acid from GH antagonist mice. *Endocrinology* *142*, 2937-2945. <https://doi.org/10.1210/endo.142.7.8233>.
- Lill, R., Hoffmann, B., Molik, S., Pierik, A.J., Rietzschel, N., Stehling, O., Uzarska, M.A., Webert, H., Wilbrecht, C., and Mühlenhoff, U. (2012). The role of mitochondria in cellular iron-sulfur protein biogenesis and iron metabolism. *Biochimica et biophysica acta* *1823*, 1491-1508. <https://doi.org/10.1016/j.bbamcr.2012.05.009>.
- Lin, M.-Y., and Sheng, Z.-H. (2015). Regulation of mitochondrial transport in neurons. *Experimental Cell Research* *334*, 35-44. <https://doi.org/10.1016/j.yexcr.2015.01.004>.
- Lin, Q.-T., and Stathopoulos, P.B. (2019). Molecular Mechanisms of Leucine Zipper EF-Hand Containing Transmembrane Protein-1 Function in Health and Disease. *International Journal of Molecular Sciences* *20*. <https://doi.org/10.3390/ijms20020286>.
- Lin, Y.-C., Boone, M., Meuris, L., Lemmens, I., van Roy, N., Soete, A., Reumers, J., Moisse, M., Plaisance, S., and Drmanac, R., et al. (2014). Genome dynamics of the human embryonic kidney 293 lineage in response to cell biology manipulations. *Nat Commun* *5*, 4767. <https://doi.org/10.1038/ncomms5767>.
- Lisak, D.A., Schacht, T., Enders, V., Habicht, J., Kiviluoto, S., Schneider, J., Henke, N., Bultynck, G., and Methner, A. (2015). The transmembrane Bax inhibitor motif (TMBIM) containing protein family: Tissue expression, intracellular localization and effects on the ER  $Ca^{2+}$ -filling state.
- Liu, G., Sil, D., Maio, N., Tong, W.-H., Bollinger, J.M., Krebs, C., and Rouault, T.A. (2020a). Heme biosynthesis depends on previously unrecognized acquisition of iron-sulfur cofactors in human aminolevulinic acid dehydratase. *Nat Commun* *11*, 6310. <https://doi.org/10.1038/s41467-020-20145-9>.
- Liu, J.C., Liu, J., Holmström, K.M., Menazza, S., Parks, R.J., Fergusson, M.M., Yu, Z.-X., Springer, D.A., Halsey, C., and Liu, C., et al. (2016). MICU1 Serves as a Molecular Gatekeeper to Prevent In Vivo Mitochondrial Calcium Overload. *Cell reports* *16*, 1561-1573. <https://doi.org/10.1016/j.celrep.2016.07.011>.
- Liu, T., Woo, J.-A.A., Bukhari, M.Z., LePochat, P., Chacko, A., Selenica, M.-L.B., Yan, Y., Kotsiviras, P., Buosi, S.C., and Zhao, X., et al. (2020b). CHCHD10-regulated OPA1-mitofilin complex mediates TDP-43-induced mitochondrial phenotypes associated with frontotemporal dementia. *FASEB journal : official publication of the Federation of American Societies for Experimental Biology* *34*, 8493-8509. <https://doi.org/10.1096/fj.201903133RR>.

Liu, W., Duan, X., Xu, L., Shang, W., Zhao, J., Wang, L., Li, J.-C., Chen, C.-H., Liu, J.-P., and Tong, C. (2020c). Chchd2 regulates mitochondrial morphology by modulating the levels of Opa1. *Cell Death and Differentiation* 27, 2014-2029. <https://doi.org/10.1038/s41418-019-0482-7>.

Lucertini, F., Gervasi, M., D'Amico, G., Sisti, D., Rocchi, M.B.L., Stocchi, V., and Benelli, P. (2017). Effect of water-based recovery on blood lactate removal after high-intensity exercise. *PLoS one* 12, e0184240. <https://doi.org/10.1371/journal.pone.0184240>.

Luongo, T.S., Lambert, J.P., Gross, P., Nwokedi, M., Lombardi, A.A., Shanmughapriya, S., Carpenter, A.C., Kolmetzky, D., Gao, E., and van Berlo, J.H., et al. (2017). The mitochondrial Na<sup>+</sup>/Ca<sup>2+</sup> exchanger is essential for Ca<sup>2+</sup> homeostasis and viability. *Nature* 545, 93-97. <https://doi.org/10.1038/nature22082>.

Luongo, T.S., Lambert, J.P., Yuan, A., Zhang, X., Gross, P., Song, J., Shanmughapriya, S., Gao, E., Jain, M., and Houser, S.R., et al. (2015). The Mitochondrial Calcium Uniporter Matches Energetic Supply with Cardiac Workload during Stress and Modulates Permeability Transition. *Cell Reports* 12, 23-34. <https://doi.org/10.1016/j.celrep.2015.06.017>.

MacVicar, T., and Langer, T. (2016). OPA1 processing in cell death and disease - the long and short of it. *Journal of cell science* 129, 2297-2306. <https://doi.org/10.1242/jcs.159186>.

Madreiter-Sokolowski, C.T., Klec, C., Parichatikanond, W., Stryeck, S., Gottschalk, B., Pulido, S., Rost, R., Eroglu, E., Hofmann, N.A., and Bondarenko, A.I., et al. (2016). PRMT1-mediated methylation of MICU1 determines the UCP2/3 dependency of mitochondrial Ca<sup>2+</sup> uptake in immortalized cells. *Nat Commun* 7, 12897. <https://doi.org/10.1038/ncomms12897>.

Mallilankaraman, K., Cárdenas, C., Doonan, P.J., Chandramoorthy, H.C., Irrinki, K.M., Golenár, T., Csordás, G., Madireddi, P., Yang, J., and Müller, M., et al. (2012a). MCUR1 is an essential component of mitochondrial Ca<sup>2+</sup> uptake that regulates cellular metabolism. *Nat Cell Biol* 14, 1336-1343. <https://doi.org/10.1038/ncb2622>.

Mallilankaraman, K., Doonan, P., Cárdenas, C., Chandramoorthy, H.C., Müller, M., Miller, R., Hoffman, N.E., Gandhirajan, R.K., Molgó, J., and Birnbaum, M.J., et al. (2012b). MICU1 is an essential gatekeeper for MCU-mediated mitochondrial Ca<sup>2+</sup> uptake that regulates cell survival. *Cell* 151, 630-644. <https://doi.org/10.1016/j.cell.2012.10.011>.

Manor, U., Bartholomew, S., Golani, G., Christenson, E., Kozlov, M., Higgs, H., Spudich, J., and Lippincott-schwartz, J. (2015). A mitochondria-anchored isoform of the actin-nucleating spire protein regulates mitochondrial division. *eLife Sciences Publications, Ltd.*

Mantena, S.K., King, A.L., Andringa, K.K., Eccleston, H.B., and Bailey, S.M. (2008). Mitochondrial dysfunction and oxidative stress in the pathogenesis of alcohol- and obesity-induced fatty liver diseases. *Free radical biology & medicine* 44, 1259-1272. <https://doi.org/10.1016/j.freeradbiomed.2007.12.029>.

Marchi, U. de, Santo-Domingo, J., Castelbou, C., Sekler, I., Wiederkehr, A., and Demarex, N. (2014). NCLX protein, but not LETM1, mediates mitochondrial Ca<sup>2+</sup> extrusion, thereby limiting Ca<sup>2+</sup>-induced NAD(P)H production and modulating matrix redox state. *J. Biol. Chem.* 289, 20377-20385. <https://doi.org/10.1074/jbc.M113.540898>.

Martin, W. & Mentel, M. (2010). The Origin of Mitochondria. Mitochondria arose through a fateful endosymbiosis more than 1.45 billion years ago. Many mitochondria make ATP without the help of oxygen. *nature education* 2010.

Marzo, I., Brenner, C., Zamzami, N., Susin, S.A., Beutner, G., Brdiczka, D., Rémy, R., Xie, Z.H., Reed, J.C., and Kroemer, G. (1998). The permeability transition pore complex: a target for apoptosis regulation by

- caspsases and bcl-2-related proteins. *The Journal of Experimental Medicine* 187, 1261-1271. <https://doi.org/10.1084/jem.187.8.1261>.
- Mayr, J.A. (2015). Lipid metabolism in mitochondrial membranes. *Journal of inherited metabolic disease* 38, 137-144. <https://doi.org/10.1007/s10545-014-9748-x>.
- Mears, J.A., Lackner, L.L., Fang, S., Ingerman, E., Nunnari, J., and Hinshaw, J.E. (2011). Conformational changes in Dnm1 support a contractile mechanism for mitochondrial fission. *Nat Struct Mol Biol* 18, 20-26. <https://doi.org/10.1038/nsmb.1949>.
- Medina, D.L., Di Paola, S., Peluso, I., Armani, A., Stefani, D. de, Venditti, R., Montefusco, S., Scotto-Rosato, A., Prezioso, C., and Forrester, A., et al. (2015). Lysosomal calcium signalling regulates autophagy through calcineurin and TFEB. *Nat Cell Biol* 17, 288-299. <https://doi.org/10.1038/ncb3114>.
- Meng, H., Yamashita, C., Shiba-Fukushima, K., Inoshita, T., Funayama, M., Sato, S., Hatta, T., Natsume, T., Umitsu, M., and Takagi, J., et al. (2017). Loss of Parkinson's disease-associated protein CHCHD2 affects mitochondrial crista structure and destabilizes cytochrome c. *Nat Commun* 8. <https://doi.org/10.1038/ncomms15500>.
- Meyer, J.N., Leuthner, T.C., and Luz, A.L. (2017). Mitochondrial fusion, fission, and mitochondrial toxicity. *Toxicology* 391, 42-53. <https://doi.org/10.1016/j.tox.2017.07.019>.
- Mildaziene, V., Baniene, R., Nauciene, Z., Marcinkeviciute, A., Morkuniene, R., Borutaite, V., Kholodenko, B., and Brown, G.C. (1996). Ca<sup>2+</sup> stimulates both the respiratory and phosphorylation subsystems in rat heart mitochondria. *Biochem J* 320 ( Pt 1), 329-334. <https://doi.org/10.1042/bj3200329>.
- Miranda, É.G.A., Araujo-Chaves, J.C., Kawai, C., Brito, A.M.M., Dias, I.W.R., Arantes, J.T., and Nantes-Cardoso, I.L. (2019). Cardiolipin Structure and Oxidation Are Affected by Ca<sup>2+</sup> at the Interface of Lipid Bilayers. *Front. Chem.* 7, 930. <https://doi.org/10.3389/fchem.2019.00930>.
- Murphy, E., Pan, X., Nguyen, T., Liu, J., Holmström, K.M., and Finkel, T. (2014). Unresolved questions from the analysis of mice lacking MCU expression. *Biochemical and biophysical research communications* 449, 384-385. <https://doi.org/10.1016/j.bbrc.2014.04.144>.
- Nagel, J.E., Smith, R.J., Shaw, L., Bertak, D., Dixit, V.D., Schaffer, E.M., and Taub, D.D. (2004). Identification of genes differentially expressed in T cells following stimulation with the chemokines CXCL12 and CXCL10. *BMC immunology* 5, 17. <https://doi.org/10.1186/1471-2172-5-17>.
- Nicholls, D.G. (2005). Mitochondria and calcium signaling. *Cell calcium* 38, 311-317. <https://doi.org/10.1016/j.ceca.2005.06.011>.
- Niewiadomski, W., Palasz, E., Skupinska, M., Zylinski, M., Steczkowska, M., Gasiorowska, A., Niewiadomska, G., and Riedel, G. (2016). TracMouse: A computer aided movement analysis script for the mouse inverted horizontal grid test. *Scientific Reports* 6, 39331. <https://doi.org/10.1038/srep39331>.
- Nowikovsky, K., Froschauer, E.M., Zsurka, G., Samaj, J., Reipert, S., Kolisek, M., Wiesenberger, G., and Schweyen, R.J. (2004). The LETM1/YOL027 gene family encodes a factor of the mitochondrial K<sup>+</sup> homeostasis with a potential role in the Wolf-Hirschhorn syndrome. *Journal of Biological Chemistry* 279, 30307-30315. <https://doi.org/10.1074/jbc.M403607200>.
- Nunnari, J., and Suomalainen, A. (2012). Mitochondria: in sickness and in health. *Cell* 148, 1145-1159. <https://doi.org/10.1016/j.cell.2012.02.035>.

Oka, T., Sayano, T., Tamai, S., Yokota, S., Kato, H., Fujii, G., and Mihara, K. (2008). Identification of a Novel Protein MICS1 that is Involved in Maintenance of Mitochondrial Morphology and Apoptotic Release of Cytochrome c. *MBoC* 19, 2597-2608. <https://doi.org/10.1091/mbc.e07-12-1205>.

Okada, S. (1996). Iron-induced tissue damage and cancer: the role of reactive oxygen species-free radicals. *Pathology international* 46, 311-332. <https://doi.org/10.1111/j.1440-1827.1996.tb03617.x>.

Ott, M., Robertson, J.D., Gogvadze, V., Zhivotovsky, B., and Orrenius, S. (2002). Cytochrome c release from mitochondria proceeds by a two-step process. *Proceedings of the National Academy of Sciences of the United States of America* 99, 1259-1263. <https://doi.org/10.1073/pnas.241655498>.

Paillard, M., Csordás, G., Szanda, G., Golenár, T., Debattisti, V., Bartok, A., Wang, N., Moffat, C., Seifert, E.L., and Spät, A., et al. (2017). Tissue-Specific Mitochondrial Decoding of Cytoplasmic Ca<sup>2+</sup> Signals Is Controlled by the Stoichiometry of MICU1/2 and MCU. *Cell reports* 18, 2291-2300. <https://doi.org/10.1016/j.celrep.2017.02.032>.

Palty, R., Hershinkel, M., Yagev, O., Saar, D., Barkalifa, R., Khananshvili, D., Peretz, A., Grossman, Y., and Sekler, I. (2006). Single alpha-domain constructs of the Na<sup>+</sup>/Ca<sup>2+</sup> exchanger, NCLX, oligomerize to form a functional exchanger. *Biochemistry* 45, 11856-11866. <https://doi.org/10.1021/bi060633b>.

Palty, R., Ohana, E., Hershinkel, M., Volokita, M., Elgazar, V., Beharier, O., Silverman, W.F., Argaman, M., and Sekler, I. (2004). Lithium-calcium exchange is mediated by a distinct potassium-independent sodium-calcium exchanger. *Journal of Biological Chemistry* 279, 25234-25240. <https://doi.org/10.1074/jbc.M401229200>.

Palty, R., Silverman, W.F., Hershinkel, M., Caporale, T., Sensi, S.L., Parnis, J., Nolte, C., Fishman, D., Shoshan-Barmatz, V., and Herrmann, S., et al. (2010). NCLX is an essential component of mitochondrial Na<sup>+</sup>/Ca<sup>2+</sup> exchange. *Proceedings of the National Academy of Sciences of the United States of America* 107, 436-441. <https://doi.org/10.1073/pnas.0908099107>.

Pan, X., Liu, J., Nguyen, T., Liu, C., Sun, J., Teng, Y., Fergusson, M.M., Rovira, I.I., Allen, M., and Springer, D.A., et al. (2013). The physiological role of mitochondrial calcium revealed by mice lacking the mitochondrial calcium uniporter. *Nature cell biology* 15, 1464-1472. <https://doi.org/10.1038/ncb2868>.

Paradies, G., Paradies, V., Ruggiero, F.M., and Petrosillo, G. (2014). Oxidative stress, cardiolipin and mitochondrial dysfunction in nonalcoholic fatty liver disease. *World Journal of Gastroenterology : WJG* 20, 14205-14218. <https://doi.org/10.3748/wjg.v20.i39.14205>.

Park, J., Lee, Y., Park, T., Kang, J.Y., Mun, S.A., Jin, M., Yang, J., and Eom, S.H. (2020). Structure of the MICU1-MICU2 heterodimer provides insights into the gatekeeping threshold shift. *IUCr* 7, 355-365. <https://doi.org/10.1107/S2052252520001840>.

Patron, M., Checchetto, V., Raffaello, A., Teardo, E., Vecellio Reane, D., Mantoan, M., Granatiero, V., Szabò, I., Stefani, D. de, and Rizzuto, R. (2014). MICU1 and MICU2 finely tune the mitochondrial Ca<sup>2+</sup> uniporter by exerting opposite effects on MCU activity. *Molecular cell* 53, 726-737. <https://doi.org/10.1016/j.molcel.2014.01.013>.

Patron, M., Granatiero, V., Espino, J., Rizzuto, R., and Stefani, D. de (2019). MICU3 is a tissue-specific enhancer of mitochondrial calcium uptake. *Cell Death and Differentiation* 26, 179-195. <https://doi.org/10.1038/s41418-018-0113-8>.

Paupe, V., Prudent, J., Dassa, E.P., Rendon, O.Z., and Shoubridge, E.A. (2015). CCDC90A (MCUR1) is a cytochrome c oxidase assembly factor and not a regulator of the mitochondrial calcium uniporter. *Cell Metabolism* 21, 109-116. <https://doi.org/10.1016/j.cmet.2014.12.004>.

- Penttilä, S., Jokela, M., Bouquin, H., Saukkonen, A.M., Toivanen, J., and Udd, B. (2015). Late onset spinal motor neuronopathy is caused by mutation in CHCHD10. *Annals of neurology* 77, 163-172. <https://doi.org/10.1002/ana.24319>.
- Perocchi, F., Gohil, V.M., Girgis, H.S., Bao, X.R., McCombs, J.E., Palmer, A.E., and Mootha, V.K. (2010). MICU1 encodes a mitochondrial EF hand protein required for Ca<sup>2+</sup> uptake. *Nature* 467, 291-296. <https://doi.org/10.1038/nature09358>.
- Petronilli, V., Miotto, G., Canton, M., Brini, M., Colonna, R., Bernardi, P., and Di Lisa, F. (1999). Transient and Long-Lasting Openings of the Mitochondrial Permeability Transition Pore Can Be Monitored Directly in Intact Cells by Changes in Mitochondrial Calcein Fluorescence. *Biophysical journal* 76, 725-734. [https://doi.org/10.1016/S0006-3495\(99\)77239-5](https://doi.org/10.1016/S0006-3495(99)77239-5).
- Philippaert, K., Roden, M., Lisak, D., Bueno, D., Jelenik, T., Radyushkin, K., Schacht, T., Mesuere, M., Wüllner, V., and Herrmann, A.-K., et al. (2020). Bax inhibitor-1 deficiency leads to obesity by increasing Ca<sup>2+</sup>-dependent insulin secretion. *Journal of Molecular Medicine (Berlin, Germany)* 98, 849-862. <https://doi.org/10.1007/s00109-020-01914-x>.
- Plovanich, M., Bogorad, R.L., Sancak, Y., Kamer, K.J., Strittmatter, L., Li, A.A., Girgis, H.S., Kuchimanchi, S., Groot, J. de, and Speciner, L., et al. (2013). MICU2, a paralog of MICU1, resides within the mitochondrial uniporter complex to regulate calcium handling. *PLoS one* 8, e55785. <https://doi.org/10.1371/journal.pone.0055785>.
- Prakriya, M., and Lewis, R.S. (2015). Store-Operated Calcium Channels. *Physiological reviews* 95, 1383-1436. <https://doi.org/10.1152/physrev.00020.2014>.
- Radyushkin, K., Hammerschmidt, K., Boretius, S., Varoqueaux, F., El-Kordi, A., Ronnenberg, A., Winter, D., Frahm, J., Fischer, J., and Brose, N., et al. (2009). Neuroligin-3-deficient mice: model of a monogenic heritable form of autism with an olfactory deficit. *Genes, Brain and Behavior* 8, 416-425. <https://doi.org/10.1111/j.1601-183X.2009.00487.x>.
- Raffaello, A., Stefani, D. de, Sabbadin, D., Teardo, E., Merli, G., Picard, A., Checchetto, V., Moro, S., Szabò, I., and Rizzuto, R. (2013). The mitochondrial calcium uniporter is a multimer that can include a dominant-negative pore-forming subunit. *The EMBO journal* 32, 2362-2376. <https://doi.org/10.1038/emboj.2013.157>.
- Rainbolt, T.K., Lebeau, J., Puchades, C., and Wiseman, R.L. (2016). Reciprocal Degradation of YME1L and OMA1 Adapts Mitochondrial Proteolytic Activity during Stress. *Cell reports* 14, 2041-2049. <https://doi.org/10.1016/j.celrep.2016.02.011>.
- Rampelt, H., Bohnert, M., Zerbes, R.M., Horvath, S.E., Warscheid, B., Pfanner, N., and van der Laan, M. (2017). Mic10, a Core Subunit of the Mitochondrial Contact Site and Cristae Organizing System, Interacts with the Dimeric F<sub>1</sub>F<sub>o</sub>-ATP Synthase. *Journal of Molecular Biology*, 1162-1170. <https://doi.org/10.1016/j.jmb.2017.03.006>.
- Rampelt, H., and van der Laan, M. (2017). The Yin & Yang of Mitochondrial Architecture - Interplay of MICOS and F<sub>1</sub>F<sub>o</sub>-ATP synthase in cristae formation. *Microbial cell (Graz, Austria)*, 236-239. <https://doi.org/10.15698/mic2017.08.583>.
- Rao, K.N.S., Shen, X., Pardue, S., and Krzywanski, D.M. (2020). Nicotinamide nucleotide transhydrogenase (NNT) regulates mitochondrial ROS and endothelial dysfunction in response to angiotensin II. *Redox Biology* 36, 101650. <https://doi.org/10.1016/j.redox.2020.101650>.
- Rasmussen, T.P., Wu, Y., Joiner, M.A., Koval, O.M., Wilson, N.R., Luczak, E.D., Wang, Q., Chen, B., Gao, Z., and Zhu, Z., et al. (2015). Inhibition of MCU forces extramitochondrial adaptations governing

physiological and pathological stress responses in heart. *PNAS* 112, 9129-9134.  
<https://doi.org/10.1073/pnas.1504705112>.

Reimers, K., Choi, C.Y., Bucan, V., and Vogt, P.M. (2007). The growth-hormone inducible transmembrane protein (Ghitm) belongs to the Bax inhibitory protein-like family. *International journal of biological sciences* 3, 471-476. <https://doi.org/10.7150/ijbs.3.471>.

Rimessi, A., Bezzerri, V., Patergnani, S., Marchi, S., Cabrini, G., and Pinton, P. (2015). Mitochondrial Ca<sup>2+</sup>-dependent NLRP3 activation exacerbates the *Pseudomonas aeruginosa*-driven inflammatory response in cystic fibrosis. *Nat Commun* 6, 6201. <https://doi.org/10.1038/ncomms7201>.

Rizzuto, R., Brini, M., Murgia, M., and Pozzan, T. (1993). Microdomains with high Ca<sup>2+</sup> close to IP<sub>3</sub>-sensitive channels that are sensed by neighboring mitochondria. *Science (New York, N.Y.)* 262, 744-747. <https://doi.org/10.1126/science.8235595>.

Roger, A.J., Muñoz-Gómez, S.A., and Kamikawa, R. (2017). The Origin and Diversification of Mitochondria. *Current biology : CB* 27, R1177-R1192. <https://doi.org/10.1016/j.cub.2017.09.015>.

Rojas-Rivera, D., and Hetz, C. (2015). TMBIM protein family: ancestral regulators of cell death. *Oncogene* 34, 269-280. <https://doi.org/10.1038/onc.2014.6>.

Rudolf, J., Makrantonis, V., Ingledew, W.J., Stark, M.J.R., and White, M.F. (2006). The DNA repair helicases XPD and FancJ have essential iron-sulfur domains. *Molecular cell* 23, 801-808. <https://doi.org/10.1016/j.molcel.2006.07.019>.

Rysted, J.E., Lin, Z., Walters, G.C., Rauckhorst, A.J., Noterman, M., Liu, G., Taylor, E.B., Strack, S., and Usachev, Y.M. (2021). Distinct properties of Ca<sup>2+</sup> efflux from brain, heart and liver mitochondria: The effects of Na<sup>+</sup>, Li<sup>+</sup> and the mitochondrial Na<sup>+</sup>/Ca<sup>2+</sup> exchange inhibitor CGP37157. *Cell calcium* 96, 102382. <https://doi.org/10.1016/j.ceca.2021.102382>.

Ryu, S.-Y., Beutner, G., Kinnally, K.W., Dirksen, R.T., and Sheu, S.-S. (2011). Single channel characterization of the mitochondrial ryanodine receptor in heart mitoplasts. *J. Biol. Chem.* 286, 21324-21329. <https://doi.org/10.1074/jbc.C111.245597>.

Sancak, Y., Markhard, A.L., Kitami, T., Kovács-Bogdán, E., Kamer, K.J., Udeshi, N.D., Carr, S.A., Chaudhuri, D., Clapham, D.E., and Li, A.A., et al. (2013). EMRE is an essential component of the mitochondrial calcium uniporter complex. *Science (New York, N.Y.)* 342, 1379-1382. <https://doi.org/10.1126/science.1242993>.

Schiaffino, S., and Reggiani, C. (2011). Fiber types in mammalian skeletal muscles. *Physiological reviews* 91, 1447-1531. <https://doi.org/10.1152/physrev.00031.2010>.

Scorrano, L., Ashiya, M., Buttle, K., Weiler, S., Oakes, S.A., Mannella, C.A., and Korsmeyer, S.J. (2002). A Distinct Pathway Remodels Mitochondrial Cristae and Mobilizes Cytochrome c during Apoptosis. *Developmental cell* 2, 55-67. [https://doi.org/10.1016/s1534-5807\(01\)00116-2](https://doi.org/10.1016/s1534-5807(01)00116-2).

Seitaj, B., Maull, F., Zhang, L., Wüllner, V., Wolf, C., Schippers, P., La Rovere, R., Distler, U., Tenzer, S., and Parys, J.B., et al. (2020). Transmembrane BAX Inhibitor-1 Motif Containing Protein 5 (TMBIM5) Sustains Mitochondrial Structure, Shape, and Function by Impacting the Mitochondrial Protein Synthesis Machinery. *Cells* 9. <https://doi.org/10.3390/cells9102147>.

Shadel, G.S., and Horvath, T.L. (2015). Mitochondrial ROS signaling in organismal homeostasis. *Cell* 163, 560-569. <https://doi.org/10.1016/j.cell.2015.10.001>.

- Shao, J., Fu, Z., Ji, Y., Guan, X., Guo, S., Ding, Z., Yang, X., Cong, Y., and Shen, Y. (2016). Leucine zipper-*EF*-hand containing transmembrane protein 1 (LETM1) forms a Ca<sup>2+</sup>/H<sup>+</sup> antiporter. *Scientific Reports* 6, 34174. <https://doi.org/10.1038/srep34174>.
- Simões, I.C.M., Fontes, A., Pinton, P., Zischka, H., and Wieckowski, M.R. (2018). Mitochondria in non-alcoholic fatty liver disease. *The International Journal of Biochemistry & Cell Biology* 95, 93-99. <https://doi.org/10.1016/j.biocel.2017.12.019>.
- Sliter, D.A., Martinez, J., Hao, L., Chen, X., Sun, N., Fischer, T.D., Burman, J.L., Li, Y., Zhang, Z., and Narendra, D.P., et al. (2018). Parkin and PINK1 mitigate STING-induced inflammation. *Nature* 561, 258-262. <https://doi.org/10.1038/s41586-018-0448-9>.
- Smirnova, E., Griparic, L., Shurland, D.L., and van der Blik, A.M. (2001). Dynamin-related protein Drp1 is required for mitochondrial division in mammalian cells. *MBoC* 12, 2245-2256. <https://doi.org/10.1091/mbc.12.8.2245>.
- Sommakia, S., Houlihan, P.R., Deane, S.S., Simcox, J.A., Torres, N.S., Jeong, M.-Y., Winge, D.R., Villanueva, C.J., and Chaudhuri, D. (2017). Mitochondrial cardiomyopathies feature increased uptake and diminished efflux of mitochondrial calcium. *Journal of molecular and cellular cardiology* 113, 22-32. <https://doi.org/10.1016/j.yjmcc.2017.09.009>.
- Sparagna, G.C., Gunter, K.K., Sheu, S.S., and Gunter, T.E. (1995). Mitochondrial calcium uptake from physiological-type pulses of calcium. A description of the rapid uptake mode. *The Journal of biological chemistry* 270, 27510-27515. <https://doi.org/10.1074/jbc.270.46.27510>.
- Spiekerkoetter, U. (2010). Mitochondrial fatty acid oxidation disorders: clinical presentation of long-chain fatty acid oxidation defects before and after newborn screening. *Journal of inherited metabolic disease* 33, 527-532. <https://doi.org/10.1007/s10545-010-9090-x>.
- Srinivasan, S., Guha, M., Kashina, A., and Avadhani, N.G. (2017). Mitochondrial dysfunction and mitochondrial dynamics-The cancer connection. *Biochimica et Biophysica Acta (BBA) - Bioenergetics* 1858, 602-614. <https://doi.org/10.1016/j.bbabi.2017.01.004>.
- Stanton, R.C. (2012). Glucose-6-phosphate dehydrogenase, NADPH, and cell survival. *IUBMB Life* 64, 362-369. <https://doi.org/10.1002/iub.1017>.
- Stefani, D. de, Patron, M., and Rizzuto, R. (2015). Structure and function of the mitochondrial calcium uniporter complex. *Biochimica et biophysica acta* 1853, 2006-2011. <https://doi.org/10.1016/j.bbamcr.2015.04.008>.
- Stefani, D. de, Raffaello, A., Teardo, E., Szabò, I., and Rizzuto, R. (2011). A forty-kilodalton protein of the inner membrane is the mitochondrial calcium uniporter. *Nature* 476, 336-340. <https://doi.org/10.1038/nature10230>.
- Stehling, O., Vashisht, A.A., Mascarenhas, J., Jonsson, Z.O., Sharma, T., Netz, D.J.A., Pierik, A.J., Wohlschlegel, J.A., and Lill, R. (2012). MMS19 assembles iron-sulfur proteins required for DNA metabolism and genomic integrity. *Science* 337, 195-199. <https://doi.org/10.1126/science.1219723>.
- Stephan, T., Brüser, C., Deckers, M., Steyer, A.M., Balzarotti, F., Barbot, M., Behr, T.S., Heim, G., Hübner, W., and Ilgen, P., et al. (2020). MICOS assembly controls mitochondrial inner membrane remodeling and crista junction redistribution to mediate cristae formation. *The EMBO journal* 39, e104105. <https://doi.org/10.15252/embj.2019104105>.
- Strauss, M., Hofhaus, G., Schröder, R.R., and Kühlbrandt, W. (2008). Dimer ribbons of ATP synthase shape the inner mitochondrial membrane. *The EMBO journal* 27, 1154-1160. <https://doi.org/10.1038/emboj.2008.35>.

(2021). SUIT-008 O2 pfi D014 - Bioblast. [https://wiki.oroboros.at/index.php/SUIT-008\\_O2\\_pfi\\_D014](https://wiki.oroboros.at/index.php/SUIT-008_O2_pfi_D014). 29.01.2021.

Suzuki, J., Kanemaru, K., Ishii, K., Ohkura, M., Okubo, Y., and Iino, M. (2014). Imaging intraorganellar Ca<sup>2+</sup> at subcellular resolution using CEPIA. *Nat Commun* 5, 4153. <https://doi.org/10.1038/ncomms5153>.

Tang, J., Zhang, K., Dong, J., Yan, C., Hu, C., Ji, H., Chen, L., Chen, S., Zhao, H., and Song, Z. (2020). Sam50-Mic19-Mic60 axis determines mitochondrial cristae architecture by mediating mitochondrial outer and inner membrane contact. *Cell Death and Differentiation* 27, 146-160. <https://doi.org/10.1038/s41418-019-0345-2>.

Tarasova, N.V., Vishnyakova, P.A., Logashina, Y.A., and Elchaninov, A.V. (2019). Mitochondrial Calcium Uniporter Structure and Function in Different Types of Muscle Tissues in Health and Disease. *International Journal of Molecular Sciences* 20. <https://doi.org/10.3390/ijms20194823>.

Tiepolo, T., Angelin, A., Palma, E., Sabatelli, P., Merlini, L., Nicolosi, L., Finetti, F., Braghetta, P., Vuagniaux, G., and Dumont, J.-M., et al. (2009). The cyclophilin inhibitor Debio 025 normalizes mitochondrial function, muscle apoptosis and ultrastructural defects in Col6a1<sup>-/-</sup> myopathic mice. *British Journal of Pharmacology* 157, 1045-1052. <https://doi.org/10.1111/j.1476-5381.2009.00316.x>.

Tilokani, L., Nagashima, S., Paupe, V., and Prudent, J. (2018). Mitochondrial dynamics: overview of molecular mechanisms. *Essays in Biochemistry* 62, 341-360. <https://doi.org/10.1042/EBC20170104>.

Tomar, D., Thomas, M., Garbincius, J.F., Kolmetzky, D.W., Salik, O., Jadiya, P., Carpenter, A.C., and Elrod, J.W. (2019). MICU1 regulates mitochondrial cristae structure and function independent of the mitochondrial calcium uniporter channel.

Trenker, M., Malli, R., Fertschai, I., Levak-Frank, S., and Graier, W.F. (2007). Uncoupling proteins 2 and 3 are fundamental for mitochondrial Ca<sup>2+</sup> uniport. *Nat Cell Biol* 9, 445-452. <https://doi.org/10.1038/ncb1556>.

Tsai, M.-F., Jiang, D., Zhao, L., Clapham, D., and Miller, C. (2014). Functional reconstitution of the mitochondrial Ca<sup>2+</sup>/H<sup>+</sup> antiporter Letm1. *The Journal of General Physiology* 143, 67-73. <https://doi.org/10.1085/jgp.201311096>.

Urbani, A., Giorgio, V., Carrer, A., Franchin, C., Arrigoni, G., Jiko, C., Abe, K., Maeda, S., Shinzawa-Itoh, K., and Bogers, J.F.M., et al. (2019). Purified F-ATP synthase forms a Ca<sup>2+</sup>-dependent high-conductance channel matching the mitochondrial permeability transition pore. *Nat Commun* 10, 4341. <https://doi.org/10.1038/s41467-019-12331-1>.

Vásquez-Trincado, C., García-Carvajal, I., Pennanen, C., Parra, V., Hill, J.A., Rothermel, B.A., and Lavandero, S. (2016). Mitochondrial dynamics, mitophagy and cardiovascular disease. *The Journal of physiology* 594, 509-525. <https://doi.org/10.1113/JP271301>.

Vecellio Reane, D., Vallese, F., Checchetto, V., Acquasaliente, L., Butera, G., Filippis, V. de, Szabò, I., Zanotti, G., Rizzuto, R., and Raffaello, A. (2016). A MICU1 Splice Variant Confers High Sensitivity to the Mitochondrial Ca<sup>2+</sup> Uptake Machinery of Skeletal Muscle. *Molecular cell* 64, 760-773. <https://doi.org/10.1016/j.molcel.2016.10.001>.

Verma, M., Callio, J., Otero, P.A., Sekler, I., Wills, Z.P., and Chu, C.T. (2017). Mitochondrial Calcium Dysregulation Contributes to Dendrite Degeneration Mediated by PD/LBD-Associated LRRK2 Mutants. *The Journal of Neuroscience* 37, 11151-11165. <https://doi.org/10.1523/JNEUROSCI.3791-16.2017>.

Wachnowsky, C., Fidai, I., and Cowan, J.A. (2018). Iron-sulfur cluster biosynthesis and trafficking - impact on human disease conditions. *Metallomics*. 10, 9-29. <https://doi.org/10.1039/c7mt00180k>.

- Waldeck-Weiermair, M., Jean-Quartier, C., Rost, R., Khan, M.J., Vishnu, N., Bondarenko, A.I., Imamura, H., Malli, R., and Graier, W.F. (2011). Leucine zipper EF hand-containing transmembrane protein 1 (Letm1) and uncoupling proteins 2 and 3 (UCP2/3) contribute to two distinct mitochondrial Ca<sup>2+</sup> uptake pathways. *J. Biol. Chem.* *286*, 28444-28455. <https://doi.org/10.1074/jbc.M111.244517>.
- Wang, J.-Q., Chen, Q., Wang, X., Wang, Q.-C., Wang, Y., Cheng, H.-P., Guo, C., Sun, Q., Chen, Q., and Tang, T.-S. (2013). Dysregulation of mitochondrial calcium signaling and superoxide flashes cause mitochondrial genomic DNA damage in Huntington disease. *J. Biol. Chem.* *288*, 3070-3084. <https://doi.org/10.1074/jbc.M112.407726>.
- Wei, A.-C., Liu, T., Winslow, R.L., and O'Rourke, B. (2012). Dynamics of matrix-free Ca<sup>2+</sup> in cardiac mitochondria: two components of Ca<sup>2+</sup> uptake and role of phosphate buffering. *The Journal of General Physiology* *139*, 465-478. <https://doi.org/10.1085/jgp.201210784>.
- Wei, M.C., Lindsten, T., Mootha, V.K., Weiler, S., Gross, A., Ashiya, M., Thompson, C.B., and Korsmeyer, S.J. (2000). tBID, a membrane-targeted death ligand, oligomerizes BAK to release cytochrome c. *Genes & development* *14*, 2060-2071.
- Weinberg, S.E., Sena, L.A., and Chandel, N.S. (2015). Mitochondria in the regulation of innate and adaptive immunity. *Immunity* *42*, 406-417. <https://doi.org/10.1016/j.immuni.2015.02.002>.
- Westphalen, B.C., Wessig, J., Leyboldt, F., Arnold, S., and Methner, A. (2005). BI-1 protects cells from oxygen glucose deprivation by reducing the calcium content of the endoplasmic reticulum. *Cell Death and Differentiation* *12*, 304-306. <https://doi.org/10.1038/sj.cdd.4401547>.
- Winqvist, R.J., and Gribkoff, V.K. (2020). Targeting putative components of the mitochondrial permeability transition pore for novel therapeutics. *Biochemical pharmacology* *177*, 113995. <https://doi.org/10.1016/j.bcp.2020.113995>.
- Witkowski, A., Thweatt, J., and Smith, S. (2011). Mammalian ACSF3 protein is a malonyl-CoA synthetase that supplies the chain extender units for mitochondrial fatty acid synthesis. *J. Biol. Chem.* *286*, 33729-33736. <https://doi.org/10.1074/jbc.M111.291591>.
- Wollweber, F., Malsburg, K. von der, and van der Laan, M. (2017). Mitochondrial contact site and cristae organizing system: A central player in membrane shaping and crosstalk. *Biochimica et biophysica acta. Molecular cell research* *1864*, 1481-1489. <https://doi.org/10.1016/j.bbamcr.2017.05.004>.
- Wu, Y., Rasmussen, T.P., Koval, O.M., Joiner, M.A., Hall, D.D., Chen, B., Luczak, E.D., Wang, Q., Rokita, A.G., and Wehrens, X.H.T., et al. (2015). The mitochondrial uniporter controls fight or flight heart rate increases. *Nat Commun* *6*, 6081. <https://doi.org/10.1038/ncomms7081>.
- Xu, Q., and Reed, J.C. (1998). Bax Inhibitor-1, a Mammalian Apoptosis Suppressor Identified by Functional Screening in Yeast. *Molecular Cell* *1*, 337-346. [https://doi.org/10.1016/s1097-2765\(00\)80034-9](https://doi.org/10.1016/s1097-2765(00)80034-9).
- Xu, Z., Zhang, D., He, X., Huang, Y., and Shao, H. (2016). Transport of Calcium Ions into Mitochondria. *Current Genomics* *17*, 215-219. <https://doi.org/10.2174/1389202917666160202215748>.
- Yang, S., and Lian, G. (2020). ROS and diseases: role in metabolism and energy supply. *Molecular and Cellular Biochemistry* *467*, 1-12. <https://doi.org/10.1007/s11010-019-03667-9>.
- Yoshida, T., Nagata, S., and Kataoka, H. (2006). Ghitm is an ortholog of the Bombyx mori prothoracic gland-derived receptor (Pgdr) that is ubiquitously expressed in mammalian cells and requires an N-terminal signal sequence for expression. *Biochemical and biophysical research communications* *341*, 13-18. <https://doi.org/10.1016/j.bbrc.2005.12.141>.

- Zamzami, N., and Kroemer, G. (2001). The mitochondrion in apoptosis: how Pandora's box opens. *Nature reviews. Molecular cell biology* 2, 67-71. <https://doi.org/10.1038/35048073>.
- Zhang, K., Li, H., and Song, Z. (2014). Membrane depolarization activates the mitochondrial protease OMA 1 by stimulating self-cleavage. *EMBO Rep* 15, 576-585. <https://doi.org/10.1002/embr.201338240>.
- Zhang, L., Joshi, A.K., Hofmann, J., Schweizer, E., and Smith, S. (2005). Cloning, expression, and characterization of the human mitochondrial beta-ketoacyl synthase. Complementation of the yeast CEM1 knock-out strain. *Journal of Biological Chemistry* 280, 12422-12429. <https://doi.org/10.1074/jbc.M413686200>.
- Zhou, J., Dhakal, K., and Yi, J. (2016). Mitochondrial Ca(2+) uptake in skeletal muscle health and disease. *Science China. Life sciences* 59, 770-776. <https://doi.org/10.1007/s11427-016-5089-3>.
- Zhou, Z., Austin, G.L., Young, L.E.A., Johnson, L.A., and Sun, R. (2018). Mitochondrial Metabolism in Major Neurological Diseases. *Cells* 7, 229. <https://doi.org/10.3390/cells7120229>.
- Zou, S., Meadows, S., Sharp, L., Jan, L.Y., and Jan, Y.N. (2000). Genome-wide study of aging and oxidative stress response in *Drosophila melanogaster*. *Proceedings of the National Academy of Sciences of the United States of America* 97, 13726-13731. <https://doi.org/10.1073/pnas.260496697>.

## 8. Appendix

### 8.1. Abbreviations

$\alpha/\beta$ -tub	$\alpha/\beta$ -Tubulin	b-MCC	bursting mitochondrial calcium channel
(BN) PAGE	(blue native) polyacrylamide gel electrophoresis	bp	base pairs
(m)NCX	(mitochondrial) Na <sup>+</sup> /Ca <sup>2+</sup> -exchanger	BSA	bovine serum albumin
[Ca <sup>2+</sup> ] <sub>cyt</sub>	cytosolic calcium concentration	C	complex I/II/III/IV/V
[Ca <sup>2+</sup> ] <sub>mit</sub>	mitochondrial calcium concentration	I/II/III/IV/V	
ADP	adenosine diphosphate	CGP	CGP-37157
AmA	antimycin A	CHCHD	coiled-coil-helix-coiled-coil domain
ANT	adenine nucleotide transporter	CJ	cristae junction
ATP	adenosine triphosphate	CM	cristae membrane
AUC	area under the curve	CoA	coenzyme A
BAK	BCL-2 antagonist/killer	coxIV	cytochrome c oxidase subunit IV
BAX	BCL-2-associated X protein	CsA	cyclosporin A
BCA	bicinchoninic acid	CTH	Centre for Thrombosis and Haemostasis
BFP2	blue fluorescent protein 2	ctl.	control
BI-1	BAX Inhibitor 1	CypD	cyclophilin D
BM	basic medium	cyt c	cytochrome c

D326R	homozygous D326R mutant
DDM	Dodecyl- $\beta$ -D-maltoside
DMSO	dimethylsulfoxid
DRP1	dynamain-1-like protein
DTNB	5,5-dithiobis(2-nitrobenzoic acid)
DYN2	dynamain-2
EE	energy expenditure
EMRE	essential MCU regulator
EPM	elevated plus-maze
ER	endoplasmic reticulum
EtOH	ethanol
ETS	electron transport system
FA	fatty acids
FAD(H <sub>2</sub> )	flavin adenine dinucleotide (dihydroxide)
FBS	fetal bovine serum
FCCP	Carbonyl cyanide-p-trifluoromethoxyphenylhydrazo ne
Fe-S-clusters	iron-sulfur-clusters
Fig.	figure
FSC	forward scatter
G6PD	glucose-6-phosphate-dehydrogenase
GAPDH	Glyceraldehyde-3-phosphate Dehydrogenase
gDNA	genomic DNA
GH	Growth hormone
GHITM	growth hormone inducible transmembrane protein
GSH	glutathione
GSSG	oxidised glutathione
het	heterozygous
HM	homogenisation medium
HMIM	Heart Mitochondria Isolation Medium
IBc	isolation buffer cells
IL-6	interleukin 6
IMAN	Institute for Microscopic Anatomy and Neurobiology
i-MCC	intermediate mitochondrial calcium channel
IMM	inner mitochondrial membrane
IMS	intermembrane space
INF2	Inverted formin 2

IP3R	Inositol-1,4,5-triphosphate-receptor
IRES	internal ribosome entry site
IS	isolation solution
JGU	Johannes Gutenberg-University Mainz
kDa	kilo Dalton
KO	knockout
L-012	8-Amino-5-Chloro-7-Phenylpyrido[3,4-d] pyridazine-1,4-(2H,3H) Dion
LETM1	Leucine Zipper-EF-hand-containing transmembrane protein 1
I-OPA1	long isoform of OPA1
M. Soleus	Musculus Soleus
MBU	Mouse Behavior outcome Unit
mCHX	mitochondrial Ca <sup>2+</sup> -H <sup>+</sup> -exchanger
MCU	mitochondrial calcium uniporter
MCUR1	MCU regulator 1
MERC	mitochondria-ER contact sites
MFI	mean fluorescent intensity
MFN1/2	Mitofusin 1/2
MICOS	mitochondrial contact site and cristae organizing system
MIC	MICOS complex subunit
MICS1	Mitochondrial Morphology and Cristae Structure 1
MICU1/2/3	mitochondrial calcium uptake 1/2/3
MMC	mitochondrial megachannel
MMP	mitochondrial membrane potential
mNHE	Na <sup>+</sup> -H <sup>+</sup> -exchanger
MOMP	mitochondrial outer membrane permeabilisation
mPTP	mitochondrial permeability transmission pore
mRyR1	mitochondrial ryanodine receptor 1
MSS	mitochondria suspension solution
mtCU	mitochondrial calcium uniporter complex

mtDNA	mitochondrial DNA
MTS	mitochondrial targeting sequence
n.s.	not significant
NAD(P)H	nicotinamide adenine dinucleotide (phosphate)
NCLX	mitochondrial Na <sup>+</sup> -Ca <sup>2+</sup> -Li <sup>+</sup> -exchanger
NNT	nicotinamide nucleotide transhydrogenase
Norm.	normalised
OF	open field
OMA1	overlapping with the m-AAA protease 1 homolog
OMM	outer mitochondrial membrane
Omy	Oligomycin
OPA1	optical atrophy 1
ORF	open reading frame
OXPHOS	oxidative phosphorylation
PAMP/DAMP	pathogen- /damage-associated pattern
PBR	peripheral-type benzodiazepine receptor
PBS	phosphate-buffered saline
PDBU	Phorbol-12,13-Dibutyrate
PDH (E2/3BP)	pyruvate dehydrogenase (E2/3 binding protein)
PEG	polyethyleneglycol-3350
PFA	paraformaldehyde
PLA	proximity ligation assay
pMEF	primary mouse embryonic fibroblast
PPI	prepulse inhibition
RaM	rapid mode of uptake
REE	resting energy expenditure
RER	respiratory exchange rate

ROI	region of interest
ROS	reactive oxygen species
ROX	residual oxygen consumption
RT	room temperature
RuR	Ruthenium Red
RyR	ryanodine receptor
SEM	standard error of the mean
SERCA	sarcoplasmic/endoplasmic reticulum Ca <sup>2+</sup> ATPase
SOCE	store-operated calcium entry
s-OPA1	short isoform of OPA1
SSA	5-sulfosalicylic acid
SSC	sideways scatter
SUIT	substrate-uncoupler-inhibitor-titration
T5	Transmembrane BAX Inhibitor Motif containing protein 5
tBid	truncated BH3-interacting domain death agonist
TBS(T)	tris-buffered saline (+ Tween20)
TCA cycle	tricarboxylic acid cycle
TMBIM (5)	Transmembrane BAX Inhibitor Motif containing protein (5)
TMRM	Tetramethylrhodamine methyl ester
TNB <sup>-</sup>	2-Nitro-thiobenzoat
TRPC3	Transient receptor potential channel 3
UCP 2/3	uncoupling proteins 2/3
V. facialis	Vena facialis
VDAC	voltage-dependent anion channel
WT	wildtype
xl-MCC	xl-mitochondrial calcium channel
YME1L	YME-1-like protein

## 8.2. Acknowledgements



[REDACTED]

### 8.3. Curriculum Vitae

[Redacted]

Name [Redacted]

Born [Redacted]

[Redacted]

2018/01 - 2021/12 [Redacted]

[Redacted]

2016/04 - 2017/09 [Redacted]

[Redacted]

2015/11 - 2016/01 [Redacted]

[Redacted]

2015/07 - 2015/09 [Redacted]

[Redacted]

[Redacted]

2014/07 - 2014/08 [Redacted]

[Redacted]

[Redacted]

2011/05 - 2012/05 [Redacted]

[Redacted]

[Redacted]

2015/10 - 2017/10 [Redacted]

[Redacted]

[Redacted]

[Redacted]

[Redacted]

2012/10- 2015/10

[Redacted]

[Redacted]

[Redacted]

[Redacted]

2011/05- 2012/05

2002/09- 2011/05

[Redacted]

Languages [Redacted]

Qualifications [Redacted]

[Redacted]

[Redacted]

[Redacted]

Since 2021/03 [Redacted]

2019/11- 2022/01 [Redacted]

[Redacted]

2018/01- 2021/12 [Redacted]

[Redacted]

2021 [Redacted]

[Redacted]

2021 [Redacted]

[Redacted]

2020 [Redacted]

[Redacted]

[Redacted]

[Redacted]

[Redacted]